

In Partnership with
LITHUANIA

XIV JENA
LASER
CONFERENCE



#JLT14

CONFERENCE PROCEEDINGS

Lasers and processes for
digital manufacturing technology

JENA, NOV 6+7 24

LASERTAGUNG-JENA.DE





OptoNet e. V. (Publisher)

14th Jena Laser Conference

Lasers and processes for digital manufacturing technology

Topics

Laser welding
Advanced laser coatings and optics
Optics and beam shaping
Ultrashort pulse laser processing
Ultrafast lasers
Laser processing of advanced materials
Additive manufacturing
Metrology and characterization in laser processing

Event Partners

OptoNet e. V.
University of Applied Sciences Jena
Günter-Köhler-Institute for Joining Technology and Materials Testing (ifw Jena)
Institute of Applied Physics Friedrich Schiller University Jena



Bibliographic information of the German National Library

The German National Library lists this publication in the German National Bibliography; detailed data is available on the Internet at <https://portal.dnb.de/>.

Publisher: OptoNet e.V.

eISBN (PDF) 978-3-932886-45-4

© 2024 Verlag Ernst-Abbe-Hochschule Jena, Jena, Germany

Reproduction, even in part, is only permitted with the permission of the University of Applied Sciences Jena.

University of Applied Sciences Jena
Carl-Zeiss-Promenade 2
07745 Jena
Germany

Typesetting/Layout: Manuela Lohse, ML Verlagswesen, Jena, Germany
Proofreading: The contributions and posters were set as manuscripts.

Next Level – The Jena Laser Conference Expands!

For many years, the Jena Laser Conference has been a must-attend event for experts in laser technology, especially for those with focus in ultrashort pulse lasers. This year, we are taking an exciting step by expanding the conference to a broader, more international audience. For the first time, the event will be held entirely in English, and we are delighted to welcome Lithuania as our special partner region for 2024.

What brings us together?

Jena and Lithuania have long been recognized as leaders in laser and photonics innovation. Both regions boast a strong tradition of excellence in research and development, particularly in cutting-edge laser technologies. Lithuania is known for its expertise in ultrafast lasers and optical solutions, while Jena continues to be a hub for pioneering advancements in photonics. By coming together, we seek to foster collaboration, share knowledge, and spark new ideas that will drive the future of laser technology forward.

What can you expect?

The Jena Laser Conference 2024 will spotlight significant advancements in laser technology and its diverse applications. Key topics will include ultrashort pulse lasers, high-power laser systems, and innovative laser-based manufacturing processes such as welding, cutting, and additive manufacturing (3D printing). Another central theme will be the integration of lasers with sensors, enhancing precision and automation in industrial processes.

Additionally, the conference will cover the latest trends in micro-optics and beam shaping, with discussions on how these technologies are enabling new possibilities in various industries. Innovative material processing technologies will also play a prominent role in the agenda. Keynote speakers, who are leaders in the global laser industry and research, will offer invaluable insights into the future of these technologies and their potential to reshape industries worldwide.

We are excited to welcome many participants to Jena for what promises to be an inspiring and forward-looking event!

Anke Siegmeier, Nora Kirsten

Program Commission

Prof. Dr. Hartmut Bartelt	Leibniz Institute of Photonic Technology e. V.
Prof. Dr.-Ing. habil. Jean-Pierre Bergmann	Ilmenau University of Technology
Prof. Dr.-Ing. Jens Bliedtner	Ernst Abbe University of Applied Sciences Jena
Prof. Dr. rer. nat. habil. Alexander Horn	Mittweida University of Applied Sciences
Thomas Hucke	Linde AG, Linde Gas Division
Dr.-Ing. Simon Jahn	ifw Jena Günter-Köhler-Institute for Joining Technology and Materials Testing
Nora Kirsten	OptoNet e. V.
Prof. Dr. Stefan Nolte	Friedrich Schiller University Jena
Klaus Stolberg	JENOPTIK AG
Prof. Dr. rer. nat. habil. Andreas Tünnermann	Fraunhofer Institute for Applied Optics and Precision Engineering IOF

Sponsors and supporters

We would like to thank our sponsors and supporters for organizing and conducting the conference.



MORE LIGHT



Table of contents

Editorial	4
Program Commission.....	5
Sponsors and supporters	5
 <u>KEYNOTE</u>	
Laser Industry from Lithuania.....	9
 <u>SESSION 1A – LASER WELDING</u>	
Direct Ultrafast Laser Welding of Transparent to Non-Transparent Materials	10
Welding of ceramics using ultrashort pulse lasers	17
Handheld laser welding – systems, applications and safe usage.....	24
 <u>SESSION 1B – ADVANCED LASER COATINGS AND OPTICS</u>	
Highly Absorptive Coatings for Laser Components.....	32
PARMS coating technology for UV to IR laser applications.....	38
IBS optics for high-capacity laser processing	39
 <u>KEYNOTES</u>	
Democratization of Laser Technology: A Journey of Unlimited Opportunities.....	40
Laser applications for sustainable electrical energy storage and converters.....	41
 <u>SESSION 2A – OPTICS AND BEAM SHAPING</u>	
Tailored refractive diffusers for broadband beam shaping	42
Combining freeform optics and Zwobbel technology for line structuring of large substrates with ultrashort pulsed 2 μ m lasers	43
Manufacturing and assembly of a High-Finesse Cavity	44
Minimisation of process times in high-quality laser cutting through dynamic beam shaping in propagation direction.....	51

SESSION 2B – ULTRASHORT PULSE LASER PROCESSING

Ultrafast laser processing on large surfaces – Machine concepts and applications.....	52
High strength micro-welded glass	55
Influencing factors on the creation of subsurface damages during ultrashort pulse laser machining of glass	56
Customized edge cutting of display glasses from structured ultrashort laser pulses.....	61

KEYNOTES

Laser Inertial Fusion – Critical Advancement for Germany's Optics and Laser Sectors.....	68
TRUMPF Laser Amplifier – The high power laser source for EUV lithography“	69

SESSION 3A – ULTRAFAST LASERS

Industrial-grade 2- μ m ultrafast fiber CPA for silicon processing	70
Industrial Ultrafast kW-Class Lasers Above 10 mJ Enabled by Thin-Disk Multipass Amplifier.....	71
Highly efficient, high-power thulium-doped fiber laser systems	74

SESSION 3B – LASER PROCESSING OF ADVANCED MATERIALS

SiC high-tech ceramics – a comparison of laser processes	77
Laser Swelling induced Freeform Microlenses in Polymers	82
Dielectric Material Processing with Ultra-Short Pulses	83

ADVANCED LASER TECHNOLOGIES

Femtoseconds. Creating new possibilities	88
--	----

KEYNOTE

Industrialization of Additive Manufacturing (AM).....	89
---	----

SESSION 4A – ADDITIVE MANUFACTURING

Design Criteria for the Functionalisation of Additively Manufactured Aluminium Components by Integrating Sensors during the Manufacturing Process	90
Design and fabrication of a TPMS-based micro heat exchanger via micro selective laser melting.....	98
Additive manufacturing of pure Molybdenum utilizing ultra-short laser pulses	108
Structured metal coatings on glass enabled by ultrashort laser processes	109

SESSION 4B – METROLOGY AND CHARACTERIZATION IN LASER PROCESSING

Laser assisted analytical depth profiling (LAADP) – an innovative method for high-precision analysis	110
Classification of surface structures in ultrashort pulse laser processing using machine learning based on light microscopic images	119
Multi-sensor conception for process monitoring in laser welding with beam oscillation	120
Predictable laser material processing by combining ultrafast metrologies with modeling	121
Posters	123
Author directory	134

Laser Industry from Lithuania

Kristina Ananičienė
LITEK™, Lithuania

Abstract

The laser industry in Lithuania has rapidly evolved into a key player in the global photonics market. This sector showcases notable strengths in optics, ultrafast lasers, and laser systems integration. Collaborative efforts between academia, research institutes, and industry have driven significant advancements in laser-based manufacturing, scientific and medical applications, semicon, defence and more. Despite challenges, ongoing strategic initiatives aim to sustain Lithuania's competitive edge and foster continued innovation within the laser industry.



Direct Ultrafast Laser Welding of Transparent to Non-Transparent Materials

Blothe, M.¹; Chambonneau, M.¹; Markogiannaki, S.¹; Keça, A.¹; Nolte S.^{1,2}

¹ Friedrich Schiller University Jena, Institute of Applied Physics, Abbe Center of Photonics, Jena, Germany

² Fraunhofer Institute for Applied Optics and Precision Engineering IOF, Jena, Germany

In this contribution, ultrafast laser welding of transparent materials to metals is presented. The laser pulse energy, scanning speed and intra-burst delay dependency for joining Borofloat glass B33 to Ti/Al6/V4 are explored, and a maximum shear joining strength >6 MPa is achieved, allowing to envision various applications. To explore the resistivity towards a thermal cycle, samples are heated to different temperatures and the residual shear joining strength is measured after cool down. A failure of the connection is seen for temperatures surpassing 120°C. The possibility to join fused silica to Kovar, a metal with an adapted thermal expansion coefficient, is demonstrated next, to possibly increase the thermal cycle stability. To highlight the universal applicability of this joining method, welding of a semiconductor to metal is shown, here illustrated with silicon and copper. In the narrow-band gap semiconductor material, the nonlinear propagation of high intensity laser pulses needs to be considered to optimize the deposited energy at the interface and enhance the resulting connection. A maximum shear joining strength >2 MPa is achieved, demonstrating industrial compatibility.

1 Introduction

The industrial need of joining materials can be met by various techniques. Such techniques include adhesive or anodic bonding and bonding by heat treatment, but they all come with individual drawbacks. For example, glue as an additional material is needed in the case of adhesive bonding, which can show aging and outgassing, making it unsuitable for vacuum and space applications.

On the other hand, the laser is a versatile tool for countless applications in research and industry. Especially in the field of material processing, ultrashort laser pulses (USP) are a driver to enable processes that are not addressable with other techniques by providing a high control on the energy deposition. The applications range from ablation to restructuring, either on the surface or in the bulk of transparent materials.

Besides these, USP can also be used to join a wide variety of materials in a fast, clean and contactless way [1,2]. This technique can overcome different drawbacks of standard techniques, e.g., no additional material is needed, which otherwise could present a weak point. When one of the joined pieces is transparent, the laser can be directed through the transparent joining partner onto the interface. The localized energy deposition leads to melting, mixing, and re-solidification of the materials at the interface and with this the formation of bonds. An area can be scanned by translating the laser focus with respect to the work pieces. With this approach, more area can be processed in comparison to standard contour welding to increase the welding strength. The joining of different material combinations has been demonstrated by this technique, including glass–metal [3], glass–glass [2,4], glass–semiconductor [5], polymer–polymer [6] and recently ceramic–ceramic [7].

This contribution is divided into two main parts. In the first part, the joining of different glass–metal combinations is explored. Optimized laser parameters are determined for achieving the highest shear joining strength. Following, thermal cycles are carried to explore the robustness towards thermal loads of the joint parts. To increase the robustness towards temperature changes, the feasibility of the material combination of fused silica–Kovar, an iron-nickel-cobalt alloy showing similar thermal expansion coefficients (TEC) as glass, is explored.

In the second part, ultrafast laser welding is demonstrated for a different type of material combination, semiconductor–metal [8]. Here, not only a change of wavelength into the transparency domain of the semiconductor, silicon, is needed, but the nonlinear propagation has to be considered to optimize the deposited energy at the interface [9].

2 Glass–Metal welding

2.1 Experimental setup

For glass–metal welding, a TRUMPF TruMicro 2030 laser with a wavelength of 1030 nm and a pulse duration of 365 fs is utilized, as shown in the schematic of the experimental setup in Figure 1. For the experiments, the pulse energy is split into 8 sub-pulses, so called burst, with an intra-burst delay of 20 or 40 ns. The fundamental pulse repetition rate is 125 kHz. The beam is guided through a half-wave plate and polarizer combination to adjust the pulse energy. A telescope adapts the beam size to the opening aperture of the 10× focusing objective lens (Mitutoyo M Plan Apo NIR 10×, NA=0.26). A top-view observation is realized by the same objective lens and a combination of a dichroic mirror, an indirect sample illumination, a tube lens, and a camera. It is used to facilitate precise positioning of the focus with respect to the sample. The sample is placed on a translation stage and together with a movement possibility of the objective lens, a 3D positioning of the focus with respect to the sample is enabled. The chosen welding path of the laser is a spiral with a minimal diameter of 0.16 mm, a line distance of 20 μm, and a maximum diameter of 4.96 mm, to suppress stress accumulation at the edges. In terms of sample preparation, a cleaning step with Isopropanol and consecutive optical contacting is performed before the samples are placed on the stage.

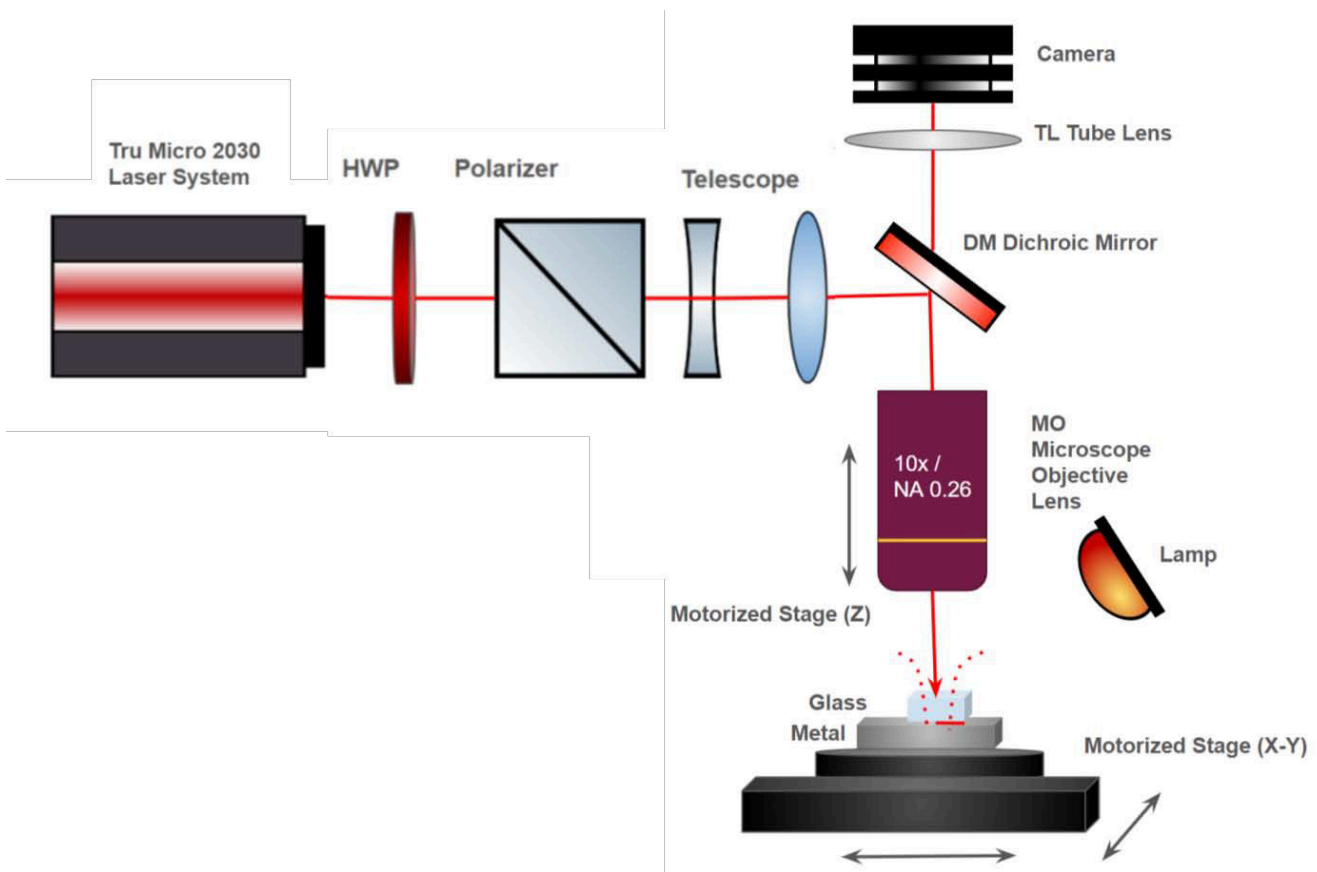


Figure 1: Experimental setup for glass–metal welding

To access the quality of the welded samples, the shear joining strength is measured by a test-stand consisting of a clamping possibility and a force gauge, as shown in Figure 2. The indenter, connected to the force gauge, pushes the welded top part of the sample parallel to the interface and records the force until the pieces are separated. The maximum force F_{\max} is used to calculate the shear-joining-strength P by:

$$P = \frac{F_{\max}}{A},$$

where A is the considered area. In a first approximation, we consider the area between the minimal and maximal diameter of the laser spiral path.

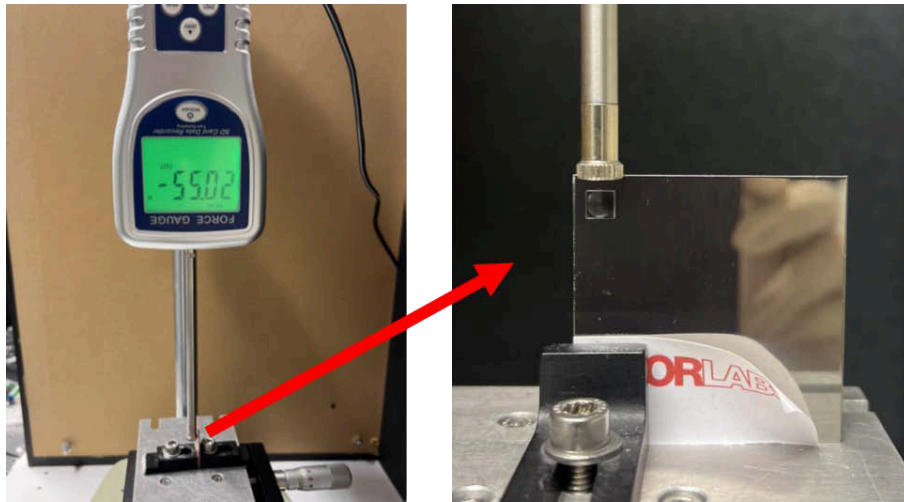


Figure 2: Shear joining test stand with a placed sample.

2.2 Process parameter: Pulse energy, intra-burst distance, and scanning speed

At the beginning, fundamental dependencies for the material combination of a borosilicate glass (Schott B33) and Ti/Al6/V4 are explored with respect to the employed pulse energy and the scanning speed. It has to be noted that in general, a large variation in the measured shear joining strength is observed between identical parameters. We ascribe this mostly to the critical step of optical contacting before the sample is placed on the stage. If the gap between the material is not homogeneously small (<1 μm), certain regions will not be welded and with this not contribute to the measured force. To keep the experimental work manageable, repeatability tests were carried out for some conditions and the determined uncertainty is applied to all data.

Figure 3 compares the measured shear joining strength in dependency of the pulse energy for two intra-burst delays of 20 (red) and 40 ns (blue). A systematically higher shear joining strength is measured for the 40 ns case, showing a value >6 MPa for a pulse energy of 225 nJ per pulse in the burst (1.8 μJ total burst energy). This indicates that heat accumulation happening between the individual pulses in a burst influences the material response. A delay of 40 ns between consecutive pulses exalts the formation of bonds. A local optimum is identified around 225 nJ, so either energies too low or too high lead to a reduced bonding quality. The achieved maximum shear joining strength >6 MPa indicates applicability to industrial processes.

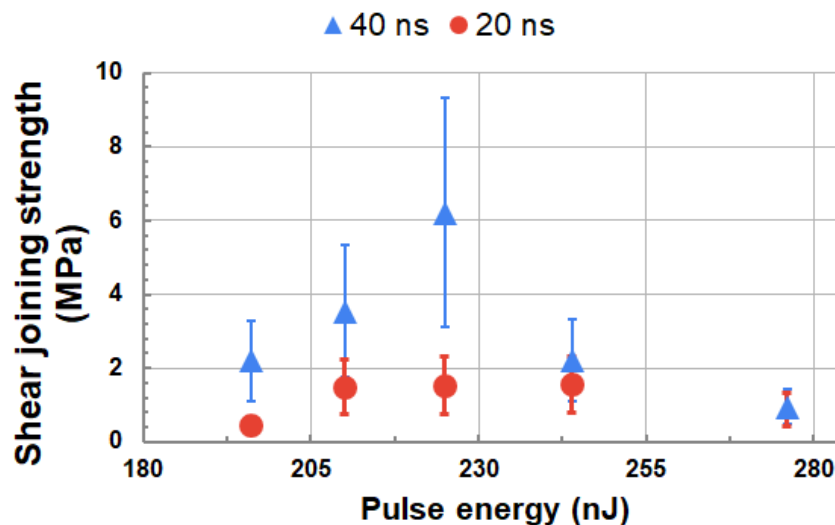


Figure 3: Shear joining strength in dependence of input pulse energies for 20 ns (red) and 40 ns (blue) intra-burst delay.

While the energy shows an optimal window around 225 nJ with decreased values to both sides, the scanning speed has an influence only when the speed is increased beyond 1 mm/s, as shown in Figure 4. By taking the estimated beam diameter at the focus of approx. 4 μm into account, an overlap of at least 500 pulses per spot is needed to achieve sufficient bonding. Further reduction of scanning speed does not elevate the resulting strength. For these data, an intra-burst delay of 20 ns and a pulse energy of 210 nJ was used.

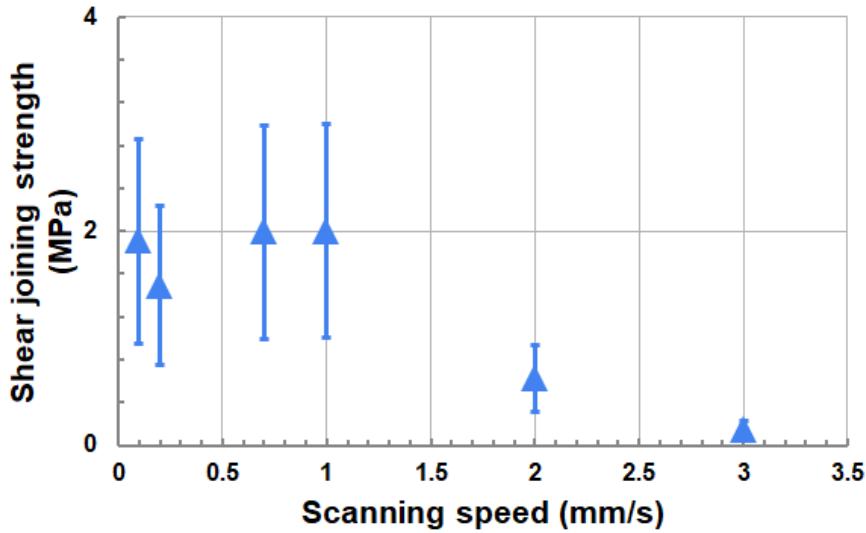


Figure 4: Shear joining strength for different scanning speeds for a burst delay of 20 ns and a pulse energy of 210 nJ.

2.3 Thermal cycle resistance

While welding with ultrashort laser pulses offers numerous advantages, the localized heat deposition could lead to residual stress in the joint workpiece. By heat-cycling, this stress might be released. This is investigated here by putting different samples processed with different pulse energies into a furnace for one hour, where they were heated to different maximum temperatures ranging from 50°C up to 200°C. After removing the samples from the furnace, they cooled down to room temperature and the shear joining strength was measured afterwards. The data and a comparison to non-cycled samples is shown in Figure 5 for three different pulse energies.

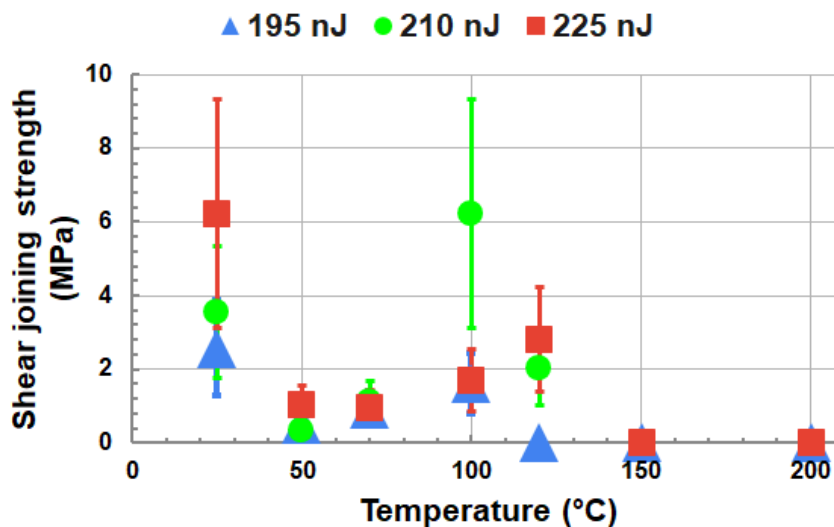


Figure 5: Shear joining strength for different maximum temperatures of a cycle for different pulse energies.

The first major finding is that after a temperature cycle of only 50°C, the joining seems to be drastically weakened. This might be related to the aforementioned large variation between identical samples, as for higher maximum temperatures of 100°C a re-establishment of measured shear joining strength is observed. For samples heated to temperatures of 150°C and 200°C, no force could be measured, indicating a temperature region which leads to a permanent failure of the joint for the material combination of B33 and Ti/Al6/V4. This can be related to the difference in coefficient of thermal expansion (CTE). $CET_{Ti/Al6/V4} = 9 \times 10^{-6} \text{ K}^{-1}$, $CET_{B33} = 3 \times 10^{-6} \text{ K}^{-1}$. This leads to accumulation of stress that is in the first approximation proportional to the temperature.

2.4 Outlook: Kovar–Fused silica

To explore the possibility of more temperature resistant joints, a different material combination is currently explored. Kovar, an Iron (54%) Nickel (29%) Cobalt (17%) alloy, showing a CTE closer to the one of glass ($4 \times 10^{-6} \text{ K}^{-1}$), is chosen as the metal partner. A preliminary result, showing the general feasibility of ultrashort laser welding of SiO₂-Kovar is shown in Figure 6. Experiments for detailed results are currently conducted, but similar shear joining strength >6 MPa could be achieved for non-thermal cycled samples.



Figure 6: A 5x5 mm fused silica sample welded to Kovar

3 Semiconductor–Metal welding

Silicon, the base material in the microelectronic industry, is not transparent in the visible range but to wavelengths >1.1 μm, a result of its narrow band gap of 1.12 eV. To show the broad applicability of ultrashort laser pulse welding, it is used here as the transparent partner together with a metal, copper in this case. As a first consequence, a different laser source is needed to be able to reach the interface. An Er-fiber laser emitting pulses of 875 fs with a wavelength of 1.55 μm is utilized. The pulse duration is adaptable and can reach up to 10 ps, which is used throughout the experiments presented here.

3.1 Consequence of nonlinear properties

A difficulty to overcome in this narrow-band gap material is the nonlinear-propagation behavior due to the high nonlinear refractive index, that is about 100 times larger than in fused silica [9]. This leads first to a drastic delocalization of the energy deposition by alternating the shape of the focal zone even for relatively low pulse energies < 100 nJ and finally to filamentation and energy clamping. Experimental observations allow for a determination of the shift of the maximum fluence position, as shown in Figure 7 [8].

While in the linear case the fundamental shape is the expected Gaussian caustic, this changes for higher energies. A focal shift towards the input surface becomes apparent, leading to a nonlinear deviation between the focus and the plane of highest fluence. This deviation becomes larger with increasing pulse energy, in agreement with a modified Marburger formula where power losses are accounted for [8]. For the highest energies, the start of the formation of a filament is observed.

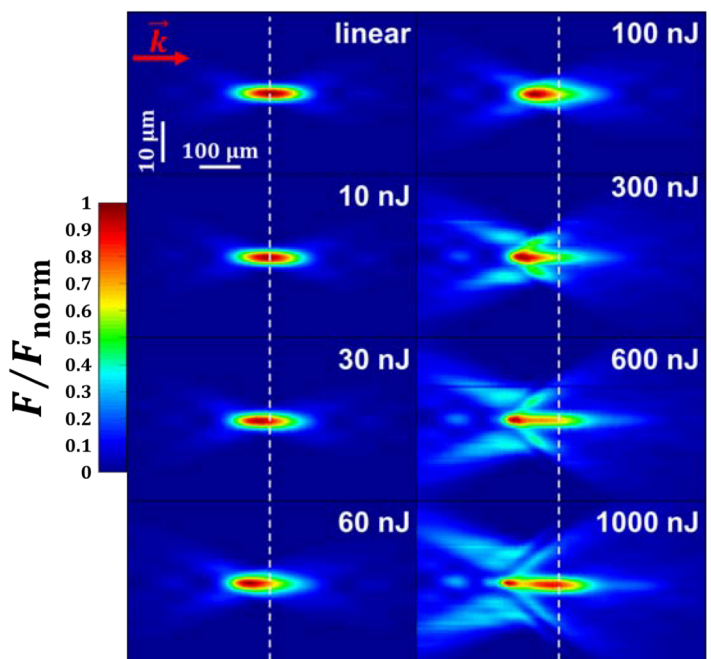


Figure 7: Normalized fluence distributions measured in silicon for the indicated input pulse energies. Nonlinear propagation effects and filamentation can be observed. [8]

3.2 Adapted focus position

With the knowledge of how much the focal zone is shifted by the nonlinear propagation, one can anticipate and adapt the focusing depth accordingly to deposit the highest amount of energy at the interface. Figure 8 compares the shear joining strength for samples welded at the geometrical focus (red) and with the pre-compensated position for the nonlinear focal shift (green).

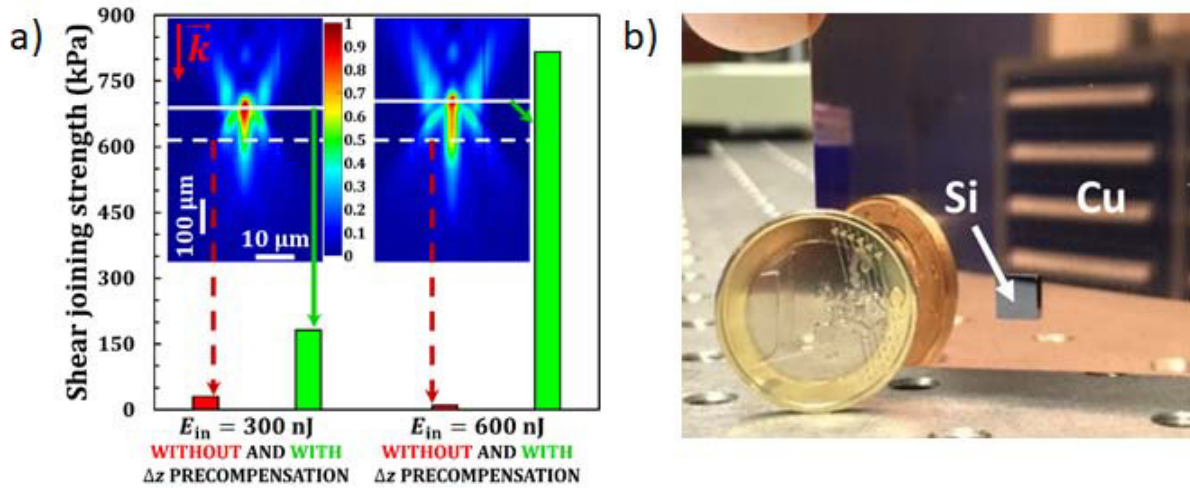


Figure 8: Shear joining strength for the case of the geometrical focus setting (red) and the pre-compensation of the focal shift due to nonlinear effect (green). b) Silicon sample welded to copper. [8]

It becomes quite clear that the increased amount of deposited energy enhances the bonding drastically, as the shear joining strength is higher by more than a factor of ten in the case of pre-compensation. A joint silicon piece on the copper is shown in Figure 8 (b). The welding pattern follows a raster scan with a line distance of 10 μ m, a translation speed of 1 mm/s, at 100 kHz laser repetition rate. A total area of 4.5x4.5 mm² is processed. The energy dependence of the achievable shear joining strength is shown in Figure 9.

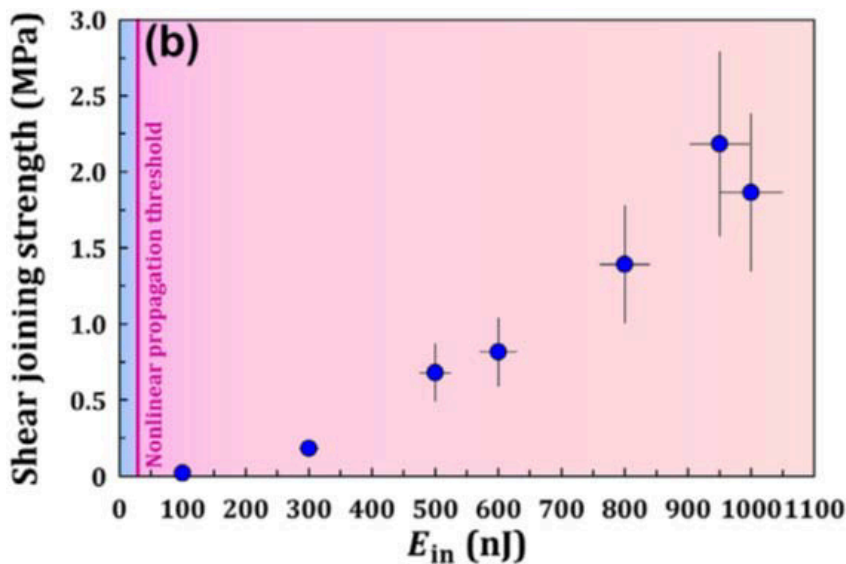


Figure 9: Shear joining strength of Silicon to copper for different input energies.[8]

The measured shear joining strength increases with input energy when the nonlinear focal shift is considered. A maximum shear joining strength >2 MPa for an input pulse energy of 950 nJ is measured, allowing to envision new applications with this joining method for this semiconductor material.

4 Conclusion

Overall, it was shown that direct ultrafast laser welding can be used to join various glasses to non-transparent materials in a fast, clean, and contactless way. The specific laser conditions as well as the requirement of optical contact determine the quality of the joint. In the case of B33 to Ti/Al6/V4 the joint seems to be quite sensitive towards thermal cycling above 125°C. The possibility to transpose this technique to semiconductors, as long as the nonlinear propagation effects are considered to increase the deposited energy at the interface, is demonstrated.

5 Acknowledgement

We acknowledge funding by the German Federal Ministry of Education and Research through the projects glass2met (grant no. 13N15290) and RUBIN-UKPiño (grant no. 03RU2U033H).

6 References

- [1] Carter, R. M., Chen, J., Shephard, J. D., Thomson, R. R., & Hand, D. P., Picosecond laser welding of similar and dissimilar materials. *Applied Optics*, 53(19), 4233. (2014)
- [2] Richter, S., Zimmermann, F., Tünnermann, A., & Nolte, S., Laser welding of glasses at high repetition rates - Fundamentals and prospects. *Optics and Laser Technology*, 83, 59–66. (2016)
- [3] Zhang, G., & Cheng, G., Direct welding of glass and metal by 1 kHz femtosecond laser pulses. *Applied Optics*, 54(30), 8957–8961. (2015)
- [4] Cvecek, K., Dehmel, S., Miyamoto, I., & Schmidt, M., A review on glass welding by ultra-short laser pulses. *International Journal of Extreme Manufacturing*, 1(4). (2019)
- [5] Zhang, G., Stoian, R., Zhao, W., & Cheng, G., Femtosecond laser Bessel beam welding of transparent to non-transparent materials with large focal-position tolerant zone. *Optics Express*, 26(2), 917. (2018)
- [6] Mingareev, I., Weirauch, F., Olowinsky, A., Shah, L., Kadwani, P., & Richardson, M., Welding of polymers using a 2 μm thulium fiber laser. *Optics and Laser Technology*, 44(7), 2095–2099. (2012)
- [7] Penilla, E. H., Devia-Cruz, L. F., Wieg, A. T., Martinez-Torres, P., Cuando-Espitia, N., Sellappan, P., Kodera, Y., Aguilar, G., & Garay, J. E., Ultrafast laser welding of ceramics. *Science*, 365(6455), 803–808. (2019)
- [8] Chambonneau, M., Li, Q., Fedorov, V. Y., Blothe, M., Schaarschmidt, K., Lorenz, M., Tzortzakis, S., & Nolte, S., Taming Ultrafast Laser Filaments for Optimized Semiconductor–Metal Welding. *Laser and Photonics Reviews*, 15(2), 2000433. (2021)
- [9] Chambonneau, M., Grojo, D., Tokel, O., Ilday, F. Ö., Tzortzakis, S., & Nolte, S., In-Volume Laser Direct Writing of Silicon—Challenges and Opportunities. *Laser and Photonics Reviews*, 15(11), 2100140. (2021)

Welding of ceramics using ultrashort pulse lasers

Conrad, D.¹; Reichenbacher, M.¹; Münch, M.²

¹ ifw Jena – Günter-Köhler-Institut für Fügetechnik und Werkstoffprüfung GmbH, Jena

² Friedrich-Schiller-Universität, Jena

Technical ceramics are known as materials with outstanding properties such as high hardness, abrasion resistance, chemical resistance, electrical insulation and dielectric strength. However, joining fired ceramic components is a huge challenge, especially if the joint is meant to retain the above-mentioned properties while being resistant to high temperatures and hermetically sealed. In this case, conventional joining methods such as bonding or soldering reach their limits. A permanent joining process that does not require any additional material is highly needed.

Since laser welding of ceramics with nanosecond lasers has so far led to cracks and non-vacuum-tight seams, the ifw Jena is currently investigating whether this task can be solved with ultrashort pulses (USP). While these have been extensively researched for transparent glasses, there are hardly any publications on ceramics. The USP laser welding of Al_2O_3 and AlN shall now be developed in a butt joint arrangement. The influence of parameters such as fluence, repetition rate and scanning speed is investigated, starting from multi-pulse experiments over blind weld seams up to actual joints. Due to the small weld seam widths ($< 100 \mu\text{m}$) and the short process time, the thermal load on the material can be kept low compared to conventional furnace-based processes. This should potentially make it possible to encapsulate thermally sensitive elements in ceramic components.

1. Introduction

Due to their outstanding properties, technical ceramics are used in almost all fields of technology [1, 2]: Ceramic roller bearings can absorb very high loads while showing only minimal wear. This also applies to implants for bones, joints and teeth, which furthermore exhibit good biocompatibility. In the high-temperature sector, e. g. in furnaces and turbines, special ceramic materials can withstand operating temperatures of up to 2500°C without warpage or fatigue. In electrical engineering and electronics, ceramic components are used as insulators or in capacitors. Moreover, state-of-the-art ceramic membranes enable the energy-efficient filtering of liquids or even gas molecules [3]. Alumina (Al_2O_3), which is the most important representative of technical ceramics with a market share of 80 %, features excellent corrosion resistance and is therefore widely used in the chemical industry as a pipe and wall material. Aluminum nitride (AlN), on the other hand, is characterized by its good thermal conductivity, which makes it an ideal substrate material for power electronics.

The production of ceramic components from a raw mass requires an energy-intensive and time-consuming sintering process in order to achieve the necessary high temperatures while keeping thermally induced stresses low. In the case of complicated geometries and large dimensions, it can therefore be advantageous to assemble a component from several small, pre-fired parts instead of sintering it completely. This allows for a smaller kiln system, which minimizes firing time and energy costs. However, joining ceramic components is extremely challenging. The established methods of bonding and soldering suffer from various disadvantages. Either the joints are not sufficiently gas-tight or heat-resistant for certain applications or, as in electronics, temperature-sensitive components have to be integrated so that a furnace-based process is not an option at all. Joining technologies that work with high temperatures or additional materials such as adhesives or solder are unsuitable in these cases. A material-locking process that only requires limited, local heat input and no additives to create a joint with similar properties in comparison to the base material would therefore be desirable.

Such a technology can be found in the USP laser welding of glasses, which has already been extensively studied [4]. As ceramic materials show similar mechanical and thermal properties to glasses (brittle-hard, high melting temperature), this joining technology is expected to have great potential with comparable

advantages. For instance, thermally induced stresses could be minimized as the joining process - with its extremely short melting and cooling times and tiny melting volumes - hardly heats the substrate. Unlike the nanosecond laser welding of ceramics, which often requires the components to be tempered [5, 6] or results in joints that are not gas-tight due to microcracks [7], the use of USP lasers could produce reliable micro seams. The few publications dealing with USP welding of non-transparent ceramics [8, 9] indicate that the process is in principle feasible. The aim of the presented research is the fundamental investigation of the USP welding process for Al_2O_3 and AlN . We focus on the quality assessment of blind welds in order to reveal the influence of the material- and process-related parameters on the melt formation. In this way, the possibilities and limitations of the process shall be evaluated.

2. Experimental Setup

The advantages of ultrashort pulses are well known. Due to their extremely high peak intensities, the energy input is dominated by non-linear absorption mechanisms. This is particularly useful for the processing of ceramics, since these only show weak linear absorption at the used near infrared wavelength. In addition, thermal diffusion and plasma expansion are negligibly small during the extremely short pulse durations, allowing for a “cold ablation” and a particularly precise, localized energy input. However, in the case of an especially small local and temporal pulse spacing, heat accumulation effects and the formation of a melt phase may nevertheless occur. It is exactly this circumstance that can be used for welding.

The process window required to form a melt pool was initially investigated by means of spot-welding experiments. In these, a defined laser pulse train is applied to the workpiece surface without any relative movement. By varying the parameters pulse energy E_p , number of pulses n and repetition rate f_R , the material-specific thresholds of both ceramics have been determined and the formation of the melting phase has been observed in order to identify suitable parameter ranges. These were subsequently transferred to experiments with linear movement in order to investigate the influence of other parameters such as scanning speed v_s , focal position z_f and scanning method on the formation of blind weld seams.

The spot-welding experiments were carried out with a *Hyper Rapid 25* laser system from *Coherent*. This provides a pulse duration of 9 ps at a wavelength of 1064 nm. The repetition rate can be varied between 100 kHz and 1000 kHz at a maximum power of 20 W. The beam, which is focused by an F-Theta lens with a focal length of 80 mm, has a focus diameter of about 16 μm . In order to extend the parameter range, the blind welding experiments were carried out with a *Carbide* laser from *Light Conversion* at a similar wavelength of 1030 nm. This features a maximum repetition rate of 2 MHz, a maximum power of 80 W and a focus diameter of about 25 μm . The pulse duration can be varied between 190 fs and 20 ps, but was initially kept constant at 9 ps. The substrate material was sourced from *CoorsTek*. We used Al_2O_3 plates with a thickness of 0.6 mm to 1 mm, a purity of > 96 % and a roughness of about $Ra = 0.4 \mu\text{m}$. The AlN substrates were available in a plate thickness of 0.6 mm with a roughness of $Ra = 1.3 \mu\text{m}$.

The melt zones created by multi-pulses and scanning lines were measured and evaluated. The analysis criteria included the melt diameter and depth, its formation at the surface and the occurrence of cracks and pores. A laser scanning microscope (LSM) and a scanning electron microscope (SEM) have been used. In addition to the top views, cross-sections have been taken to examine the geometry and structure of the melting zone inside the bulk material.

3. Results

The multi-pulse experiments resulted in craters surrounded by a molten rim, what characterizes the process as a combination of melting and ablation. Thereby, shape and size of the molten areas are strongly dependent on the material and the process parameters. As an example, Figure 1 shows how the crater shape differs between the two investigated ceramics for otherwise identical parameters. In the case of Al_2O_3 , a larger melt ring diameter with a higher throw-up is generally formed. This is due to the lower thermal conductivity of Al_2O_3 ($\geq 15 \text{ W/mK}$) compared to AlN ($\geq 80 \text{ W/mK}$) [10]. While the accumulated heat in the AlN ceramic can be dissipated better into the surrounding areas, the Al_2O_3 ceramic tends to create a heat build-up, causing the melting temperature to be reached earlier.

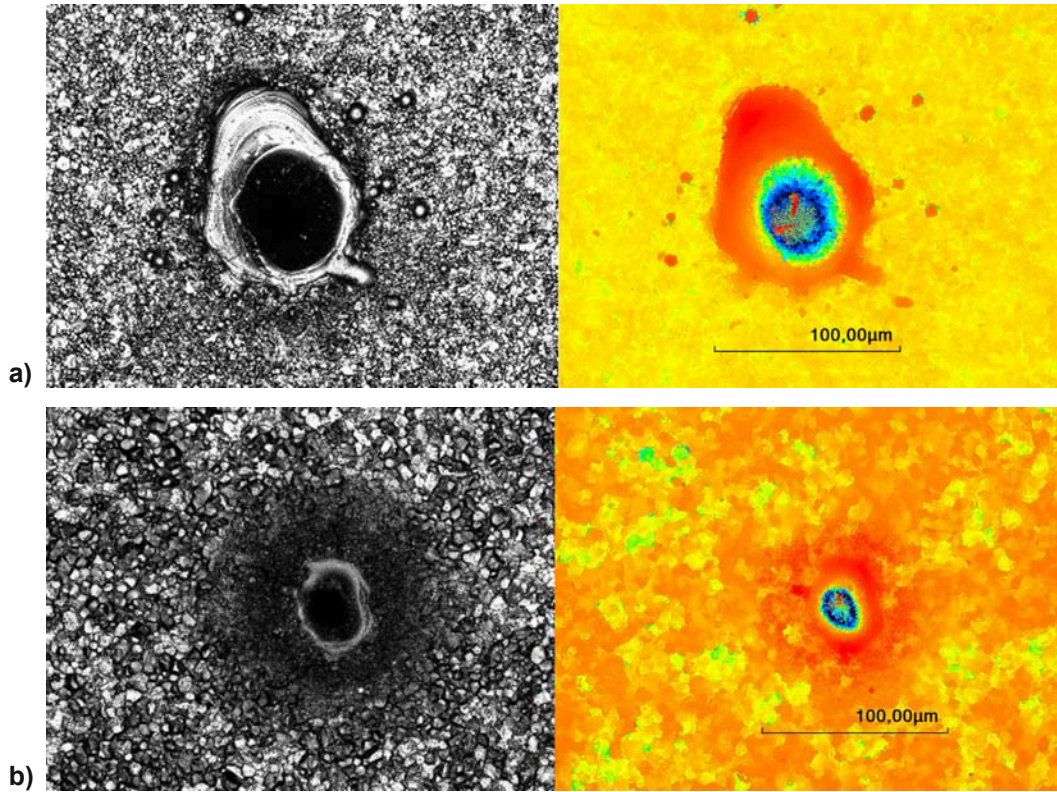


Figure 1: LSM images (intensity image and height image in false colors) of melting areas resulting from multi-pulse experiments ($f_R = 1000$ kHz, $n = 300000$, $E_P = 18.1$ μ J); a) Al_2O_3 ; b) AlN.

Figure 2 shows the development of the ablation and melting ring diameter as a function of the number of pulses and the repetition rate. The experiments were carried out with the maximum usable pulse energy of 18.1 μ J. It is evident that the melt formation in AlN only starts at particularly high repetition rates and at a significantly higher number of pulses compared to Al_2O_3 . For both ceramics, the diameters of the ablation and melting rings initially increase proportionally with the number of pulses (< 3,000 pulses). Especially for Al_2O_3 , it can be clearly seen that this is followed by a saturation, so that the diameters do not increase any further for higher pulse numbers (up to 600,000). In addition, the melt formation decisively depends on the repetition rate. At 100 kHz, no melting could be observed for either material, even for the highest pulse energy and number of pulses tested. It is only from 600 kHz for Al_2O_3 and 1000 kHz for AlN that the time intervals between the successive pulses are so short that the applied energy cannot fully dissipate into the surrounding material, resulting in heat accumulation. With increasing repetition rate, this is further intensified, resulting in an enlargement of the ablation and melting diameters.

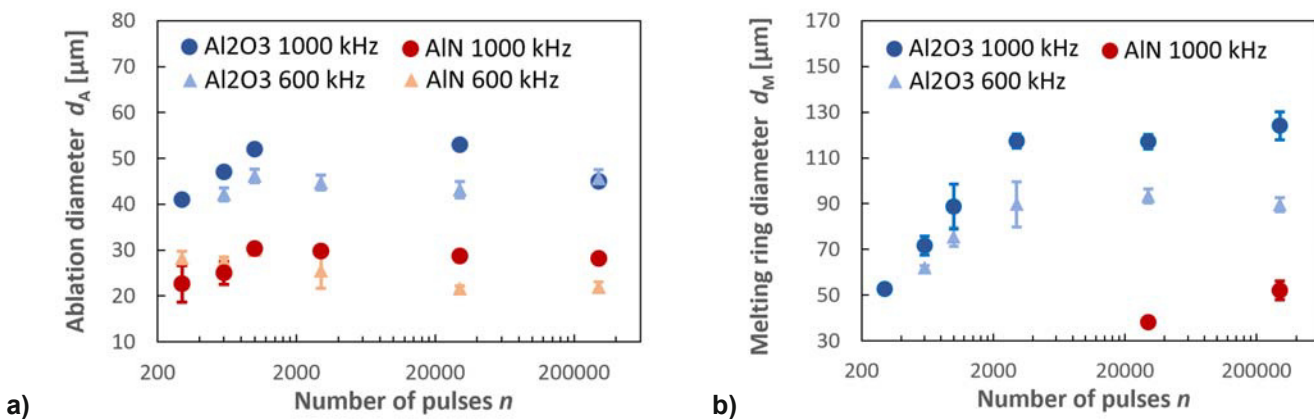


Figure 2: Development of the a) ablation diameter d_A and b) melting ring diameter d_M as a function of the number of pulses n and the repetition rate f_R for Al_2O_3 and AlN.

Based on the spot-welding experiments, the tested parameter settings have been transferred to the generation of blind weld seams by adding a linear scanning movement. Figure 3 shows how the melt tracks develop with increasing pulse spacing for both materials and two different repetition rates. The images for Al_2O_3 show that too small pulse spacings lead to a strong melt ejection with craters and melt spatter, while too large pulse spacings leave a track predominantly characterized by ablation, with the melting process repeatedly being interrupted. A pulse overlap between 99.75 % and 99.85 % was found to be optimal for the selected parameter window. In order to be able to compare the different repetition rates directly with each other, the scanning speeds have been adjusted so that the same pulse spacings were generated. It can be seen that lower repetition rates lead to more irregular weld seams due to a weaker heat accumulation.

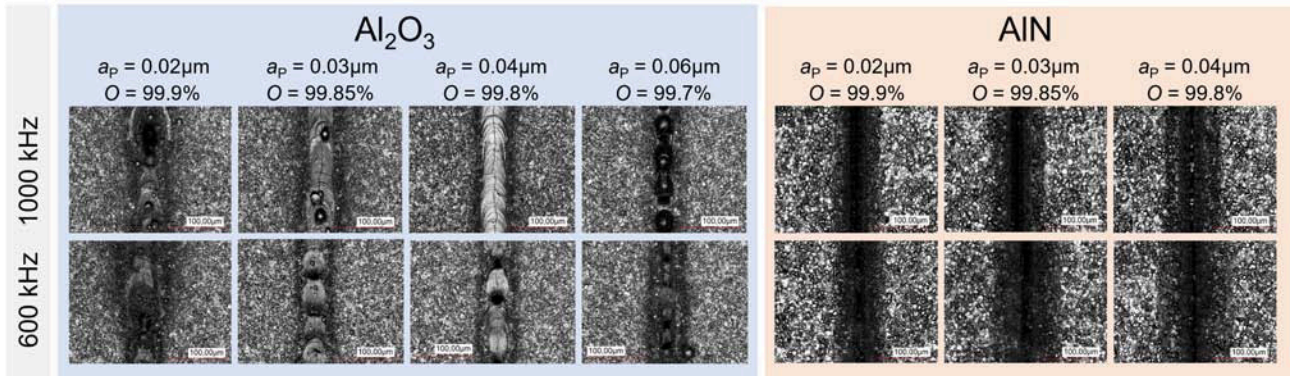


Figure 3: Comparison of blind weld seams in Al_2O_3 and AlN for varying repetition rate f_R and pulse spacing a_P / overlap O at constant pulse energy $E_P = 18.1 \mu\text{J}$. The scanning speed v_S was adjusted according to the repetition rate (1000 kHz: $v_S = 20\text{...}60 \text{ mm/s}$, 600 kHz: $v_S = 12\text{...}36 \text{ mm/s}$).

The processing lines for AlN differ fundamentally from those taken for Al_2O_3 . The top view shows a simple ablation trench with no evidence for melting. However, it is interesting to point out that the trench width appears to increase with increasing pulse spacing. This is quantitatively confirmed in Figure 4a by means of the measured values for the trench width and cross-sectional area. This behavior would be atypical for a pure ablation process, as the energy input per area segment decreases with increasing scanning speed. However, the cross-sections shown in Figure 4b provide an explanation for this. They reveal that the near-surface trenches are followed by sub-surface material changes up to several 100 μm deep. Narrow molten channels are formed, which taper into depth. With increasing energy input due to lower scanning speeds, the channel depth deepens. It can be assumed that the rising amount of sub-surface melt leads to a narrowing of the trenches on the surface.

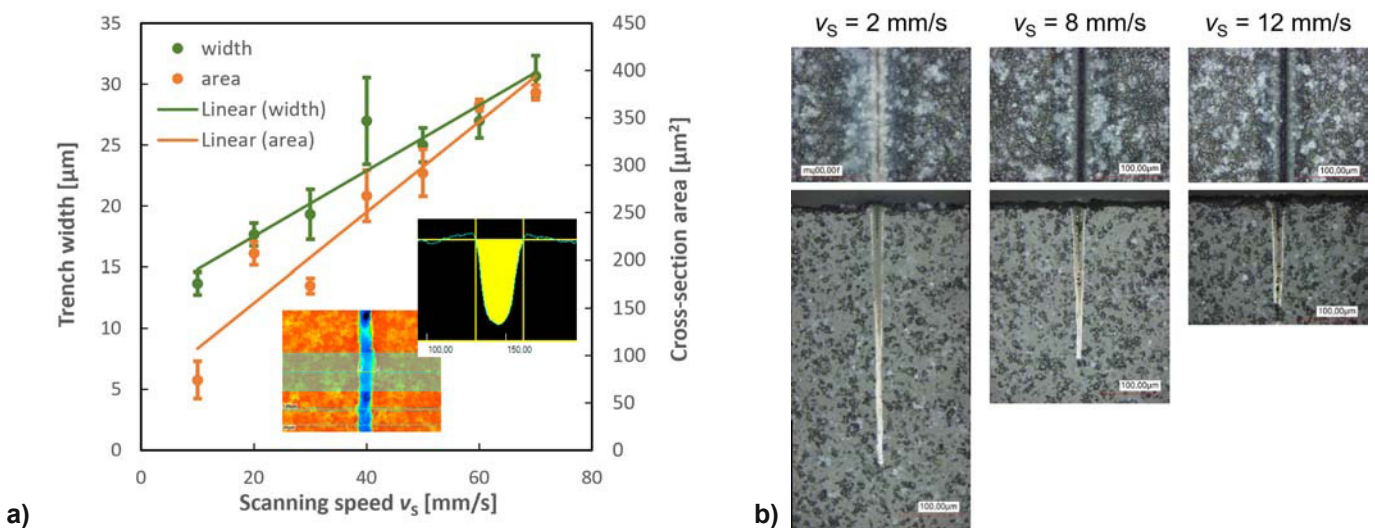


Figure 4: Influence of the scanning speed v_S on the weld seam formation of AlN ($E_P = 18.1 \mu\text{J}$; $f_R = 1 \text{ MHz}$);
a) Development of width and cross-section area of the surface trench;
b) Top views and cross-sections of the entire melting zones at particularly low scanning speeds.

In order to gain more flexibility for the creation of future weld seams, various experiments have been carried out to widen the melt tracks. One possible method is the so-called "wobbling", in which a high-frequency oscillation is superimposed on the linear scanning movement. Figure 5 shows examples of blind weld seams for both materials using the wobble mode. Since the pulses are spread over a larger area due to the circular wobble movement, the effective pulse overlap is reduced, which makes heat accumulation more difficult. For the processing of Al_2O_3 , the pulse energy therefore had to be significantly increased compared to the previous investigations. The resulting weld seam, which has a width in the order of the wobble amplitude, is characterized by the formation of a particularly high dome as well as subjacent pores and cavities. These indicate a strong mixing of the molten material and the injection of air into the inside of the material.

Such effects can be partially avoided when processing AlN. Although the blind weld seams obtained in wobble mode have a porous, foamy layer on the surface, a particularly homogeneous, pore-free melting zone spreads into the bulk material. While circular wobble movements were used for the processing of Al_2O_3 , an entirely transverse oscillation proved to be optimal for the processing of AlN. Due to the deflection points at the edges of the weld seam and the locally increased energy per area there, a characteristic tooth root shape is formed. For both materials, it was possible to increase the welding depth by varying scanning speed and pulse energy in wobble mode to such an extent that the material was completely welded through.

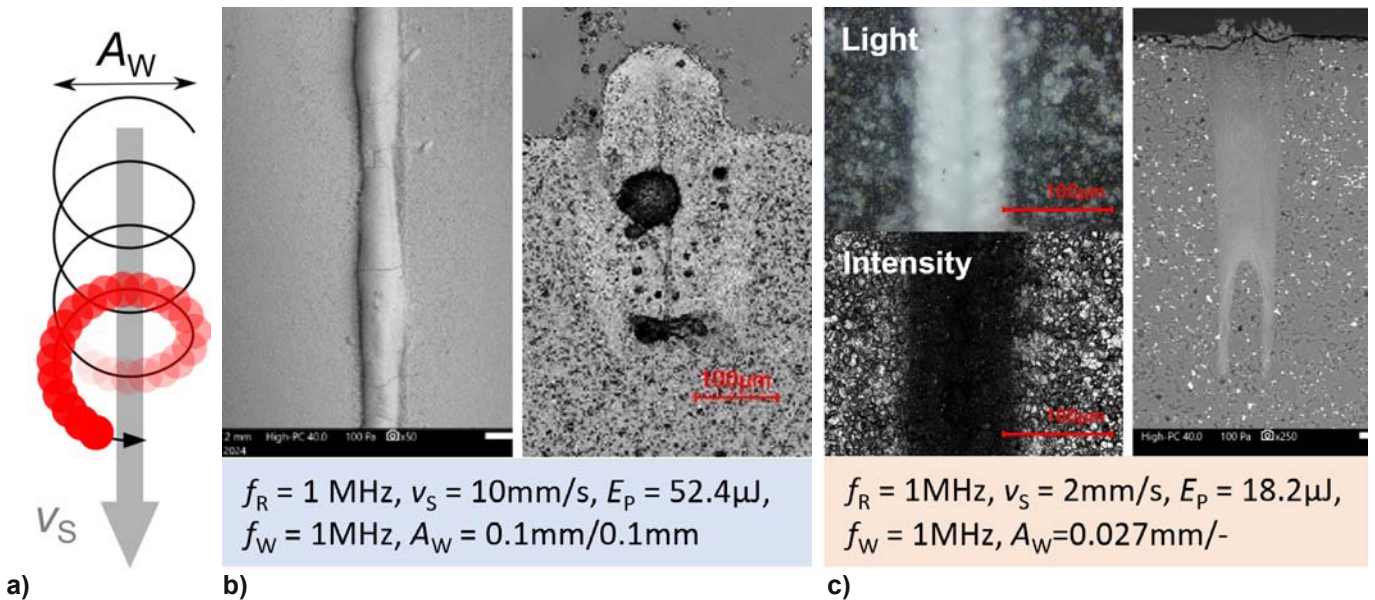


Figure 5: Exemplary results for the generation of blind weld seams in wobble mode;
a) principle illustration of "wobbling"; top view and cross-section for
b) Al_2O_3 and c) AlN for specific wobble frequencies f_w and amplitudes A_w .

Another simple way to widen the weld seam is to increase the size of the laser spot by defocusing. Figure 6 shows how a blind weld seam created in Al_2O_3 changes with increasing defocusing. All three melt tracks have been generated with the same fluence by increasing the pulse energy according to the actual spot size. If the scanning speed now remains the same (compare Figures 6a and 6b), the defocusing leads to a widened weld seam due to the larger spot size and the increased pulse overlap. If, on the other hand, the scanning speed is increased as well – so that a comparable pulse overlap is created for the enlarged, defocused spot diameter (compare Figures 6a and 6c) – the widening of the weld seam is only marginal. This is due to the fact that the Gaussian tails of the enlarged beam profile remain below the intensity threshold for the melting process. Inside the Gaussian profile, however, the increased pulse energy causes a larger melting volume compared to a smaller spot size. This demonstrates that a careful choice of defocusing can help to produce both wider and more homogeneous weld seams.

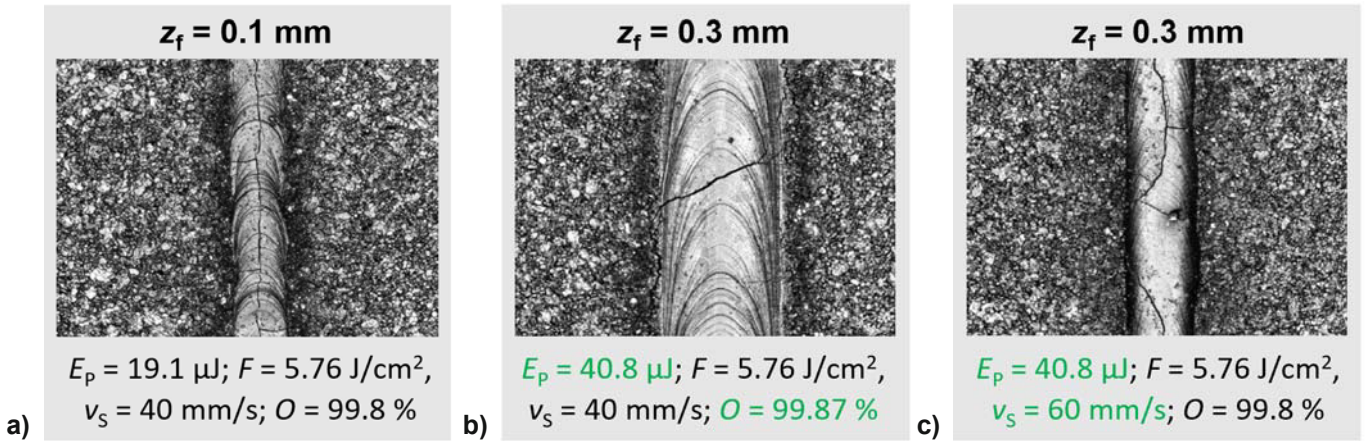


Figure 6: Comparison of differently defocused blind weld seams in Al_2O_3 ;
a) initial position; b) adjustment of fluence F by change of pulse energy E_p ;
c) additional adjustment of pulse overlap O by change of scanning speed v_s .

4. Summary and outlook

The multi-pulse and blind welding experiments made it possible to determine promising process windows for the USP laser welding of Al_2O_3 and AlN . The two materials differ significantly from each other. In the case of the easy-to-melt Al_2O_3 , an extensive melt pool forms on the surface and a broad melt zone of relatively small depth, which often contains pores, forms inside the material. In contrast, trenches and particle deposits on the surface of AlN mainly suggest ablation as the dominant process. However, cross-sections showed that a narrow, predominantly homogeneous melt channel continues deep into the inside of the material. For both materials, an increase in welding depth and width can be achieved by wobbling and defocusing. Despite extensive parameter investigations, it was not possible to achieve completely damage-free processing results. The blind weld seams are always infiltrated with pores and/or hairline cracks. Nevertheless, selected process parameters have already been successfully transferred to "real" weld seams. Figure 7 shows such a result in Al_2O_3 . In addition to the top view (Figure 7a), the broken cross-sectional areas of the two joining partners are shown with a clearly visible color transition from the weld seam (depth: 300 μm – 350 μm) to the base material (Figure 7b).

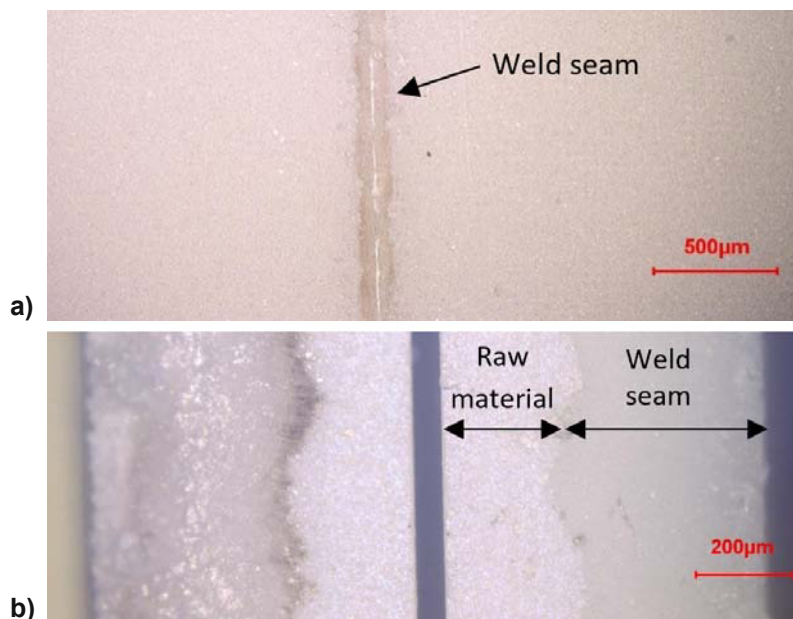


Figure 7: Initial results for joining Al_2O_3 ceramics using USP laser welding;
a) Top view of the weld seam; b) Fracture pattern of the weld seam along the joining zone.

The extent to which USP laser welding is suitable for realizing crack-free, gas-tight welded joints with sufficient strength must be shown by further investigations in the ongoing research project. Welding is to be examined for both planar and rotationally symmetrical joining partners in butt joint arrangements. In addition to the laser-specific parameters, the welding gap width and shape shall also be part of the investigations.

5. Acknowledgement

The research project is funded by the Federal Ministry of Economics and Climate Protection based on a decision of the German Bundestag under reference number 49MF220074. The authors gratefully acknowledge this support on behalf of ifw Jena.

6. References

- [1] Kriegesmann, J. (ed.): „DKG – Technische Keramische Werkstoffe“, HvB-Verlag, Ellerau (2005)
- [2] Kollenberg, W. (ed.): „Technische Keramik – Grundlagen, Werkstoffe, Verfahrenstechnik“, Vulkan-Verlag, Essen (2004)
- [3] Schulze, M.: „Keramik trennt Wasserstoff und Sauerstoff“, In: VDI Nachrichten (24.01.2014), accessed on 11.05.2022 at <https://www.vdi-nachrichten.com/technik/werkstoffe/keramik-trennt-wasserstoff-und-sauerstoff/>
- [4] Cvecek, K.; Dehmel, S.; Miyamoto, I.; Schmidt, M.: „A review on glass welding by ultra-short laser pulses“, In: International Journal of Extreme Manufacturing, IOP Publishing, 1.4 (2019)
- [5] Exner, H.; Gerber, B.; Kimme, T.; Seifert, U.; Straube, U.: "Further progress in laser welding of ceramics", In: International Congress on Applications of Lasers & Electro-Optics, Laser Institute of America (1993)
- [6] Riviere, C.; Robin, M.; Fantozzi, G.: "Comparison between two techniques in laser welding of ceramics", In: Journal de Physique IV, Vol. 4, 135-138 (1994)
- [7] Winkler, M.: "Untersuchungen zum Mikro-Laserfügen von Al₂O₃", Bachelorarbeit Hochschule Mittweida (2016)
- [8] Penilla, E. H.; Devia-Cruz, L. F.; Wieg, A. T.; Martinez-Torres, P.; Cuando-Espitia, N.; Sellappan, P.; Kodera, Y.; Aguilar, G.; Garay, J. E.: "Ultrafast laser welding of ceramics", In: Science, Vol. 365, 803 – 808 (2019)
- [9] Yuan, H.; Li, C.; Yang, B.; Gao, J.; Zhao, W.; Li, M.; Cao, J.: "Direct welding of diffuse alumina ceramics by ultrashort pulse laser", In: Journal of the European Ceramic Society, Vol. 44, 574–578 (2024)
- [10] <https://www.coorstek.com/de/werkstoffe/ingenieurkeramikwerkstoffe> (retrieved on 11.10.2023)

Handheld laser welding – systems, applications and safe usage

Jahn, S.; Schmitz, M.; Lange, J.; Prowaznik, R., König, M.
Günter-Köhler-Institut für Fügetechnik und Werkstoffprüfung GmbH (ifw Jena)

Abstract

Since 2023 at the latest, handheld laser welding systems have attracted the interest of users. This is mainly due to two factors. Firstly, the cost of such a system has decreased significantly in recent years. Secondly, there is economic pressure in manufacturing of welded products, also due to the shortage of skilled workers. The publication will cover various aspects of handheld laser welding.

A steadily growing number of distributors and resellers are active on the European market. The systems on offer differ in various criteria, such as laser type, power, cooling or parameter range. The influence of various features on the resulting properties is shown using examples.

Due to the higher welding speed, substituting TIG welding with handheld laser welding can lead to increased productivity. The speed itself is 2 to 7 times higher compared to the arc process, depending on the conditions and requirements. Some companies claim an increase in productivity of 30 % to 70 %. To achieve this, the weld seam design and preparation must be adapted to the handheld laser welding process.

The potential of handheld laser welding helps to overcome the shortage of skilled welders. It should also be mentioned that the process could be learned more easily and in less time compared to TIG welding. Experience is replaced by technical features, e.g. the wobbling of the torch by linear beam scanning or the preset welding speed by the set wire feed rate.

Laser safety is very important, especially for newcomers. Most people are not aware of the dangers associated with the laser process. Many systems offer 3-in-1 processing, cutting and cleaning in addition to welding. The contactless cleaning in particular is often carried out without regard to laser safety, e.g. without protective eyewear. In addition to the coherent radiation, the resulting UV radiation must also be mentioned and taken into account, too. The contribution therefore provides information on the regulations for safe use.

Typical applications will be shown, e.g. from the field of switch cabinet and casing manufacturing. The presentation is based on three years of experience with various handheld laser welding system.



Figure 1: Two different handheld laser welding systems

1 Introduction

In general, the term "manual welding laser" refers to systems in which the laser head is fixed and the welding movement is carried out by manually sliding or moving the workpiece. It also refers to systems in which the laser head is mechanized/partially automated and the motion of the laser head or the workpiece is controlled via a joystick.

Handheld laser welding (Figure 1), on the other hand, is comparable to hand-guided arc welding processes. A handpiece/welding head/gun is guided over the workpiece, but the energy used to melt the material is not an arc, but coherent radiation. The laser "torch" is in the welder's hand ("handpiece" or "gun") and is guided by the welder.

2 History

Historically, a first patent (DE2145921 – Device for material processing by means of a laser beam with a flexible light guide) for handheld laser beam welding was registered in Germany in 1971, and welding results were published by Nath in 1974 [1]. This was followed by further patents worldwide, including for various processing heads, such as the gun shape, around 1980 (US 4237364 – Welding tools and method), for the integration of sensors or material supply. However, the main obstacles to widespread use were the costs of the beam source and the sometimes unhandy as well as heavy weight handpieces.

Since the turn of the millennium, there have been repeated phases in which the topic of handheld laser welding has come to the fore, for example after the introduction of laser welding in automobile manufacturing and due to the desire for process-like repair methods or for welding plastics with handheld laser processes. For example, a final report on "Constructive safety devices for handheld lasers for material processing" was published as early as 2011 [2].

Processing heads existed that completely shielded the laser radiation from the environment. However, the disadvantages were the weight and size and the resulting difficulty in handling. It was only since the beginning of the 2020s that the costs for 1 kW laser beam sources fell to a level, which allowed the process to be more widely used. Furthermore, the handpieces could be miniaturized (down to 680 g). Complete systems are currently offered in the lower five-digit dollar range.



Figure 2. Handpieces for single-axis (left) and two-axis (middle) pendulum movement and with active plasma monitoring (right)

3 Systems setup

The systems currently offered consist of the following components: laser beam source with control, optical fiber ("hose package"), handpiece and optional wire feeder. Depending on the supplier, the complete systems are portable or installed on a trolley. The systems currently offered commercially are mostly equipped with a fiber laser beam source that can have an output of up to 4 kW. The laser beam source is a major cost factor in handheld laser beam welding systems. Until a few years ago, the price of 1 kW of laser beam power was well into the six-figure range, but today beam sources with 1 kW are already available on the market in the four-figure range. This means that complete systems can be starting around 10,000 €.

Both multimode and singlemode laser beam sources versions are offered, with the latter typically offering a smaller minimum focus diameter a so a higher maximum penetration depth. Depending on the maximum power and the type of the beam source as well as the material to be welded, welding depths of up to 7 mm are possible. The cooling of the beam sources also differs. Both water- and air-cooled systems are offered. The decisive factor is the duty cycle at the set power. The systems differ here, regardless of the cooling version.

In the hose package, media (gas, sometimes cooling water), control lines and the laser radiation are guided to the handpiece in an optical fiber. The handpieces vary in their design, particularly with regard to the oscillation of the laser beam. There are single-axis (perpendicular to the feed direction) or two-axis (perpendicular and in the feed direction) versions (Figure 2) available. The design variant also affects the weight and dimensions.

If welding is to be carried out with additional material, among other things to increase the gap bridging capacity, a wire feeder is required. Again, the designs differ in terms of continuous or pulsed wire feed and wire retraction. If it is necessary to achieve a given design throat thickness for fillet weld, sometimes 2 or more wire feeders are in use.

A wide range of parameters can be set on the systems. In addition to the laser power, these include the operating mode (continuous (cw) or pulsed operation) as well as the beam oscillation frequency and width or shape and their size for two-axis oscillation. In addition to circles (widely used for laser spot welding), more complex shapes are also possible for the beam oscillation figure in order to influence the heat input (Figure 3).

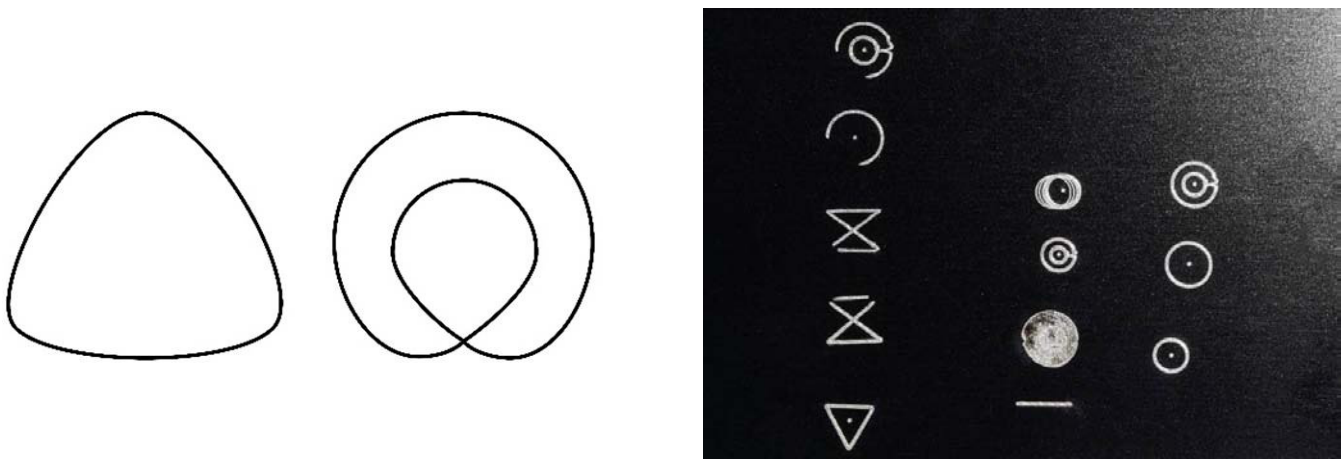


Figure 3. Beam oscillation figures in two-axis beam pendulums: principle sketches (left) and engraving on anodized sheet metal (right)

Depending on the system, the focus diameter (possible both via spacer tube and electronic control) and the welding nozzles, which serve as guide in addition to establishing contact for the safety circuit, can also be varied. The parameters affect, among other things, the welding speed, the welding depth, the seam width and the penetration on the flanks.

4 Laser Safety Considerations

The handheld laser beam welding systems are assigned to laser class 4 ("open laser system"). Therefore, special attention must be paid to the laser safety regulations during operation. In order to operate a handheld laser beam welding system, a laser safety officer must be appointed within the company.

A distinction is made between the protection of the welder and the protection of third parties. Companies that already use a laser system, for example for cutting, already know the requirements. However, newcomers are often unaware of this, which poses a risk.

On the welding side, the system must meet safety requirements and only release the laser beam if certain conditions are met. Most systems offer multi-level monitoring. The first stage is contact monitoring: the laser beam is only released if there is an electrical contact between the handpiece and the workpiece ("ground cable" between the workpiece and the system). The second stage is a release button on the handpiece with "laser on" signaling. For safe use, the systems have the mandatory third stage in order to meet the requirements, for example with regard to the Laser Protection Ordinance (Occupational Health and Safety Ordinance on Artificial Optical Radiation). This can be an additional foot switch or plasma monitoring.

Similar to arc welding, the welder must wear personal protective equipment. The clothing used for arc welding can be used. However, due to the reflection of the scattered laser radiation and the material-related generation of UV radiation ("UV radiation during hand laser material processing" (DGUV-FP439 [3])), care must be taken to ensure that the welder's skin is covered (gloves, e.g. according [4]). To protect the face and eyes, either welding helmet approved for laser use with integrated laser safety glazing (Fig. 4) or laser safe faceshield must be worn. If the welder uses both processes for joining, handheld laser beam welding and arc welding (e.g. TIG/GTAW), the use of a hybrid helmet, providing protection for both processes, is highly recommended (in order to avoid the wear of a helmet with protection for the wrong process). Handheld laser welding also produces fumes that must be extracted [5] or an respiratory protection system must be worn.



Figure 4. Different helmet for handheld laser welding

The work area must be secured against unauthorized access in order to protect third parties from unprotected exposure to laser radiation (Laser Controlled Area - LCA) [6]. Ideally, the systems should be used in closed rooms or cabins with ceilings. If the work area is to be craneable, walls with a minimum height are required. With sufficient room height and crane clearance, the walls of cabins open at the top should be at least 2.8 m high. In addition, regardless of the design with or without a ceiling, further hardware equipment is mandatory: firstly, a "laser on" signal outside the work area, e.g. in front of the door. This serves as a warning against entering an area with an active class 4 laser system (Fig. 5). Secondly, a so-called interlock control is required. As soon as the door to the work area is opened, the laser radiation must be switched off. Furthermore, laser safety goggles must be kept outside the work area ready to hand for emergencies. In Germany, the employers' liability insurance association ETEM provides a checklist for inspection prior to the purchase or initial start-up of a handheld laser welding system. [8]

5 Advantages and application

Several research institution, beside the system supplier, describe the advantages of handheld laser beam welding. For example, after a week of training in TIG welding, a student was able to join two workpieces together on the last day, but after a few hours of practice, he was able to produce testable weld seams with handheld laser beam welding. The position of the handpiece and even guidance at the speed specified by

the wire feed are important. The actual welding process is almost invisible to the welder; the oscillation to capture the flanks takes place automatically in the handpiece. The findings are consistent with those of others, including for example Caprio [7]. For this study, beginners competed against professionals in a comparison. Ultimately, all results are comparable, both in the dimensions of the welded joints and in terms of strength. Only the melt pool width variation was smaller for the professionals.

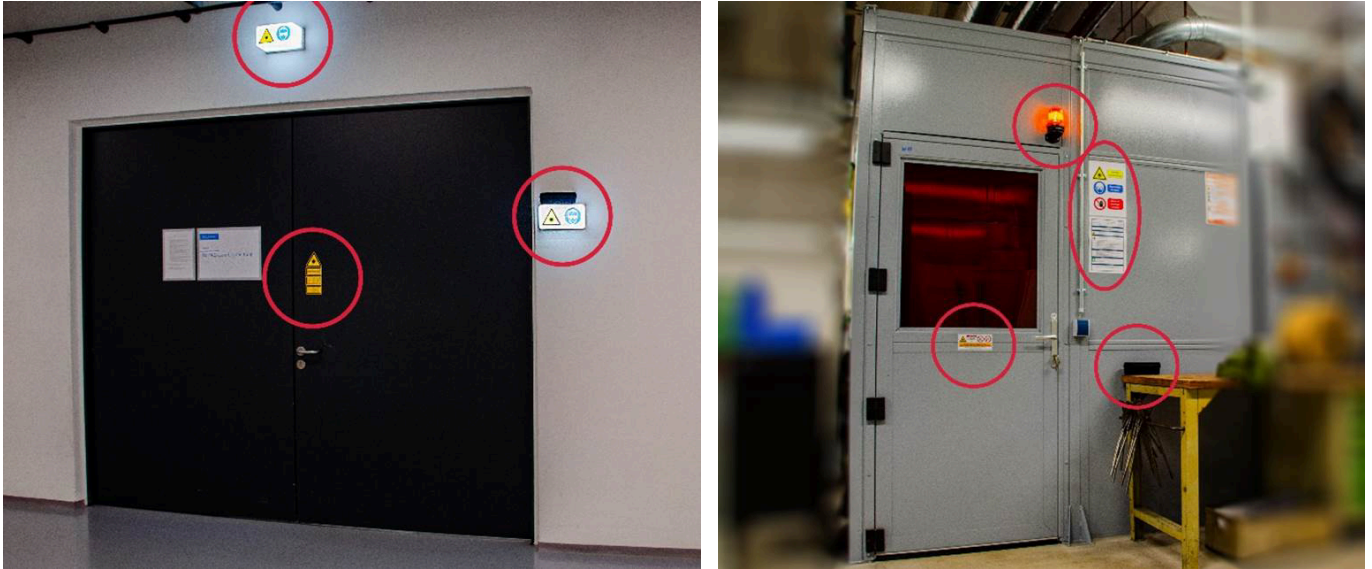


Figure 5. Information about laser systems in use and signals for “laser on”

Further, it should be noted that people with decades of welding experience do not produce better results, and in some cases even produce significantly worse welds. On the one hand, the process behaves "differently" in terms of sensory perception (particularly sight and hearing), and on the other hand, specifying the welding speed using the wire feed is unusual for trained welders.

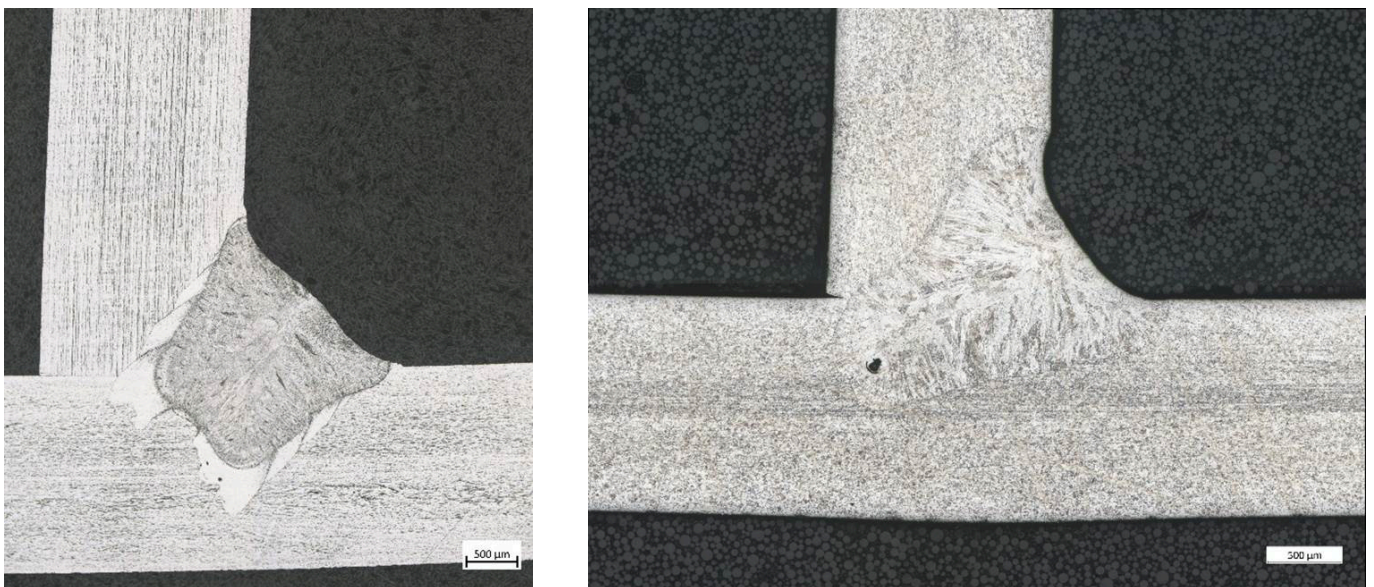


Figure 6. T-joints realized by handheld laser welding, with “high” design throat thickness (left) and close to one-sided full connection (right)

The achievable welding depths depend on the material, the power and the type of laser beam source. Due to the smaller focus diameter of single-mode laser beam sources (30–60 μm) compared to multi-mode

versions (typically 100–150 μm), welding depths that are 1.5 to 2 times higher can be achieved. Currently, 9 mm is listed as the maximum depth for steel. With a 2 kW multi-mode laser beam source, a welding depth of 4 mm can be reliably achieved in steel. One-sided full connections in a T-joint can be realized, but a flat angle of attack must be selected for this and the laser “torch” guided in an unusual angle compared to arc processes (Fig 7). Until now, in most drawings a design throat thickness is given. By handheld laser welding, a higher penetration depth can be realized to get a full connection but with a low design throat thickness that does not meet the given requirements.

Depending on the seam geometry and length, the welding speed is at least 2 times higher, typically in the range of 3 to 5 times. This also means an adjustment for experienced welders. The gap bridging ability is similar or slightly lower compared to TIG welding. Areas with a wide gap are particularly problematic for handheld laser beam welding. Therefore, both during design and during preparation phase, attention must be paid to laser welding-compatible design (“zero gap”). With TIG welding, on the other hand, such areas can be “filled”. Small tack welding distances or gap-free clamping during preparation have a positive effect.

If the process parameters are set correctly, welds can be produced that meet the highest requirements. If this is not the case, however, deficiencies in the form of pores, both in the form of chains and tubes, occur on the inside. These cannot be seen from the outside, which is why the use of X-rays is highly recommended for parameter development (Figures 6 and 7).

The advantages of the higher welding speed are particularly evident for longer seams of 20 cm or more. To compare performance, a funnel was welded, with TIG welding being used for one half and handheld laser welding for the other half (Figure 8).

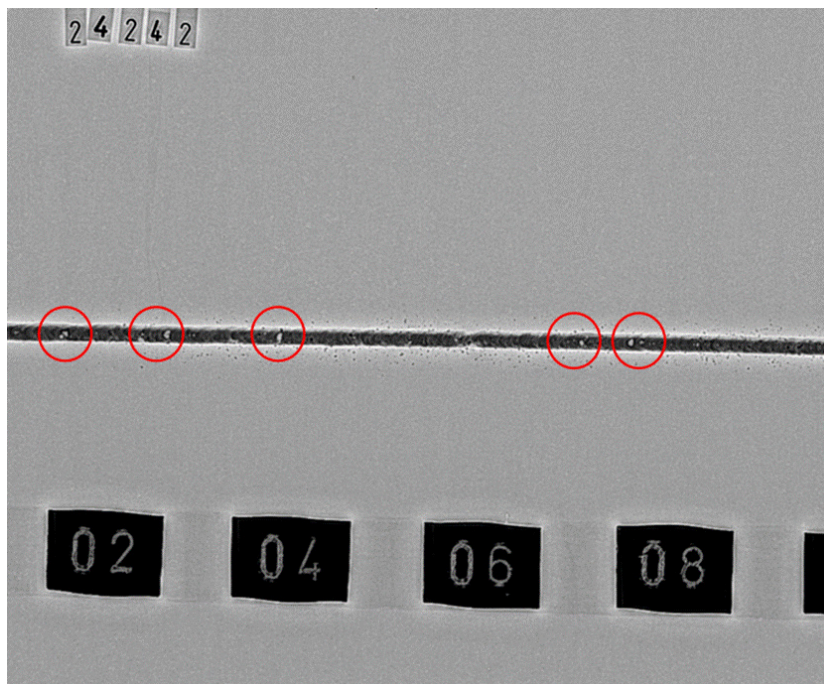


Figure 7. X-ray analysis result of a handheld laser weld joint with porosity

The advantages of the higher welding speed are particularly evident for longer seams of 20 cm or more. To compare performance, a funnel was welded, with TIG welding being used for one half and handheld laser welding for the other half (Figure 9).

With handheld laser beam welding, a higher welding speed of up to 140 cm/min was achieved compared to TIG welding on 1.4301 sheets with a thickness of two mm. Companies that already use the process report 30% to 50% higher throughput (chrome-nickel steel welding in the thin sheet area). Percentage value depends mainly on length of weld seams. The increase is attributed to the higher welding speed on the one hand and the lower straightening effort on the other.

6 Operator qualification

A manual dexterity test is also necessary for handheld laser beam welding. This manual dexterity test can be carried out as a special test based on the ISO 9606 series of standards [8]. As special, it is to mention that the process 521 for fiber laser source was carried out manually. No further set of rules is necessary, only an update, especially to name the “new” process. The aim, however, therefore is to integrate handheld laser beam welding into the standards as an own process. Initial activities have been started at ISO level for this purpose.



Figure 8. Handheld laser beam welding on the funnel

Educational institutions are already able to offer courses and examinations in the area of handheld laser beam welding. In addition to the actual manual skills required for welding samples, the examination also includes a theoretical knowledge test. This is particularly important because there is often no knowledge of laser radiation and its potential hazards and this knowledge must be transferred to welder. Two examples of “no go” or shown in the next Figure. Some welders are used to tack or straighten parts while holding these in one hand (left side). Others fell more comfortable with welding while sitting on a chair. If a work-bench with holes is used, the knee are can be hit by the laser beam (see pilot laser spot on knee on right side). It is necessary to place a thicker and larger sheet under the work piece to avoid the shown situation. Both examples prove that it necessary to train the welder about the hazards of laser welding.

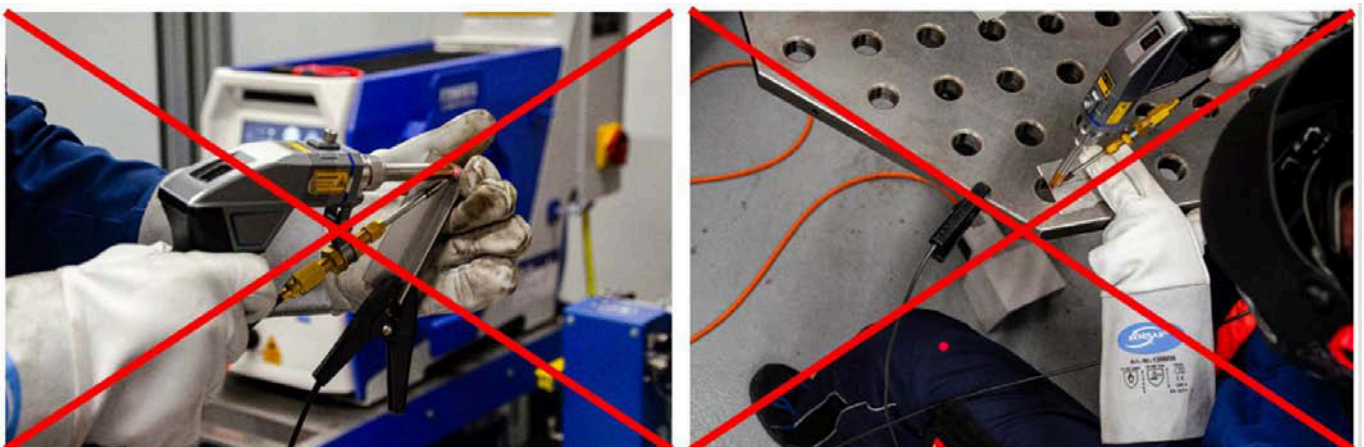


Figure 9. Examples of incorrect procedures

7 Summary

Handheld laser beam welding offers a wide range of potentials, including higher throughput, less straightening work due to the lower heat input, and the use of less experienced personnel. However, welders still

need to be qualified, especially to deal with the hazards of laser radiation. Furthermore, the application of the process requires an appointed laser safety officer in the company and a work area designed in accordance with laser protection requirements (LCA). In addition to welding, many systems for handheld laser beam welding also have a cleaning function, as described. The risks to be considered here are considerably greater, since on the one hand, a touchdown control is often omitted and on the other hand, the beam is conditioned for a larger working distance.

In order to be able to use the full potential for joining, application requirements must be taken into account during the design (“zero gap”). This continues during edge preparation. Handheld laser welding is a supplement to welding processes, although arc processes still have their place, for example with small, complex geometries or in terms of accessibility. However, if longer seams, for example 1.5 m long, are to be welded and these are prepared accordingly, then handheld laser welding is currently the norm, especially with regard to welding speed when welding by hand.

8 Literature

- [1] Nath , G.: Hand-held laser welding of metals using fibre optics, OPTICS AND LASER TECHNOLOGY, OCTOBER 1974
- [2] Püster , T. et al.: Constructive safety devices for handheld lasers for material processing, Research Project F 2158, Federal Institute for Occupational Safety and Health, 2011
- [3] Hilck, A. et al.: “UV radiation during handheld laser material processing” (DGUV-FP439), 20221/7.0000746, 2022
- [4] German Institute for Standardization (DIN), Protective gloves against laser radiation, DIN SPEC 91250, Berlin: Deutsches Institut für Normung
- [5] Khaligh M. et al.: Emission factors and fume generation rates of particles from various welding processes, Annals of Work Exposures and Health, Volume 68, Issue Supplement_1, June 2024, Page 1, <https://doi.org/10.1093/annweh/wxae035.253>
- [6] American National Standards Institute (ANSI) Accredited Standards Committee Z136, American National Standard for Safe Use of Lasers, ANSI Z136.1, Orlando, FL: Laser Institute of America (LIA).
- [7] Caprio , L. et al.: Hand-Held Laser Welding of AISI301LN for components with aesthetic requirements: Toward the integration of machine and human intelligence, <https://doi.org/10.235>
- [8] Checkliste Hand-Laser-Maschinen, <https://www.bgetem.de/medien-service/medienankuendigungen/hand-laser-maschinen#>
- [9] International Organization for Standardization (ISO), Approval testing of welders — Fusion Welding — Part 1: Steels, ISO 9606-1, Approval testing of welders — Fusion Welding — Part 2: Aluminum and aluminum alloys, ISO 9606-2, Approval testing of welders — Fusion Welding — Part 3: Copper and copper alloys, ISO 9606-3, Approval testing of welders — Fusion Welding — Part 4: Nickel and nickel alloys, ISO 9606-4, and Approval testing of welders — Fusion Welding — Part 5: Titanium and titanium alloys, zirconium and zirconium alloys, ISO 9606-5, Geneva: International Organization for Standardization.

Highly Absorptive Coatings for Laser Components

Mehri Hashemzadeh, Andreas Pfuch, Jürgen Schmidt
INNOVENT e. V., Jena, Germany

Abstract

When lasers operate, they produce residual energy that must be converted into thermal energy through absorption mechanisms. To manage this, alongside design strategies, special coatings with high absorption capacity for specific laser wavelengths are often utilized. Plasma chemical oxidation (PCO), also referred to as plasma electrolytic oxidation (PEO), has been successfully employed for several years to create highly absorbent oxide coatings tailored to various laser devices across different wavelengths. These PCO coatings demonstrate superior absorption properties in the UV/VIS and near-infrared (NIR) regions compared to commercially available anodized surfaces. This article explores the PCO process for developing these coatings, highlighting its unique advantages over traditional anodization methods, and provides application examples to illustrate its effectiveness. Additionally, we discuss the damage thresholds of these coatings. In the outlook, we briefly outline potential advancements to further enhance absorption coefficients at specific wavelengths and improve resistance to higher laser powers through ongoing development.

1. Introduction

Since Theodore H. Maiman's pioneering invention of the laser over half a century ago, this remarkable technology has enabled a wide range of applications across various fields. In telecommunications, the focus has been on achieving the highest possible transmission frequencies in the gigahertz range. In industrial production, on the other hand, the goal is often to generate ultra-fast, high-power light pulses in the nanosecond range to enable precise and efficient manufacturing processes [1].

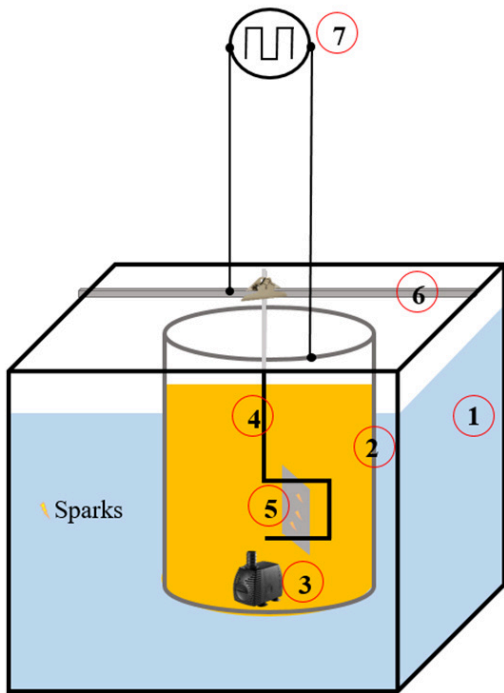
During the generation of various laser wavelengths, residual laser energy is produced within the laser housings. This unused energy must be converted into harmless thermal energy through absorption mechanisms. To achieve this, laser radiation traps or specialized coatings are applied to the components. These surfaces are engineered to exhibit high absorption capabilities for the specific laser wavelength being generated. This is typically achieved by creating rough textures, either through corundum blasting or by mechanically introducing grooves onto the component surfaces. Through these intentionally designed surfaces, residual laser energy undergoes multiple reflections, effectively converting it into heat, which can then be dissipated by leveraging the thermal conductivity of the materials used.

Enhanced absorption can be achieved by applying highly absorptive coatings specifically tailored to the wavelength of the laser. However, organic layers or dyes are unsuitable due to contamination risks and inadequate radiation resistance. While aluminum alloys are commonly anodized and dyed black with organic dyes to improve absorption, this method has limitations, particularly in the near-infrared (NIR) range beyond approximately 800 nm. In this spectral region, absorption diminishes significantly, resulting in surfaces that reflect a large portion of the incident light. To address this limitation, plasma chemical oxidation (PCO), also known as plasma electrolytic oxidation (PEO), has been successfully used for several years to produce oxide coatings that meet the requirements of various laser devices across different wavelengths. These PCO coatings exhibit superior absorption characteristics compared to anodized coatings in the NIR range. However, further improvements in absorption and laser resistance at higher power densities remain desirable.

2. The Plasma Chemical Oxidation Process (PCO) and Coating Properties

PCO process is an advanced surface treatment process that combines principles of electrochemistry and plasma physics to create oxide coatings on metal surfaces. This process is particularly effective for light

metals such as aluminum, magnesium, and titanium, as well as their alloys. The process principle of plasma chemical oxidation is shown in figure 1.



- 1 Polyethylene container containing cooling water
- 2 stainless steel container containing coating electrolyte (Counter electrode)
- 3 Submersible Aquarium Pump
- 4 Holder of working electrode
- 5 Working electrode (substrate)
- 6 Ti bar connected to the rectifier
- 7 Rectifier

The black lines are insulated.

Fig. 1: Schematic of plasma chemical oxidation set up.

In the PCO process, the component to be coated serves as the anode in an electrolytic cell, similar to conventional anodic oxidation. The counter electrode, typically made of an inert material like stainless steel, acts as the cathode. As the anode potential increases, the initial thin, natural oxide/hydroxide layer on the component's surface thickens. This layer transitions into a more compact, non-porous oxide barrier layer through electrochemical reactions. The thickness of the barrier layer is limited by the dielectric breakdown voltage, which is specific to the metal/electrolyte system. When the applied voltage exceeds this threshold, dielectric breakdowns occur through the barrier layer. These breakdowns manifest as visible spark discharges at the anode surface/electrolyte interface. These discharges are accompanied by both light emission and acoustic effects, indicating the formation of localized plasma. Figure 2 illustrates the characteristic light emission on an aluminum surface (sample size 50x50 mm).



Fig. 2: Characteristic plasma discharge on an aluminum sample

Figure 3 presents a scanning electron microscope (SEM) image illustrating the typical surface morphology of a PCO coating on an aluminum alloy. The image reveals a characteristic porous structure, highlighting the distinct surface topography associated with the plasma-assisted oxidation process. While porosity is also a feature of conventional anodizing, the PCO process typically results in a more complex and varied pore structure due to the dynamic nature of plasma discharges. This enhanced porosity can contribute to improved functional properties, such as increased surface area.

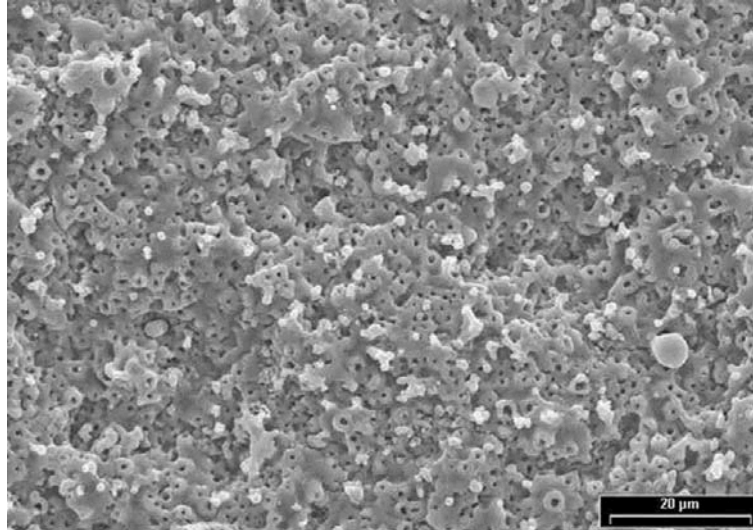


Fig. 3: SEM image of the surface morphology of a PCO coating on an aluminum sample.

PCO layers offer multifunctional benefits beyond corrosion protection for light metal alloys. These coatings exhibit exceptional versatility, particularly in optical applications. The PCO process produces ceramic-like coatings with tailored surface properties, including controlled porosity and roughness, which can be optimized for specific optical characteristics. In recent years, PCO coatings have gained significant recognition in high-precision optical and electronic industries, finding applications in the production of premium optical devices such as binoculars, cameras, and projectors. The coatings are particularly valuable for aluminum and magnesium alloy components, where they provide both protective and functional properties. A key advantage of PCO coatings is their entirely inorganic composition, primarily consisting of metal oxides. This inorganic nature imparts remarkable long-term stability to the coatings, maintaining their structural integrity and functional properties even under challenging environmental conditions. Notably, these coatings demonstrate high absorptivity across a broad spectrum of wavelengths, a characteristic that remains stable even in extreme operating environments. The combination of durability, optical performance, and stability makes PCO coatings an increasingly preferred choice for applications requiring both protective and functional surface properties in the optics and electronics sectors.

3. Coated Optomechanical Components

In laser technology, optomechanical components such as mirror holders, lens carriers, apertures, optical tables, beam blockers, beam shields, beam traps, shutter diaphragms, absorber plates, and beam filters are crucial for precise optical manipulation. These components often integrate electronic elements to perform specific functions efficiently within a compact design. Traditionally, many of these components are manufactured from commercially available aluminum alloys and anodized black using an adsorptive coloring method. Figure 4 illustrates the difference in appearance between uncoated and plasma-chemically oxidized (PCO) lens holders, highlighting the enhanced surface characteristics achieved through PCO. The introduction of plasma-chemically produced, highly absorbent coatings in laser technology aims to enhance the capability of optomechanical components, such as apertures, mirror and lens carriers, and beam dumps, to absorb stray laser radiation effectively. These coatings convert potentially damaging radiation into harmless thermal energy through absorption effects, thereby protecting the components.



Fig. 4: Lens holder (left uncoated, right PCO coated)

A critical property of these highly absorbent coatings is their reflective behavior across a broad wavelength range, from 220 nm to 2,000 nm. Figure 5 illustrates the wavelength-dependent reflection characteristics for three different PCO coatings. The data indicate that the reflection of these coatings is less than 8% for the lasers examined, providing optimal conditions for absorbing stray laser radiation, particularly in the near-infrared (NIR) range. This low reflectivity ensures that the coatings maintain their performance even under extreme conditions, making them ideal for high-precision optical applications.

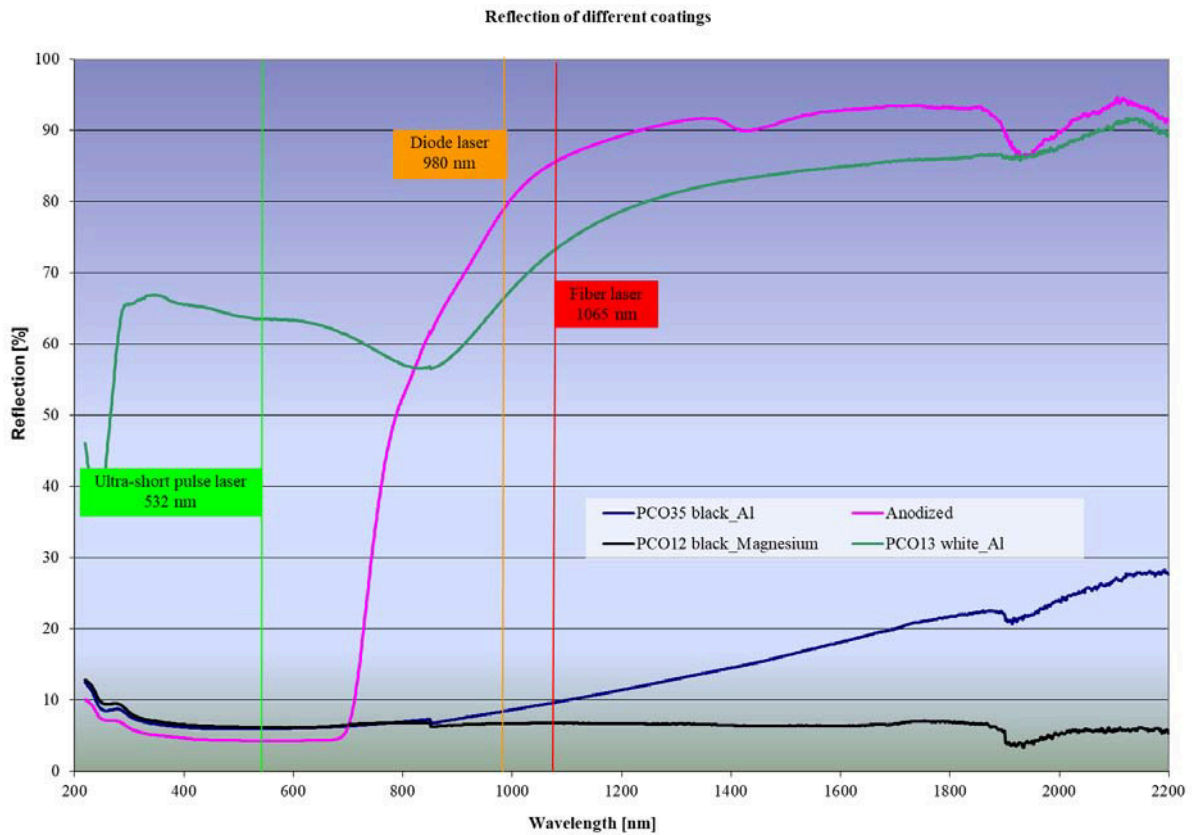


Fig. 5: Spectral response of an anodized sample compared to three different PCO coatings

The spectra reveal that the reflection of the black anodized layer increases significantly from approximately 730 nm, reaching 80 to 90% in the near-infrared (NIR) range. In this wavelength range, these layers

function more as mirrors than absorbers, making them unsuitable for absorbing 'radiation waste.' In contrast, the plasma-chemically produced layers exhibit distinct differences in reflection properties. Notably, the reflection values of the two doped PCO layers (PCO35 black and PCO12 black) remain well below 10% at the three laser wavelengths examined, demonstrating their superior absorptive capabilities. However, the undoped PCO coating (PCO13 white) shows a similar spectral response in the NIR range to that of the black anodized coating, indicating limited effectiveness in this specific application. The highly absorbent black surface of the PCO layers is achieved by a special electrolyte composition, which is dominated by corresponding contents of suitable metal salts.

Only one example of determining the damage threshold is provided here. For additional details, please refer to publication [6]. The damage threshold was measured using a Coherent COMPexPro™ 205F UV laser system (30 W) with the following parameters:

- Max. Pulse energy 700 mJ (250 mJ/cm²)
- Wavelength 248 nm
- Pulse duration 20 ns
- Max. Frequency 50 Hz
- Laser spot size 24 × 10 mm² (flattop)
- Laser spot size with aperture 15×5 mm²

A PCO-coated aperture was subjected to extensive testing to evaluate its durability under intense laser exposure. The experiment involved approximately 20,000,000 laser pulses with an average fluence of 100 mJ/cm². Figure 6 illustrates the results of this rigorous testing. The highly absorbent PCO coating demonstrated remarkable resilience, effectively withstanding laser radiation in a fluence range up to 250 mJ/cm². This performance indicates the coating's robust nature and its ability to maintain integrity under prolonged, high-energy laser exposure.

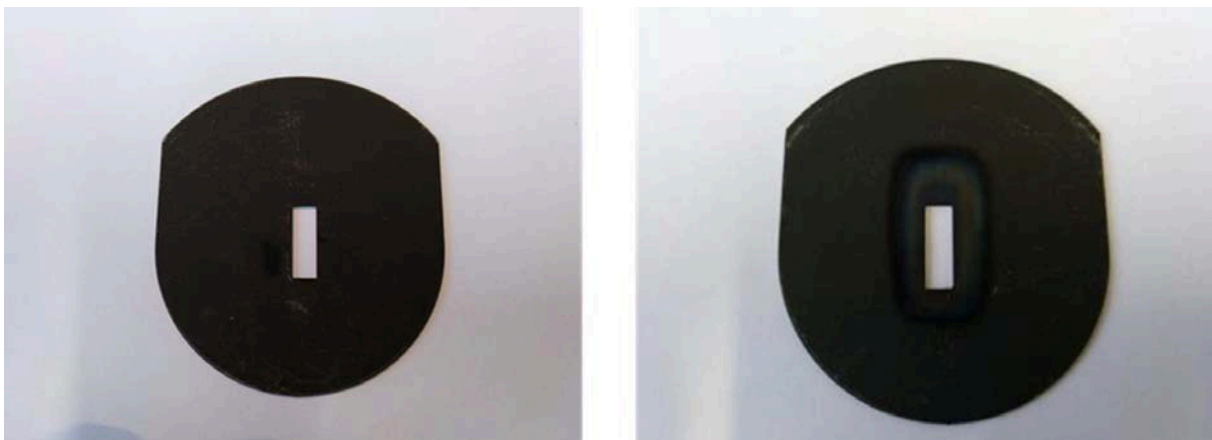


Fig. 6: Aperture before (left) and after (right) laser exposure

4. Conclusion

The plasma chemical oxidation (PCO) process enables the production of highly absorbing coatings for optomechanical components used in laser technology. By adjusting the composition of these coatings, it is possible to optimize both their reflective properties and their resistance to laser damage. Future research and development will aim to further refine the chemical composition of plasma-chemically produced oxide layers to enhance their reflectivity and laser resistance.

5. References

- [1] Kurze, P., Schreckenbach, J., Schwarz, Th., Krysmann, W.: „Beschichten durch anodische Oxidation unter Funkenentladung (ANOF)“, *Metalloberfläche*, 40 (1986) 12, S. 539–540

- [2] Schreckenbach, J. P.; Marx, G.; Bayer, U.; Kreisel: „Plasmachemische Oxidationsverfahren, Teil 1: Historie und Verfahrensgrundlagen“, Galvanotechnik, 94 (2003) 4, S. 816–823
- [3] Bayer, U., Schmidt, J., Schwarz, Th.: „Anwendungen von plasmachemisch oxidierten Leichtmetalloberflächen“, Galvanotechnik 84 (1993) 6, S. 1898-1901
- [4] Schmidt, J., Schrader, Ch., Tzschach, M.: „Die plasmachemische Oxidation von Leichtmetallen für optische und medizinische Anwendungen“, Jahrbuch Oberflächentechnik 67 (2011), S. 192–202
- [5] Schrader, C. et al.: „Erzeugung von Oberflächen auf Titanimplantaten mit biologisch funktionellen Eigenschaften zur Verbesserung der Biokompatibilität und Osteoinduktivität“, EUGEN G. LEUZE VERLAG KG, Galvanotechnik 102 (2011) 2, S. 242–248
- [6] Schmidt, J, Conrad. D.: Beschichtung von Leichtmetallen für Anwendungen in der Lasertechnik, EUGEN G. LEUZE VERLAG KG, Galvanotechnik 1/2013 (Sonderdruck)

PARMS coating technology for UV to IR laser applications

Myslivets, A., Sazinas, R.; Hohlov, E.
I-Photonics UAB, Avizieniu, Lithuania

Reactive sputtering with MF dual magnetron is a highly developed technique and successfully used for many thin film applications. For high performance low loss optical filter coatings based on oxides the reactive process has to avoid any kind of arcing, hard arcs as well as μ -arcs. This requirement is solved by Plasma Assisted Reactive Magnetron Sputtering PARMS as well as a high deposition rate for an economic production of high-end optical filter coatings.

Traditionally, the principle of PARMS is based on a two-step process, the reactive deposition of a thin oxide layer with a controlled deficit of oxygen followed by a RF plasma assist process with reactive oxygen for the transformation to a stoichiometric oxide layer. This sequence is repeated until the final layer thickness is stopped by time control or by an optical monitoring system [1].

In this technical note, we focus on the fabrication of precision optical coatings using a newly PARMS coater "Meridian" developed by I-Photonics UAB. This coater has a number of differences that improve the reproducibility and quality of the obtained optical coatings for a wide range of wavelengths.

Several types of the coatings based on Ta_2O_5/SiO_2 and Nb_2O_5/SiO_2 layers demonstrate the capability of I-Photonics PARMS for production of high-performance filter coatings.

References

- [1] M. Scherer et. al., "UV- and VIS Filter Coatings by Plasma Assisted Reactive Magnetron Sputtering (PARMS)," Optica Publishing Group, paper MA7, (2010).
- [2] P. Frach et. al., "Reactive Magnetron Sputter Technologies for Precision Optical Coatings," Optica Publishing Group, paper ThB.7 (2013).
- [3] Y. Khakhlou et. al. A vacuum unit for producing multilayer interference coatings on an optical element (EU patent EP4163416A1) (2023).

IBS optics for high-capacity laser processing

Adomaitis, M.
OPTOMAN, Vilnius, Litauen

Ultrafast lasers, such as Ti:Sapphire, Yb:YAG, Yb:KYW/KGW or Yb doped fiber lasers that generate pulses with durations down to a few femtoseconds, have opened up a new chapter in various fields. Industrial manufacturing applications like material processing, precision machining, and microstructuring greatly benefit from ultrafast laser developments. Scientific research fields such as multiphoton microscopy and attosecond physics also are driven by ultrafast, high average-power lasers. Many medical applications, such as ophthalmology, dermatology, and non-invasive surgical procedures employ high-power ultrafast lasers as well.

Ultrafast lasers operate at high power levels and generate intense pulses, putting significant strain on the optics. The field of ultrafast laser optics faces significant challenges in maintaining optimal performance and longevity. Short-lifetime optics lead to performance degradation, reduced efficiency, production downtime, and frequent maintenance requirements, thus significantly reducing the laser system's duty cycle. Enhancing the lifetime of optical components can noticeably lower the total cost of ownership as optics maintain the same performance over the increased amount of time ensuring uninterrupted manufacturing operations.

Furthermore, the demand for precise microfabrication techniques has risen in the field of high-capacity laser processing. Short pulse durations offer unparalleled control over material ablation and deposition processes, enabling intricate feature creation with high resolution and minimal heat-affected zones. This capability finds application in diverse fields such as semiconductor manufacturing, photovoltaics, and bio-medical device fabrication.

In the context of high-capacity laser processing, the versatility of ion beam sputtering (IBS) optics becomes a game changer. With the capability to cover a broad spectral range spanning from 193nm up to 5000nm, IBS optics empower manufacturers to integrate various laser sources for diverse applications. Whether it's ultraviolet lithography in semiconductor fabrication or infrared processing for polymer welding, IBS-coated optics ensure consistent performance and durability across the entire spectrum.

Through a combination of theoretical insights, experimental demonstrations, and real-world case studies, we illustrate how the strategic integration of IBS optics optimizes the efficiency, throughput, and quality of short pulse or high-power microfabrication processes.

Democratization of Laser Technology: A Journey of Unlimited Opportunities

Dr. Ulrike Fuchs
asphericon GmbH, Germany

A paradigm shift is underway in laser technology, marked by the democratization of light. This shift aims to empower individuals beyond expert circles, offering the capability to shape and utilize light according to unique requirements. The talk delves into the evolution of laser technology, emphasizing its transformation from a specialized field to a ubiquitous tool across various industries, particularly in laser cutting, welding, and surface structuring. Central to this evolution is the concept of democratization, which hinges on enhancing accessibility through simplicity, adaptability, and performance.



Laser applications for sustainable electrical energy storage and converters

Dr. Jens Standfuß
Fraunhofer IWS, Germany

Laser applications play a crucial role in optimizing and advancing technologies that are of great importance for a sustainable energy future. The presentation describes the use of laser applications in batteries, fuel cells, transformers, and electric motors with a focus on material properties.

In the field of battery technology, lasers enable precise machining of electrode materials to improve performance and capacity. This contributes to the development of efficient energy storage solutions that are essential for expanding renewable energy and electrifying the transportation sector. In fuel cells, laser applications allow for precise machining of membranes and electrodes to increase efficiency and durability. This supports the realization of clean and emission-free energy systems, providing an alternative solution to conventional power generation. Laser applications are also used in transformers and electric motors to reduce electrical losses, improving performance and efficiency. This supports the development of energy-efficient systems. Through further development and application of laser applications, the next generations of batteries, fuel cells, transformers, and electric motors can be designed, making a significant contribution to addressing the challenges of climate change and resource scarcity.



Tailored refractive diffusers for broadband beam shaping

Kraus, M.; Katzer, S.; Deparnay, A.
Carl Zeiss Jena GmbH, Jena

Abstract

Beam shaping is a common task for a large number of laser applications. This includes beam homogenization, pattern projection or the creation of top-hat profiles. For most applications, e.g. laser material processing, diffractive beam shapers are used. They are beneficial because a single element creates large deviation angles with high precision. Furthermore, design and fabrication are well established and thus, the elements are available for a reasonable price. However, the diffractive working principle is also connected to several drawbacks. As the profile shape of the diffractive structure determines the efficiency and far field distribution, the fabrication precision and accuracy are crucial for the functionality. Furthermore, diffraction is strongly wavelength-dependent and thus, efficiency drops for wavelengths deviating from the design wavelength. As a consequence, disturbing light is observable in the zeroth order and in ghost images.

A solution is the use of refractive diffusers which can be used for homogenization and the generation of arbitrary beam profiles. The refractive working principle allows high efficiencies and suppresses ghost images and the zero order. As the wavelength dependency of refraction is small, refractive diffusers are the best choice for broadband sources and multi-wavelength laser systems. Fields of application include systems with different laser sources like LED and laser projection systems or systems for medical treatment and laser surgery. Furthermore, the diffusers are beneficial for systems employing tunable lasers and femtosecond lasers. A challenge for refractive diffusers is the generation of distinct beam profiles which require large deviation angles and high accuracy. This contribution focusses on the fabrication and characterization of refractive diffusers which achieve large deviation angles of 15 degrees up to 30 degrees. The optical functionality is created by a tailored microstructured surface which generates the required intensity distribution. For the fabrication, the microstructure is generated firstly in photoresist by direct writing laser lithography. Subsequently, the photo resist profile is transferred into laser-resistant fused silica by reactive ion etching. The characterization is done by white light interferometry. The generated intensity distributions can be designed with a high degree of flexibility. The presented distributions include an elliptical top-hat and a cross.

Combining freeform optics and Zwobbel technology for line structuring of large substrates with ultrashort pulsed 2 μ m lasers

Fuchs, U.¹; Schlutow, H.¹; Burkhardt, I.²; Fischer, M.²; Reinlein, C.²

¹ asphericon GmbH, Jena, Germany

² ROBUST AO GmbH, Jena, Germany

Abstract

Ultrashort pulsed lasers with a wavelength of 2 μ m are ideal for material processing applications of plastics, such as welding, marking and cutting. Scanning systems are essential for the processing of large substrates. We present a novel approach for line structuring using the Zwobbel technology in combination with freeform optics, which has been developed in the collaborative project UKPino. With this concept we envision faster processing times on larger substrates, particularly applicable to roll-to-roll processes. Generating a line structure by scanning across a cylindrical lens suffers from strong image field curvature. This can be compensated by extending the lens geometry to a freeform lens. Our studies have shown that the processing field can be further extended by combining the freeform lens with a deformable mirror that additionally shifts the focal position. The Zwobbel technology has been selected. This is a piezo actuator-based focus-only deformable mirror with fast step responses of <2 milliseconds and scanning ability up to 2000Hz. Herewith, we can generate kilohertz line scan frequencies on large substrates. The number of Zwobbel deformable mirror defines the achievable scan length. We discuss possible designs based on one and two deformable mirrors.

In summary, the paper discusses application requirements, the optical design possibilities, and the opto-mechanical implementation. A compact setup is required based on a robust opto-mechanical design to achieve long-term stability. Therefore, we consider electro-mechanical integration already in the design phase and derive the mechanical degrees of freedom for the optical components from this.

Manufacturing and assembly of a High-Finesse Cavity

Burkhardt, T.; Drechsler, M.; Hanke, P.; Schippel, S.
Layertec GmbH, Mellingen

Abstract

Ultra-stable laser systems with sub-Hz linewidth require High-Finesse cavities as a fundamental tool for precise frequency stabilization. Two highly reflective mirrors with a common base body (spacer) can form such a Fabry-Pérot resonator. We present a High-Finesse cavity with a finesse of more than 270,000 at a wavelength of 1542 nm. The cavity consists of a Low Thermal Expansion glass body and fused silica mirrors. The resonator mirrors are coated using magnetron and ion-beam sputtering techniques with reflectivity in the order of $R > 99.999\%$ with a residual 5 ppm mirror transmittance. During the assembly the mirror substrates are optically contacted to the spacer and additionally welded by ultra-short pulse laser welding. The advantage of this approach is the opportunity of a preliminary characterization of the finesse before laser welding joins the mirrors inseparably. Finesse characterization of the cavity is carried out by spectrally resolved cavity ring-down measurements. The localized laser welding process preserves the adjustment state and the high finesse of the cavity. This joint is completely free of additives, especially free of organic adhesives, thus aiding the ultra-high stability of the resonator's length. It provides high mechanical strength, high robustness against environmental loads, and long term stability. These beneficial characteristics of laser welding make this technology suitable for rugged applications in harsh environments or for aero-space use.

1. Introduction

Ultra-stable laser systems with sub-Hz linewidth require High-Finesse cavities as a fundamental tool for the precise stabilization of free-running laser sources [1]. These optical resonators can be used, for example, as laser resonators, for frequency stabilisation, mode selection, in the field of measurement technology for high-resolution spectroscopy, and other metrology applications [2], [7]. Optical resonators of very high finesse provide references for optical atomic clocks or optical frequency standards, stabilized laser systems with ultra-narrow bandwidth, as well as optical frequency combs. Another use of optical cavities is in optical gas refractometry and a respective gas pressure standard, a technique known as Fixed Length Optical Cavity (FLOC) – a compact and portable yet high-performance system [11].

Two highly reflective mirrors with a common base body (spacer) can form such a Fabry-Perot resonator. The spacer defines the resonator length and is typically made of a material of low thermal expansion and low thermal noise (e.g. Ultra-Low Expansion ULE[®] Glass, Zerodur, fused silica) to ensure its thermal stability. The reflectivity, absorption losses, surface irregularity of the mirrors, as well as tilt errors during assembly, determine the finesse of the cavities. A resonator made from separate spacer and mirrors allows for the selection of the mirrors (i.e. pairing). Furthermore, the spacer can be made from a material of favorable thermo-mechanical properties without regard for its optical properties.

Ultra-stable optical cavities require a low thermal expansion and low hysteresis of the spacer and the joint, robustness to thermo-mechanical and environmental loads, and long-term stability. The position of both mirrors with respect to each other and the spacer body needs to be of high precision. Both the joint itself and the respective joining techniques should therefore support these requirements. Joints should preferably be formed without an additive layer, e.g. solder alloys or organic adhesives. The process of joining should not significantly deform the spacer or the mirrors or introduce stress, i.e. a minimal thermal load during joining is preferable.

Optical contacting is a precision joining technique for polished optical components. It is based on the adhesion forces between the contacting optical elements. It requires high quality surfaces in terms of fit, roughness, and cleanliness. For this joining variant the joining partners must have surfaces facing them that are either flat or have an identical surface curvature with a very high degree of shape accuracy. During assembly a high cleanliness is required so that no impurities, especially in the form of particles and filmic

contaminations are present. Optical contacting, however, is of limited mechanical strength and susceptible to various environmental and mechanical loads (e.g. humidity, shock, and vibration), but these limitations also provide a benefit: joint components can be removed and reworked.

Laser welding with ultrashort pulses in the fs or ps regime in transparent materials is based on the nonlinear absorption in the focal point and the heat accumulation through the interaction of a large number of consecutive pulses at repetition rates in the high kHz or MHz range [12], [8]. With ultrafast lasers fluences greater than 10^{13} W/cm² are easily reached in the focal spot. This leads to a nonlinear interaction with the dielectric material, i.e. multiphoton absorption and field ionization. The free charge carriers generated in the resulting plasma can then be excited by avalanche ionization, so the absorption in the plasma increases further. In order to melt a sufficiently large glass volume, i.e. to achieve a heat-affected zone larger than the focus diameter, the thermal energy of many individual pulses must be accumulated. To do this, it is necessary that the time interval between successive pulses is smaller than the time constant of thermal diffusion in the material. For fused silica, this is in the order of one microsecond for a focus diameter in the micrometer range, i.e. the repetition rate of the laser system used must be in the order of MHz [10]. Ultra-short pulse (USP) laser welding [8], [10], [4] is characterized as a joining process for fused silica and other optical glasses with a high achievable strength and resistance to thermo-mechanical loads. It is a localized welding process, which minimizes global stresses and deformation of the assembly and enables the sequential construction of highly precise, multi-component systems. Using USP laser welding, gaps in the micrometer range between the joining partners can also be bridged, although gap-less joints are preferable to minimize stress during resolidification of the melting pool [9], [5] welding furthermore secures optical contacting against penetration of humidity and against thermal or mechanical shocking and vibrations.

A third joining technique relevant to the assembly of optical cavities, especially of spacer bodies is a wet chemical bonding process “hydroxide-catalyzed bonding” (HCB). Similar to optical contacting conformal surfaces of high flatness and low roughness are required to initiate a successful bond. The technique is easy to use, very precise, highly reproducible, and results in very strong bonds [6], [13].

2. High-finesse optical cavity

2.1 Requirements and design

Goal of the project „Quantensensor mit Strontiumstrahlen (QUASENS)“ is to demonstrate an optical clock with stability of better than 10^{-15} with a few hours of averaging time. This clock is based on atom interferometry on a thermal atom beam. For this purpose, a laser is stabilized at the transition frequency of the entangled state. Then the optical frequency is divided by a frequency comb into a usable frequency in the microwave range, so that the output of the clock is compatible with established radio frequency clocks such as hydrogen masers and Cs atomic clocks, which is a crucial criterion for typical applications, e.g. in navigation, interconnecting satellite systems, or astronomical telescopes. In this paper we present the high-finesse cavity that is central part of the frequency comb at 1542 nm. The design goals are a reflectivity of 99.998% to 99.9992% with a transmission of 4 ppm to 20 ppm, resulting in a finesse of 314.000.

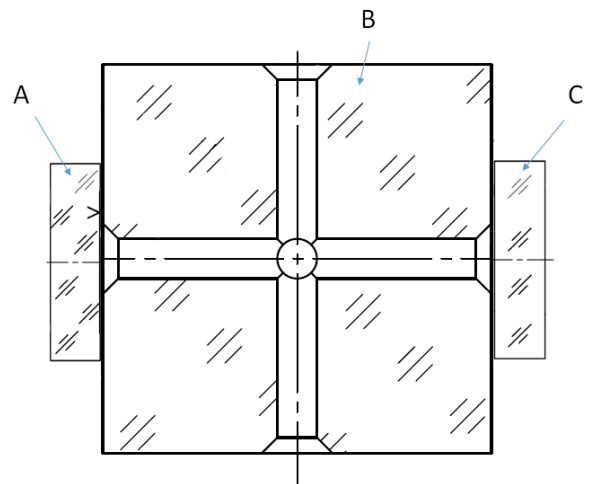


Fig. 1: Simplified schematic cross section of the optical cavity with the concave mirror (A), the spacer body (B), and the plano mirror (C).

An optical resonator is an arrangement of at least two mirrors and a spacer body. The mirrors are mounted on the spacer’s opposite faces, which fixates their distance and position with respect to each other. The QUASENS cavity is stable semi-confocal resonator that consists of a plano and a concave mirror (Fig. 1). Its cubic spacer’s design is insensitive to inertial forces acting in any direction and to compressive force used to constrain it. Four supports are placed symmetrically about the optical axis in a tetrahedral configuration [14]. The specific cubic design is licensed by the National Physical Laboratory (NPL).

2.2 Manufacturing of components

The cuboid spacers made from ULE[®] are batch processed to achieve a high parallelism (better than 1 arcmin) and high perpendicularity (better than 2 arcmin) by grinding and polishing (Fig. 2). More demanding angular precision could be achieved during polishing if required by the cavity's performance specification. For plano-concave resonator geometries this is, however, often not necessary. The crossed-axis boreholes are grinded, chamfered, and wet etched. Acid etching removes debris from grinding and other microscopic surface flaws. This removal of a surface layer reduces number and size of surface flaws as well as dulling their sharp edges, an effect commonly referred to as "healing" of the glass. Etched glass surfaces are usually stronger since both the emergence and growth of cracks during mechanical stress are significantly reduced.

Resonators with ultra-high finesse require mirrors with extremely low losses. Both optimized coating technologies and advanced substrate manufacturing techniques are required to achieve this goal by minimizing absorption and scattered light losses. Especially the surface roughness has a significant impact on losses due to scattering. Plano and concave substrates (\varnothing 25 mm, thickness 6.35 mm) are made from fused silica and are polished to 0.15 nm (S_q micro-roughness) and surface imperfections typically better than 5/1x0.010 (plano) and 5/1x0.025 (concave). Super-polishing to a roughness better than 0.1 nm is also possible and will be required at reduced wavelengths. The concave substrates are also fitted with polished flat bevel that is used for optical contacting and laser welding.

Besides the micro-roughness of the substrate's surface the volume scattering effects of the thin-layer system and absorption sources in the coating system, such as stoichiometry errors or impurities (e.g. Fe, Cr, Cu) have to be minimized. Ion Beam Sputtering and Magnetron Sputtering are used both for the cavity forming highly reflective coatings as well as the antireflection coatings on the rear side of the mirrors. These are the most advanced depositions technologies for lowest losses of absorption and scattering. They provide high density layers with an excellent microstructure and low impurities that guarantee ultra-high reflectivity and lowest absorption. The high precision in film growth allows furthermore a well defined residual transmission in the ppm range as required for an ultra-high finesse cavity. Sputtering techniques are also well suited for high power applications and an increased intensity within an ultra-high finesse cavity.

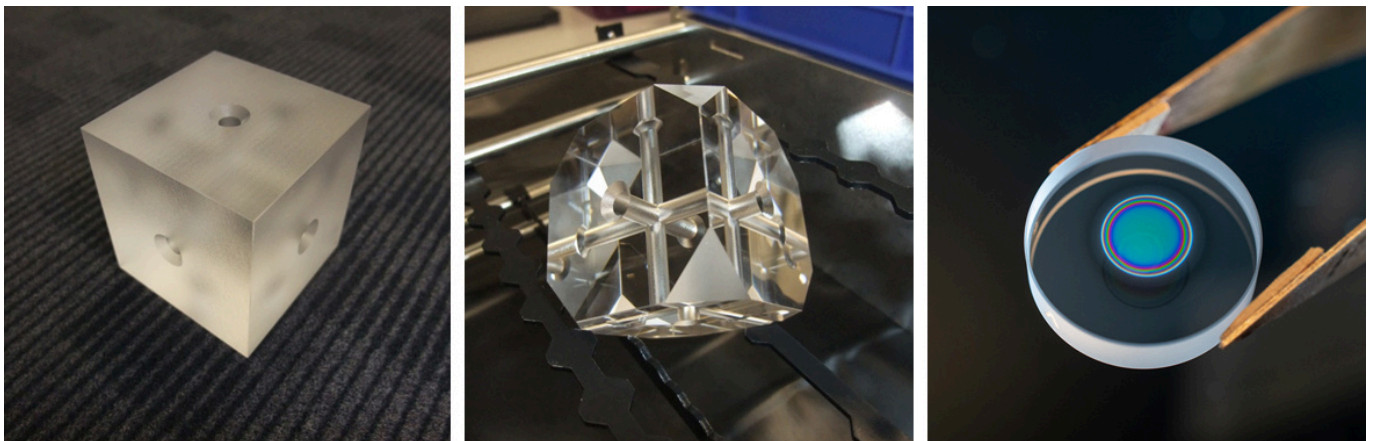


Fig. 2: ULE[®] cube after grinding, drilling, and etching (left); polished ULE[®]-spacer after ultrasonic cleaning (middle); low-loss substrate with localized magnetron sputtered highly reflective coating.

2.3 Assembly of the optical cavity

The components of the optical cavity are assembled in a clean room environment after ultrasonic cleaning in a two-stage process. In accordance with the requirements of the resonator, the mirrors' positions with respect to the spacer are passively adjusted and then optically contacted. This optical contact is essentially seamless and already sufficiently stable to allow for a first measurement of the finesse using a cavity ring-down setup or any other suitable performance test. Rework is possible if the finesse is not within an

acceptable range or other defects or flaws are observed, since optical contacting is non-permanent. The mirrors can be removed from the spacer, cleaned, and the assembly can be restarted.



Fig. 3: Ultra high-finesse optical cavity with a 50x50x50 mm³ cubic spacer, crossed-axis boreholes, and magnetron sputtered mirrors contacted through optical contacting followed by USP laser micro welding.

If in this preliminary characterization the finesse is found to be within specification the final assembling step is performed to inseparably join the mirrors: ultra-short pulse laser welding. A TruMicro 2030 (1030 nm, 400 fs, max. pulse energy 20 μJ, f_{rep} 2 MHz, max. average power 20 W) is used with a Thorlabs LMH-5x-1064 and LMH-10x-1064 focussing optics. Further details of the setup used for laser beam welding can be found in [3]. The laser micro welding results in a localized welding seam. The welding seam is placed well outside the clear aperture of the components. In case of the concave mirror, the placement is restricted to the area of the polished flat bevel. After laser welding all components are permanently and with high stability connected. The final result of an ultra high-finesse optical cavity with a cubic spacer, crossed-axis boreholes, and magnetron sputtered mirrors contacted through optical contacting followed by USP laser micro welding is displayed in Fig. 3.

2.4 Measurements and results

Plano and concave mirrors for a 1542 nm resonator are fabricated with an optimized process chain of polishing, cleaning, and coating. The design goals of reflectivity between 99.998% and 99.9992% and a transmission between 4 ppm and 20 ppm are reproducibly achieved. Figure 4 shows an example of reflection and transmission measurements by means of spectrally resolved cavity ring-down with $T=5$ ppm and $R=99.999\%$ at 1542 nm. Paired mirrors with these values form a symmetric cavity with a finesse of 314.000.

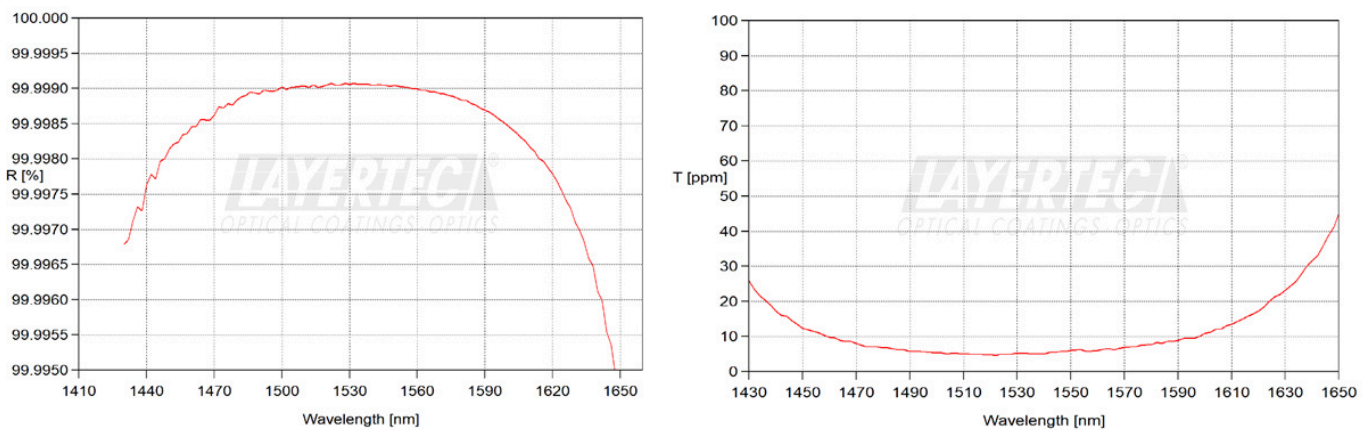


Fig. 4: Reflection (left) and transmission (right) measurements for a 1542 nm resonator mirror.

Fabry-Pérot cavities are assembled from these mirrors and ULE[®] spacers. Finesse measurements after optical contacting, USP laser welding, and delivery to the customer show a finesse of greater than 270.000, and respective average reflection values of the single mirrors of greater than 99.9988% assuming a symmetric cavity (see Fig. 5). Laser micro welding proves to not influence the adjustment of the system and therefore does not change finesse. The optical cavity can be used for laser stabilization and enable a relative frequency stability in the range of 10^{-15} at integration times of 1 s even outside laboratory environments.

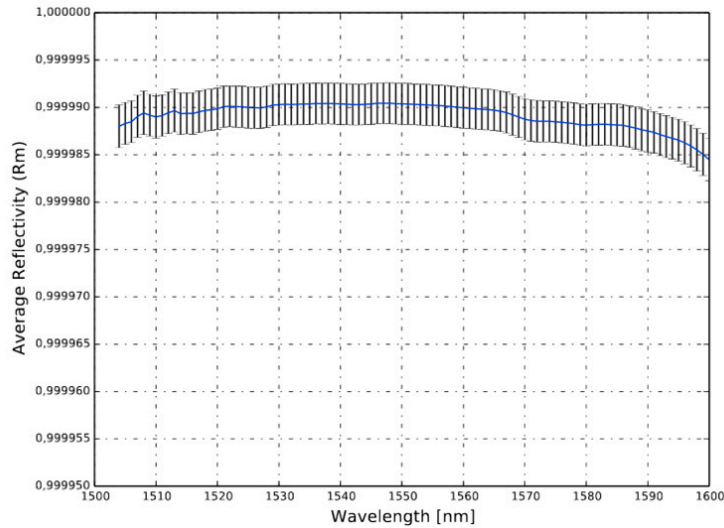


Fig. 5: Average reflectivity of a Fabry-Pérot Cavity at 1542 nm.

3. Further examples of Fabry-Pérot Cavities

We have established a process chain for manufacturing components and respective optical cavities for different application as shown in Figures 6. This includes multi-axis systems (“crossed-cavity”) with cuboid spacers as well as single axis systems with spacer lengths of up to 150 mm.

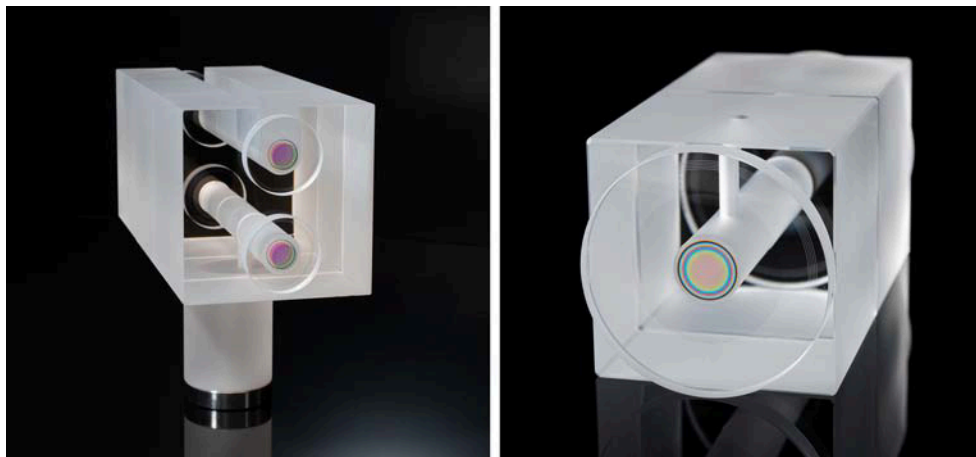


Fig. 6: Dual FLOC cavity with a base body 63x63x150 mm³ comprised of three separate elements and CF vacuum flange for evacuation of one channel (left) and cavity 25x25x56 mm³ with a spacer body comprised of two bonded elements (right).

Longer spacer bodies can be assembled from multiple smaller components using the HCB wet chemical bonding. This approach is both cost efficient and allows for the fabrication of quasi-monolithic spacers with unfavorable aspect ratios, i.e. long boreholes of small diameters. As demonstrated in a previous publication [3] optical contacting, USP laser welding, and HCB create hermetically sealed bonds that are a neces-

sity for a gas pressure sensor or optical refractometer. As mentioned in the previous section, the assembly is conducted in a clean room environment after ultrasonic cleaning of the components.

To evaluate the surface deformation of mirrors joined to a spacer body we manufactured a testing vehicle of reduced dimensions to accommodate for restrictions during interferometric measurements. Four planar/planar mirror blanks (Ø 25 mm, thickness 6.35 mm, fused silica) are joined to an ULE[®] spacer (63x63x50 mm³) by optical contacting followed by USP laser welding. The mirror blanks show a typical total surface deformation of below 30 nm (PV) within a clear aperture of Øe 21 mm. With U-shaped open channels we find an increase of deformation of up to 50 nm (PV) during optical contacting that can be attributed to the asymmetrical joining area. We find, however, no significant change during USP laser welding despite the necessary asymmetrical welding seam. This supports the hypothesis that stress and deformation introduced by laser welding is negligible. O-shaped closed channels show significantly less deformation during optical contacting and only small changes during the welding of a symmetrical circular welding seam (see Table 1).

Part	Channel Type	Optically contacted		Laser welded	
		PV (nm) RMS_t (nm)		PV (nm) RMS_t (nm)	
1	Open	48,9	9,9	48,0	10,4
2	Closed	16,6	3,6	22,3	5,0
3	Open	48,7	10,4	48,1	10,3
4	Closed	24,8	5,6	24,8	5,6

Table 1: Total surface deformation (Øe 21 mm) of the outside planar surfaces of mirror blanks joined with a dual FLOC cavity spacer with „U“-type channels (open) and „O“-typed channels (closed).

4. Summary

We present the manufacturing of the components and the assembly of a High-Finesse cavity with a finesse of more than 270,000 at a wavelength of 1542 nm. The cavity consists of a low-expansion ULE[®] spacer body and fused silica mirrors. The resonator mirrors are coated using magnetron and ion-beam sputtering (IBS) technologies with reflectivities in the order of $R > 99.999\%$ with 5 ppm mirror transmittance. Highly reflective coatings can be also manufactured for other and/or multiple wavelengths, allowing to simultaneously stabilize different laser sources. During the assembly of the optical resonator the mirror substrates are optically contacted to the spacer and additionally locally welded by USP laser welding. The advantage of this approach is the opportunity of a preliminary characterization of the finesse before laser welding to inseparably join the mirrors and thus a possible rework if the required finesse is not achieved.

We show that larger spacer bodies can be manufactured from multiple smaller elements that are quasi-monolithically bonded using a wet chemical process. This approach is beneficial to a cost effective manufacturing large cavity spacers with unfavorable aspect ratios of their respective boreholes. Both laser welding and chemical bonding have been proven to provide hermetical sealing.

We find that the strongly localized USP laser micro welding process preserves the adjustment state and the high finesse of the assembly as is achieved by optical contacting. Both the optical contacting and the additional welding provide joints without additional intermediate layers aiding the ultra-high stability of the resonator’s length. It is completely free of additives, especially free of organic adhesives. This is also advantageous with respect to a low thermal expansion of the whole assembly, a low outgassing to minimize contamination of optical surfaces, and an overall high stability. Major contributions to surface deformation of mirrors joined to a spacer body stem from optical contacting and the residual differences in surface deformation of both components to be joined, with only small changes due to USP laser welding. Laser welded joints surpass optical contacting, which is susceptible to thermal and mechanical shocks as well as significantly less robust against environmental influences, while preserving its main benefits of high

accuracy and additive free joining. USP laser welding provides joints of high mechanical strength, high robustness against thermal cycling and other environmental loads (e.g. humidity), and long term stability. These beneficial characteristics of laser welding make this technology suitable for rugged applications in harsh environments or aero-space use. Layertec can provide high-finesse optical cavities and components such as low-loss mirrors and precision spacer bodies for the most demanding scientific and industrial applications.

5. Acknowledgements

Parts of the work presented here were funded by the Federal Ministry of Education and Research (BMBF) under FKZ 13N15728, Project „Quantensensor mit Strontiumstrahlen (QUASENS)“. The authors gratefully acknowledge the cooperation with Menlo Systems within the project QUASENS. Responsibility for the content of this publication lies with the authors.

6. References

- [1] Alnis, J.; Matveev, A.; Kolachevsky, N.; Udem, T.; Hänsch, T. W.: “Subhertz linewidth diode lasers by stabilization to vibrationally and thermally compensated ultralow-expansion glass Fabry-Pérot cavities”, *Physical Review A* 77, 053809 (2008).
- [2] Bober, M.; et al: “Strontium optical lattice clocks for practical realization of the metre and secondary representation of the second”, *Measurement Science and Technology* 26 075201 (2015).
- [3] Burkhardt, T.; Schmitz, P.; Drache, F.; Schippel, S.: “Ultrakurzpulslaserschweißen für die Montage optischer Baugruppen”, In: DVS-Berichte Band 384, DVS Media GmbH, 2022.
- [4] Cvecek, K., Odato, R., Dehmel, S., Miyamoto, I., Schmidt, M.: “Gap bridging in joining of glass using ultra short laser pulses”, *Optics Express* 23(5), 5681–5693, (2015).
- [5] Cvecek, K., Dehmel, S., Miyamoto, I., Schmidt, M.: “A review on glass welding by ultra-short laser pulses”, *Int. J. Extrem. Manuf.* 1, 042001, (2019).
- [6] Gwo, D.-H.: “Ultra-precision bonding for cryogenic fused-silica optics”, *Proc. SPIE* 3435, *Cryogenic Optical Systems and Instruments VIII*, (1998).
- [7] Hill, I. R.; et al: “A low maintenance Sr optical lattice clock”, *J. Phys.: Conf. Ser.* 723 012019 (2015).
- [8] Miyamoto, I., Cvecek, K., Okamoto, Y., Schmidt, M.: “Novel fusion welding technology of glass using ultrashort pulse laser”, *Physics Procedia* 5, 483–493, (2010).
- [9] Miyamoto, I., Cvecek, K., Schmidt, M.: “Advances of Laser Welding Technology of Glass – Science and Technology”, *Journal of Laser Micro/Nanoengineering* 15(2), 63–76, (2020).
- [10] Richter, S., Nolte, S., Tünnermann, A.: “Ultrashort pulse laser welding – a new approach for high stability bonding of different glasses”, *Physics Procedia* 39, 556–562, (2012).
- [11] Ricker, J.; Douglass, K. O.; Hendricks, J.; White, S.; Syssoev, S.: “Determination of distortion corrections for a fixed length optical cavity pressure standard”, *Measurement: Sensors* 18 (2021) 100286.
- [12] Tamaki, T., Watanabe, W., Nishii, J., Itoh, K.: “Welding of transparent materials using femtosecond laser pulses”, *Jpn. J. Appl. Phys* 44, 687–689, (2005).
- [13] van Veggel, A.-M. A., Killow, C. J.: “Hydroxide catalysis bonding for astronomical instruments”, *Adv. Opt. Techn.* 3(3), 393–307, (2014).
- [14] Webster, S.; Gill, P.: „Force-insensitive optical cavity“, *Optics Letters* Vol. 36, Issue 18, pp. 3572-3574 (2011).

Minimisation of process times in high-quality laser cutting through dynamic beam shaping in propagation direction

Ulrich, S.¹; Burkhardt, I.¹; Langebach, J.²; Banse, H.²; Reinlein, C.¹

¹ ROBUST AO GmbH, Jena

² JENOPTIK Automatisierungstechnik GmbH, Jena

Abstract

In the field of sheet metal processing, laser cutting is an industrially established process that is subject to continuous optimization. The focus here is on increasing productivity. The cutting speed has a significant influence on productivity. To increase this, the current trend is a combination of ever higher laser power with machine axis acceleration of up to 6G. In laser fusion cutting, a compromise must be made between productivity through high cutting speed and optimum cutting-edge quality.

Increased productivity through higher cutting speeds has already been demonstrated and integrated into industrial processes using dynamic beam shaping in the processing plane (X-Y oscillation). Whereas dynamic beam shaping is the fast movement/oscillation of the laser beam over the part surface. However, this X-Y oscillation technology is associated with a more complex process control due to the additional process parameters required for dynamic beam shaping in the working plane (four to nine) compared to static beams. In contrast, dynamic beam shaping in the beam propagation direction reduces the number of degrees of freedom to a further two to three (oscillation amplitude and frequency). This is helpful for rapid process optimization.

In addition to the pure increase in cutting speed, the product quality (grade, distortion, thermal material change) is the important decision criterion that is listed in favour of or against a technology. In cases where post-processes such as welding or painting are involved, the decision is made for higher cutting edge quality in order to avoid intermediate preparation steps.

The present work focuses on experimental evaluations of dynamic beam shaping the beam propagation direction through high-frequency beam oscillation in. By adjusting the oscillation parameters, the intensity distribution and the virtual focal length, the energy disposition in the kerf and its geometry can be adjusted. We will show that this has a positive effect on the cutting speed and edge quality with constant laser power. For sheet thicknesses ranging from 0,5 mm to 10 mm, the speed could be increased by up to 30 % while simultaneously reducing the gas pressure. Furthermore, the cutting edge smoothness is significantly increased that results in less needed rework. In conclusion, it can be demonstrated that despite the higher cutting speed, a higher cutting edge quality is achieved compared to the static beam through the use of dynamic beam shaping.

Ultrafast laser processing on large surfaces – Machine concepts and applications

Eifel, S.
Pulsar Photonics GmbH, Aachen, Germany

1. Introduction

In view of the increasing availability of industrially suitable USP laser beam sources with high average laser power in the >200W range, large-area applications for laser micromachining with ultrashort pulse lasers are also becoming increasingly interesting from an economic point of view. Driven by the regulatory restriction of environmentally harmful manufacturing processes in the EU (e.g. REACH) and the growing trend towards digital production chains, commercial enterprises are increasingly striving for more environmentally friendly manufacturing processes. Laser micromachining with ultrashort pulse lasers offers a more environmentally friendly and interesting alternative to galvanic and etching processes. For large-area laser micromachining with USP lasers, so far only machine technology is available for processing components in cylindrical geometry, for example for manufacturing embossing rollers. For the laser micromachining of large-area flat components with surfaces up to 10-20 m², however, there is still a lack of suitable machine concepts on the market, especially for applications that go beyond thin-film processing. By using a new developed machine platform for the USP laser micromachining of large flat components this limitation in the market will be overcome. By using multi-beam concepts in combination with high-power USP lasers, the necessary scaling of the process speed can be achieved.

2. Requirements in the market

In the last 10 years, laser micromachining with ultrashort pulse lasers was primarily relevant for applications requiring precise but comparatively small volume removal (e.g. thin-film processing, micro-drilling) or modification of workpieces (e.g. filamentation, surface modification). Due to the availability of increasingly powerful industrial-grade USP laser beam sources in recent years, applications involving significantly larger volume ablation (e.g. deep-engraving, laser roughening) are now also economically feasible on the laser side. While the current power class of 200-300 W average power has been available for industrial use for some time, the first demo systems for industrially suitable USP laser beam sources with an average power of up to 1000 W are already available. With these power classes, large-area volume ablation of workpieces in square meter size is economically feasible. This has already been proven several times for the lower power range for the processing of embossing rollers and has now resulted in industrially suitable machine concepts for the processing of roller-shaped components (see Brüning et. al. 2022). Driven by regulatory restrictions on the use of chemicals in the EU (e.g. REACH), companies that use environmentally harmful manufacturing processes such as etching and electroplating are increasingly having to develop and use alternative manufacturing processes. With laser micromachining as a more environmentally friendly alternative in combination with industrial-grade high-power ultrafast lasers, the foundations are in place for a technological shift from these traditional manufacturing processes to laser machining. Until now, no suitable machine technology was available for the volume removal of large-area flat components in the square meter range.

3. Machine Concept RDX2800

In cooperation with reference customers, Pulsar Photonics GmbH has developed a new machine concept for processing flat components with areas of up to 10-20m². The machine concept provides for a modular approach, i.e. there are individual machine modules that can process a defined working area of currently 1.5m x 2.5m. Up to 5 machine modules can be combined to process larger workpieces. This means that each machine module processes an area of the workpiece. Parallel processing is essential, especially for large-area volume removal. In addition to parallel processing across several machine modules, further parallel processing takes place in each machine module. For precise and melt-free processing with a high-power ultrashort pulse laser, the laser power must be distributed over a large area of the workpiece. Various optical concepts are used for this purpose. The use of a polygon scanner or a multi-beam system

enables the laser power to be distributed over the workpiece within a processing head. An alternative approach is to distribute the laser power over several processing heads. For this purpose, the machine concept provides for a multi-scanner design. Several galvanometer scanners can be integrated into each machine module, which can realize autonomous laser processing of a workpiece area. Depending on the requirements and area of application of the machine, the process speeds can be increased by a factor of 10-1000 in order to achieve cost-effective processing.



Figure 1: Modular gantry system RDX2800 for large area laser processing with ultrafast lasers.

The strength of the machine concept lies primarily in the individualized machining of the component in each workpiece area, i.e. each scan head can execute a different scan program. This requires a sophisticated CAM chain that is able to derive a sum of machining programs for each individual scan head from a large data set that defines the target geometry of the workpiece to be produced. The machine concept has already been realized in a pilot system of the type RDX2800 and is being further developed together with the reference customers. For demonstration purposes a plate with 1000mm x 1000mm dimension has been processed with samples structures for deep engraving and functional surfaces on the pilot machine (cf. Figure3).

4. Summary

With the availability of USP high-power lasers, alternative manufacturing processes for large-area micromachining of tools and workpieces can be realized.



Figure 2: Machine module RDX2800 with ultrafast laser for parallel processing of a workpiece with dimensions 2.5m x 1.5m.

With the RDX2800, a modular machine concept is available that is able to use the power of these laser beam sources for large-area volume ablation and individualized processing of each workpiece area. A parallelization concept and a powerful machine control system were developed for this purpose. The concept was implemented and demonstrated together with pilot customers. As a result, industrial-grade machine solutions are now available for any large-area micromachining or functionalization of flat components.



Figure 3: Demonstrator plate (1000 mm x 1000 mm) for large-area USP laser processing with sample structures for functional surfaces and deep engravings.

5. References

[1] S. Bruening, K. Du, and A. Gillner, "High-throughput ultrafast laser micromachining with multiple parallel spots," in *Conference on Lasers and Electro-Optics*, Technical Digest Series (Optica Publishing Group, 2022), paper AM3I.3. https://opg.optica.org/abstract.cfm?URI=CLEO_AT-2022-AM3I.3

High strength micro-welded glass

Thomas, J. U.¹; Günther, L.¹; Lundén, H.²; Polojärvi, V.²; Määttänen, A.²; Herrmann, J.¹; Ohlinger, A.¹; Steckermeier, A.¹

¹ SCHOTT AG, Mainz, Germany

² SCHOTT Primoceler Oy, Tampere, Finland

Ultrashort pulse lasers are a surprisingly apt tool for joining glass with glass or glass with a non-transparent material without using any adhesives or a third joining partner like glass frits. Tailoring the spatio-temporal beam shape and with it the non-linear absorption processes in the vicinity of the glass interface, weld-lines of less than 50 μm width or even narrower can be achieved without affecting the surrounding material. Joining of various glass material combinations have been demonstrated, e.g. glass with metal, glass with silicon, crystal with metal or even silicon with silicon.

However, one remaining bottleneck towards industrial applications is to consistently ensure weld lines that can withstand high shear strengths. In this talk we outline a statistical shear strength testing procedure. It relies on providing a large number of test samples by a wafer-based production process as well as a low torque shearing setup. This method can be applied both to glass to glass as well as to glass to metal interfaces. We show that for both cases, welds with shear strengths in a narrow interval around 50 MPa range can be achieved.

Influencing factors on the creation of subsurface damages during ultrashort pulse laser machining of glass

Seiler, M.¹; Frank, S.¹; Thelemann, D.¹; Elies, O.¹; Teymori, P.²; Bliedtner, J.¹

¹ Ernst-Abbe-University of Applied Sciences Jena, Jena

² Friedrich-Schiller-Universität Jena, Jena

Abstract

Conventional lapping and grinding in the optics industry induce cracks – so called surface damage (SSD) – during the process, which should be minimized for the subsequent polishing step. In addition to the utilization of mechanical processing methods, the question of whether the laser beam might be suitable as a tool for manufacturing optical components has been raised for years. In addition to the economic efficiency of laser material processing with ultrashort pulses, the rapid and precise validation of SSD for a variety of laser and scan parameters is essential to establish a reliable process for the optics industry. The aim of this study is to fundamentally investigate the damage phenomena that occur during the processing of glass with ultrashort laser pulses. Non-destructive optical characterization methods are applied here, featuring high resolution and the recording of three-dimensional data. The main focus of the processing experiments lies on the influence of polarization and laser fluence on the formation of SSD. The planar and volumetric effects are described for the first time both qualitatively and quantitatively using optical coherence tomography (OCT). The samples are fabricated using a scanner-based beam deflection unit. For the results, aerial laser ablations are evaluated and correlated to each other. The first pass can result in very high SSD depths, which need to be corrected by subsequent passes. In general, the findings provide important insights for the future minimization of damages in laser material processing of technical glasses. Finally, the relevance of optical coherence tomography as a tool for evaluating a large number of parameters is demonstrated.

1. Introduction

During conventional mechanical manufacturing processes, especially for optical materials, microcracks, known as subsurface damage (SSD), can be induced. Due to iterative processes in optics manufacturing, a nearly SSD-free optical surface can be obtained for the final polishing steps. The remaining SSD reduces the overall performance of optics, including imaging quality, laser induced damage threshold (LIDT), and breaking strength. Due to an increasing demand in high-performance optics (e.g., EUV lithography), the urgency to develop a nondestructive measurement procedure to control SSD along the process chain rises. Introducing laser-based techniques instead of conventional grinding in optical industry can offer a promising alternative for shaping optical surfaces. By focusing an ultrashort laser pulse down to tens of μm diameter, very high intensities are achievable that trigger nonlinear absorption and result in precise material removal on a micro and nano scale. The small tool dimensions and the reduced thermal damage are some of the many advantages applying laser radiation in this process chain. In literature defects occurring due to laser radiation are called laser induced damage (LID). Further, SSD known from conventional manufacturing can also occur during laser material processing of optical materials and are also referred to SSD in this paper.

In the industry, both destructive and nondestructive methods can be applied to characterize SSD. The main drawbacks of destructive SSD evaluation, like taper polishing, are long processing times and the incapability to measure inline at multiple and specific locations. For the nondestructive characterization of SSD, there exist several imaging methods and each show their own disadvantages. Currently no universal nondestructive measurement technique is available on the markets which fits all the needs of optics industry. To understand the difficulty of imaging SSD, it is important to know some key characteristics of the microcracks. After pre-grinding, the cracks can reach a depth of 100 μm , which should be reduced to a few micrometers ($< 5 \mu\text{m}$) before polishing. Understanding the formation of defect shapes, along with quantifying their depth and distribution, are critical parameters in process development. Recent literature presents the potential application of optical coherence tomography (OCT) for the detection of surface defects, in particular LID and SSD. OCT is based on white light interferometry and is well-known from various medical and industrial applications for its tomographic imaging capabilities with high sensitivity, high speed

and resolution in the order of a few microns. Those features make it a powerful tool for non-destructive testing not only limited to SSD.

In this section one application from the current field of research is introduced, highlighting the benefits of OCT for laser ablation of optical materials. Schindler et. al cited in [1] introduced a destructive method for evaluation of SSD after laser processing using stepwise polishing. His work investigated ablation strategies for pico- and femtosecond and three different wavelengths applying fused silica and glass N-BK7 as a substrate. The results lead to a coloring of the SSD distribution, as shown in Figure 1 a) for a specific polishing depth.

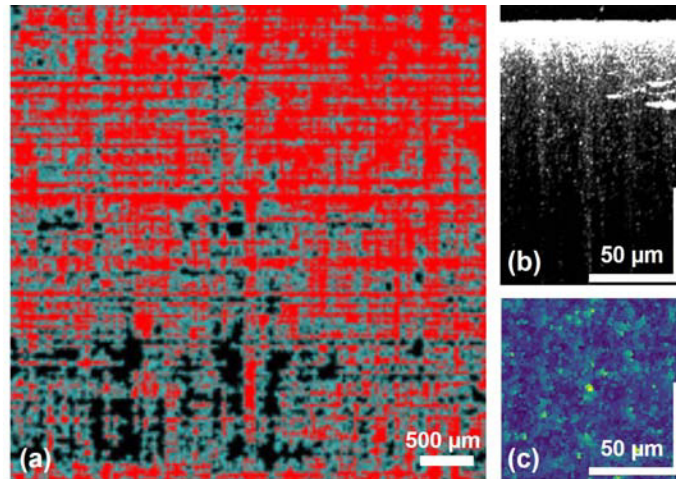


Figure 1 Comparison of two SSD evaluation methods for laser ablation of optical materials.

- a) Microscopical image of destructive stepwise polishing of the surface.
- b) Sagittal visualization of non-destructive tomographic imaging with OCT.
- c) color-coded SSD depth information (color scale: 0...156 µm) from OCT (top view).

On the other hand, the three-dimensional imaging with OCT can offer a non-destructive way to measure the depth and shape of SSD. It thus allows much more insights in the crack formation during ultra-short pulse laser ablation, see Figure 1 b) and c). Frank et al. used the technology to reveal the effect of material- and process parameters on morphological features and detailed spatial distributions of SSD when processing glass N-BK7 and fused silica. In this work, the method has been expanded to analyze effects of scan direction and polarization on damage generation and patterns.

2. Experimental setup, materials and methods

Flame polished fused silica glass (FN08) served as the sample material for this experiment. The 60 mm x 60 mm samples were cleaned in an ultrasonic bath before laser processing and measurements.

Experiments have been performed with an industrial laser machine RDX1000FBS from Pulsar Photonics. The machine houses an ultra-short pulse laser (Trumpf TruMicro 5250) combined with a scanning unit ExcelliSCAN. The laser source provides a maximum average power $PL = 30$ W using a wavelength $\lambda = 515$ nm. By means of a F-Theta objective with a focal length of 100 mm, a focus diameter of 23 µm (measured with Spiricon SP620U) can be achieved.

To measure the ablation depth, an industrial white light interferometer TMS-1400 from Polytech GmbH was used. A spectral domain OCT system GAN621 from Thorlabs was used to perform OCT measurements. With each measurement, a 3D volume of up to $1.0 \times 1.0 \times 1.38$ mm³ is acquired. The raw data is further processed using various visualization techniques, e.g., 2D projections along the x-axis were generated to obtain cross-sectional images. Those methods including the calculation of the SSD is explained in detail in [5]. The SSD values presented in this report are calculated based on a 1 % area threshold, meaning that at the given depth, only 1 % of the total area contains deeper defects. Using SSD depths calculated from a suitable area threshold, rather than maximum SSD depths, prevents single outlying defects from impairing the comparison between processing parameters.

3. Results and discussion

The experimental investigations are focused on the basic understanding of the SSD formation. Therefore, the polarization of the laser beam as well as the pulse overlap and laser fluence are varied (see sample #1 and #2 in Table1). The number of passes is set to one and repetition rate is kept constant at 100 kHz. The pulse spacing and line spacing are set to be equal. For each parameter, a field of 8 x 8 mm² was processed. The aim is to demonstrate the influence of the first ablation layer and its resulting damage to the substrate. To further investigate the influence of the scan direction on the formation of SSD during laser processing, one additional experiment was carried out. (see sample #3 in Table 1). This section presents the results for spatial distribution and shape of SSD using 3D OCT images and topographic evaluation of the processed area concerning roughness and ablation depth.

Table 1 Processing parameters for laser ablation of fused silica

Sample #	Passes	Polarization	Scan Direction for each field	Fluence [J·cm ⁻²]	PO [%]
1	1	Linear ↓	Left to right →	20, 30	90, 80
2		Circular ⊙	Left to right →	20, 30	90, 80
3		Linear ↓	Right to left ← Up to bottom ↓ Bottom to top ↑	20	90

Figure2 shows a photograph of the 5x5 matrix on sample #1. The camera image visualizes different material interactions depending on pulse overlap and laser fluence. As can be seen, only the pulse overlap of 90 % and laser fluence from 15 to 30 J/cm² exhibit homogenous laser ablation. In tests conducted to assess reproducibility, the fields highlighted in orange exhibited alterations in the ablation pattern. There are several fields with inhomogeneities as well as parameter combinations with nearly no interaction in the lower fluence regime including smaller overlapping.

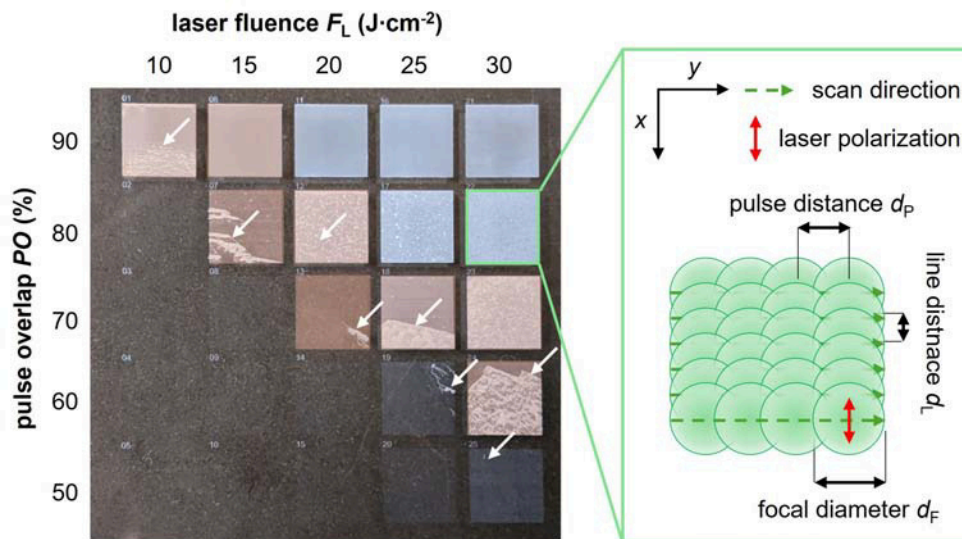


Figure 2 Photograph of the 5x5 matrix on sample #1 after laser ablation. White arrows indicate areas of inhomogeneous processing results and only partial ablation on the substrate surface.

Figure3 displays the correlation between ablation and SSD depth as a function of laser fluence for linear und circular polarization after laser ablation. The diagrams include all parameter combinations that lead to homogenous ablation. Both a higher pulse overlap and circular polarization result in larger ablation depth compared to linear polarization. This correlation changes analyzing the SSD depth for the treated fields. Applying 90 % pulse overlap the biggest amount of laser intensity is absorbed close to the surface, which

leads to a homogenous treated area. Reducing the overlap result in a process threshold with an instable interaction between the laser radiation and the material surface. The radiation can cause damages under the surface and therefore higher SSD values. It can be seen that the SSD depth can be higher as the ablation depth for these parameter combinations. This understanding is crucial if the number of passes is insufficient to remove the damage caused by the first pass, starting from a polished surface.

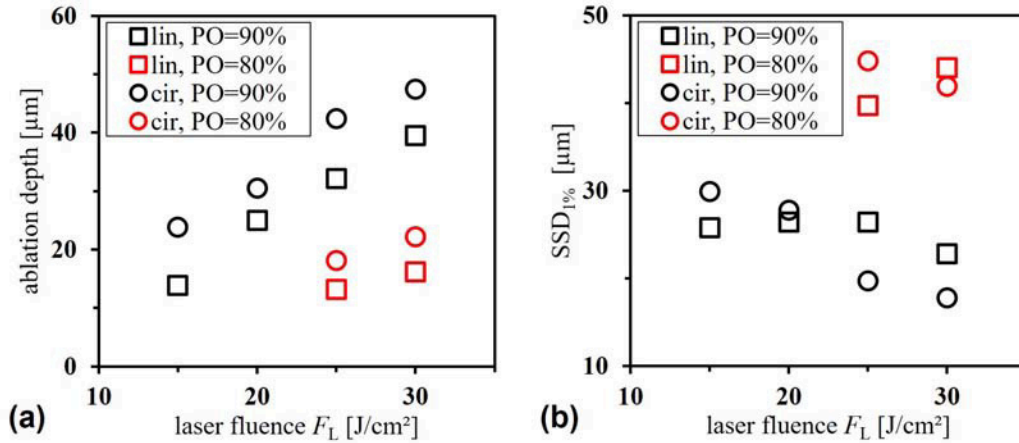


Figure 3 a) Ablation depth of linear (lin - sample #1) and circular polarization (cir - sample #2) depending on laser fluence FL and pulse overlap PO for selected parameter sets with homogeneous ablation, b) corresponding SSD depths for an area threshold of 1 %.

Besides quantitative information, the OCT technology offers more insights in the formation of defects. Especially the patterns generated in the transition zone between stable and non-stable processing (see orange fields and white arrows in Figure 2) can lead to subsurface defects with very high SSD depth. A more detailed view on such defects is shown in Figure 4, investigating the influence of polarization and scan direction. At the same laser fluence and pulse overlap, the scan direction was rotated by 90°, while maintaining constant linear polarization. The formation of wave-like defects demonstrated a dependence on the scan direction, as observed for all altered directions. These defects consistently orientated relative to the scan direction, as shown in Fig. 5 e) and 5 f).

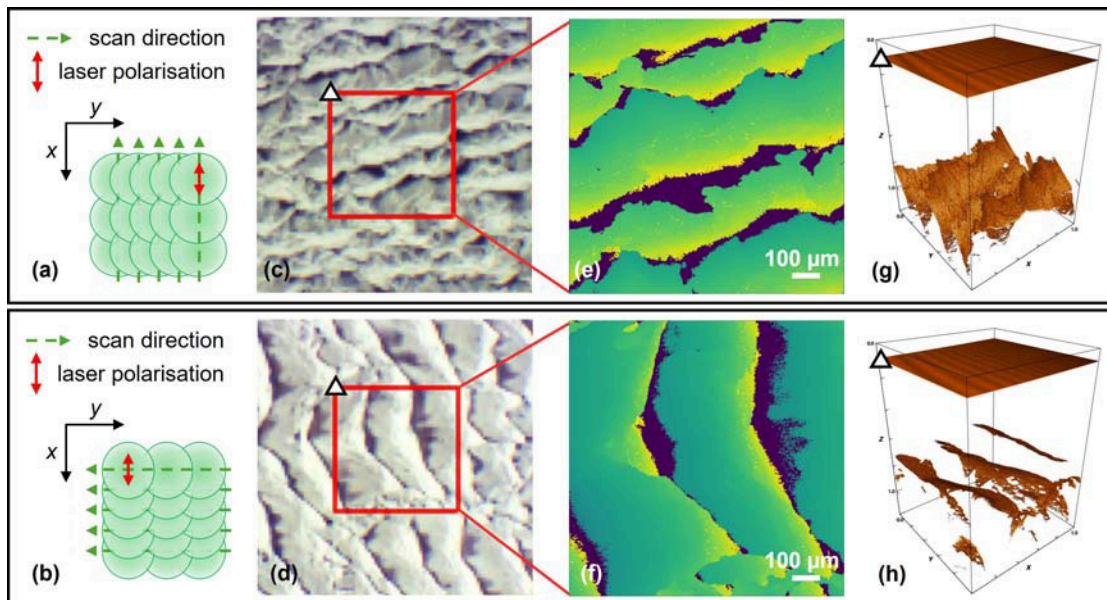


Figure 4 Influence of an aligned (a, c, e, g) and perpendicular (b, d, f, h) scan direction relative to laser polarization on defect patterns and orientation at laser fluence FL = 20 J/cm^2 and pulse overlap PO = 90%. (a, b) Depiction of scan direction and laser polarization. (c, d) Microscope preview image of OCT measurement area. (e, f) Color-coded depth maps with SSD in the range of 0...1300 μm . (g,h) 3D-rendering of the acquired OCT data (xyz: 1 mm x 1mm x 1.38 mm).

4. Summary and outlook

The work demonstrates the application of OCT technologies for laser ablation of optically transparent materials. OCT is a powerful tool for 3D visualization as well as analysis of the process. These insights deepen the understanding of defect formation and can accelerate process optimization. The observations can further help to find the causes of different morphologies. Future work can benefit from a stronger correlation of other monitoring methods as well as simulative approaches.

5. References

- [1] Hed, P.P.; Edwards, D.F.; Davis, J. Sub-Surface Damage in Optical Materials: Origin, Measurement, and Removal. In *Optical Fabrication and Testing, Technical Digest Series*. Spring Topical Meeting, Tuscon, AZ; Optica Publishing Group, Ed., 1989.
- [2] Suratwala, T.I. *Materials science and technology of optical fabrication*; John Wiley and Sons Inc: Hoboken, NJ, USA, 2018, ISBN 9781119423744.
- [3] Miller, P.E.; Suratwala, T.I.; Bude, J.D.; Laurence, T.A.; Shen, N.; Steele, W.A.; Feit, M.D.; Menapace, J.A.; Wong, L.L. Laser damage precursors in fused silica. In *Laser-Induced Damage in Optical Materials: 2009. Laser Damage Symposium XLI: Annual Symposium on Optical Materials for High Power Lasers*, Boulder, CO, Monday 21 September 2009; Exarhos, G.J., Gruzdev, V.E., Ristau, D., Soileau, M.J., Stolz, C.J., Eds.; SPIE, 2009; 75040X.
- [4] Lakhdari, F.; Belkhir, N.; Bouzid, D.; Herold, V. Relationship between subsurface damage depth and breaking strength for brittle materials. *Int J Adv Manuf Technol* 2019, 102, 1421–1431, doi:10.1007/s00170-018-03284-8.
- [5] Seiler, M.; Tianis, L.; Bliedtner, J.; Berlinger, M.; Gürtler, S. Approaches For A Destructive Measurement Method Of Subsurface Damages. *EPJ Web Conf.* 2019, 215, 8001, doi:10.1051/epjconf/201921508001.
- [6] Schnurbusch, G.; Brinksmeier, E.; Riemer, O. Influence of Cutting Speed on Subsurface Damage Morphology and Distribution in Ground Fused Silica. *Inventions* 2017, 2, 15, doi:10.3390/inventions2030015.
- [7] Liu, H.; Ye, X.; Zhou, X.; Huang, J.; Wang, F.; Zhou, X.; Wu, W.; Jiang, X.; Sui, Z.; Zheng, W. Subsurface defects characterization and laser damage performance of fused silica optics during HF-etched process. *Optical Materials* 2014, 36, 855–860, doi:10.1016/j.optmat.2013.11.022.
- [8] Menapace, J.A.; Davis, P.J.; Steele, W.A.; Wong, L.L.; Suratwala, T.I.; Miller, P.E. Utilization of magnetorheological finishing as a diagnostic tool for investigating the three-dimensional structure of fractures in fused silica. In *Laser-Induced Damage in Optical Materials: 2005. Boulder Damage Symposium XXXVII: Annual Symposium on Optical Materials for High Power Lasers*, Boulder, CO, Monday 19 September 2005; Exarhos, G.J., Guenther, A.H., Lewis, K.L., Ristau, D., Soileau, M.J., Stolz, C.J., Eds.; SPIE, 2005; p 599102.
- [9] Liu, J.; Liu, J.; Liu, C.; Wang, Y. 3D dark-field confocal microscopy for subsurface defects detection. *Opt. Lett.* 2020, 45, 660–663, doi:10.1364/OL.384487.
- [10] Shen, J.; Liu, S.; Yi, K.; He, H.; Shao, J.; Fan, Z. Subsurface damage in optical substrates. *Optik* 2005, 116, 288–294, doi:10.1016/j.ijleo.2005.02.002.
- [11] Catrin, R.; Neauport, J.; Legros, P.; Taroux, D.; Corbineau, T.; Cormont, P.; Maunier, C. Using STED and ELSM confocal microscopy for a better knowledge of fused silica polished glass interface. *Opt. Express* 2013, 21, 29769–29779, doi:10.1364/OE.21.029769.
- [12] Frank, S.; Reichenbächer, M.; Seiler, M.; Thelemann, D.; Arnold, T.; Bliedtner, J. Revealing Subsurface Damage Morphology and Patterns in areal Ultrashort Pulse Laser Machining of Glass. *Lasers Manuf. Mater. Process.* 2024, 11, 631–648, doi:10.1007/s40516-024-00262-9.

6. Acknowledgments

The research was funded by the Federal Ministry of Education and Research (funding label: 03RU2U033I and 03RU2U031F, abbreviation “UKPino”, www.ukpino.com)

Supported by:



on the basis of a decision
by the German Bundestag



Customized edge cutting of display glasses from structured ultrashort laser pulses

Kumkar, M.¹; Kaiser, M.²; Wimmer, M.²; Kleiner, J.²; Flamm, D.²

¹ TRUMPF Laser SE, Schramberg

² TRUMPF Laser- und Systemtechnik SE, Ditzingen

Abstract

The fabrication procedure and corresponding optical concept for ultrashort pulsed laser cleaving of transparent materials with tailored edges in a single pass is discussed. The procedure is based on holographically sampling an arbitrary edge contour with Gaussian focus copies. This 3D-beam splitter allows to induce full-thickness modifications inside the volume of display glasses, for example, along C-like curved trajectories with local 45-deg tangential angles. Here, single-side access to the workpiece is sufficient without inclining the optical head. After having induced laser modifications with feed rates of ~1 m/s, separation is achieved using wet chemical etching or by applying thermal stress from CO₂-lasers.

1. Introduction

Conventional glass cutting techniques usually provide orthogonal glass edges [1]. Stresses accumulate in the 90-deg corners of such edges and the substrate tends to break on impact [2]. By reducing the tangential angle at the glass surface via mechanical grinding and polishing the resistance to impact can be increased [3]. Using ultra-short pulse laser-based glass cutting techniques with state-of-the-art Bessel-like beams, intrinsically vertical glass edges result [4]. But substantial advantages such as quality, tool wear and throughput, speak in favor of the laser modification process. These advantages and the possibility to generate modifications in a single pass over the entire material thickness along any edge shape geometry are united using holographic 3D beam splitters [3, 5]. This structured light concept enables arranging a large number of focus copies arbitrarily within the glass substrate.

Following the ultrafast laser modification step a second step is required, that separates along the weakened areas of the material. Here, we report on two strategies. First, we make use of the fact that laser-induced modifications exhibit a higher selective etchability – a process well known as selective laser etching (SLE) [6]. A numerical approach is introduced where etch simulations allow to optimize the spot distribution for complex edge shapes confirmed by in-situ diagnostics and fabrication experiments [7]. The second separation strategy is based on inducing thermal stress from absorbing CO₂-laser radiation [8]. Due to the temperature changes in the substrate, glass separation is achieved from balancing tensile and compressive stresses. As another non-contact tool is used, this method is more cost-effective – even if not as scalable and flexible as the SLE approach.

In this paper, qualitative separation results of tailored glass edges depending on laser parameters and the two mentioned separation strategies are presented. Additionally, we will discuss mechanical properties based on evaluating the substrate's surface roughness. With this optical and numerical toolchain, we want to further improve the robustness of displays and simplify the manufacturing process which in total improves their ecological footprint.

2. Tailored-edges from selective laser etching (SLE)

Using holographic 3D-beam splitting, a large number of focus copies can be distributed in a working volume of a focusing unit at arbitrary positions [9]. This allows to sample complex edge curves such as, e.g., chamfers, bevels or C-shapes and to induce modifications on large scales inside a transparent sample within a single pass. Applying aqueous solutions of chemical such as potassium hydroxide (KOH), sodium hydroxide (NaOH) or hydrofluoric acid (HF) to these glasses, the laser-modified material can be removed with selectivities > 1000 (e.g., quartz glass and KOH [6]). As the etch rates of the unmodified glass and those of the laser-modified regions can be determined experimentally [6] the SLE process is also well

predictable from simulations [7]. Coming back to our glass-cutting approach, this means that the required focus shape for a target substrate edge can be optimized. Here, our model is based on cellular automaton [10] for solving the problem of a reaction diffusion equation [11]. The initial condition of the numerical model is a homogeneous glass sample, with a constant glass concentration $A_{m,n}$ for each lattice site m,n along the horizontal and the vertical axis, respectively. Here, $A_{m,n} = 1$ describes a point in the simulation domain where the glass concentration is 100% and opposite $A_{m,n} = 0$ a point at which the glass is completely etched. For the simulations, we distinguish only between these two binary states. However, for the sake of visualizing the etch dynamics, continuous concentrations are shown [7].

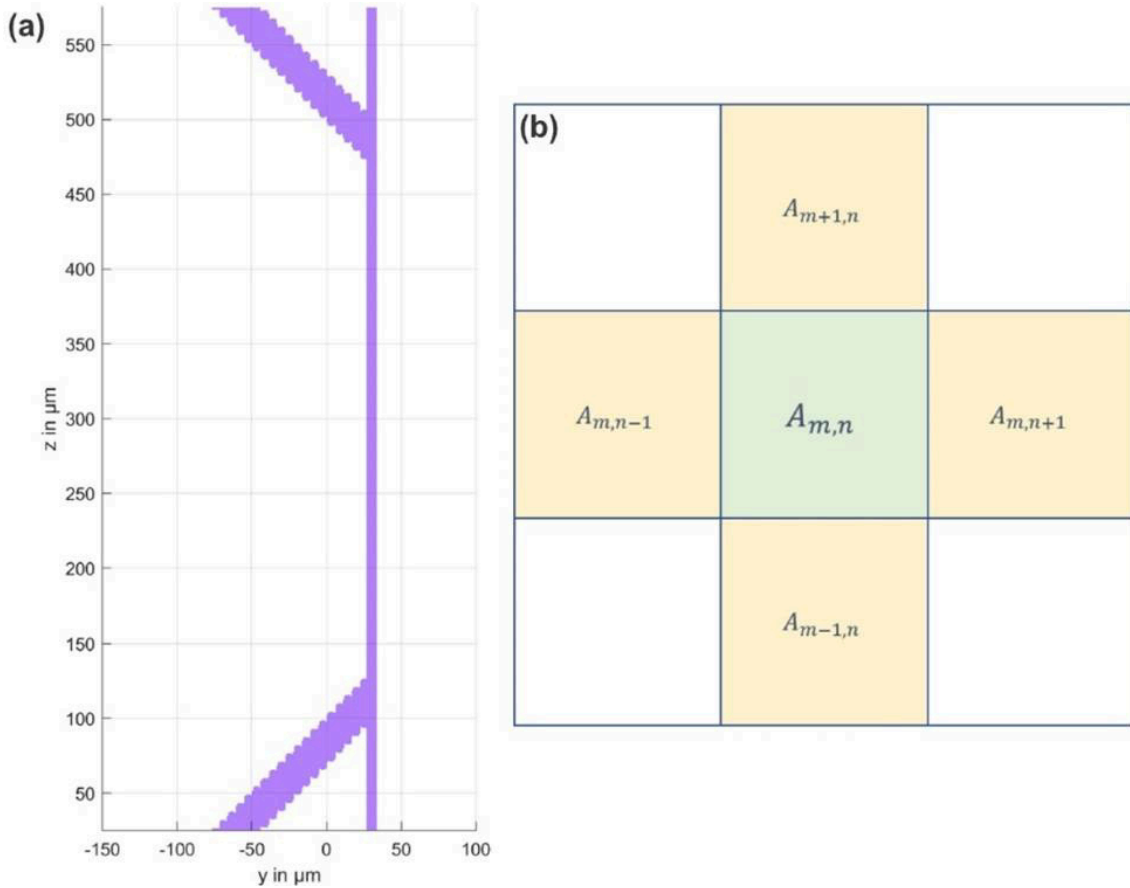


Figure 1: Entirety of modifications generated by a single laser pulse propagating parallel to the z-axis highlighted in purple (left). Here, the focus shape generates modifications along a 45° chamfer trajectory and, additionally two assist lines facilitating the edge process. For processing and contour cutting the focus distribution is moved relatively to the workpiece in x-direction. Sketch of the mesh model in the simulation (right). Only nearest neighbors are included. The full simulation domain in 2D is approximately 250 μm x 625 μm large, for simulating the chamfer of a 500 μm thick glass sample [7]

The etching process itself is driven by surrounding areas, where each next neighbor contributes to the etching at site m,n with an etching rate of the bare glass B . The evolution equation is completed by introducing the etch selectivity $S_{m,n}$ [7]

$$A_{m,n}^{t+\Delta t} = A_{m,n}^t - B \sum_{m',n'} (1 - A_{m',n'}^t) - S_{m,n} \times (1 - A_{m,n}^t) . \tag{1}$$

For tailoring the etching behavior to a specific form of the chamfer, in the experiment glass is modified by focusing ultra short laser pulses at a given position. The high intensity of the laser pulse triggers a cascade of nonlinear processes resulting in a type-III-regime modification of the glass. Here, the modification volume is determined by the size of the focal spot and consequently, we assume in experiments a spot diameter of $\sim 2 \mu\text{m}$ in transversal direction and the resulting Rayleigh length of $\sim 10 \mu\text{m}$ in longitudinal direction at 1030

nm wavelength. Furthermore, the focusing of the ultrashort pulses leads to extreme mechanical stress inside the glass resulting in micro explosions. In our heuristic model, we assume a much higher etch selectivity inside the volume of the focus. We model these modifications by Super-Gaussian distributions [7]

$$S_{m,n} = S_0 \times \exp \left(-\frac{|n|^N}{|w_n|^N} - \frac{|m|^N}{|w_m|^N} \right) . \tag{2}$$

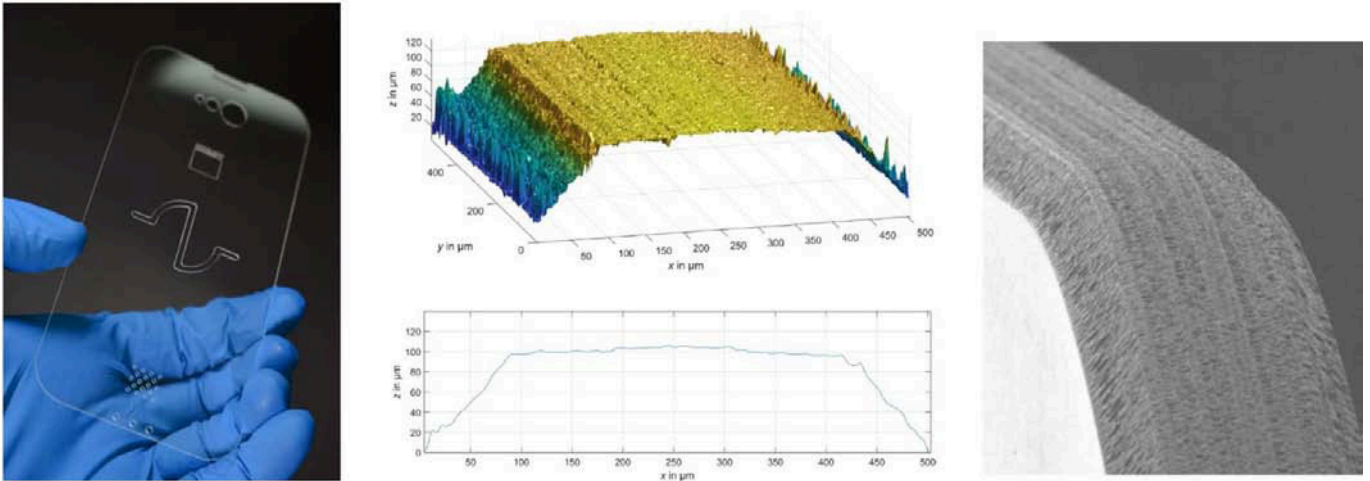


Figure 2: Photography of the selectively laser etched sample (left) with laser scanning microscope measurements (center) of the chamfer and averaged cross section. The right panel depicts a scanning electron microscope image of the etched chamfer [7]

To further refine the model, the shape and extent of the individual voids could be deduced from measurements of type-III-regime modifications [12] caused by single Gaussian spots. Additionally, for determining the degree of etch selectivity S_0 we refer to Hermanns et al. [6] where etch rates were measured using polarization contrast microscopy.

In the experiments, we use 3 ps pulses from a TruMicro Series 2000 laser in burst-mode with a total pulse energy of $< 300 \mu\text{J}$. The pulses of the laser pass a liquid-crystal-on-silicon-based spatial light modulator (SLM), which splits the light according to our principle of the holographic 3D beam splitter in several directions, each focusing inside a Corning® Gorilla® glass sample after traveling through an NA-0.4 microscope objective with long working distance. After inscribing the modifications the good part is separated from the bad part by wet chemical etching with 30 wt-% KOH inside a heated bath [6, 7]. The resulting sample with the 45° chamfer is shown in Fig. 2, together with laser scanning microscope and scanning electron microscope images [7]

For comparing the processed sample with our etch model, the LSM-measured cross section is averaged in y -direction for noise reduction purposes. The etch simulation covers ≈ 2000 discrete time steps corresponding to an overall etch time of 30 min, where the parameter B was adjusted that $\approx 2 \mu\text{m}$ are etched per minute. In the simulation, the selectivity of the modifications is assumed to be 18 and the Super-Gaussian exponents of $N = 4$ for type-III-regime modifications with diameters of $w_y = 2.5 \mu\text{m}$ in transversal and $w_z = 13 \mu\text{m}$ in propagation direction. In Fig. 3, three different signals are plotted in five different time steps from $t = (45 \dots 1800) \text{ s}$. With the red curve, again, we show the measured edge height profile from our glass sample, cf. Fig. 3. Highlighted in yellow, the modified glass region is denoted where we expect an etchable chain of voids. The light purple area shows the spatial progress of the etch solution penetrating the substrate. At time $t = 1351 \text{ s}$ the glass is completely etched as the solution has progressed to the substrate's center from both sides. Additionally, the benefit of the two assist etch lines becomes visible. The good part of the workpiece is no longer interlocked in the substrate and can be detached upwards/downwards. This approach is mandatory if complex internal contours are to be extracted.

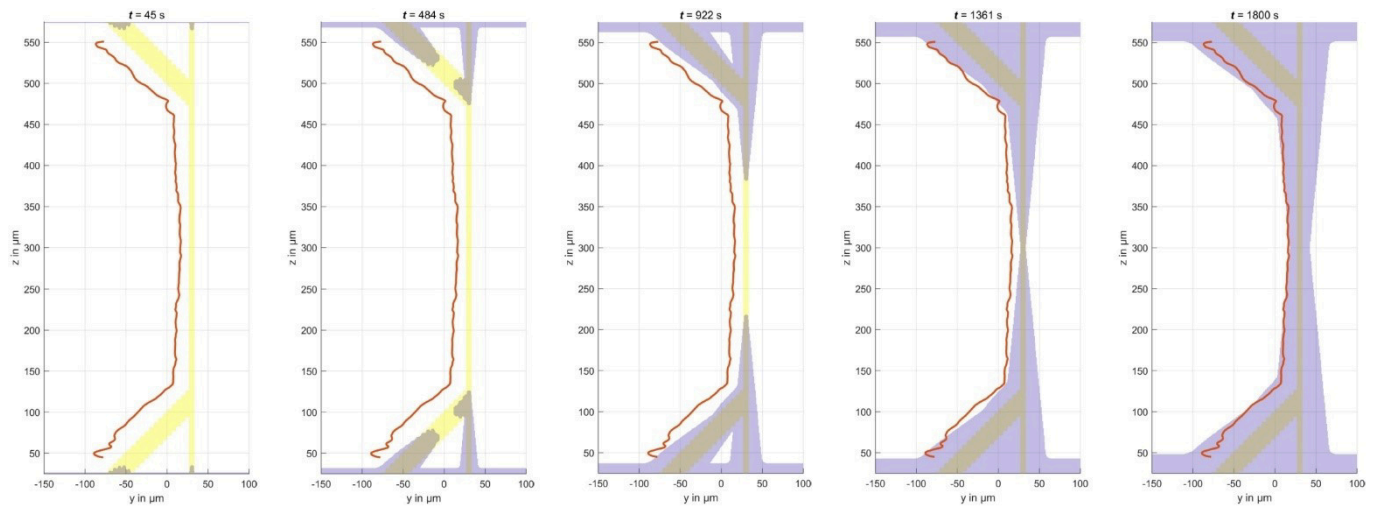


Figure 3: Simulation of the selective laser etching for five different time steps of the process until the sample is etched down to a total thickness of 500 μm . The design includes two 45° chamfers at the top and bottom side of a 500 μm thick glass sample. For improving the etch results, two additional vertical channels are modified, which lead to a fast transport of the etching solution to the central part of the sample. The shape of the simulated chamfer fits well to the experimental results (solid red curve) based on the LSM measurements shown in Fig. 2. The yellow shaded region indicates the modified region, where spots according to Eq. (2) are placed [7]

The overall and mid-frequent shape of the chamfer is very well reproduced in simulations and fits to the experimental results overlayed in Fig. 3. Higher frequent deviations result from noise in the LSM measurement as well as deviations in the etching properties of individual type-III-regime modifications.

The final glass thickness in the simulation is 503 μm and fits well to the experimental values. For further characterizing the quality of the experiments, we evaluate the angles of the chamfer on the top and bottom side, which are close to 45° (strong dependence on fitting parameters). Due to the symmetry of the simulation, we expect these values to be identical up to deviations in fitting a linear function in the region of the chamfer. Very near the edge of the sample, the light scanning microscope measurements show pronounced noise, which strongly influences the fitting. This is also visible in the central panel of Fig. 2. Additionally, we evaluated the standard deviation between experiment and simulation within the central part of the sample and find slowly varying shape deviations to be the root cause for the 2 μm difference [7].

3. Tailored-edges using laser-only machining

The separation strategy from previous section (SLE) [6, 13] is particularly profitable if economies of scale need to be achieved, i.e., if a large number of items have to be produced at the same time. However, considering a more reasonable number of elements to be fabricated, thermal separation is about a factor of 4 cheaper than chemical separation [8], with additional disadvantages regarding sustainability and occupational safety. Finally, as the system technology (machine with precise axis stages) is already available from the ultrafast-laser in-volume modification step, it is straightforwardly used for precisely inducing thermal stress, e.g. using CO₂-lasers. Here, radiation at 10.6 μm wavelength with nanosecond pulses or longer is applied to the glass surface and absorbed close to the area where the ultrafast laser was inducing type-III-regime modifications [12]. Due to the temperature changes in the material, local stresses arise that finally lead to the separation of the glass. We would like to point out that the success of this separation strategy strongly depends on the type of glass and, in particular, on the linear thermal expansion coefficients [14].

Our processing strategy starts identical as the SLE variant. Using holographic 3D beam splitting, a set of in-volume modifications are induced from a beam shaped ultrafast laser [3], cf. Sec. 2 and Fig. 1 (left). For the task at hand, three different focus distributions have been designed. All take the shape of a “C” and are defined for a glass thickness of 550 μm . The spatial trajectory at which foci are split equals a circular

arc with a given radius r_c . This radius was chosen so that the arc's tangent at the intersection with the top and bottom surface equals $\alpha = 60^\circ, 45^\circ$ and 30° . Figure 4 provides an overview of the three cases and shows the simulated intensity distribution $I(x,z)$ of the designed focus, see right-hand-side of (a) – (c). Clearly visible are the spatially separated Gaussian-like spots with similar peak intensities. Please note, that not all spots are visible as an intensity cross section is plotted. During the processing a relative movement of workpiece and processing head is carried out in y -direction. Ultrashort laser pulses propagate parallel to the z -axis and are generating all spots simultaneously in a single pass – a flipping of the workpiece is not required [3]. Processing was conducted with 3 ps pulses from a TruMicro Series 2000 laser operating in burst-mode with a total pulse energy of $< 300 \mu\text{J}$. For the thermal separation step a pulsed CO2 laser system (Synrad p400, Novanta PHOTONICS) with a feed rate of $\sim 3 \text{ m/min}$ at $< 40 \text{ W}$ average power was employed [8].

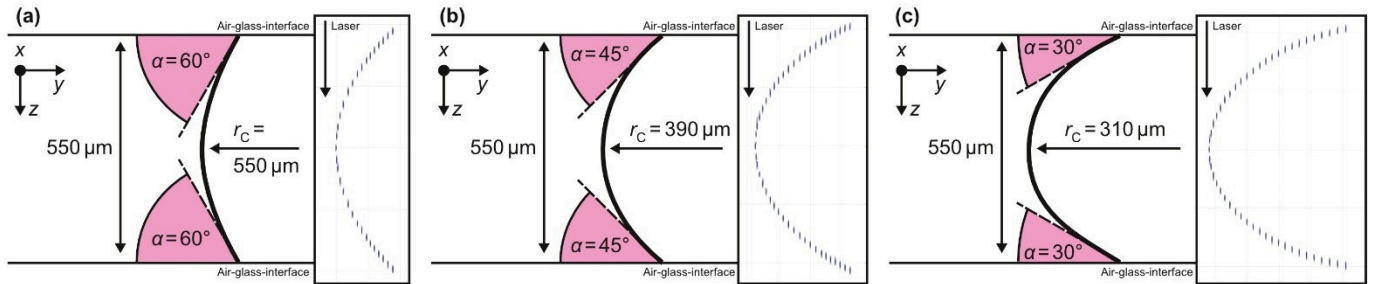


Figure 4: Overview of used focus distributions. The schematic denotes the glass sample with both interfaces and the definition of the focus shape's tangential angle to the surface α . In this work three different C-shapes are to be processed with $\alpha = 60^\circ$ (a), $\alpha = 45^\circ$ (b) and $\alpha = 30^\circ$ (c), and stated radii of corresponding circular arcs r_c . On the right-hand-side of each subfigure the simulated intensity distribution $I(x,z)$ in an isosurface representation is depicted. While laser propagation is parallel to the z -axis, processing is done in x -direction [8].

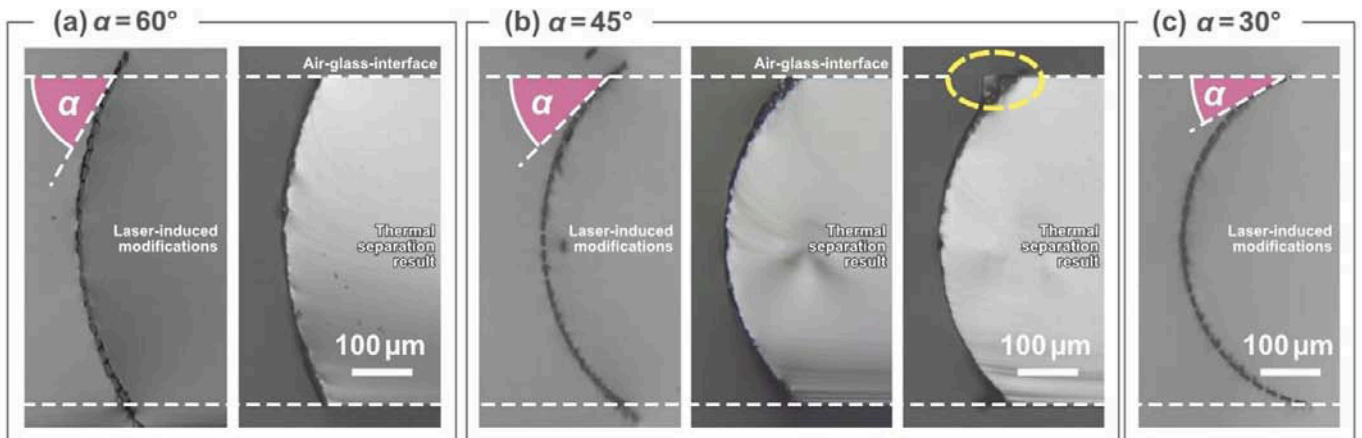


Figure 5: Light micrographs of tailored-edge glass processing and CO2 laser-based separation. In the 60° case (a) modifications and resulting edge shape clearly follow the target shape, cf. Fig. 4. The 45° -C-shape (b) enabled thermal separation with small target geometry deviations close to both interfaces, highlighted in yellow. For the 30° -C-shape (c) laser induced modifications follow the circular arc. A thermal separation was not possible [8].

Figure 5 depicts processing results with the three focus shapes. Using the case with the largest r_c ($\alpha = 60^\circ$), see Fig. 5 (a), a broad process window can be found, where the substrate separates without showing steps. The edge closely follows our target trajectory and separation is completely performed along the induced modifications [8].

In Fig. 5 (b), we decreased α to 45° . Again, as by design, our focus shape allows to deposit energy along the 45° -arc proven by the type-III-regime modifications visible with light microscopy. Thermal substrate

separation is enabled as can be seen from the microscoped edges. They largely follow our design, especially at the vertex of the C-shape in the center of the substrate. However, considering the edge shape close to the air-glass-interface larger deviations become visible. In a z-distance of a few tens-of-micrometers away from both interfaces separation is no longer guided along the modifications, but takes the direct path to both surfaces. This often results in an isolated stair step, highlighted in yellow, see (b). Although, due to the local 90° angle, edge protection is no longer guaranteed, we still see high potential here. This is especially due to the fact that post-treatment by mechanical grinding and polishing [1] is not excluded. The preforming that we can achieve with our double-laser process should significantly reduce the effort required for accuracy and process times of the grinding tools. Optimal chamfering of transparent workpieces could therefore also be achieved by combining laser processing and mechanical post-treatment. For the 30° -case only a light microscope signal of the ultrafast laser-induced modifications is provided. Although the void chain follows the desired trajectory, in this particular case, a thermal separation was not possible, see (c).

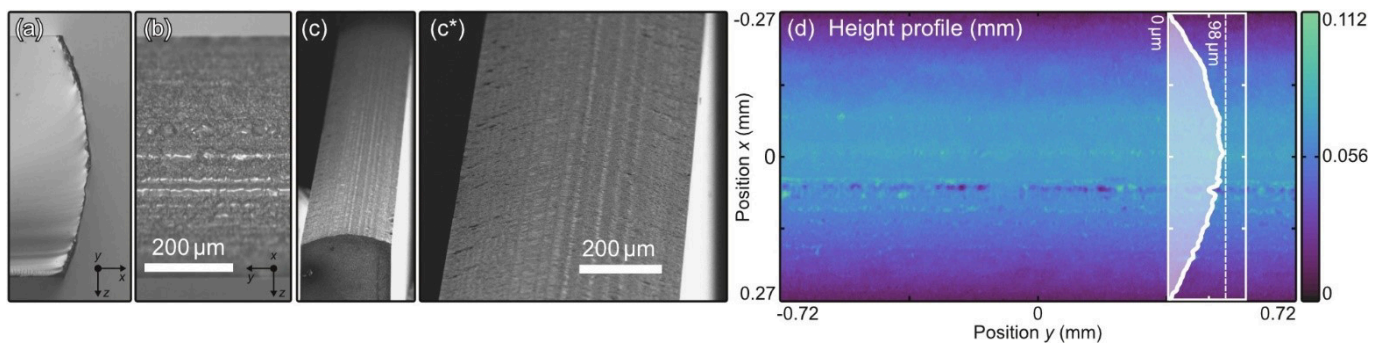


Figure 6: Investigating shape and surface quality of a C-shaped Corning® Gorilla® glass sample with $\alpha = 60^\circ$ separated by means of CO₂ laser radiation, cf. Fig. 5 (a). Light microscope signals from different perspectives, note the coordinate system (a), (b). Scanning electron microscopy of the tailored edge (c) with details of the surface grooves (c*). Height profile of the glass edge in 2D and 1D reconstructed from a laser scanning microscope [8].

A more detailed examination of the sample obtained is carried out by scanning electron microscopy (SEM) and laser scanning microscopy, respectively, see Fig. 6. Here, for the sake of completeness we again plot the light microscope signal of the edge from two perpendicular perspectives, (a) and (b). One outcome of our processing strategy with discrete focal spots is the existence of smallest grooves parallel to the feed direction (y-axis). However, the 3D impression from the SEM image shows that the grooves are very shallow and can be assigned to the transverse dimensions of the spots, see (c) and corresponding details in (c*). The reconstructed height profile from the LSM is depicted in (d). Here, surface roughness S_a is determined to $\approx 2 \mu\text{m}$ and the edge's tangential angle at the air-glass-interfaces amounts to $\alpha = (60 \pm 5)^\circ$, cf. Fig. 4. Fitting the white profile denoted in Fig. 6 (d) to a circular arc results in a radius of $r'_C \approx 510 \mu\text{m}$ (least square method). The fact that this value is slightly smaller than our target value of $r_C \approx 550 \mu\text{m}$ is due to the propagation direction of the split spots. Regardless of the position along our C-trajectory, whether at the vertex or at the glass interface, the propagation direction of the focal points is always parallel to the z-axis, cf. Fig. 4. As the Rayleigh lengths are larger than the focus diameter, the resulting modifications at the glass edge protrude more into the sample's good part than those at the vertex, cf. Fig. 5, resulting in a reduced r_C , see also Ref. [3]. However, this small mismatch could be compensated in the trajectory design, for example, by slightly increasing r_C .

4. Conclusion

We have discussed the two-step procedure for tailored-edge glass cutting with ultrashort pulsed lasers. First, full-thickness in-volume modifications are induced from spatially shaped pulses using a holographic 3D beam splitter in a single pass. Considering the second processing step, actual separation was achieved using two strategies. Selective laser etching benefits from the fact that laser-induced modifications exhibit a higher etchability than the bare glass. Here, we established a numerical model that allows to optimize the required focus shape for a given target edge geometry and etch recipe. A more sustainable

alternative is provided by realizing the separation from applying thermal stress using CO₂ laser radiation. For glasses with suitable thermal expansion coefficients, such as soda-lime or Corning® Gorilla® glass, well-defined temperature gradients can be generated finally allowing to separate the substrate using another non-contact tool. In both separation variants achieved surface qualities are high with edge surface roughnesses $S_a < 2\mu\text{m}$.

5. References

- [1] Bukieda, Paulina, et al. "Study on the optical quality and strength of glass edges after the grinding and polishing process." *Glass Structures & Engineering* 5 (2020): 411-428.
- [2] Marjanovic, S., et al. "Edge chamfering methods." US Patent 10 (2019): 442-719.
- [3] Flamm, Daniel, et al. "Protecting the edge: Ultrafast laser modified C-shaped glass edges." *Journal of Laser Applications* 34.1 (2022).
- [4] Tsai, Wu-Jung, et al. "Internal modification for cutting transparent glass using femtosecond Bessel beams." *Optical Engineering* 53.5 (2014): 051503-051503.
- [5] Flamm, Daniel, et al. "Structured light for ultrafast laser micro- and nanoprocessing." *Optical Engineering* 60.2 (2021): 025105-025105.
- [6] Hermans, Martin, Jens Gottmann, and Frank Riedel. "Selective, Laser-Induced Etching of Fused Silica at High Scan-Speeds Using KOH." *Journal of Laser Micro/Nanoengineering* 9.2 (2014).
- [7] Wimmer, Martin, et al. "Selective laser etching of displays: Closing the gap between optical simulations and fabrication." *Laser Applications in Microelectronic and Optoelectronic Manufacturing (LAMOM) XXIX*. Vol. 12872. SPIE, 2024.
- [8] Kaiser, Myriam, et al. "Customized edge cutting of display glass with laser-only machining." *Frontiers in Ultrafast Optics: Biomedical, Scientific, and Industrial Applications XXIV*. Vol. 12875. SPIE, 2024.
- [9] Flamm, Daniel, et al. "Light along curves: Photonic shaping tools." *Advanced Optical Technologies* 12 (2023): 1237132.
- [10] Weimar, Jörg R., and Jean-Pierre Boon. "Class of cellular automata for reaction-diffusion systems." *Physical review E* 49.2 (1994): 1749.
- [11] Zhu, Zhenjun, and Chang Liu. "Simulation of anisotropic crystalline etching using a continuous cellular automata algorithm." *CMES- Computer Modeling in Engineering & Sciences* 1.1 (2000): 11-19.
- [12] Itoh, Kazuyoshi, et al. "Ultrafast processes for bulk modification of transparent materials." *MRS bulletin* 31.8 (2006): 620-625.
- [13] Kaiser, M., et al. "Selective etching of ultrafast laser modified sapphire." *Laser Applications in Microelectronic and Optoelectronic Manufacturing (LAMOM) XXIV*. Vol. 10905. SPIE, 2019.
- [14] Deng, Binghui, Ying Shi, and Fenglin Yuan. "Investigation on the structural origin of low thermal expansion coefficient of fused silica." *Materialia* 12 (2020): 100752.

Laser Inertial Fusion – Critical Advancement for Germany's Optics and Laser Sectors

Dr. Jochen Stollenwerk
Fraunhofer ILT, Aachen



Abstract

With the world's first time ever ignition of a burning plasma through inertial confinement of a dense plasma, fusion energy has garnered global attention. Plasma confinement and ignition were driven by the world's largest and most energetic laser in this experiment: the National Ignition Facility in the United States.

Germany, recognized for its leadership in basic research on magnetic fusion plasmas, has not been particularly active in ICF fusion research over the past two decades. However, the German photonics and engineering sectors have played a significant role in providing key components for high energy lasers, and provided materials, targets, precision instrumentation, electronics, and optical technologies to leading fusion experiments worldwide. Additionally, German research institutions maintain a high level of expertise in essential technologies for laser fusion, as well as in shared technologies between magnetic fusion energy (MFE) and inertial fusion energy (IFE), such as research in fuel cycle or reactor materials.

Germany is strategically prioritizing the long-term adoption of fusion technology, given the robust foundation of this technology. This initiative is positioned alongside other renewable energy sources like solar and wind. The focus on fusion technology highlights the necessity for continuous research and development in these critical technological areas to maintain and advance Germany's leadership in high-tech technologies and the energy sector.

This presentation will provide an introduction to Laser Inertial Fusion Energy, offer insights into current research from an international and specifically German viewpoint, and identify opportunities within the laser and optics industry.

TRUMPF Laser Amplifier – The high power laser source for EUV lithography“

Dr. Michael Kösters
TRUMPF AG

EUV lithography is the most advanced lithography technique used in the semiconductor industry allowing mass production of high performance microchips with low energy consumption. The light source behind this technology is a laser-produced plasma (LPP): the TRUMPF Laser Amplifier, an extremely powerful laser with an average power of 30 kW at roughly 100 ns pulse length, shoots at small metal droplets at a rate of 50 kHz converting the droplets into a highly-energetic plasma, which emits light at 13.5 nm wavelength. This extreme ultraviolet light (EUV light) is used to image the chip mask onto the waver with features as small as a few nanometer. In this talk, we give insights into which extremely challenging requirements we are facing in this application and how the TRUMPF laser amplifier is capable of fulfilling them.



Industrial-grade 2- μm ultrafast fiber CPA for silicon processing

Gaida, C.; Heuermann, T.; Herrfurth, O.; Breitkopf, S.; Eidam, T.; Limpert, J.
Active Fiber Systems GmbH, Jena, Germany

Our latest advancements involve the development of a novel compact laser utilizing thulium-based fiber CPA technology. This laser emits a central wavelength of 2 μm and boasts impressive capabilities: pulse energies exceeding 100 μJ and an average power output surpassing 15 W. Designed for longevity, it is tailored for industrial applications, seamlessly integrating into laser machines used for materials processing. The laser's parameters are particularly well-suited for working with semiconductors like silicon. It enables essential tasks such as microwelding or precision cutting of filaments.

In the realm of cutting-edge ultrafast-laser applications, particularly in silicon processing, longer laser wavelengths are often favored over 1- μm lasers. This preference arises from the transparency of semiconductors in the wavelength region beyond 1 μm . Consequently, there exists a strong demand for ultrafast lasers with compact footprints and wavelengths around 2 μm [1-3].

Thulium-based fiber lasers have emerged as promising candidates for efficiently generating high average- and peak-power in this wavelength range [4-9]. Our recent progress involves the development of an industrial-grade Tm-based fiber laser that emits pulses exceeding 100 μJ at a central wavelength of 1980 nm. These pulses have an impressively short duration of less than 150 fs and a repetition rate of 150 kHz, resulting in an average power output exceeding 15 W.

The system allows precise adjustment and control of critical process parameters, including pulse energy, repetition rate, and pulse duration. Notably, this laser operates without the need for vacuum equipment, avoiding water-vapor absorption. As a result, it achieves nearly diffraction-limited beam quality and exceptional pointing stability.

Engineered for industrial-grade performance, our laser is optimized for long-term operation. Its packaging is well-suited for seamless integration into laser machines used for materials processing. The laser's parameters make it particularly well-suited for semiconductor processing tasks, such as microwelding or filament cutting.



Abb. 1: Left: Rendered view of the activeTwo-15. Right: Long term measurement of output power. Inset shows beam profile at full output power

References

- [1] S. Nolte et al., "Ultrashort pulse laser processing of silicon,"; Paper 12411-34; PW2023
- [2] M. Chambonneau et al., "Silicon–metal and silicon–silicon ultrafast laser welding with domesticated filaments,"; Paper 12409-1; PW2023
- [3] M. Chambonneau et al., "In-Volume Laser Direct Writing of Silicon—Challenges and Opportunities"; Laser & Photonics Review (2021) DOI: 10.1002/lpor.202100140
- [4] F. Stutzki, C. Gaida et al., Opt. Lett. 39, 4671–4 (2014).
- [5] C. Gaida et al, Opt. Lett. 43, 5853-5856 (2018)
- [6] F. Stutzki, C. Gaida et al, Opt. Lett. 40, 9–12 (2015).
- [7] C. Gaida et al., Opt. Lett. 41, 4130–4133 (2016).
- [8] T. Heuermann et al., Opt. Lett. 47, 3095-3098 (2022).
- [9] D. Kracht et al. "Innovative Laser Sources Operating Around 2 μm " Physics Procedia 83, 1184-1195 (2016)

Industrial Ultrafast kW-Class Lasers Above 10 mJ Enabled by Thin-Disk Multipass Amplifier

Dannecker, B.¹; Scharun, M.¹; Hoeck, H.¹; Bauer, D.¹; Kumkar, M.¹; Ruebling, S.¹; Quentin, U.²; Sutter, D.¹; Albers, K.¹; Killi, A.¹

¹ TRUMPF Laser SE, Schramberg

² TRUMPF Laser- und Systemtechnik SE, Ditzingen

Abstract

Emerging applications like EUV and X-ray generation, as well as scaled micromachining require ultrafast lasers at average powers in the kilowatt regime. Based on the approach of using Yb-doped active materials and combining the different laser architectures fiber, slab and thin disk as pre, intermediate and main amplifier stages in the chain, respectively, an efficient system emitting at a wavelength of 1.03 μm is realized, providing a pulse energy of more than 10mJ and a pulse duration of less than 1 ps at a spectral width of less than 2 nm (FWHM). An excellent beam quality at output powers exceeding 1 kW is achieved. By using a thin-disk in multi-pass configuration, a purely linear amplification scheme is realized, offering a wide range of repetition rates, extended burst functionality and dynamic control of pulse energy, e.g. pulse-on-demand operation, due to the combination with the integrated external modulator.

1. Introduction

Ultrashort laser pulses at average powers in the kilowatt level, offering energies exceeding ten millijoules will boost emerging applications such as the generation of secondary radiation such as of EUV or X-ray and machining like large scale surface processing [1,2].

Chirped pulse amplification (CPA) in combination with scaling of the beam diameter within the amplifier chain is a suitable approach for increasing pulse energy and peak power. The average power can be scaled, and nonlinear effects lowered compared to fiber or slab lasers by main amplifiers based on thin-disk technology with beam diameters of several millimeters [1]. The combination of thin disk technology with an all-glass multipass mirror array welded with femtosecond pulses allows for a linear amplifier module with comparatively high gain and suitability for high pulse energies as well as high repetition rates while simultaneously offering superior alignment stability [2].

2. Results

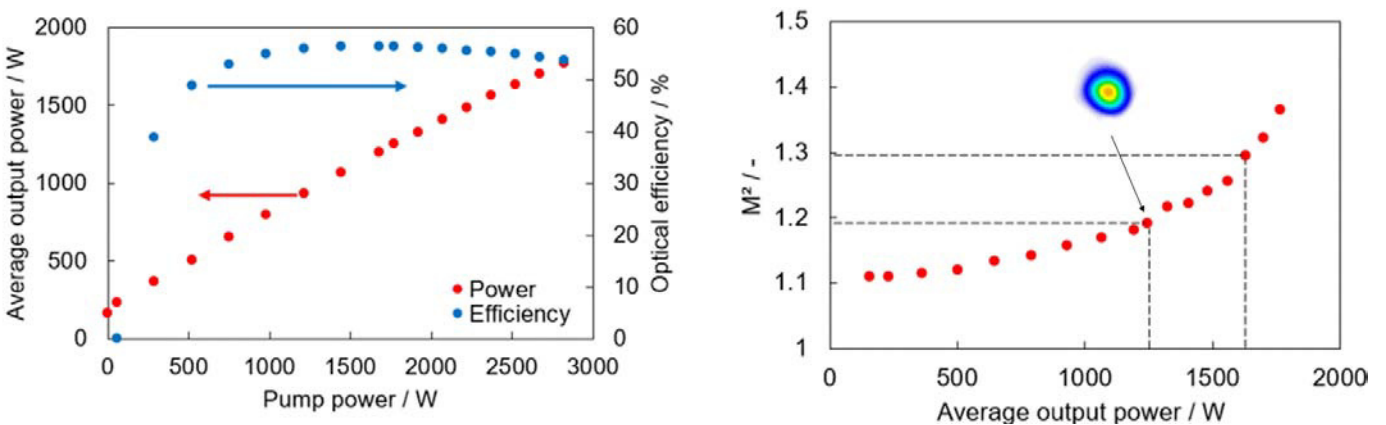


Fig. 1. Left: power and efficiency of the thin-disk multipass amplifier at seed power of ~200 W Right: $M^2 < 1.3$ is observed up to an output power of 1.6 kW, a sufficient margin for a 1 kW industrial laser. Inset: spot image of the focal plane at 1.3 kW

Using a thin-disk multipass amplifier in combination with a 200 W-level seed laser, an average output power of more than 1.5 kW can be obtained while still maintaining very good beam quality at a beam propagation factor of $M^2 < 1.3$ (see Fig. 1).

Recently the TruMicro 9000 (see Fig. 2), an industrial laser system, combining fiber, slab and thin-disk amplifier technology at their sweet spot of operation has been realized. A TruMicro-6000-based seed laser for a disk multipass amplifier enables tailored, flexible and stabilized pulse trains for the desired application. By applying CPA technology in a configuration with a 200 W slab laser for seeding the main amplifier, the system delivers pulses with an energy of 10 mJ at a duration of about 1 ps (see Fig. 3) at a repetition rate of 100 kHz. The repetition rate can be varied from 100 kHz to 1 MHz at a maximum constant output power of 1 kW and high beam quality with a beam propagation factor of $M^2 < 1.3$. For these repetition rates, single pulse control is available. Even higher frequencies of up to 50 MHz can be offered with the amplifier technology. Furthermore, the laser system also offers flexible burst mode capability, can rapidly deliver 10 mJ-pulses with a peak power of up to 11 GW even in a 40 mJ-burst of 4 pulses, making it an ideal beam source for laser produced plasma generation.



Fig. 2. TruMicro 9000 laser head

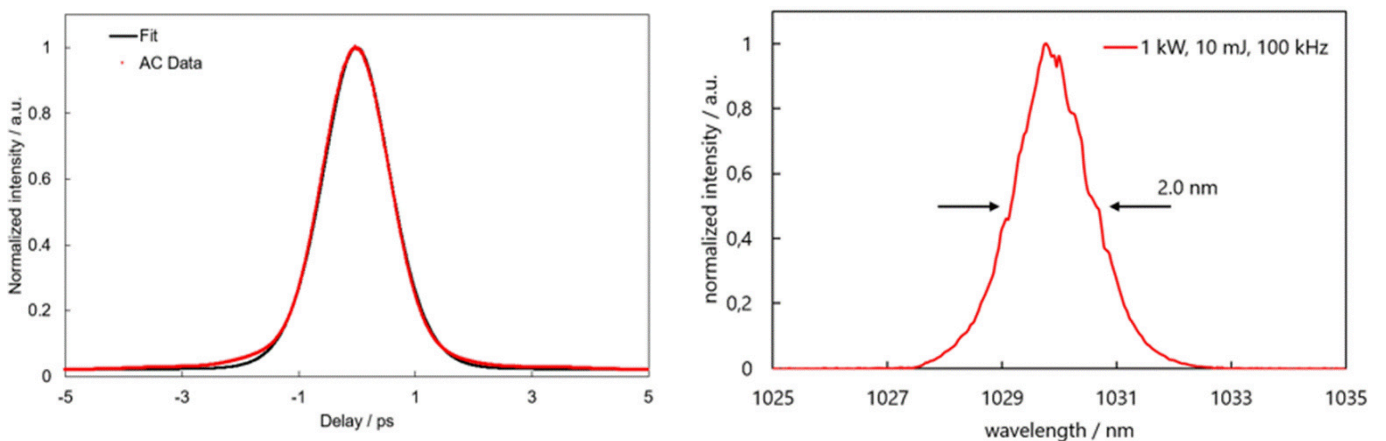


Fig. 3. Left: autocorrelation at pulse energy of 10mJ, showing pulse duration of 900fs assuming a sech² fit
 Right: spectrum at pulse energy of 10 mJ at pulse duration of 900 fs

The new approach based on combining the well-established and reliable laser amplifier technologies fiber, slab and thin-disk paves the way towards a new industrial platform for advanced laser applications. In

another configuration without CPA, 40 mJ of pulse energy with a small spectral width of < 0.5 nm at pulse duration of 100 ps and high beam quality ($M^2 = 1.3$) could be realized, allowing for interference-based applications such as DLIP.

3. Acknowledgements

Results presented were partially achieved during the "XProLas" project (FKZ13N16660, FKZ13N16670), funded by the BMBF, within the framework "Hochenergie-Strahlquellen".

4. References

- [1] Negel, Jan-Philipp, et al. "1.1 kW average output power from a thin-disk multipass amplifier for ultra-short laser pulses." *Optics Letters* 38.24 (2013): 5442-5445.
- [2] Dietz, Thomas, et al. "Ultrafast thin-disk multi-pass amplifier system providing 1.9 kW of average output power and pulse energies in the 10 mJ range at 1 ps of pulse duration for glass-cleaving applications." *Optics Express* 28.8 (2020): 11415-11423.

Highly efficient, high-power thulium-doped fiber laser systems

Lenski, M.¹; Jauregui, C.^{1,2}; Heuermann, T.^{1,3}; Wang, Z.¹; Gierschke, P.^{1,2}; Xu, Q.¹; Aleshire, C.¹; Gaida, C.³; Limpert, J.^{1,2,4,5}

¹ Institute of Applied Physics, Abbe Center of Photonics, Friedrich-Schiller-Universität Jena, Jena, Germany

² Fraunhofer Institute for Applied Optics and Precision Engineering, Jena, Germany

³ now with: Active Fiber Systems GmbH, Jena, Germany

⁴ GSI Helmholtzzentrum für Schwerionenforschung, Darmstadt, Germany

⁵ Helmholtz-Institute Jena, Jena, Germany

Many applications require high energy, high-power laser sources in the 2 μm spectral region. Thulium (Tm)-doped fiber laser systems can be an ideal platform for medical and industrial applications (e.g. surgery, lithotripsy, welding and cutting of polymer), as well as for nonlinear conversion processes such as mid-infrared or EUV generation [1–4]. Drawback of this technology is that, when using the conventional pump wavelength at around 790 nm, these fibers tend to generate a high heat load even at moderate output powers, especially for pulsed operation. In order to achieve high energy extraction, the fiber length must be short due to nonlinearities, so the inversion must be increased, and therefore the cross-relaxation rates were reduced, and in the worst case, negative [5]. This leads to rather low slope efficiencies in the range between 25 % to at most 60 % [6,7]. Additionally, high temperature operation tends to further reduce this slope efficiency. That is why these active fibers have to be water cooled even at moderate output powers [7]. The penalty which arises with water cooling is that it increases the size, weight and cost of the system and reduces the overall efficiency. In order to achieve higher slope efficiencies and, therefore, lower heat generation (that can potentially allow even for air-cooling), Tm-doped fibers should be pumped in the in-band wavelength span between 1550 nm and 1900 nm, where slope efficiencies of 62 % up to 92 % could already be shown [8,9]. A pump wavelength around 1692 nm seems a sweet spot that nicely balances pump source availability, high slope efficiencies and high energy storage [5]. In this contribution we present the results of three highly efficient, Tm-doped fiber laser systems that were cladding pumped at 1692 nm. The first experiment shows the output average power scaling potential with in-band pumping. The setup is schematically depicted in Figure 1 (left side).

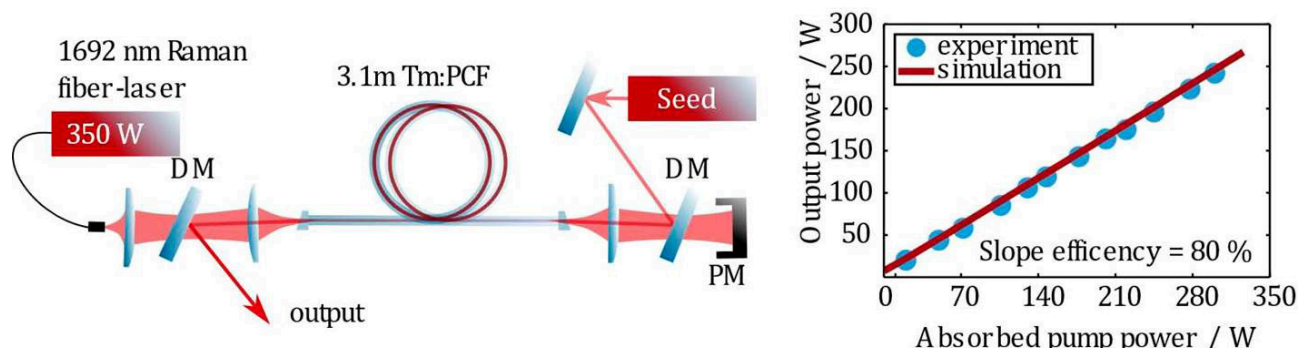


Figure 1: High power setup of a water-cooled, Tm-doped fiber amplifier in-band pumped at 1692 nm (left). Output power measurements as function of the absorbed pump (right).

It consists of a commercially available Tm-doped photonic crystal fiber (PCF core/clad ratio 50/250 μm) that is actively water cooled. When seeding this fiber with 10 W average power (80 MHz repetition rate and a centered wavelength at 1960 nm) we reached an output power of 242 W with a slope efficiency of 80 %, which is the highest slope efficiency of a Tm-doped fiber laser reported to date above 150 W. In the second experiment, we set up an air-cooled fiber system using the same type of PCF and achieved up to 80 W of average power with 71% slope efficiency, as shown in Figure 2. This is, to the best of our knowledge, the highest output power with the highest slope efficiency for an air-cooled Tm-doped fiber laser system. In a third experiment we set up a Q-switched master oscillator power amplifier, which schematic setup is depicted in Figure 3 on the left. For this experiment a 1.3 m long, rod-type fiber was used with a large mode-field diameter of 70 μm .

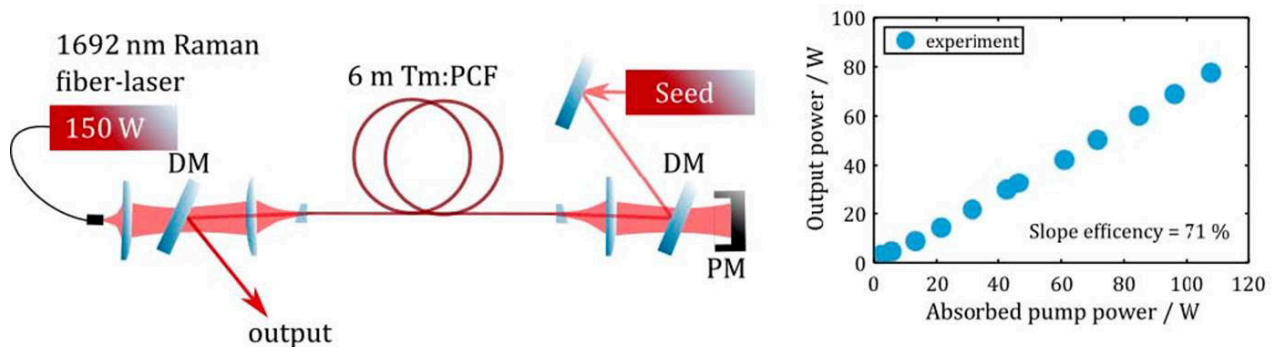


Figure 2: High power setup of an air-cooled, Tm-doped fiber amplifier in-band pumped at 1692 nm (left). Output power measurements as function of the absorbed pump (right).

As can be seen from the results (Figure 3 right), a similar slope efficiency of 77 % was reached. The amplifier delivers at the maximum 140 W of average output power at 20 kHz repetition rate, 7 mJ of pulse energy and a pulse duration of 83 ns. In fact, this is the highest slope efficiency and average output power to date for a single-emitter, mJ-class Tm-doped fiber laser.

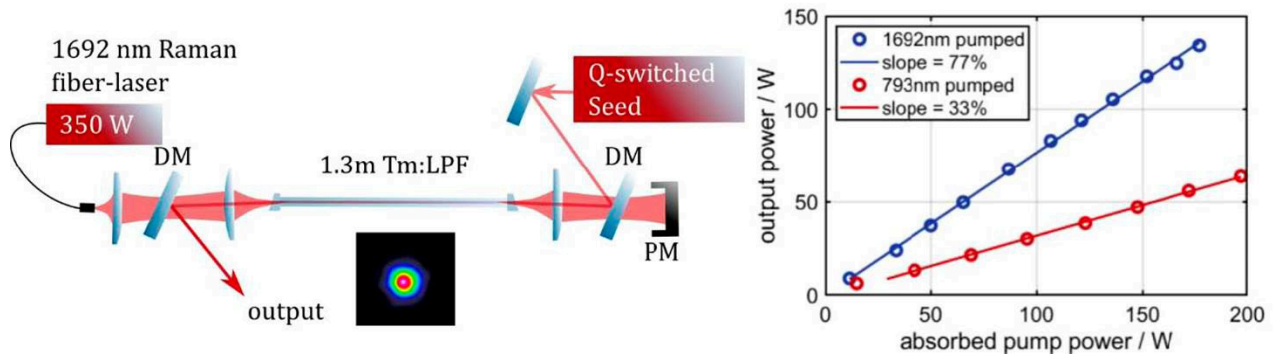


Figure 3: Setup of a MOPA, in-band pumped at 1692 nm in a Q-switched scheme (left). Output power measurements as function of the absorbed pump for conventional 793 nm and in-band pumping (right).

In summary, the in-band pumping approach could already show the efficiency scaling potential in different kinds of Tm-doped amplifier setups. The reduced heat-load even allows for air-cooled solutions. The higher efficiency at high extracted energy paves the way for even higher average powers from Tm-doped fiber lasers, with the potential to deliver multi-mJ energy at kW-level average powers from a single 2 μm amplifier channel. These sources can be an attractive platform for EUV or mid-infrared generation, as well as for various industrial applications in the medical field as well as in laser material processing.

Funding

Bundesministerium für Bildung und Forschung (03RU2U031E, UKPino); Carl-Zeiss- Stiftung (EHLAP).

References

[1] D. Pal, S. Das Chowdhury, A. Dhar, S. Saraf, K. Maiti, D. K. Pal, R. Sen, and A. Pal, "Ex vivo testing of air-cooled CW/modulated 30 W thulium fiber laser for lithotripsy," *Appl. Opt.* **58**, 6720 (2019).
 [2] C. W. Rudy, M. J. F. Digonnet, and R. L. Byer, "Advances in 2-μm Tm-doped mode-locked fiber lasers," *Opt. Fiber Technol.* **20**, 642–649 (2014).
 [3] X. Wei, S. Zhang, Z. Liu, X. Ye, W. Yin, H. Ren, B. Kang, Z. Yuan, W. Wang, and Y. Ma, "High-power mid-infrared ZGP optical parametric oscillator directly pumped by pulsed Tm:YLF laser at 1908 nm," *Opt. Laser Technol.* **161**, 109135 (2023).

- [4] Y. Mostafa, L. Behnke, D. J. Engels, Z. Bouza, J. Sheil, W. Ubachs, and O. O. Versolato, "Production of 13.5 nm light with 5% conversion efficiency from 2 μ m laser-driven tin microdroplet plasma," *Appl. Phys. Lett.* **123**, (2023).
- [5] M. Lenski, T. Heuermann, M. Gebhardt, Z. Wang, C. Gaida, C. Jauregui, and J. Limpert, "Inband-pumped, high-power thulium-doped fiber amplifiers for an ultrafast pulsed operation," *Opt. Express* **30**, 44270 (2022).
- [6] T. Heuermann, Z. Wang, M. Lenski, M. Gebhardt, C. Gaida, M. Abdelaal, J. Buldt, M. Müller, A. Klenke, and J. Limpert, "Ultrafast Tm-doped fiber laser system delivering 1 . 65-mJ , sub-100-fs pulses at a 100-kHz repetition rate," **47**, 3095–3098 (2022).
- [7] C. Gaida, M. Gebhardt, T. Heuermann, Z. Wang, C. Jauregui, and J. Limpert, "Transverse mode instability and thermal effects in thulium-doped fiber amplifiers under high thermal loads," *Opt. Express* **29**, 14963 (2021).
- [8] M. Meleshkevich, N. Platonov, D. Gapontsev, A. Drozhzhin, V. Sergeev, and V. Gapontsev, "415W single-mode CW thulium fiber laser in all-fiber format," *Opt. InfoBase Conf. Pap.* 57299 (2007).
- [9] D. Creeden, B. R. Johnson, G. A. Rines, and S. D. Setzler, "High power resonant pumping of Tm-doped fiber amplifiers in core- and cladding-pumped configurations," *Opt. Express* **22**, 29067 (2014).

SiC high-tech ceramics – a comparison of laser processes

Rochholz, C., Meudtner, A.
LCP Laser-Cut-Processing GmbH, Hermsdorf

Abstract

Within extensive R&D work different laser sources ranging from nanosecond VIS-wavelength over pico- and femtosecond IR-sources to water-jet guided laser beam processing had been applied to improve the quality and efficiency of the laser structuring as well as fine cutting and laser drilling of silicon-carbide materials. A wide variety of parameter fields had been tested with focus on surface and cutting line roughness on the one hand and very high ablation rates on the other hand. Caused by very different material compositions for example diamond layers, the challenge was to combine different methods and strategies to develop idle approaches for dissimilar contours and requirements. To meet economics constraints for some developments mechanical grinding with recurring laser processing was combined.

1. Introduction

Silicon carbide (SiC) and its variants (sintered SiC (SSiC), silicon infiltrated SiC (SiSiC), diamond SiC, ...) is a material that is very popular nowadays. The areas of application range from high-temperature applications such as the lining of steel furnaces and waste incineration plants to composite materials as components in gas turbines and other refractory products. Other areas of application include sealing rings, soot filters and brake disks in the automotive industry as well as structural and functional ceramics. The material owes this wide range of applications to its special properties in combination. Very good oxidation and corrosion resistance, low density and low thermal expansion coefficient meet high thermal conductivity as well as very high hardness and abrasion resistance .

One specific example is the components for pumps and other units for subsea applications developed as part of the SubseaSlide R&D project. The environmental conditions make the maintenance of the components used extremely difficult, which is why materials such as SiC-bonded diamond materials, which are extremely resilient and wear-resistant, are used here. However, the properties mentioned pose problems for mechanical manufacturing processes, which is why alternatives such as laser processing come into play here. In laser material processing, for example, technologies such as nanosecond pulsed laser processing, pico- and femtosecond IR sources and water-jet guided laser beam processing are used.

Compared to other mechanical cutting and grinding processes, laser material processing is characterized by tool-free and contact-free processing without mechanical stress on the workpiece. Although the use of conventional, rather long-pulse nanosecond laser sources reduces the energy input and leads to minimal heat conduction effects, the process still belongs to the thermal processes in which the material is melted or directly vaporized in the processing zone .

Modern ultra-short pulse laser material processing uses very short pulses (in the range of femtoseconds and picoseconds) in which the exposure time of the individual pulse in the material is so short that heat conduction effects do not occur or are so small that they can be neglected. It is therefore considered an athermal ablation process. Due to the short pulse durations, the penetration depth and therefore the removal per individual pulse in the material to be processed is less than with thermal processes. However, this increases the accuracy that can be achieved in comparison .

The water-jet guided (WJG) laser technology is characterized by the fact that a thin laminar water jet is generated into which a laser beam is threaded. Multiple reflections of the laser beam at the inner edges of the water jet ensure that the intensity distribution of the laser beam is approximately the same over the length of the water jet. In this way, the caustic typical of a laser beam is avoided, allowing vertical cutting edges ($< 1^\circ$) to be produced. Similar to ultra-short pulse processing, this is an ablative process. The additional cooling of the water jet reduces the thermal input into the material, which means that ceramics such as SiC can also be machined without cracks.

The tests for machining SiC were carried out as part of the funded R&D projects SubseaSlide, SAPHIR and UKPino.

2. Technology

The laser processes that are compared here in relation to the processing of SiC are processing using nanosecond pulsed (ns), ultra-short pulsed (USP) and water-jet guided laser radiation, as well as fusion cutting. The ns-pulsed system works with a maximum average power of 100 watts at 1 mJ pulse energy and with a pulse length of 120 ns at a wavelength of 355 nm. The diameter of the laser beam at the focus is 50 µm. The laser beam is positioned by means of scanner optics. The system also has an additional processing head, which was used for the fusion cutting experiments. The cutting optics are operated with a solid-state laser (1070 nm) in cw mode and provide a power of 1 kW. The focus is 60 µm and positioning is carried out using an X/Y table.

The laser for ultra-short pulse processing is characterized by pulses up to 1 ps at a wavelength of 1030 nm and a maximum average power of 100 W. The diameter of the laser beam at the focus is 60 µm and positioning is carried out in the same way as with the nanosecond laser using scanner optics.

The water-jet guided system uses a fiber laser with a wavelength of 1070 nm. The diameter of the water jet and thus also the focus of the laser beam can be adjusted using different nozzles. Nozzles with a diameter of 50 - 80 µm were available for the experiments. As the quality of the water has a decisive influence on the processing result, it is filtered until it has a conductivity value of less than 0.1 µS/cm. An X/Y table is used to position the workpiece relative to the water jet, as in the dry processing station.

Table 1: Overview of technologies with associated systems engineering

Laser processes	Minimal pulse duration [µs]	Beam Positioning	Focal diameter [µm]
Fusion Cutting	cw	X/Y table	60
Water-jet guided machining (WJG)	10	X/Y table	50 - 80
Nanosecond (ns) machining	0,12	scanner	50
Ultra-short pulse machining (USP)	0,000001	scanner	60

3. Evaluation

A direct comparison of test sequences, laser parameters and their optimization make little sense when comparing the technologies, as their physical modes of action differ too greatly. The processing results are therefore compared with each other.

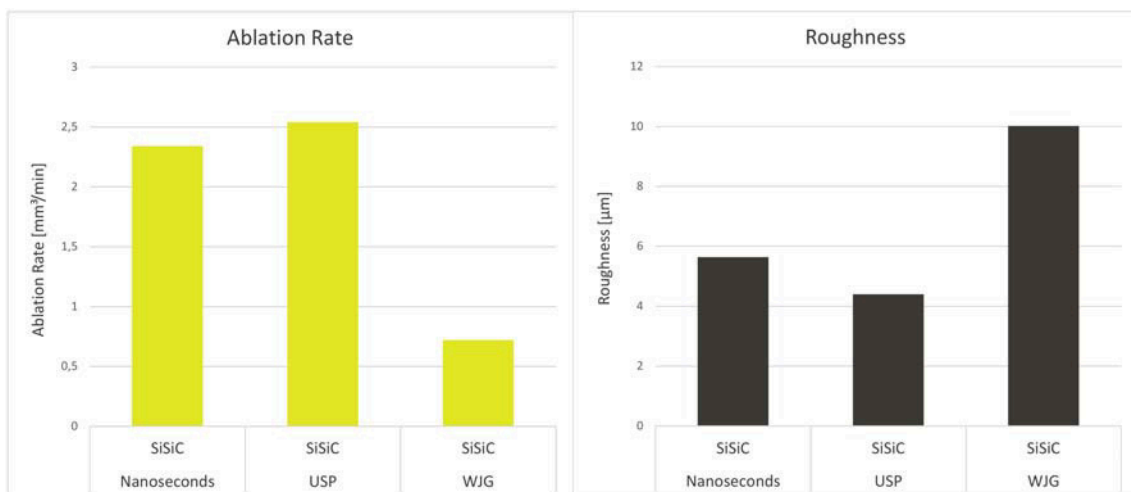


Figure 1: Comparison of technologies in terms of ablation rate and roughness for structuring

As ablation processes, ns, ultra-short pulse and water-jet guided technology offer the possibility of producing 3-dimensional structures using 2.5 D machining. Important target parameters here are the removal rate, which determines how quickly a volume can be processed, and the quality of the processing surface that can be generated, which can be measured using roughness, for example.

Figure1 shows the comparison of the technologies during structuring in terms of ablation rate (left) and roughness (right). It can be seen that the ablation rate for the nanosecond pulsed and the ultra-short pulse system is significantly higher than for the water-jet guided technology. The ultra-short pulse and nanosecond processing systems offer the possibility of significantly higher feed rates due to the beam positioning using a scanner. In addition, the repetition rates for the machining/preferred parameters are higher (10 kHz (ns), 400 kHz (USP); 500 Hz (WJG)), which results in a higher ablation rate overall.

A comparison of the roughness of the ablated surface shows the opposite picture. Here, the lowest values are achieved when processing using ultra-short pulse technology ($R_a = 4.4 \mu\text{m}$), followed by the ns-pulsed system ($R_a = 5.64 \mu\text{m}$). The surfaces ablated using a water-jet guided laser beam have a significantly higher value in comparison with an R_a of $10.02 \mu\text{m}$. The reason for this lies in the selected track spacing. This is $20 \mu\text{m}$ for the preferred parameters of ns and ultra-short pulse machining and $40 \mu\text{m}$ for water-jet guided technology. The track spacing has a significant influence on the roughness to be achieved when processing with pulsed laser. The smaller the track spacing, the lower the roughness. To remove a given geometry, the total processing time increases with reduced track spacing, which has a negative effect on the ablation rate. Fast, scanner-based systems can compensate for this better than the slower systems with an X/Y table.

In a comparison of the technologies, structuring using ultra-short pulses achieves the highest ablation rate ($2.54 \text{ mm}^3/\text{min}$) with the lowest roughness ($4.4 \mu\text{m}$) within the process parameters considered for this publication. For pure structuring tasks on SiC materials, ultra-short pulse technology is the preferred variant

A side effect during removal using ns and ultra-short pulse technology is the resulting taper. Vertical cuts are possible due to the constant diameter in the working area of the water-jet guided technology. However, the removal of SiC also generates a taper with this process (Figure2 right).

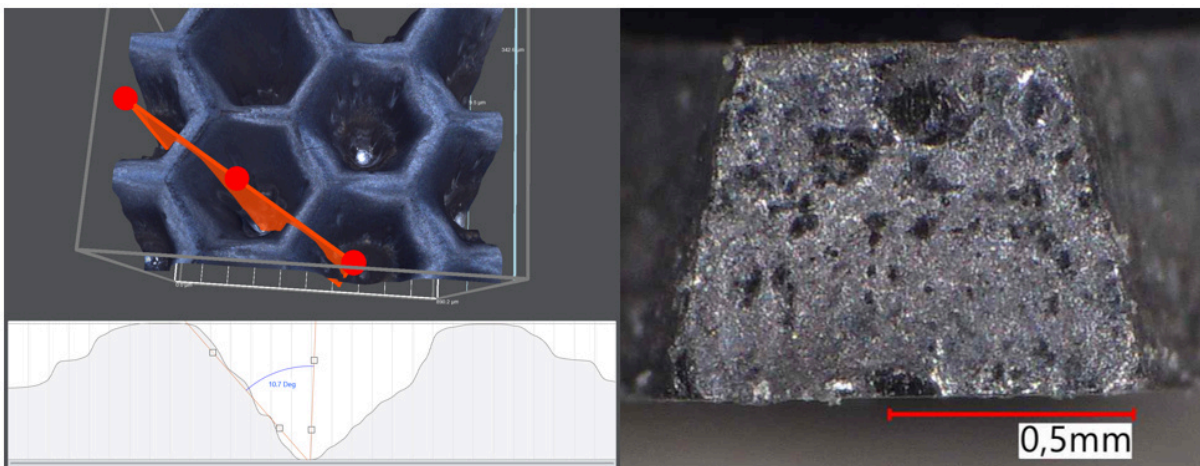


Figure 2: Taper created during structuring (left: ultra-short pulse/right: water-jet guided laser machining)

Figure2 shows a comparison of the resulting taper when structuring using ultra-short pulse and water-jet guided technology. Due to the process, ns and ultra-short pulse processing requires a widening of the kerf with additional tracks for material thicknesses $>100 \mu\text{m}$. The tests showed a taper of 11° for the preferred parameters, which would result in a kerf widening of 1.94 mm for a material thickness of 5 mm . Depending on the machining geometry, this is not desired or possible, which is why ns and ultra-short pulse technology are not considered for the cutting tests.

For material thicknesses from 0.5 mm (fusion cutting) and 0.2 mm (water-jet guided processing), several passes are required to cut the SiC. The required number of passes depends on the material thickness and

is 10 - 15 for both processes with a material thickness of 2 mm. An exact number of passes cannot be determined, as the number can vary slightly even on the same substrate. One reason for this may be minimal, spatially limited deviations that occur as a result of the material production or as local deviations in the material composition/grain structure.

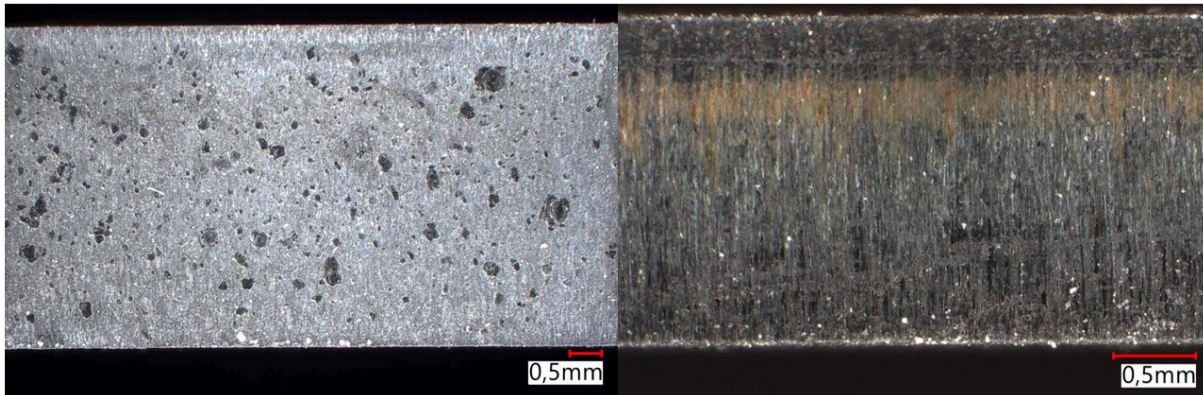


Figure 3: Comparison image of cutting-edge using water-jet guided technology (left) and fusion cutting (right)

Figure 3 shows a comparison of the cutting edge of the water-jet guided technology (left) and fusion cutting (right). The measured cutting-edge angle is 0.18° (material thickness $t = 5 \text{ mm}$) for the water-jet guided technology and 0.72° (material thickness $t = 1 \text{ mm}$) for fusion cutting. A determination of the roughness of the cut edge resulted in an average value of $R_a = 1.585 \text{ }\mu\text{m}$ (min/max = $0.997 \text{ }\mu\text{m} / 3.553 \text{ }\mu\text{m}$) for the water-jet guided technology and $R_a = 2.952 \text{ }\mu\text{m}$ (min/max = $1.585 \text{ }\mu\text{m} / 4.952 \text{ }\mu\text{m}$) for fusion cutting.

4. Conclusion

A direct comparison of influencing parameters does not lead to a satisfactory result when comparing the different technologies, as the effects of the technologies differ too greatly. It therefore only makes sense to compare the processing results with each other. Depending on the objectives, each technology has its own purpose, whereby the strengths of the individual processes can be combined.

In terms of material removal, nanosecond pulsed and ultra-short pulse technologies have an advantage. Due to the high feed rates that can be achieved here thanks to the scanner optics, significantly higher ablation rates are possible with low roughness. For pure cutting geometries, fusion cutting and water-jet guided technology have the advantage. Almost vertical cutting edges ($< 1^\circ$) can be produced here. The appropriate process must be selected depending on the geometry to be machined. It is possible to combine different processes in order to achieve the best possible machining result. See Figure 4 for an example.



Figure 4: Combined processing using ultra-short pulse (trenching) and water-jet guided technology (drilling) from SiC.

5. References

- [1] F. W. Zok, „Ceramic-matrix composites enable revolutionary gains in turbine engine efficiency,“ *American Ceramic Society Bulletin* 95(5), pp. 22-28, 2016.
- [2] F. Aldinger und W. Böcker, „Entwicklung keramischer Hochleistungswerkstoffe. I: Stand der Forschung und Entwicklung,“ *Keramische Zeitschrift*, pp. 164-172, 1992.

-
- [3] W. Kollenberg, Technische Keramik Grundlagen - Werkstoffe - Verfahrenstechnik, Vulkan-Verlag, 2009.
- [4] bmwk, „SubseaSlide – Robuste Gleitlager für Subsea-Pumpen,“ 4 September 2024. [Online]. Available: <https://www.bmwk.de/MAFO/projekte/projekt-03SX508-SubseaSlide.html>.
- [5] Y. Deng, Y. Zhou, Y. Zhang, D. Chen und X. Zhou, „Numerical and experimental analysis of nanosecond laser ablation of SiC,“ *Materials Science in Semiconductor Processing Volume 151*, 15 November 2022.
- [6] W. Li, R. Zhang, Y. Liu, C. Wang, J. Wang, X. Yang und L. Cheng, „Effect of different parameters on machining of SiC/SiC composites via pico-second laser,“ *Applied Surface Science Volume 364*, pp. 278-287, 28 Februar 2016.
- [7] Y. Huang, Y. Zhou, J. Li und F. Zhu, „Femtosecond laser surface modification of 4H-SiC improves machinability,“ *Applied Surface Science Volume 615*, April 2023.
- [8] B. Cheng, Y. Ding, Y. Li und L. Yang, „Theoretical and Experimental Investigation on SiC/SiC Ceramic Matrix Composites Machining with Laser Water Jet,“ *Applied Sciences Volume 12 Issue 3*, 24 Januar 2022.
- [9] J. Bliedtner, H. Müller und A. Barz, Lasermaterialbearbeitung: Grundlagen - Verfahren - Anwendungen - Beispiele, Carl Hanser Verlag, 2013.
- [10] F. A. Sfregola, R. De Palo, C. Gaudiuso, F. P. Mezzapesa, P. Patimisco, A. Ancona und A. Volpe, „Influence of working parameters on multi-shot femtosecond laser surface,“ *Optics and Laser technology*, 27 April 2024.
- [11] Synova, „The Laser MicroJet® Technology,“ Synova, [Online]. Available: <https://www.synova.ch/technology/synova-laser-microjet.html#water>. [Zugriff am 9 9 2024].

Laser Swelling induced Freeform Microlenses in Polymers

Mäder-Heinrich, M.; Höche, T.; Schusser, G.

Fraunhofer Institute for Microstructures of Materials and Systems IMWS, Halle (Saale), Germany

Microstructures on polymer surfaces have become of wide interest in the past two decades. Especially in the field of tailoring adhesion or other surface functionalities [1] and for optical applications [2], the demand for polymer microstructures is growing. In addition to that, freeform micro-optics are of growing interest as well [3]. We present a simple and fast method to prepare freeform micro lenses or lens arrays in polymers. Using a Tm-fiber Laser with a wavelength of 1,940 nm, the lenses are directly written into the polymers surface. By choosing a power density below the ablation threshold the irradiated volume experiences an expansion which leads to a swelling on the surface. Stopping the irradiation leads to a fast cooling which leaves no time to rearrange back to the ordered manner the polymer had before. The elevation at the surface is permanent up to threshold temperatures where the polymer reaches rubber state in most polymers that have been studied. So far mainly polymers with T_g above room temperature and mainly thermoplastics and elastomers have been studied. The effect of laser swelling has been known for a while [4], however it has not yet been commercialized to our knowledge. We will show that lenses of very accurate shapes can be produced using smart writing strategies. We will also show that the lenses have the expected refractive effect. At last, we present results of different polymers and different lens shapes fabricated in air within very short processing times.

References

- [1] Arzt, E., et al., Functional surface microstructures inspired by nature – From adhesion and wetting principles to sustainable new devices. *Progress in Materials Science*, 2021. **120**: p. 100823.
- [2] Cai, S., et al., Microlenses arrays: Fabrication, materials, and applications. *Microscopy Research and Technique*, 2021. **84**(11): p. 2784-2806.
- [3] Hua, J.-G., et al., Free-Form Micro-Optics Out of Crystals: Femtosecond Laser 3D Sculpturing. *Advanced Functional Materials*, 2022. **32**(26): p. 2200255.
- [4] Beinhorn, F., et al., Micro-lens arrays generated by UV laser irradiation of doped PMMA. *Applied Physics A*, 1999. **68**(6): p. 709-713.

Dielectric Material Processing with Ultra-Short Pulses

Andriukaitis, D.¹; Jašinskas, M.¹; Bischoff, C.²; Gečys, P.³

¹ EKSPLO UAB, Vilnius, Lithuania

² TOPAG Lasertechnik GmbH, Darmstadt, Germany

³ Center for Physical Sciences and Technology, Vilnius, Lithuania

Abstract

Femtosecond lasers have become essential tools in material processing field. Thanks to the ultra-short pulse duration, these lasers can process a wide range of materials without causing significant thermal effects, leading to superior quality. Dielectric materials, especially glass and ceramics, are among those that benefit the most from femtosecond laser technology. Traditional processing methods often struggle with these materials, but femtosecond lasers provide a solution with high precision and quality. Continuous innovations are making femtosecond lasers even more versatile. One such innovation is burst mode, which outputs bursts of pulses at MHz/GHz repetition rates. Burst mode splits a single high-energy pulse into multiple pulses, optimizing the laser’s power and increasing the process throughput. In this study, the industrial femtosecond laser FemtoLux 30 is employed in glass and ceramics processing using MHz/GHz burst mode, resulting in throughput increase ranging from several to tens of times.

1. Introduction

It is well known that femtosecond lasers are highly effective tools for processing brittle materials such as glass and ceramics. These ultra-short pulse lasers enable precise machining of dielectric materials, and with pulse durations in the hundreds of femtoseconds, the resulting quality is unparalleled [1]. However, one challenge with femtosecond laser processing is achieving higher throughput, which still lags behind traditional methods [2]. To address this, continuous advancements in ultra-short pulse laser technology have increased average optical power to several kilowatts [3]. Nevertheless, higher average power alone does not directly translate to increased throughput. There is an optimal fluence at which the most efficient material ablation occurs ($7.4 \cdot \phi_{th}$, where ϕ_{th} - material ablation threshold).

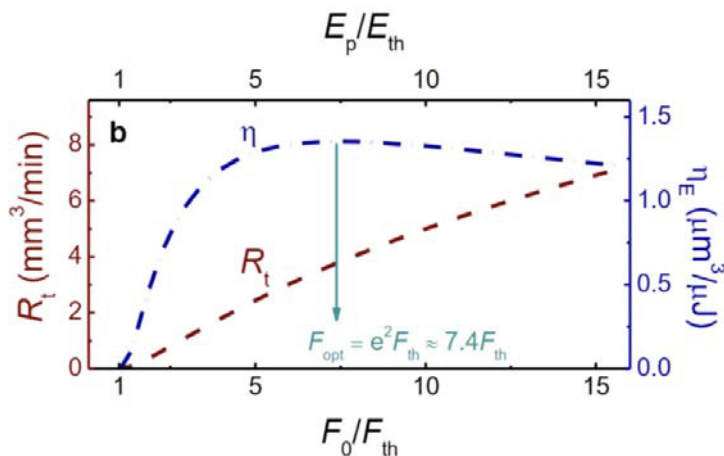


Fig. 1. Ablation efficiency and ablation rate dependence on fluence [4].

To achieve this optimal fluence, several approaches can be taken. One method is to increase the pulse repetition rate while lowering the pulse energy, thereby bringing the fluence closer to the desired value. However, there is a limit to how much the repetition rate can be increased, as excessively high rates may degrade quality and cause ablation particle shielding, ultimately reducing throughput [5]. Another approach is to increase the beam diameter, which decreases the fluence to the optimal level. A key advantage of this method is that it allows full utilization of the laser's power without complicating the processing setup, unlike

beam splitting. However, increasing the beam diameter sacrifices precision, which can be a critical factor in applications requiring small feature sizes.

Another method for achieving optimal fluence is to split high energy pulses into multiple smaller pulses using burst mode, which operates with intra-burst repetition rates in the MHz and GHz range. This approach, combining pulse splitting with high intra-burst repetition rates, has proven beneficial for material micromachining applications [6-8]. However, further studies are needed to fully understand the mechanisms behind the increase in process throughput when using MHz/GHz burst mode. A key challenge in conducting such studies is the limited availability of laser sources that offer flexible configuration of MHz/GHz burst modes. To address this, an Active Fiber Loop was developed, enabling flexible formation of GHz bursts. This was integrated into the industrial femtosecond laser FemtoLux 30, which was utilized in this study for processing dielectric materials [9].

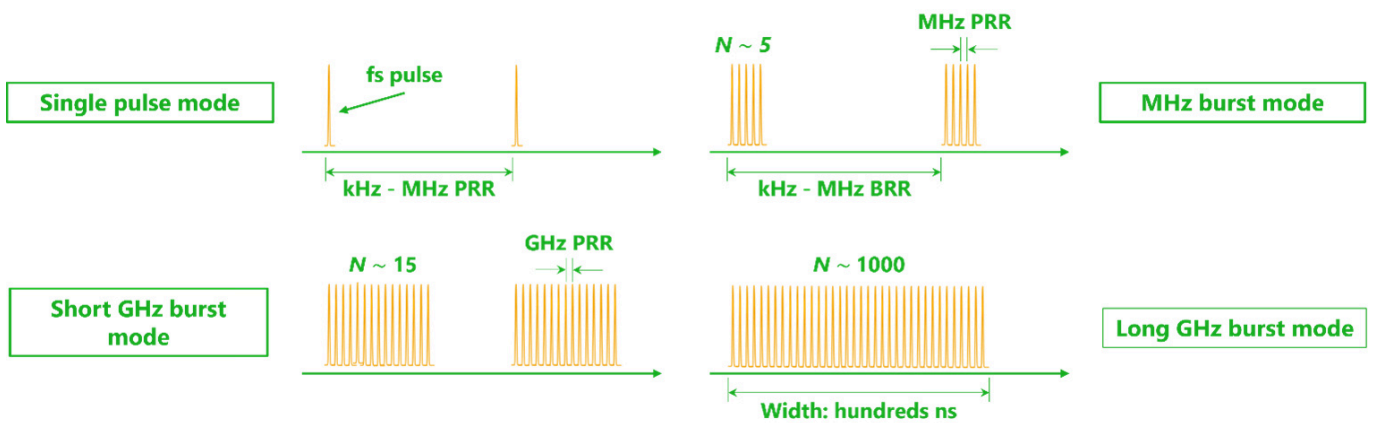


Fig. 2. Possible operation modes of ultra-short laser source

2. Active Fiber Loop (AFL) for flexible GHz burst formation

The patent pending Active Fiber Loop (AFL) technology was developed to provide unparalleled flexibility in selecting burst parameters. This all-in-fiber AFL system consists of key components such as AOM1-3 (acousto-optical modulators), FC (fiber coupler), YDF (ytterbium-doped fiber), CFBG (chirped fiber Bragg grating), and LD (laser diode) (Fig. 3). The GHz burst formation technique works by splitting and delaying pulses from the MHz master oscillator. With each round trip, delayed replicas from previous cycles are combined with an undelayed replica of the next input pulse. This allows the AFL to generate GHz bursts with broad tunability in the number of pulses per burst, using AOM3 as a pulse picker to select bursts with the desired pulse count.

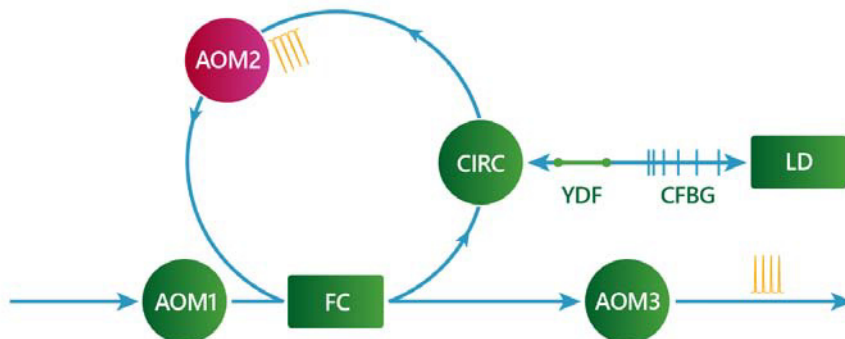


Fig. 3. Schematic of Active Fiber Loop.

The AFL method for generating GHz and combined MHz+GHz bursts has been successfully integrated into the industrial femtosecond laser system FemtoLux 30. In the GHz burst regime, AFL technology allows formation of 2.2 GHz bursts, containing 2 to 22 pulses and 44 to 1100 pulses per burst (Fig. 4, left and middle).

Additionally, the AFL enables operation in a combined MHz+GHz burst mode, offering a 50 MHz burst mode with 2 to 10 pulses and a 2.2 GHz burst mode with 2 to 22 pulses per burst (Fig. 4, right). As a result, the FemtoLux 30 stands out as the only laser on the market providing unmatched versatility and flexibility in burst mode selection. The system also features innovative direct refrigerant cooling technology, ensuring zero maintenance. With only two main components - the laser head and the power supply - connected by an umbilical cable, the FemtoLux 30 is an ideal solution for a wide range of micromachining applications.

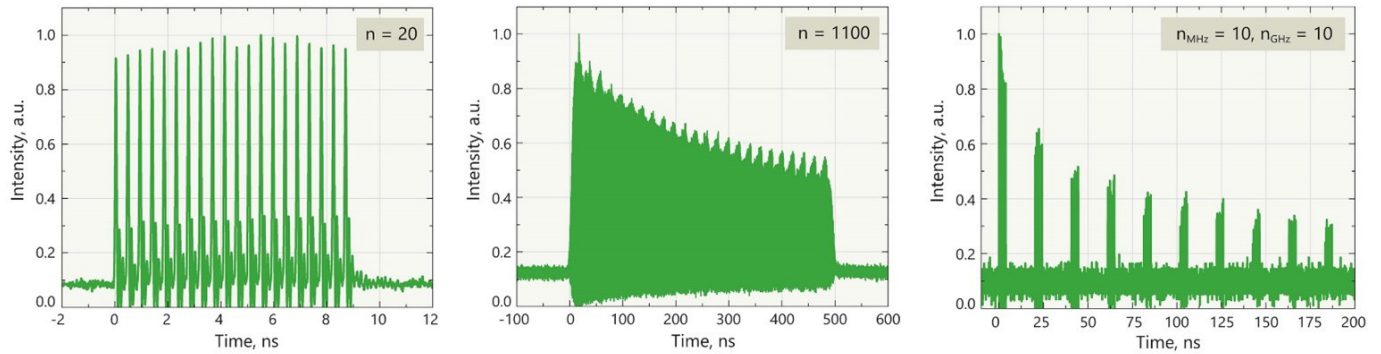


Fig. 4. FemtoLux 30 different GHz burst operation modes: (left) short GHz burst, (middle) long GHz burst, (right) combined MHz and GHz burst.

3. GHz and MHz+GHz burst modes in increasing ablation throughput in fused-silica glass

The influence of GHz and MHz+GHz burst modes on ablation rates was examined by milling 2x2 mm² areas. A beam approximately 20 μm in diameter was focused onto the sample, which was scanned using bidirectional hatching, with the scanning angle adjusted by 33 degrees for each layer. The focus position was changed with each layer to maintain focus on the processed surface. The FemtoLux 30 operated with a pulse duration of 298 fs, a repetition rate of 200 kHz, and a wavelength of 1030 nm. After processing, the depth of each square was measured, and the ablation rate was calculated.

In the GHz burst mode, the ablation rate consistently increased as the number of pulses in the burst rose, reaching a peak ablation rate of 68.3 mm³/min with 70 pulses per burst (Fig. 5 (left)). In the MHz+GHz burst mode, the ablation rate similarly increased with the number of pulses in both MHz and GHz bursts, achieving a maximum ablation rate of 52.1 mm³/min (Fig. 5 (right)), which was slightly lower than that of the GHz burst mode. The results show that the GHz burst mode is more effective in milling fused-silica glass than the MHz+GHz burst mode, increasing the ablation rate by 13.2 times compared to single-pulse mode.

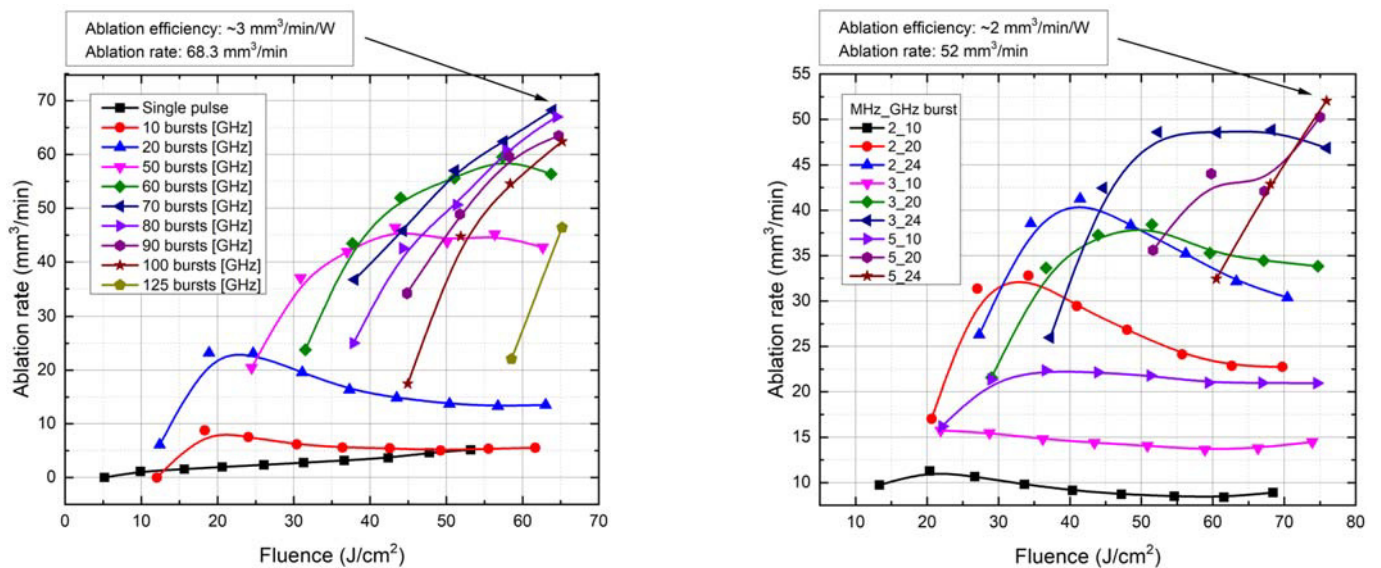


Fig. 5. Ablation rate depicted against fluence for GHz burst (left) and MHz+GHz burst (right).

4. Scribing of ceramic plates with femtosecond pulses

Ceramics are widely used dielectric materials, valued for their exceptional properties such as high thermal conductivity, electrical insulation, mechanical strength, and resistance to corrosion and wear. However, conventional mechanical processing methods often require significant force, which can lead to cracks and potential substrate breakage. Femtosecond lasers offer a high-quality, precise solution for processing hard and brittle materials like ceramics.

In this study, the FemtoLux 30 was tested for scribing ceramic materials, specifically in the formation of grooves. A comprehensive investigation was conducted to evaluate scribing speeds and quality using 1030, 515, and 343 nm wavelengths. The ablation thresholds for these wavelengths were first examined. By irradiating the ceramic plate with single femtosecond pulses at each wavelength, craters were formed. The diameters of these craters were measured, squared, and depicted graphically, allowing for the calculation of ablation thresholds. The results showed ablation thresholds of 1.14 J/cm² for 1030 nm, 1.08 J/cm² for 515 nm, and 0.95 J/cm² for 343 nm. The observed decrease in ablation thresholds at shorter wavelengths is attributed to the increased efficiency of multiphoton absorption and other nonlinear effects, which become more pronounced with higher harmonics [10].

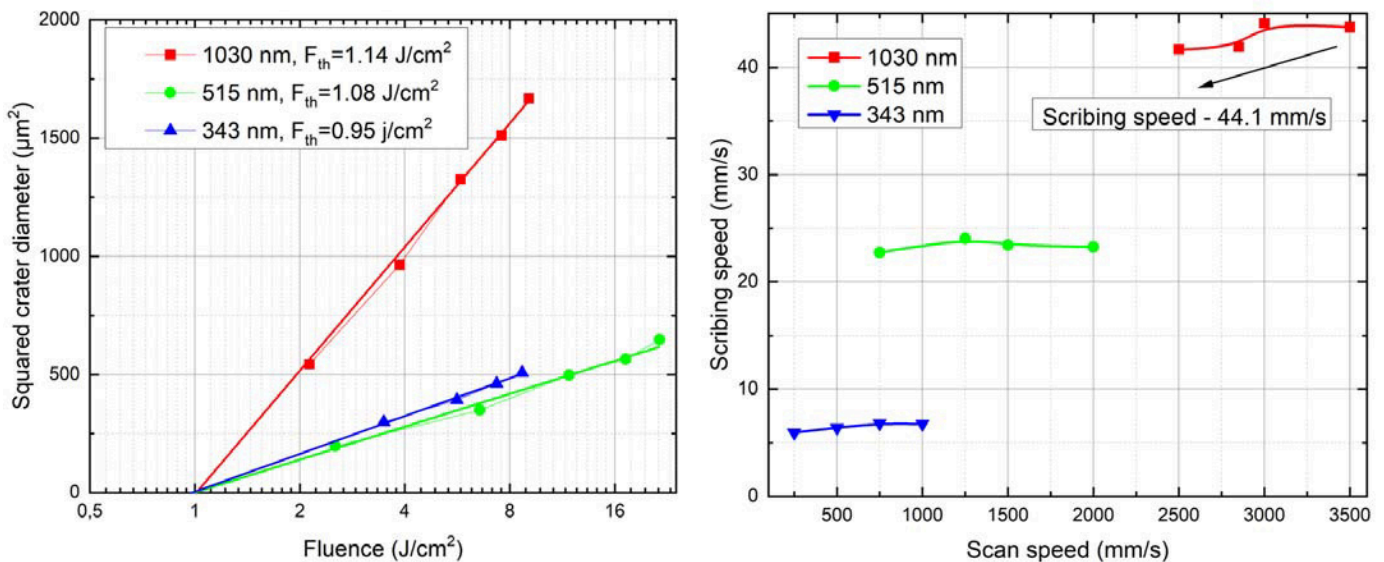


Fig. 6. Ablation threshold measurement for different wavelengths (left). Scribing speed investigation by iterating scanning speeds (right).

After calculating the ablation thresholds, the repetition rate was increased to adjust the fluence to its optimal value ($7.4 \cdot \phi_{th}$). The scanning speed was then iterated for different wavelengths to identify the maximum scribing speed. The highest scribing speed achieved was 44.1 mm/s for 1030 nm, which decreased to 25 mm/s for 515 nm and 6.82 mm/s for 343 nm. The primary reason for this drop in scanning speed at 515/343 nm is the lower average laser power available at these wavelengths. It is also worth noting that while the scribing speed at 1030 nm was the highest, the heat-affected zone (HAZ) was also the largest, measuring $8.23 \pm 1.11 \mu\text{m}$. By using the 515 nm and 343 nm wavelengths, the HAZ was significantly reduced to $5.62 \pm 1.07 \mu\text{m}$ and $4.88 \pm 0.59 \mu\text{m}$, respectively.

5. References

- [1] E. Markauskas, L. Zubauskas et al., “Femtosecond Laser Cutting of 110–550 μm Thickness Borosilicate Glass in Ambient Air and Water”, *Micromachines* (2021).
- [2] A. Žemaitis, M. Gaidys et al., “Advanced laser scanning for highly-efficient ablation and ultrafast surface structuring: experiment and model”, *Scientific Reports* (2018).
- [3] K. Michel, C. Grebing et al., “High-energy ultrafast thin-disk amplifiers”, *Proc. SPIE 10896, Solid State Lasers XXVIII: Technology and Devices* (2019).
- [4] A. Žemaitis, “Efficient laser ablation for bio-inspired 3D functional surfaces”, Vilnius University, (2022).

- [5] M. Gaidys, A. Žemaitis et al., “Efficient picosecond laser ablation of copper cylinders”, *Applied Surface Science* (2019).
- [6] D. Metzner, P. Lickschat et al., “Study on laser ablation of glass using MHz-to-GHz burst pulses”, *Appl. Phys.* (2022).
- [7] G. Bonamis, E. Audouard et al., “Systematic study of laser ablation with GHz bursts of femtosecond pulses”, *Opt. Express* (2020).
- [8] S. M. Remund, M. Gafner et al., “Milling applications with GHz burst: Investigations concerning the removal rate and machining quality”, *Procedia CIRP* (2020).
- [9] T. Bartulevicius, M. Lipnickas et al., “30 W-average-power femtosecond NIR laser operating in a flexible GHz-burst-regime”, *Opt. Express* (2022).
- [10] R. Oosterbeek, S. Ashforth et al., “Ablation threshold dependence on incident wavelength during ultrashort pulsed laser ablation”, *International Journal of Nanotechnology* (2017).

Femtoseconds. Creating new possibilities

Hellwig, C.
LIGHT CONVERSION

Abstract

Ultrashort pulse laser systems are widely used in a variety of fields, including material science, engineering, metrology, medicine, and telecommunications. They are unmatched in their ability to produce a wide range of components for microelectronics, biomedicine, lithography, optoelectronics, MEMS. Femtosecond lasers are particularly versatile, capable of performing multiple processes, such as cutting, shaping, and patterning on different materials, while maintaining high micromachining quality and a negligible heat affected zone. Additionally, implementation of novel techniques such as post-compression, can improve the quality of laser micromachining even more.

Industrialization of Additive Manufacturing (AM)

Prof. Dr.-Ing. Ingomar Kelbassa

Abstract

The presentation will be addressing all aspects in terms of Industrialization of AM along the AM manufacturing route – from Design to the finished part, end2end. Special foci will be spent on virtualization, new process approaches, finish machining and quality assurance. Success stories from industry – machine OEMs as well as end users – will be completing the presentation.



Design Criteria for the Functionalisation of Additively Manufactured Aluminium Components by Integrating Sensors during the Manufacturing Process

Schönherr, A.¹; Voigt, S.²; Schob, B.¹; Bessler, K.³; Kroll, L.¹

¹ Technical University of Chemnitz, Chemnitz

² Fraunhofer Institute for Electronic Nano Systems, Chemnitz

³ Capgemini Engineering, München

Abstract

Integrative lightweight constructions play a major role in the aerospace industry. Laser Powder Bed Fusion of metals (PBF-LB/M) is an additive manufacturing process (Additive Manufacturing – AM) which becomes more and more important for the production of high-strength, topology-optimized and functionalized components. The integration of radio-frequency identification (RFID) tags in closed cavities increases the functional diversity of such additively manufactured components. By specifically pausing the manufacturing process, a sensor can be integrated into the component after the metal powder has been removed from the inside. To protect them from thermal and mechanical manufacturing influences, the RFID tags were cast in temperature-stable epoxy resin before insertion. The shape of the moulded sensor tag and its cavity were designed for optimum positioning. An aluminium plate shields the encapsulated sensor from the laser beam while simultaneously providing a solid connection to the component. For achieving higher melting depth, selected parameters were set in layers above the aluminium plate. The RFID tags can be equipped with various low-power sensors to measure for example temperature, magnetic field, acceleration or alignment. Additionally, these RFID tags can perform simple storage function for saving component data such as designation, date of manufacture, installation time or operating hours.

1. Introduction

In order to achieve higher efficiency rates in aerospace, the level of lightweight construction of structural components must be significantly increased. For this purpose, relevant components are topology-optimized regarding the prevailing loads and manufactured using the PBF-LB/M. In this well-researched AM technology, metal powder is applied layer by layer and melted by using a laser. The process offers the possibility of producing components with closed cavities. These cavities are filled with powder due to the process. However, the PBF-LB/M process can be interrupted. At this point, an open cavity at the top can be freed from powder and filled with other media. The manufacturing process then continues, closing the cavity. This method offers the potential to integrate sensors directly into high-strength AM components. This makes a decisive contribution to increase the level of lightweight constructions. The most serious mechanical problems lie in non-destructive embedding and connection during the process.

Today, there are different approaches to integrate sensors into powder-based AM components. The integration of PT100 temperature sensors into components made of AlSi10Mg has already been investigated, for example Binder et al. cast sensors

force-fit by using a spring system into an additively manufactured cavity. The cable connection to the electronics outside the AM components was implemented with provided cable channels for this purpose. To protect the sensor from the effects of the laser, an aluminium plate was utilised as a heat shield [1]. Numerous other scientist groups have done preliminary work on the integration of wired sensors [1-5]. An obvious approach in this regard is the integration of RFID electronics for the radio-based transmission of energy and sensor data. RFID tags, consisting of an electronic IC (ASIC) and an antenna, are used in a variety of ways: They are used for clear identification and tracking during the manufacturing process, for storing information about quality control parameters and for tracing or recording operating hours among others. If these RFID tags are also combined with sensors, new functions such as measuring temperature and magnetic fields and determining the acceleration or alignment of mechanical components are conceivable. Pille et al. and Sehr et al. were able to demonstrate successful integration of RFID tags and their communication through thin-walled metal [5-6]. However, there is no indication of the RFID frequency at

which the metal could be penetrated, nor were the sensors connected to the PBF-LB/M-components with a material bond.

The main task of this paper was the solid connection of wireless sensors into components made of suitable aluminium alloys. After selecting a material the quality of the layers above the integrated sensors had to be analysed. Variants for the connection of assembled RFID tags within additively manufactured cavities were found. In addition, the radio frequency performance of the RFID tags of PBF-LB/M components were analysed in experiments and improved if necessary. Furthermore, variants were examined which enabled a secure signal connection to the sensor. The aim was to point out the solution to these problems in order to make a significant contribution to integrative lightweight construction.

2. Materials and Methods

The aluminium alloy AlSi10Mg was selected to produce test specimens with integrated sensors. The powders from different suppliers were analysed about their grain size distribution in the Camsizer X2 particle analyser from Microtrac Retsch GmbH. Additionally, the quality of the powder from different manufacturers was examined under the Zeiss EVO 15 scanning electron microscope (SEM). The integration attempts of sensors into the AM components were carried out on the SLM 250 HL from Nikon SLM Solutions AG. To determine the relative density of the produced test specimens and to study the sensor connection within the AM components, the light microscope Keyence VHX 600 has been used. Tensile samples were examined on the Zwick Z100 tensile testing machine. Regarding the developed RFID tags, the RFID reader "MRD2EVM" from Texas Instruments Incorporated and the Vector Network Analyser "ZVR" from Rohde & Schwarz GmbH & Co. KG were employed for characterisation and reading of the RFID tags.

3. Alloy Selection and Robust Process Window

The integration of RFID magnetic field sensors into metallic AM components requires the use of non-magnetic alloys. This poses a limit to the choice of alloys to aluminium. Well-known aluminium alloys suitable for aviation are, for example, AlSi7Mg SilmagAl, AlSi10Cu4, AlSi10Mg, SilcupAl, AlMgScZrMn and Scalmalloy. AlSi10Mg was chosen because it achieves comparatively high maximum tensile strengths up to 450 MPa with relatively low thermal requirements for the processing and post-treatment [7, 8]. Powders from different manufacturers with particle sizes in the range 20-63 μm were analysed. No significant differences were found between the powders. The SEM image (Figure 1) shows the aluminium particles.

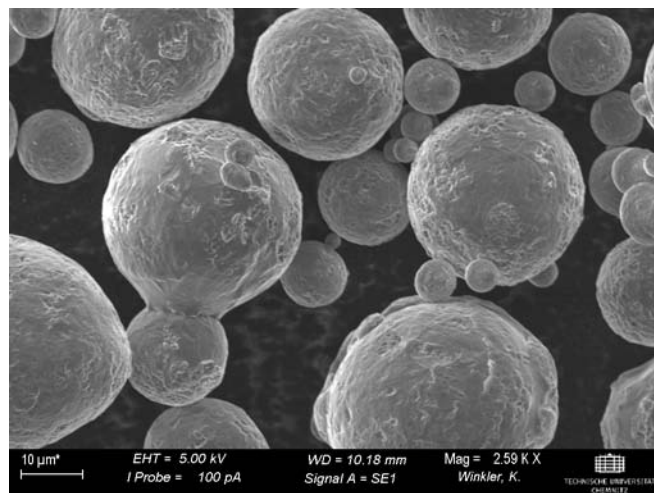


Figure 1: AlSi10Mg particles under the SEM

Scan parameters for the PBF-LB/M were developed for a layer thickness of 50 μm . The scanning speed was 930 mm/s, laser power 350 W and the hatching distance 150 μm . Seven upright, cylindrical tensile samples were produced in accordance with DIN 50125 -B and then tested on the tensile testing machine.

After the building process, the tensile strength of the alloy is approximately 460 MPa. The elongation at break without heat treatment is 5%. Heat treatments can be performed on components in order to increase tensile strength. One heat treatment at 165°C for 7 hours showed that elongation dropped to approximately 4%. Stress-relieving annealing at 240°C for 3 hours reduced the tensile strength to 390 MPa and increased the elongation at break by approx. 1%. By means of solution annealing at 520°C followed by heat treatment at 165°C, the elongation at break increased to over 10%. However, the tensile strength dropped by around 50%. The sensors can withstand just temperatures of a maximum of 165°C. This excludes effective heat treatment. Since the tempering process itself did not result in a significant increase in strength or elongation at break, no heat treatment was carried out after the sensor integration process.

The shortest possible energy input above the sensor is essential to minimise damage. A higher layer thickness about 90 µm helps to pass through the critical remelting area quickly, as the number of exposures and therefore the energy input is reduced. In addition, the higher layer thickness better compensates tolerances at the upper edge of the cavity. This reduces the chance which the sensor will remain in the cavity during the lay-up process and not be displaced. In this context, a parameter set for a layer height of 90 µm was developed. In single-track investigations, the process window was initially limited to a laser power between 325 W and 350 W as well as a scanning speed between 400 mm/s and 800 mm/s. Samples measuring 10x10x10 mm³ were then manufactured within the process window with variations of the hatching strategy. The microscopic images revealed a maximum relative density of 99,79% with a meander hatching with a laser power of 350 W and a scanning speed of 700 mm/s. With this developed set of parameters, curved samples were produced at an angle between 0° and 90°. A microscopic analysis of the sections shows the horizontal bridges with overhangs of 0° can be fundamentally generated (Figure 2). This implies that cavities can also be closed using complex overhang geometries after the sensors have been inserted into the specifically prepared cavities.

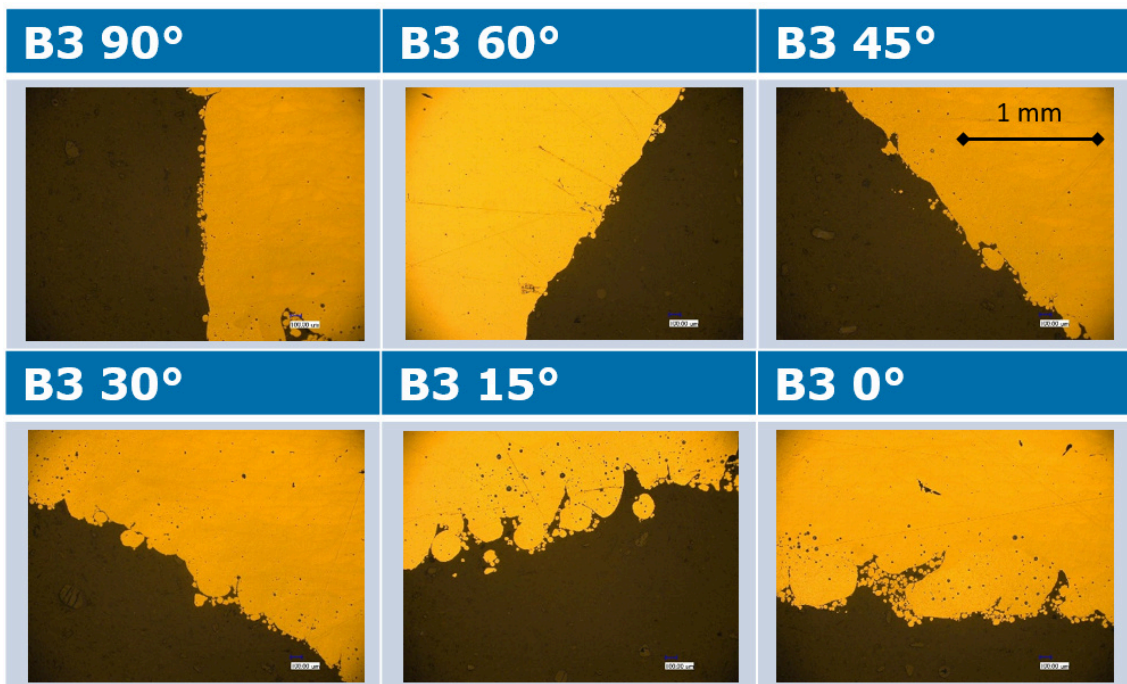


Figure 2: Light microscopic images showing downskin of 90 µm parameters

4. Characterisation of Integrated RFID Sensors

An RFID transceiver which operates in the LF range of 134.2 kHz was used as the central component of the RFID sensors intended for integration. An RFID round antenna, a microcontroller and an acceleration sensor were connected to this transceiver. The electronic components were attached to a temperature-resistant, round circuit board with a glass transition temperature of approx. 280°C and a diameter of around 20 mm using high-temperature solder. The sensor is encapsulated in a high-temperature resistant epoxy resin moulding system. This serves to protect the circuit boards, including the electronic compo-

nents. In addition, the outer shape of the sensor can be varied to adapt it to the additively manufactured cavity. Figure 3 shows a corresponding RFID sensor tag.

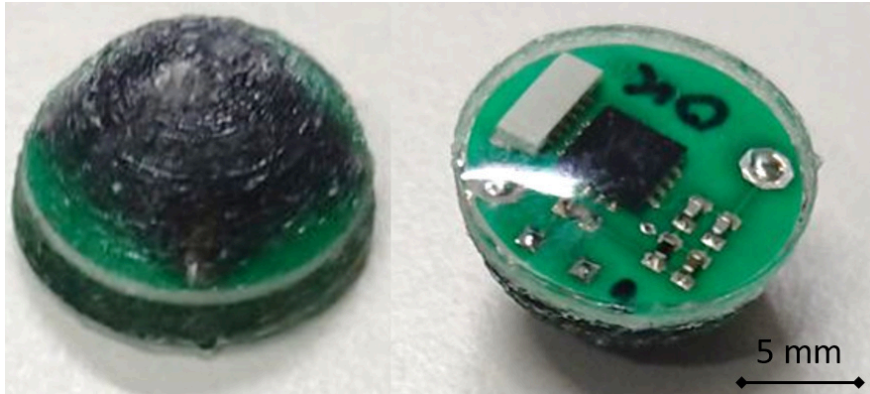


Figure 3: Molded RFID sensor tag with antenna, RFID transceiver, microcontroller and accelerometer

Experiments were carried out to analyse the radio performance of the configured RFID tags. First, the sensors were placed in additively manufactured, cube-shaped containers made of aluminium. The containers were then closed with a lid and insulated at the edges of the lid. The radio connection to the sensor tag was analysed. The tests showed that closed metal walls cannot be penetrated at the RFID frequency of 134.2 kHz (LF range) used. The root causes are considered to be absorption and reflexion as well as the detuning of the transmitting and receiving antennas due to the metal in their near field. In order to be able to establish a radio connection between the RFID sensor tags, a small opening must be provided in the AM component.

For this purpose, experiments were carried out on sparking through different hole geometries such as bores, simple slots and star-shaped slots. Figure 4 shows additively manufactured sensor cavities made of AlSi10Mg with different downward-oriented hole geometries.

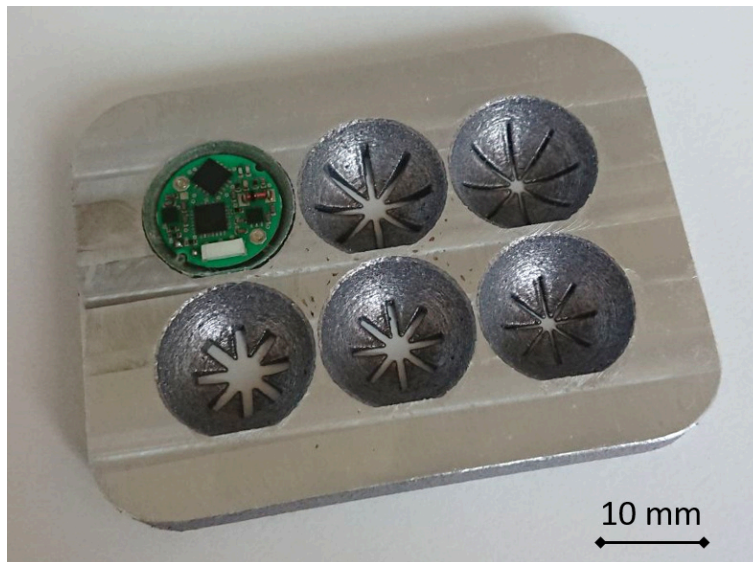


Figure 4: AM component with varied star-shaped slot geometries for investigating RFID communication

The RFID tag was inserted into the cavity. The sensor antenna was aligned in the direction of the hole geometry. The cavity was then closed with a lid and insulated. The tests showed that simple holes and slots are not suitable for establishing a radio connection. Star-shaped slot geometries, on the other hand, are suitable for achieving reliable RFID communication with slot lengths of 12 mm or more. However, the communication range is limited to a maximum of 10 mm here.

5. Continue the Building Process Above the Integrated Sensors

During the AM process, the sensors are exposed to different thermal influences from which they have to be protected. These influencing factors include the component heated during the building process, hot metal powder, weld spatter and the effect of the laser beam when exposing the powder bed. The temperature in the construction space itself is 40-60°C during the process. The epoxy resin potting system protects the sensor tags from damage caused by the process heat. In addition, the circuit board is protected from electrically conductive metal dust, which prevents short circuits during sensor operation.

In order to investigate the effect of laser exposure on the epoxy resin, 12 rectangular shell geometries measuring 24x24x7 mm³ with internal cavities measuring 20x20x2 mm³ were produced using the PBF-LB/M process. Six of the cavities were freed of metal powder within the system and then filled with different synthetic resins. The other six samples were left powder-filled for evaluating the process parameters directly in the powder bed. Metal powder was then applied over the samples and exposed. The exposure results are shown in Figure 5. A closed top layer could be created over the powder-filled cavities. On the samples filled with epoxy resin, instead of forming a top layer, the casting compound was removed, particularly in the areas of the strip overlap. The plasma column during exposure was so intense over the casting compounds that the experiment stopped after three layers.



Figure 5: Cast cavities after exposure; grey surface - powder cavities; dark surface - cavities with epoxy resin

To protect the upper surface of the casting compounds from laser application, tests were carried out with various metal adhesive tapes. For this purpose, hemispherical sensor dummies were made from casting compound and covered with aluminium adhesive tape (0.2 mm), aluminium-bitumen-tar adhesive tape (1.7 mm) or copper adhesive tape (0.2 mm). Appropriate geometries with cavities for the dummies were manufactured on the PBF-LB/M machine and the powder was removed afterwards. After inserting the dummies, the cavities were filled with powder up to the top edge and then exposed. The laser beam was reflected so strongly over the copper adhesive tape that no solid top layer could be created. The aluminium-bitumen-tar adhesive tape was partially removed by the laser. A solid top layer could only be created over the aluminium adhesive tape with a material thickness of 0.2 mm. Nevertheless, there was no solid connection to the cover layer created because the powder layer in between was not completely melted. Light microscopic examinations of the micrographs showed that in all cases the casting compounds remained undamaged. The cut samples are shown in the figure 6.



Figure 6: Cut samples with glued sensor dummies; left - with aluminium adhesive tape; centre - with copper adhesive tape; right - with aluminium-bitumen-tar adhesive tape

In order to guarantee a solid connection to the sensor surface, aluminium plates should be fixed to it. Therefore tests were carried out in which 1 mm thick aluminium plates were inserted into additively manufactured cavities and then exposed with a 90 μm parameter set. During the process, the aluminium plates bulged slightly downwards due to the heat input. Nevertheless, a continuous connection could be detected above plates. Light microscopic examinations of cut samples revealed a remelting depth of up to 0.6 mm in the metal plates (Figure 7). The material density above the metal plates was around 99.75%.

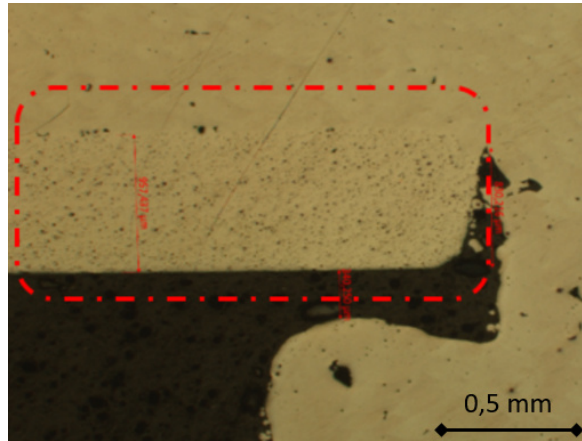


Figure 7: Microscopic micrograph of an integrated 1mm thick aluminium plate in an additively manufactured cavity

During the coating process, fundamental forces can occur on the sensor which can lead to a change in position or damage to the sensor. In order to counteract the resulting twisting and tilting of the sensor within the cavity, a functional geometry was developed for the surrounding casting compound. The geometry limits the six degrees of freedom and thus guarantees a fixed position of the sensor within the cavity. In addition, the geometry supports the correct placement of the sensor. Free fall tests were carried out to investigate self-alignment. The potting geometries produced using Fused Deposition Modeling (FDM) were held 10 mm above additively manufactured test cavities by means of suction cups and then dropped.

The sensors were rotated around the z axis with regard to the storage position and were also held horizontally at different angles. The experiments were validated with different holding positions and repeated five times. With a maximum rotation around the z axis of 30°, the sensor automatically aligns itself up to a maximum tilt of 20° when it falls into the cavity. The outer diameter of the molded sensors is 24 mm.

In the next step, ready-to-use RFID tags were cast in moulds made of water-soluble polyvinyl alcohol (PVA) using FDM. The sensors were first fixed to aluminium plates and then placed in the moulds filled with epoxy resin. After the material had hardened, the moulds have been dissolved in a water bath. The final sensor shape with aluminium plate is shown in Figure 8.

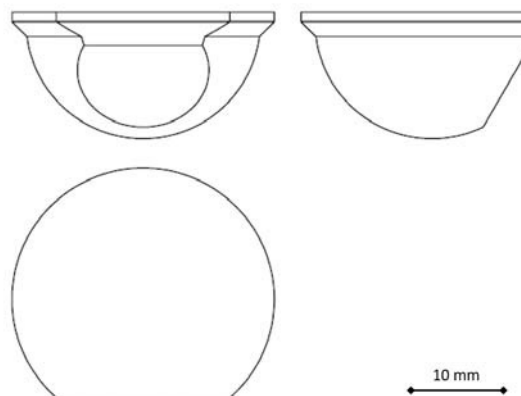


Figure 8: Normal projection of the final geometry of the moulded RFID sensor tag with aluminium plate

Specific geometries with integrated cavities were produced on the PBF-LB/M machine with a layer thickness of 50 μm , whereby the build process was interrupted shortly before the cavities were closed. The powder was then removed from the inside of the cavities. After inserting the moulded sensors, the build process was continued with a layer thickness of 90 μm . Due to the energy input and the inability to move downwards, the aluminium plates bent upwards, bringing the coater to a halt and interrupting the build process. To minimise this effect, design adjustments were made in the following tests to prevent the plates from lifting. In this process, 3 small exterior rings were additively manufactured in the three layers above the plates to fix them in their position. This successfully prevented excessive bulging of the plate. In the upper layers, a surface exposure was then made, in which the powder was melted down to the plates. A cut sample with an integrated, solid connected sensor dummy is shown in Figure 9.

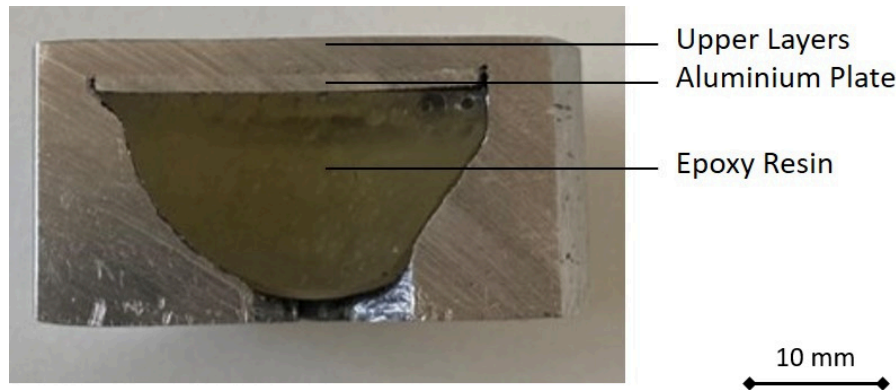


Figure 9: Cut sample with solid connected sensor dummy

The final design involved initially building up 10 layers with a thickness of 90 μm after the aluminium plates have been inserted. The building process was finally continued with a layer thickness of 50 μm . It is well known that the stiffness values of PBF-LB/M materials decrease with increasing layer thickness. Therefore, lower strengths were expected in the 90 μm range, in addition to the internal stresses that result. Before manufacturing, the test sample was sliced in the two layer thicknesses and the relevant slicing file was loaded into the machine's operating software before each restart of the building process. After the sensor integration was completed, the signal transmission of the sensors through star-shaped slots positioned on the bottom of the test specimen was analysed again. The aim was to validate the functionality after the hard connection. However, it was established that there were no functional limitations to the sensors.

6. Conclusions and Outlook

In this work, a concept for integrating RFID tags into PBF-LB/M components made of AlSi10Mg was developed. Robust process windows for layer thicknesses of 50 μm and 90 μm were generated. The 50 μm parameter set achieved maximum tensile strengths of 460 MPa. Heat treatment was analysed but excluded because of the negative effects on the sensor. RFID sensors with an LF frequency of 134.2 kHz were selected. As the radio connection could not be established through closed component walls, a possibility was found to transmit through star-shaped slots. The sensors were encapsulated in epoxy resin. One aim was to achieve a solid connection between the sensor and the metal component. Tests showed that the laser destroys the epoxy resin. To protect the moulded sensor from the laser exposure and to produce a solid connection, sensor dummies were covered with various metal adhesive tapes. The tests showed that a solid metal layer could only be created over aluminium adhesive tape. Afterwards single aluminium plates were tested. The plates were remelted up to 0.6 mm. Following this, encapsulated sensors were provided with aluminium plates with a thickness of 1 mm on the upper side and then integrated into the component. The upward bending of the plates was prevented by an outer ring which was first additively manufactured above to create a connection to the component. Finally the material on top could be completely remelted. This created a hard connection to the sensor. Increasing the layer thickness to 90 μm in the area above the RFID tag reduced the energy input to the sensor. The functionality of the sensors could be validated after the building process. The outer geometry of the moulded sensor was chosen to allow a certain degree of self-alignment when inserted into a cavity.

By integrating RFID sensors into PBF-LB/M components, they can be equipped with new, extended functions. In addition to the saving of data, the measurement of component states and positions is particularly important. To enable direct radio connection through closed component walls further possibilities for signal transmission should be investigated.

There is still a significant need for research, especially regarding the optimisation of material strength in the area of sensor connection. In addition, the solid connection of sensors in components made of other materials should be investigated in more detail.

7. Acknowledgement

Our heartfelt thanks go to the Federal Ministry of Economic Affairs and Climate Protection (BMWK) for providing financial resources of the IFUNK research project (IFUNK - Process design and design concepts for in-situ-functionalised AM components) as part of the aviation research program (LuFo VI).

8. References

- [1] Binder, M.; Kirchbichler, L.; Seidel, C.; Anstaett, C.; Schlick, G.; Reinhart, G.: „Design Concepts for the Integration of Electronic Components into Metal Laser-based Powder Bed Fusion Parts“, *Procedia CIRP*, vol. 81, pp 992-997, 2019, doi: 10.1016/j.procir.2019.03.240.
- [2] Hehr, A.; Norfolk, M.; Wenning, J.; Sheridan, J.; Leser, J.; Leser, P.; Newman, J.A.: „Integrating Fiber Optic Strain Sensors into Metal Using Ultrasonic Additive Manufacturing“, *JOM*, 70 (2018), pp 315–320.
- [3] Norfolk, M.; Wenning, J.; Hehr, A.; Johnson, H.: „3D Printing Embedded Sensors Using Solid State Welding“, Berlin, 2016.
- [4] Stoll, P.; Leutenecker, B.; Spiering, A.; Klahn, C.; Wegener, K.: „Temperature Monitoring of a SLM Part with Embedded Sensor“, *Industrializing Additive Manufacturing - AMPA 2017* (2017).
- [5] Pille, C.: „In-Process Embedding of Piezo Sensors and RFID Transponders into Cast Parts for Autonomous Manufacturing Logistics“, in: T. Gessner (Hrsg.), *Smart Systems Integration 2010: 4th European Conference & Exhibition on Integration Issues of Miniaturized Systems*, 23.–24. März 2010, Como, Italien, Berlin Offenbach: VDE Verlag GmbH, 2010, pp 1–10.
- [6] Sehrt, J.T.; Witt, G.: „Additive Manufacturing of smart parts and medical instruments“, *Proceedings of AEPR'12, 17th European Forum on Rapid Prototyping and Manufacturing*, 2012.
- [7] Buchbinder, D.; Meiners, W.; Wissenbach, K.; Poprawe, R.: „Selective laser melting of aluminum die-cast alloy—Correlations between process parameters, solidification conditions, and resulting mechanical properties“, *Journal of Laser Applications*, vol. 27, p 29205, 2015, doi: 10.2351/1.4906389.
- [8] Van Cauwenbergh, P.; Samaee, V.; Thijs, L.; Nejezchlebová, J.; Sedlák, P.; Iveković, A.; Schryvers, D.; Van Hooreweder, B.; Vanmeensel, K.: „Unravelling the multi-scale structure–property relationship of laser powder bed fusion processed and heat-treated AlSi10Mg“, *Scientific Reports*, vol. 11, 2021, doi: 10.1038/s41598-021-85047-2.

Design and fabrication of a TPMS-based micro heat exchanger via micro selective laser melting

Heinrich, F.; Reuter, J.; Erler, M.; Streek, A.
Lasereinstitut Hochschule Mittweida, Mittweida

Abstract

The use of Triply Periodic Minimal Surfaces (TPMS) for high-efficiency heat exchangers is emerging as a key area in additive manufacturing. TPMS lattices, such as the gyroid, provide excellent thermal and structural properties due to their high surface area-to-volume ratio, strength, and low material use. With advanced techniques like micro selective laser melting (Micro-SLM), developed at the Lasereinstitut Hochschule Mittweida (LHM), it is now possible to fabricate these complex TPMS structures, which were not feasible with traditional methods. In this study, we demonstrate that manufacturing TPMS lattices with feature sizes as small as 100 μm via Micro-SLM significantly enhances heat exchanger performance, achieving heat transfer coefficients up to 12 $\text{kW}/(\text{m}^2\cdot\text{K})$, over 300% higher than conventional plate heat exchangers. We examine the resolution of thin walls in these lattices and apply it to TPMS fabrication. Leakage tests confirm that these structures can withstand pressures up to 8 bar without leaks. Three heat exchangers were built, tested, and compared with a microchannel heat exchanger, confirming the superior thermal efficiency of TPMS designs.

1. Introduction

The rapid advancements across nearly all technological fields in recent years have resulted in a significant increase in energy consumption. However, many of the newly developed systems and devices do not utilize energy efficiently. As a result, excess heat is often generated as a byproduct, which must be effectively dissipated to maintain optimal performance. This challenge is evident in various applications, such as chips and integrated circuits, batteries in electric vehicles, gas turbines in airplanes, and nuclear power plants [1-5]. This is where heat exchangers come into play. Heat exchangers are devices specifically designed to transfer heat between two fluids of different temperatures without mixing them. Conventional types of heat exchangers, including tubular heat exchangers, plate heat exchangers, shell and tube heat exchangers, and printed circuit heat exchangers [6,7], are increasingly unable to meet the stringent requirements for compactness and power density, particularly in applications where lightweight design is crucial, such as in aerospace and e-mobility [6,8].

Lately, structures known as triply periodic minimal surfaces (TPMS) have emerged as a promising approach to enhance the performance of heat transfer devices [9-12]. Minimal surfaces, which locally minimize their surface area, can be visualized most easily as the shapes formed by a soap film within a wire frame. Minimal surfaces that repeat periodically and extend infinitely in all three spatial directions are referred to as TPMS, with examples including the gyroid, Schwarz diamond, and Schwarz primitive structures (Fig. 1). Because of their characteristic of dividing space into two separated yet intertwined volumes and their high surface-area-to-volume ratio they have become a focus point of recent research regarding their heat transfer capabilities [9-12]. Due to their complex structure, TPMS have long been nearly impossible to manufacture using conventional methods. However, with the emerge of additive manufacturing (AM) technologies, we can now fully exploit the unique characteristics of TPMS. Many recent studies have explored the fabrication of TPMS heat exchangers via selective laser melting (SLM), a process where parts are built layer by layer using a high-powered laser to selectively fuse metal powder particles with the resolution of this process being determined by the particle size as well as the focus diameter of the laser. TPMS lattices with wall thicknesses between 0.2 and 0.5 mm and unit cell sizes ranging from 3.33 to 10 mm have been successfully fabricated, demonstrating the anticipated enhancement in heat transfer efficiency [9,10,13]. To further optimize the performance of TPMS heat exchangers, it is essential to reduce both the wall thickness and unit cell size. This paper will focus on the design and fabrication of TPMS based micro heat exchangers using the process of micro selective laser melting (Micro-SLM) [14], aiming

to achieve these reductions and evaluate their impact on heat transfer performance. Therefore, the results of preliminary studies on the achievable wall thicknesses and their application in producing leakage-free TPMS structures are presented. Building on these findings, the design, fabrication, and thermal performance testing of micro heat exchangers will be discussed.

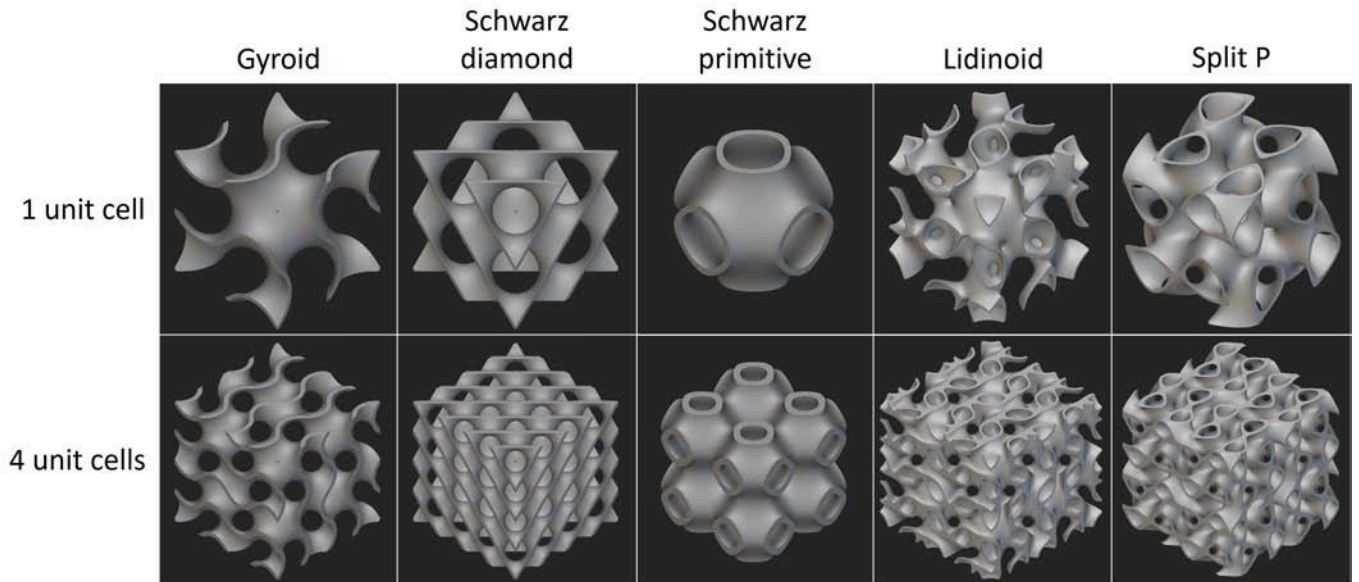


Figure 1: Different types of TPMS lattices displayed with one cubic unit cell and four (2x2) cubic unit cells.

2. Machine and material

All experiments were conducted using a custom-built Micro-SLM machine. The machine is equipped with a 400 W fiber laser from IPG Photonics, with the laser beam focused to a diameter of 23 μm using an f-theta optic. A galvanometer scanner, capable of a maximum scanning speed of 8 m/s, was used for beam deflection. Prior to each build job, the process chamber was purged with argon, reducing the oxygen content to 1000 ppm to ensure an inert atmosphere. The material used was stainless steel 316L powder from Sandvik Osprey, with a particle size distribution of $d_{90} = 10 \mu\text{m}$ (Fig. 2). Despite the particles being nearly spherical, the powder exhibited a tendency to agglomerate, which could disrupt the recoating process. To mitigate this issue, the powder was compacted within the recoater to prevent agglomeration.

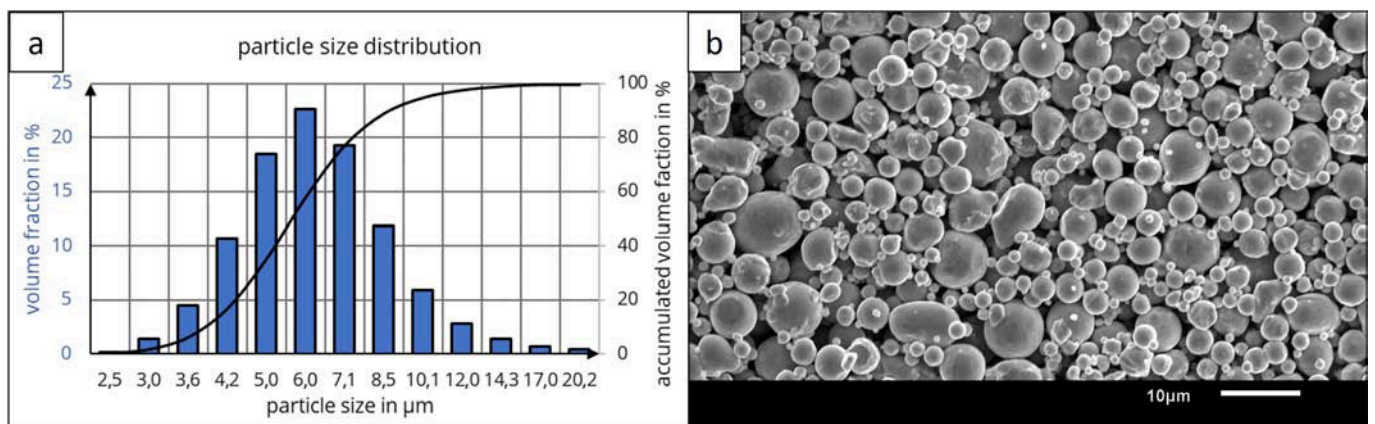


Figure 2: a) Particle size distribution and b) SEM image of the stainless steel 316L powder used in this paper.

3. Manufacturing of thin walled TPMS structures

3.1. Wall thickness

To determine the manufacturable wall thicknesses, a parameter study was conducted to examine the influence of laser power and scan speed on the thickness of single-line walls. The test samples comprised ten sets of three walls with a height of 0.4 mm each, where all three walls in a set were produced using the same laser power and scan speed, with each set being generated at different laser powers but consistent scan speeds. Separate test samples were built for each scan speed. The walls were constructed on a sub-structure with a height of 1 mm, ensuring that the test samples could be safely removed from the substrate via diamond wire cutting without damaging the walls. The parameters used in this study are detailed in Table 1. It must be noted that the specific laser power range used for each scan speed varies as the process window changes with varying scan speeds. The laser powers used for each scan speed are shown in Figure 4.

Table 1: Process parameters investigated in the parameter study for the fabrication of thin walls.

Process parameter	Value
Layer thickness in μm	10
Scan speed in m/s	0.5, 0.75, 1, 1.5, 2
Laser power in W	16 – 94

The manufactured test samples were cleaned in an ultrasonic bath to remove any residual powder. Before embedding the samples in epoxy resin for cross-sectional analysis, scanning electron microscopy (SEM) images were taken to examine the morphology of the melt tracks. The wall thickness was measured from the cross-sections using a laser scanning microscope, specifically the Olympus LEXT OLS4000. The measurement results are presented in Fig. 3. To facilitate a more accurate comparison across different scan speeds, the line energy E_L is plotted along the horizontal axis, as it accounts for both the laser power and scan speed according to the formula:

$$E_L = \frac{P_{av}}{v_s}$$

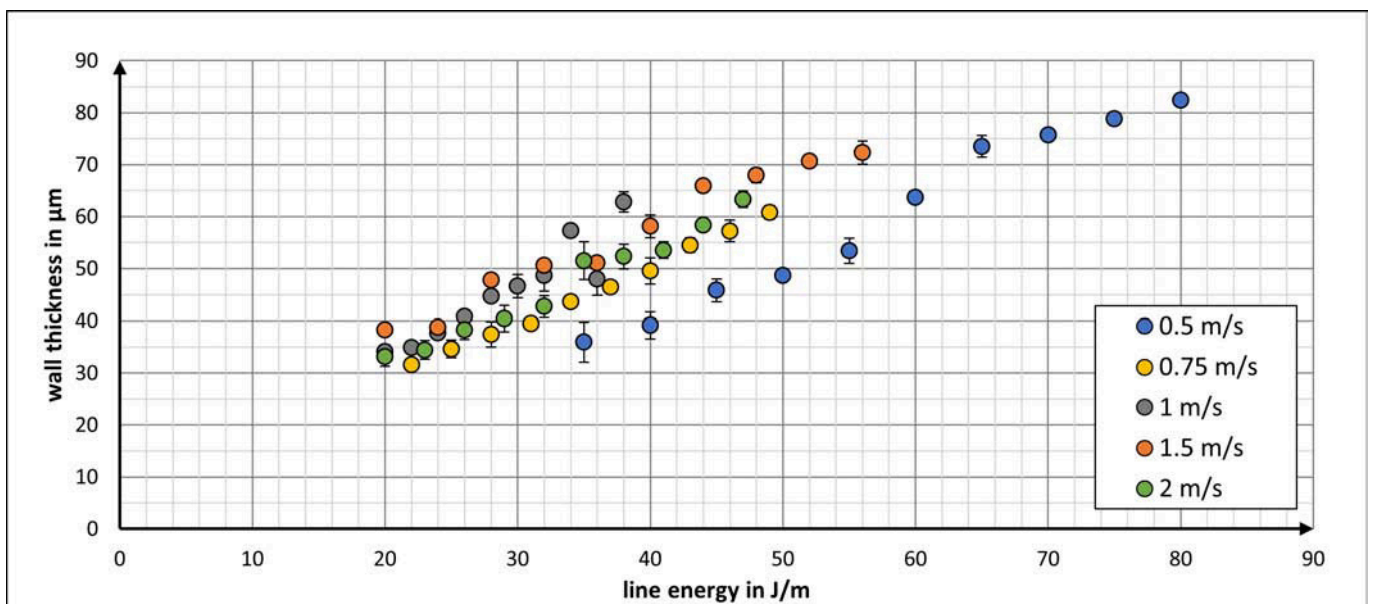


Figure 3: Wall thickness of single-track walls as a function of line energy and scanning speed.

The measured wall thickness ranges from 32 to 82 μm . The minimum wall thickness, observed across all scan speeds, is between 32 to 38 μm . Thinner walls generated with less line energy were either severely damaged during the recoating process or could not be generated at all because of lack of fusion with the previous layer. This consistency suggests that either the focus diameter or the particle size, or potentially both, are limiting the fabrication of thinner walls. As the line energy increases, the wall thickness also increases. Predictably, the thickest single-line walls were produced with a scan speed of 0.5 m/s. Additionally, the melt tracks of walls generated at this scan speed exhibited the smoothest and most continuous morphologies, as shown in Fig. 4. In contrast, higher scan speeds tended to produce discontinuous melt tracks resembling balling, a phenomenon typically associated with either insufficient laser power or excessively high layer thickness [15]. However, since these irregular melt track morphologies appeared nearly independent of the laser power, the exact cause of this pronounced difference remains unclear.

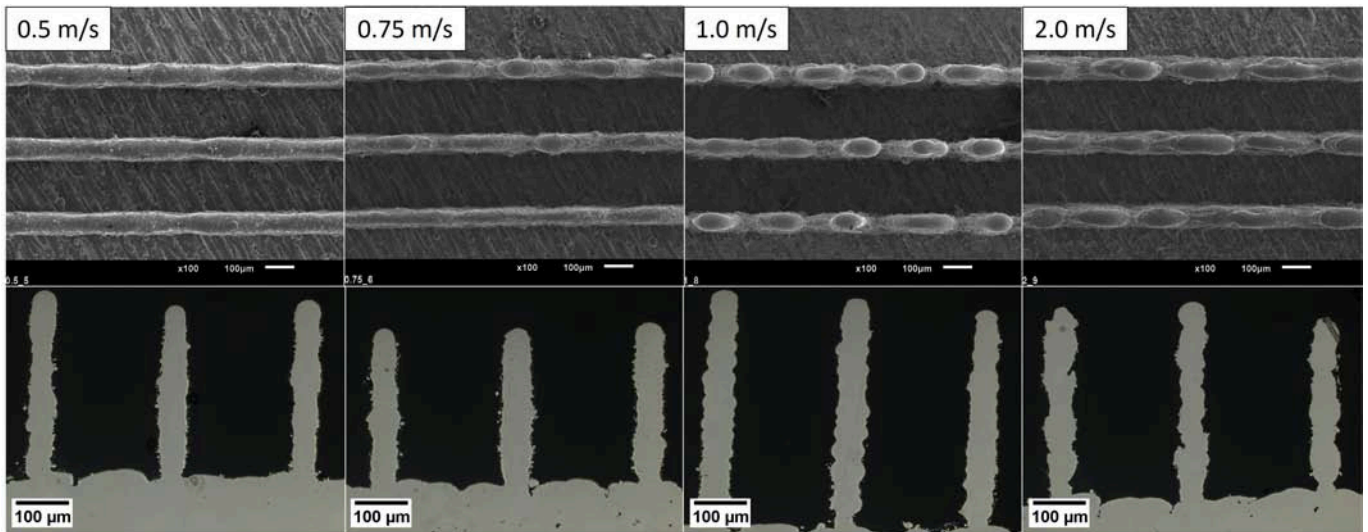


Figure 4: SEM- and cross-section-images of single walls with a thickness of approximately 60 μm generated with scan speeds of 0.5, 0.75, 1.0 and 2.0 m/s.

Examination of the cross-section images revealed that nearly all walls were free of pores and generally maintained a consistent thickness throughout the build height (Fig. 4). However, walls with thicknesses below 40 μm were found to be less stable, with some exhibiting slight bending, likely due to the cleaning process or sample transportation. For all subsequent investigations, a scan speed of 0.5 m/s was selected, as it provided the largest process window and resulted in the smoothest and most homogeneous melt tracks. The line energy was set at 65 J/m but was occasionally reduced to 50 J/m to prevent excessive overheating, particularly when generating smaller TPMS unit cell sizes.

3.2. TPMS structures

When looking at the most common TPMS lattices it becomes clear that they not only consist of thin vertical walls but rather a continuous change between vertical as well as horizontal walls (bridges), so it is necessary to investigate how the results of the previous chapter translate to the manufacturing of TPMS lattices.

Designing TPMS structures using conventional CAD software is challenging due to their complex geometries, which are best represented through mathematical formulas primarily composed of trigonometric functions. To overcome this, implicit design methods are employed using specialized software. In this investigation, nTopology was used, which allows for the straightforward adjustment of lattice types and geometric characteristics such as unit cell size and wall thickness.

Test samples measuring 8 x 8 x 8 mm³ were generated, incorporating two different TPMS types: gyroid and Schwarz diamond. These are the most studied lattices in the context of additive manufacturing for

TPMS heat exchangers. The wall thickness was set at 100 μm . Although thinner walls are feasible, as demonstrated in the previous chapter, the thickness of the bridges of the lattice are constrained by the layer thickness, which was kept constant at 10 μm . To ensure the reliable generation of these horizontal features, it was determined that at least ten solid material layers should be used. The generation of thicker walls poses the problem of requiring hatching vectors to fill the gap which forms between the contours. These short vectors can lead to overheating, potentially damaging the lattice, and significantly increasing the time required to process each layer. Therefore the 100 μm walls are generated only with two contour lines with the parameters determined in the previous chapter. The unit cell sizes were cubic, with edge lengths of 1, 2, and 3 mm.

Both TPMS types and every unit cell size could be manufactured without issues during the built process. For the removal of residual powder inside the lattices the ultrasonic bath was not sufficient especially for the smallest unit cell size. Instead, pressurized air was used after the samples were dried for an hour at a temperature of 120 $^{\circ}\text{C}$ to reduce the agglomeration of the powder particles.

Fig. 5 shows SEM- and cross-section images of the generated structures. The examination of the fabricated TPMS structures revealed no inherent pores or defects, neither in the vertical walls nor in the horizontal bridges of the lattice. Notably, the bridges were generated using the infill parameter (hatching) rather than the contour (thin wall) parameter, which was initially thought to increase their susceptibility to defects. However, no such defects were observed. Cross-sectional images indicated a higher surface roughness on the downskin areas, particularly on the bridges. This increased roughness is likely due to the sintering of powder particles to the underside of the structure and could potentially impact the heat transfer efficiency of the final heat exchanger.

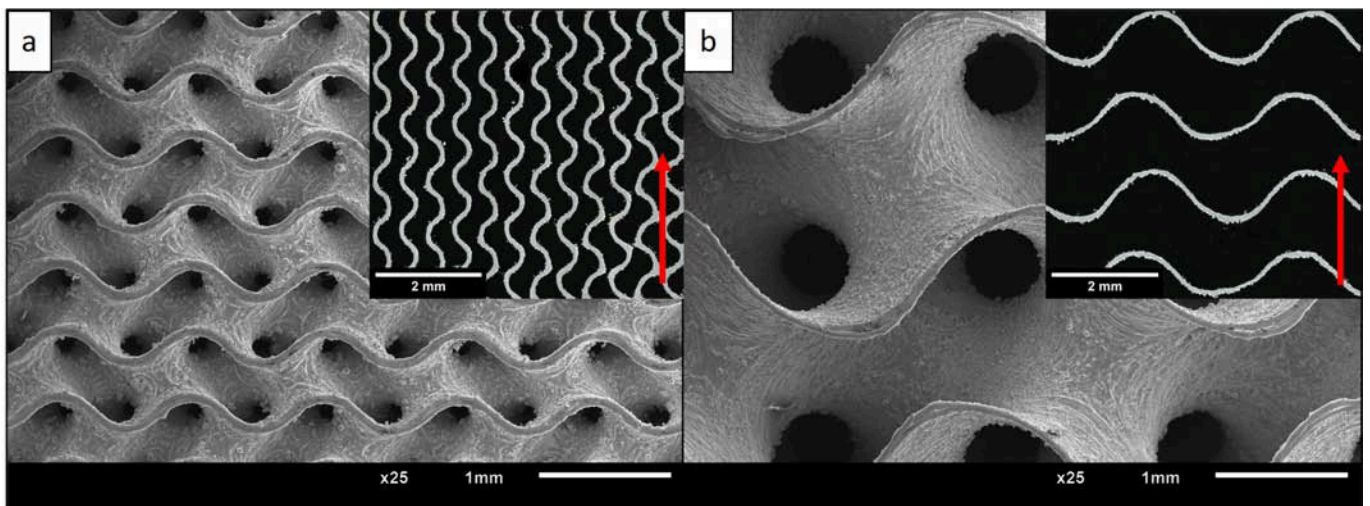


Figure 5: SEM- and cross-section images with of gyroid lattices with a) 1 mm unit cell size and b) 3 mm unit cell size. The red arrows in the cross-section images show the build direction.

3.3. Leakage Test

To further investigate the quality of the generated TPMS lattices samples were fabricated to detect possible leakages inside the structures. Cuboidal lattices with gyroid and Schwarz diamond structures each with a base edge length of 8 mm and a height of 6 mm were generated for the experiments. One side of the fluid channel was sealed with baffles, allowing fluid access solely through an inlet located at the top of the lattice. The opposing fluid side was similarly sealed with baffles at the inlet, ensuring that when pressurized air was applied, only one side of the lattice could be filled with air, as seen in Fig. 6. If the lattice is leakage-free, no air should escape from the structure. The baffle thickness was set to 100 μm .

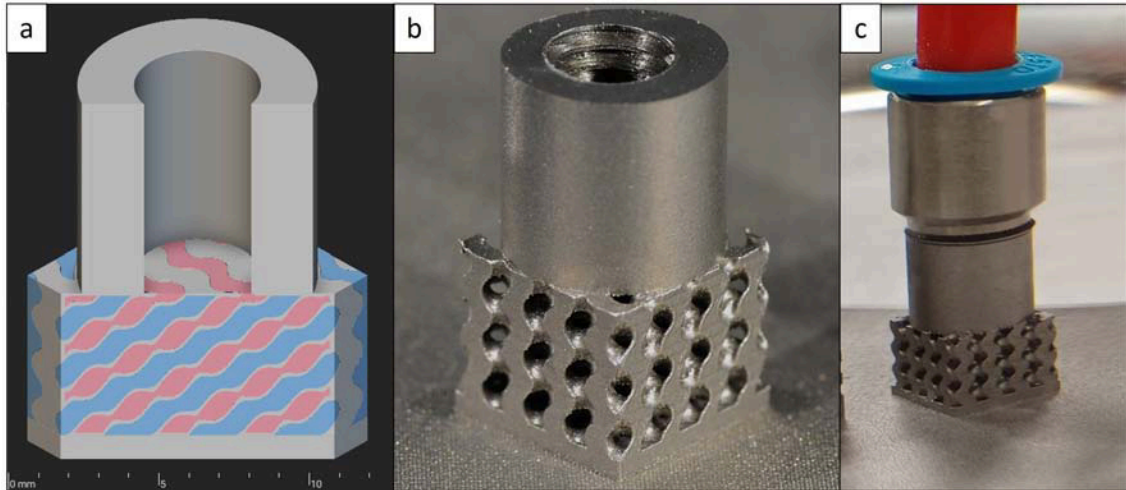


Figure 6: Sample design for the leakage test: a) Cross-sectional view of the test sample with cold (blue) and hot (red) fluid side, b) Manufactured test sample, c) Leakage-free test sample with applied pressurized air submerged in water.

For both gyroid and Schwarz diamond TPMS lattices, six samples were manufactured across three separate build jobs to evaluate repeatability. After fabrication, the samples were cleaned of residual powder using pressurized air, and threads were cut into the inlets. For leakage testing, pressurized air at 8 bar was applied through the inlet while the samples were submerged in water. A sample was considered leakage-free if no visible bubbles appeared within a 2-minute observation period.

The results of these tests are summarized in Table 2. The gyroid lattice samples were predominantly leakage-free, with only one exception, whereas all Schwarz diamond samples exhibited leakage across the first two build jobs. Despite a thorough analysis, no inconsistencies were detected during the build process, making it difficult to pinpoint where the leakage was occurring within the structure. However, in the third build job, all samples, including the Schwarz diamond lattices, were leakage-free. Due to its more consistent performance, the gyroid lattice was ultimately selected for the heat exchanger design.

Table 2: Leakage test results with qualitative evaluation.
 "O" indicates a leakage-free sample, while "X" denotes a detected leakage.

	Gyroid		Schwarz diamond	
Build job	Sample 1	Sample 2	Sample 1	Sample 2
1	O	O	X	X
2	X	O	X	X
3	O	O	O	O

4. Heat exchanger

4.1. Design and manufacturing

The design of the heat exchanger is based on a crossflow microchannel heat exchanger previously developed at the Laserinstitut Hochschule Mittweida and will be used for comparing the TPMS heat exchangers to a more conventional design. The microchannels have a cross-sectional area of 200 x 3000 μm^2 and a wall thickness of 100 μm . To enable support-free manufacturing, the end baffles were designed at a 45° angle, ensuring that downfacing features could be printed without the need for additional supports. The inlets and outlets were designed to allow for tube welding, which permitted the outer body of the heat exchanger (excluding the active heat transfer structures, such as the microchannels) to be minimized, achieving a wall thickness of approximately 1 mm. Fig. 7 shows the CAD-model with the visible inner structure and the manufactured heat exchanger with welded tubes and compression fittings.

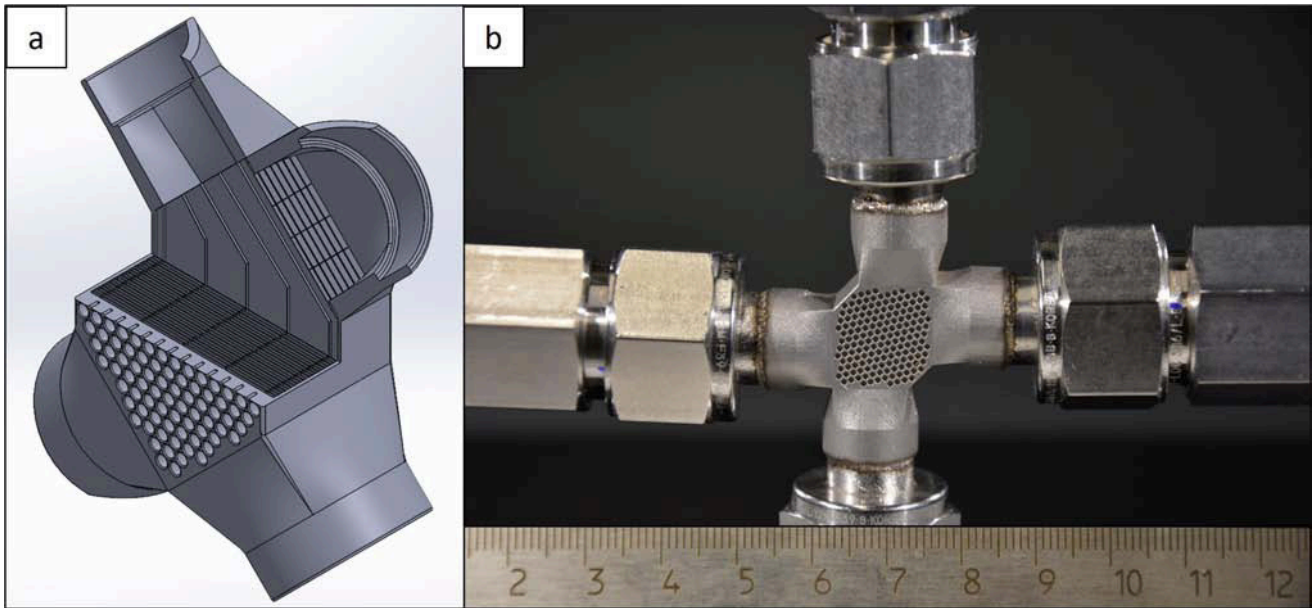


Figure 7: Design of the crossflow microchannel heat exchanger: a) Cross-sectional view of the CAD-model, b) Manufactured heat exchanger with welded tubes and compression fittings.

The updated design replaces tube welding with threaded connections for push-in fittings, necessitating a thicker outer body and larger inlet and outlet diameters to avoid damage to the heat exchanger during thread cutting (Fig. 8a, 8d). Critical downskin angles below 45° were minimized by utilizing the full 40 mm build chamber height. The outer body was designed using SolidWorks, while the lattice structure was generated in nTopology. The design of the inlet and outlet baffles turned out to be critical, as downfacing angles of 45° presented challenges for certain unit cell sizes, leading to potential overhang formation at the lattice edges (Fig. 8b, 8c). To avoid this, only unit cell sizes of 0.975 mm, 1.975 mm, and 2.51 mm were selected, as these did not require support structures. The baffle thickness was set at 100 μm, equal to the lattice wall thickness, as infill within the baffles caused overheating and posed a risk of recoater damage during the build process.

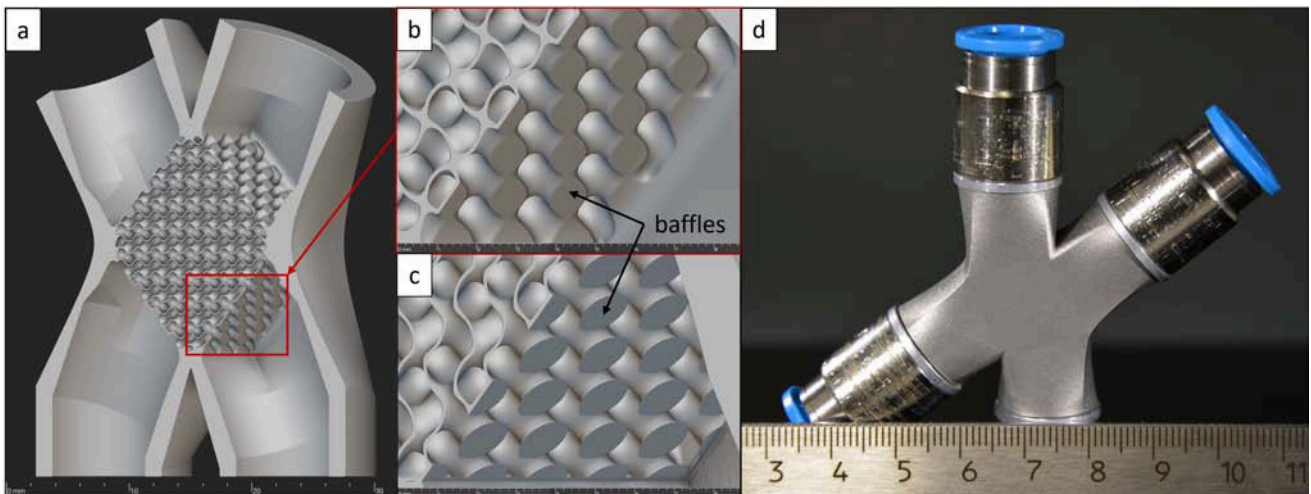


Figure 8: Design of the TPMS heat exchangers: a) Cross-sectional view of the heat exchanger featuring a unit cell size of 1.975 mm, b) Detailed view of inlet baffles designed for support-free printing, c) Example of baffles with overhanging sections, d) Final manufactured heat exchanger with push-in fittings installed.

It was more challenging to remove residual powder from the heat exchangers with smaller unit cell sizes in the lattice. To effectively apply compressed air without losing pressure, the threads needed to be cut first to allow connection through the push-in fittings. Compressed air was then applied to all inlets and outlets

multiple times until no more powder was expelled from the heat exchanger. Since water was used to measure heat transfer performance, the same cleaning procedure was repeated with water after the air cleaning. However, it cannot be guaranteed that all residual powder was fully removed. Advanced measurement techniques, such as microtomography, would be required to confirm complete powder removal.

4.2. Heat transfer performance

To evaluate the heat transfer performance of the heat exchangers, a test stand was constructed. Water was used as the working fluid, sourced from two faucets. Hot water was supplied by an instantaneous water heater with a maximum temperature of approximately 45°C and a flow rate between 80 to 120 l/h. The cold water temperature, determined by outdoor conditions, typically ranged from 15 to 20 °C. Despite these fluctuations, the temperature remained relatively stable on any given day. Fluid temperatures were measured using Pt100 temperature sensors, while the flow rates were monitored using two variable area flow meters. Additionally, the pressure drop across the heat exchanger was recorded using a differential pressure gauge.

Prior to testing the thermal performance, a leakage test was performed with compressed air. Unexpectedly, all three TPMS heat exchangers exhibited leakage, whereas the microchannel heat exchanger was leakage-free. These results differed from previous tests, possibly due to the limited number of prior samples or design-related issues, such as potential weak points in the baffles or the connection between the thin-walled lattice and the thicker outer body. The exact source of the leakages could not be identified without more advanced measuring methods such as microtomography.

A water-based leakage test revealed that heat exchangers with smaller unit cell sizes had minor leakages, amounting to 1 – 2 drops of water per minute at a pressure of 5 bar. Given the low volume of fluid loss, it was concluded that the thermal performance tests could proceed with minimal impact on the overall results.

To evaluate the thermal performance of the heat exchangers, the overall heat transfer coefficient h was calculated using the following formula:

$$h = \frac{Q}{A \cdot \Delta T_{lm}}$$

where Q is the total heat transfer rate in W, A is the effective heat transfer surface area in m² and ΔT_{lm} is the logarithmic mean temperature difference. The total heat transfer rate is calculated according to the formula:

$$Q = \dot{V} \cdot \rho \cdot c_p \cdot (T_{hot_in} - T_{hot_out})$$

where \dot{V} is the volume flow rate in m³/s, ρ is the density of water with 998 kg/m³, c_p is the specific thermal capacity of water with 4187 J/(kg·K) and T_{hot_in} and T_{hot_out} are the temperatures of the fluid at the hot inlet respectively the hot outlet in °C. The logarithmic mean temperature difference for counterflow regime is calculated according to the formulas:

$$\Delta T_{lm} = \frac{\Delta T_1 - \Delta T_2}{\ln\left(\frac{\Delta T_1}{\Delta T_2}\right)}$$

$$\Delta T_1 = T_{hot_in} - T_{cold_out}$$

$$\Delta T_2 = T_{hot_out} - T_{cold_in}$$

The results of the thermal performance measurements are shown in Fig. 9. The highest overall heat transfer coefficient, as well as the highest pressure drop, was measured with the smallest unit cell size of 0.975 mm, yielding values of 12.64 kW/(m²·K) and 415 mbar, respectively. For comparison, the VDI Heat Atlas provides benchmark values of up to 1.2 kW/(m²·K) for shell-and-tube heat exchangers and 4 kW/(m²·K) for plate heat exchangers in water-to-water applications [16].

These benchmark values were surpassed by the tested heat exchangers with unit cell sizes of 1.975 mm and 2.51 mm, as well as the microchannel heat exchanger. An increase in unit cell size resulted in a lower overall heat transfer coefficient but also a lower pressure drop. For example, heat transfer coefficients exceeding 8 kW/(m²·K) were achieved with a pressure drop of 100 mbar for the 2.51 mm unit cell size.

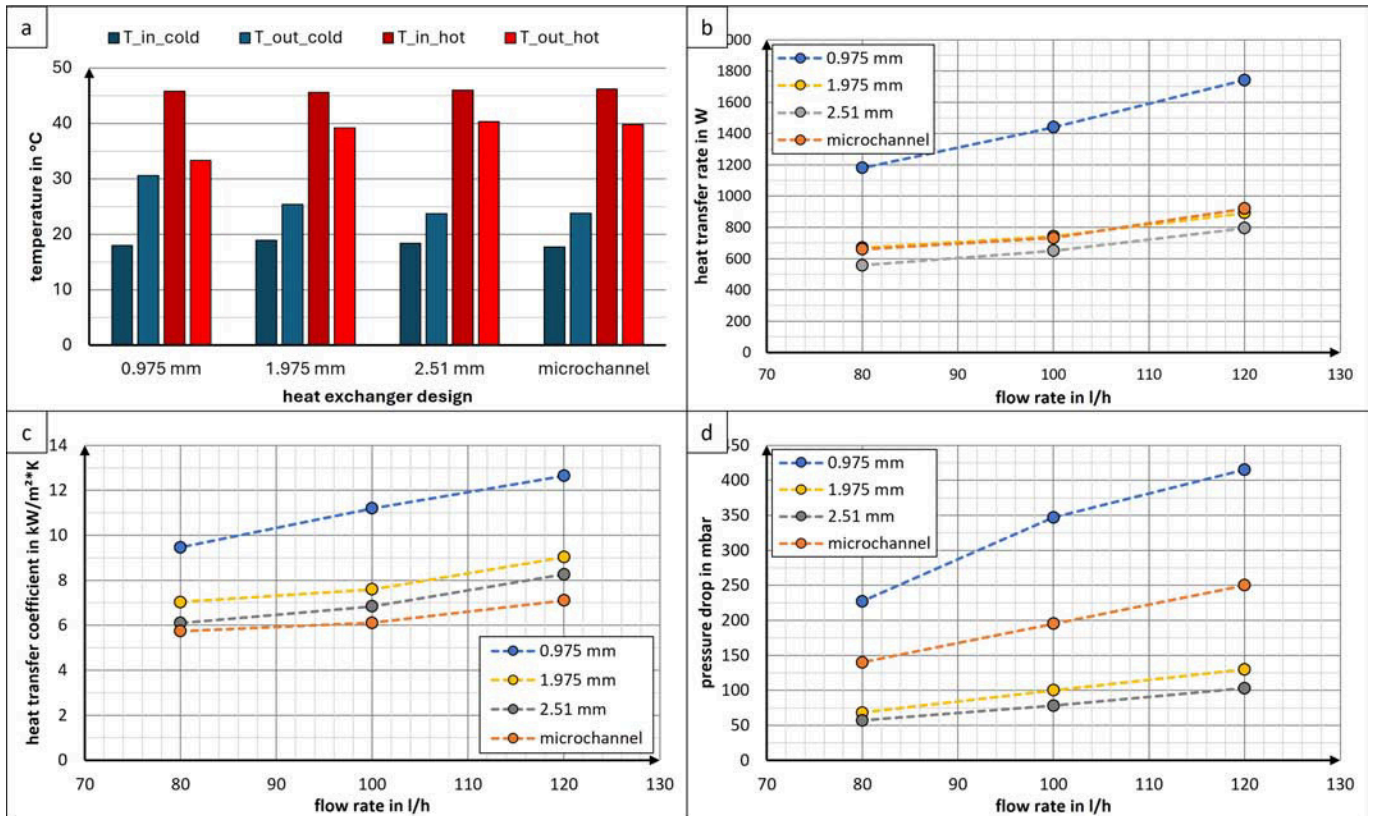


Figure 9: Results of the thermal performance measurement.
 a) Inlet and outlet temperatures for all heat exchanger designs with a flow rate of 120 l/h,
 b) Heat transfer rate, c) Heat transfer coefficient, d) Pressure drop.

The impact of unit cell size on thermal performance does not follow a linear trend, as the difference between the 0.975 mm and 1.975 mm sizes is significantly larger than that between the 1.975 mm and 2.51 mm sizes for both the heat transfer coefficient and pressure drop. Further investigation of additional unit cell sizes would be necessary to fully understand the influence of this parameter on performance.

When compared to the microchannel design, the microchannel heat exchanger exhibits similar heat transfer performance to the 1.975 mm and 2.51 mm gyroid structures. However, the pressure drop in the microchannel design is approximately twice as high, making the TPMS lattice design the preferred choice for heat exchangers.

5. Conclusions

This study demonstrates that incorporating small-structure TPMS lattices can significantly enhance the heat transfer performance of water-to-water micro heat exchangers. Compared to conventional plate heat exchangers and a microchannel heat exchanger fabricated via Micro-SLM, the TPMS-based designs, particularly gyroid structures, demonstrated higher heat transfer efficiencies. With a unit cell size of 1 mm and

a wall thickness of 100 μm , an overall heat transfer coefficient of over 12 $\text{kW}/(\text{m}^2\cdot\text{K})$ was measured with the downside of a relatively high pressure drop of over 400 mbar. By increasing the unit cell size the pressure drop could be decreased to below 100 mbar while still achieving a heat transfer coefficient of over 8 $\text{kW}/(\text{m}^2\cdot\text{K})$. Although leakage-free gyroid lattices were fabricated, leakage persisted in the final heat exchangers, warranting further research on leakage detection and elimination. TPMS lattices for heat exchangers, especially in Micro-SLM, present new research opportunities, including exploration of other lattice structures, multi-phase concepts, and advanced baffle designs.

6. Acknowledgements

The projects were co-financed by funds from the European Union and the Free State of Saxony.

7. References

- [1] Garimella, S.V. "Advances in mesoscale thermal management technologies for microelectronics." *Microelectronics Journal* 37.11 (2006): 1165-1185.
- [2] Wu, Y.; Shanglong X.; Chao W.: "Investigation of On-Chip Hot Spot Cooling Using Microchannel Heat Sink." *Applied Mechanics and Materials* 455 (2014): 466-469.
- [3] Saraireh, M.: "A Novel Method for Heat Exchange Evaluation in EV." *Intelligent Automation & Soft Computing* 36.1 (2023).
- [4] Careri, F.; et al.: "Additive manufacturing of heat exchangers in aerospace applications: a review." *Applied Thermal Engineering* (2023): 121387.
- [5] Attia, S.I.: "The influence of condenser cooling water temperature on the thermal efficiency of a nuclear power plant." *Annals of Nuclear Energy* 80 (2015): 371-378.
- [6] Zohuri, B.: "Compact heat exchangers." Cham, Switzerland: Springer, (2017).
- [7] Zhang, X.; et al.: "Recent developments in high temperature heat exchangers: A review." *Frontiers in Heat and Mass Transfer* (2018).
- [8] Zhang, X.; et al. "An additively manufactured metallic manifold-microchannel heat exchanger for high temperature applications." *Applied Thermal Engineering* 143 (2018): 899-908.
- [9] Peng, H.; Feng G.; and Hu, W.: "Design, modeling and characterization on triply periodic minimal surface heat exchangers with additive manufacturing." *Solid Freeform Fabrication 2019: Proceedings of the 30th Annual International Solid Freeform Fabrication Symposium* (2019).
- [10] Yan, K.; et al.: "Thermo-hydraulic performance evaluation through experiment and simulation of additive manufactured Gyroid-structured heat exchanger." *Applied Thermal Engineering* 241 (2024): 122402.
- [11] Mahmoud, D.; et al.: "Enhancement of heat exchanger performance using additive manufacturing of gyroid lattice structures." *The International Journal of Advanced Manufacturing Technology* 126.9 (2023): 4021-4036.
- [12] Qian, C.; et al.: "Numerical and experimental investigation of ultra-compact triply periodic minimal surface heat exchangers with high efficiency." *International Journal of Heat and Mass Transfer* 233 (2024): 125984.
- [13] Catchpole-Smith, S.; et al.: "Thermal conductivity of TPMS lattice structures manufactured via laser powder bed fusion." *Additive Manufacturing* 30 (2019): 100846.
- [14] Gronau, S.; et al.: "MANUFACTURING OF MICRO HEAT EXCHANGERS BY LASER MICRO SINTERING" *Proceedings of 9th Annual World Congress of Nano Science & Technology* (2019)
- [15] Yuan, W.; et al.: "Effects of laser scanning speeds on different states of the molten pool during selective laser melting: Simulation and experiment." *Materials & Design* 189 (2020): 108542.
- [16] Verein Deutscher Ingenieure VDI-Gesellschaft Verfahrenstechnik und Chemieingenieurwesen (GVC): "VDI-Wärmeatlas" Berlin, Heidelberg: Springer Berlin Heidelberg (2006).

Additive manufacturing of pure Molybdenum utilizing ultra-short laser pulses

Kohl, H. P.¹; Matthäus L.¹; Seyfarth, B.¹; Nolte, S.^{1,2}

¹ Institute of Applied Physics, Abbe Center of Photonics, Friedrich-Schiller-Universität Jena, Jena, Germany

² Fraunhofer Institute for Applied Optics and Precision Engineering IOF, Jena, Germany

The extreme high melting temperatures, high thermal conductivities and their extraordinary high resistance to wear make refractory metals predestine for applications with high mechanical loads at elevated temperatures, such as jet propulsion systems in aerospace, nuclear fission systems or x-ray collimators. Usually those applications require thin-walled structures, where additive manufacturing (AM) has the potential to significantly reduce material waste and fabrication cost. However, the high melting point and thermal conductivity together with high susceptibility to solidification fractures make it difficult to identify a suitable parameter window for the laser based melting process.

Here, we report on PBF-LB/M of pure Molybdenum utilizing an ultra-short pulsed (USP) laser system. USP-lasers are commonly known for their capability of cold ablation and triggering nonlinear processes where typically high pulse energies and low repetition rates up to the low MHz-regime are used. In contrast, for the PBF-LB/M processes a low pulse energy regime at high repetition rate is used to accumulate thermal energy to melt the powder particles. The main advantage of employing an USP laser in an AM process is grain refinement, which can be controlled by pulse energy and pulse repetition rate. As it has been shown by experimental and theoretical investigations grain refinement can lead to a significant reduction in hot cracking in laser-based welding and AM processes. Therefore, the use of an USP-laser source in the PBF-LB/M process could be beneficial in terms of crack free AM of pure Molybdenum. Therefore, we are going to present powder bed fusion of pure Molybdenum utilizing an USP-laser system with a central wavelength of 1030 nm, a pulse length of 270 fs, a repetition rate of 32 MHz and an average laser power output of 150 W. We demonstrate the fabrication of thin-walled structures with a width below 70 μm as well as a processing window for bulk samples with a relative density close to 100 %. As an example, Figure 1 shows cubes used to study the density of the additively manufactured molybdenum in dependence of laser power, scanning speed and hatch distance. In addition to the processing parameters the results of the microstructural analysis and mechanical testing of the fabricated samples will be presented.



Figure 1. 3 mm x 3 mm x 3 mm pure Molybdenum cubes still attached on the built platform via a 2.5 mm high support structure.

Structured metal coatings on glass enabled by ultrashort laser processes

Dreisow, F.¹; Storch, C.¹; Jose, A.¹; Eichler, R.¹; Kuckelkorn, T.¹; Seiler, M.^{1,2}; Bliedtner, J.²

¹ Schott Technical Glass Solutions GmbH, Jena, Germany

² Ernst-Abbe-Hochschule Jena, Jena, Germany

Laser assisted analytical depth profiling (LAADP) – an innovative method for high-precision analysis

Berger, N.^{1,2}; Bock, W.^{1,2}; Passlack, S.^{1,2}; Ehnert, S.^{1,2}; Schäfer, M.^{1,2}; L'huillier, J.^{1,2}

¹ Institut für Oberflächen- und Schichttechnik (IFOS GmbH), Kaiserslautern, Germany

² Landesforschungszentrum OPTIMAS, RPTU Kaiserslautern-Landau, Kaiserslautern, Germany

Analyzing material compositions that are sensitive to the introduction of heat or mechanical stress remains a challenge but is of paramount importance in various domains of material science, for example in the context of the burgeoning hydrogen economy. Often it is imperative to analyze such sensitive material systems down to a depth of several hundred micrometers, or even millimeters. However, prevailing sensitive measurement techniques like in the field of surface mass spectrometry are limited to depth profiling within the nanometer to a few tens of micrometers range. Moreover, conventional sample preparation methods may unintentionally induce undefined alterations to the material system due to the imposition of mechanical stress or heat, rendering them hardly suitable.

In the presented approach of Laser-Assisted Analytical Depth Profiling (LAADP), an ultra-short pulse laser is deployed to gently ablate surface material down to the intended depth for analysis. This material removal is done in a layer-by-layer process, whereby different stop criteria have been demonstrated. Firstly, it is possible to remove a certain number of layers to a certain depth. Especially for inhomogeneous layered material systems it can be important to actively use material feedback to stop ablation based on material transitions. For this purpose, the ablated material can be used to perform an online LIBS analysis (Laser-Induced Breakdown Spectroscopy) and define stop criteria based on its results. In both cases, the depth accuracy is mainly limited by the ablation per layer, which is in the sub-micrometer range. This was demonstrated on a sample consisting of a NiP-layer with a thickness of 10 micrometer on top of an aluminum base material.

By using an ultrashort pulsed laser and carefully choosing the process parameters the deployment of residual heat and thereby the heat affected depth can be reduced to a minimum. For a heat sensitive hydrogen enriched titanium sample experimental findings align with thermodynamic simulations that describe a laser-affected zone in the residual material with a thickness of less than 100 nanometers. Thin layers like this represent only a negligible obstacle for subsequent analytical methods such as SIMS. Our findings clearly show that the Laser-Assisted Analytical Depth Profiling is able to combine a high level of precision with a high degree of time and cost efficiency.

1 Introduction

The determination of hydrogen concentration in components is of central importance for assessing and preventing material-related damage. For instance, in rolling bearings, which are indispensable in a variety of industrial applications, Evans et al. [1] demonstrated that diffused hydrogen contributes to the formation of so-called "White Etching Cracks" (WECs). These microscopic crack structures, caused by the accumulation of hydrogen and the resulting embrittlement of the material, can penetrate deep into the component, often reaching depths of several hundred micrometers. Therefore, determining the hydrogen concentration is essential to detect potential material damage and maximize the lifespan of components.

However, detecting hydrogen within the material itself poses a significant technological challenge, as hydrogen is difficult to detect. This complicates not only the quantitative determination of hydrogen concentration but also the localization of hydrogen in specific areas of the material. While traditional analytical methods, such as Secondary Ion Mass Spectrometry (SIMS) or Secondary Neutral Mass Spectrometry (SNMS), can be used to determine hydrogen concentration, these methods are only practical for depth profiling up to a relatively shallow depth of a few micrometers. This limitation arises from the low removal rate, typically ≤ 1 nm/s, and the cumulatively increasing roughness with increasing depth. For analyses at greater depths, appropriate sample preparation is required. Due to the high volatility of hydrogen, conventional mechanical preparation methods, such as cutting and polishing the new surface, prove problematic. Mechanical stress and/or process heat can alter the hydrogen concentration in an undefined manner, ren-

dering subsequent measurements unusable. Our LAADP approach can overcome this limitation of conventional methods by using ultrashort pulse (USP) laser ablation. In this process, ultrashort laser pulses with extremely high peak powers are used to ablate small volumes of material without significantly transforming it into a liquid phase. Heat conduction to surrounding material is effectively prevented, and the heat-affected zone can be minimized [2, 3].

2 Methods

For Laser-Assisted Analytical Depth Profiling (LAADP), a USP laser is used to create a gentle, high-precision ablation down to the required depth of up to several hundred micrometers. The exact shape of the ablation can be tailored to the specific research question. In addition to individual test fields, it is also possible to create a step-like structure with fields at different depths or even a continuous ramp. The resulting analysis surface is then examined using high-resolution analytical methods. In this work, the mass spectrometric analysis techniques ToF-SIMS (Time-of-Flight SIMS) (Device used: TOF-SIMS IV, IONTOF) and SNMS (Device used: Prototype of INA-X, SPECS GmbH) were used for this purpose. This process is schematically depicted in Fig. 1.

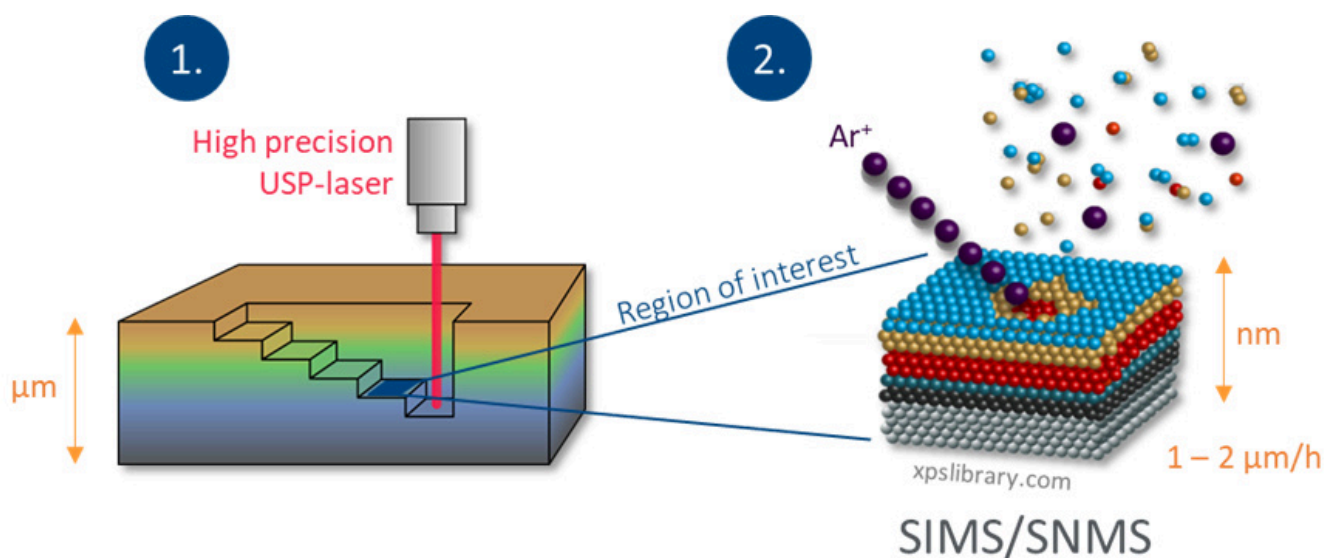


Figure 1: Schematic representation of the LAADP process in 2 steps.

Step 1: High-precision sample preparation using a USP laser. Step 2: Application of a highly sensitive mass spectrometric analysis method at the previously prepared depth.

For the ablation process, an ultrashort pulse laser with a pulse duration of 9 ps, a wavelength of 1064 nm, and a variable pulse energy of up to 150 μJ was used (HyperRapid 100, Coherent). Single laser pulses or bursts of up to ten laser pulses with a burst internal repetition rate of 50 MHz can be created at various repetition frequencies up to 1 MHz. Its beam path was deflected just before the respective sample by a galvanometer scanner (hurryScan III 14, Scanlab) and focused onto the sample through an F-Theta lens. In this work two focal lengths ($f = 199 \text{ mm}$ and $f = 255 \text{ mm}$) creating spot sizes on the samples with diameters of 19 μm and 66 μm were utilized. By using these ultrashort pulses, the heat-affected zone during ablation is minimized.

For more efficient parameter studies and increasing the understanding of the thermodynamics within the samples, simulations of the near-surface temperature gradients were carried out. These simulations are based on the methodology and formula presented by Bauer et al. [4]. The analytical solution for the temperature rise caused by a single short Gaussian laser pulse is used (Equation 1). The temperature distribution after multiple pulses is calculated as the sum of the individual temperature changes caused by each pulse.

$$T_{x_c, y_c}^{s.p.}(x, y, z, t) = \frac{2E_{res}}{\pi \rho c \sqrt{\pi \kappa t} (8\kappa t + w_0^2)} * e^{-\frac{(x-x_c)^2 + (y-y_c)^2}{4\kappa t} - \frac{w_0^2}{8\kappa t + w_0^2} - 1} \tag{1}$$

Here, E_{res} corresponds to the residual heat remaining in the material after the pulse, ρ is the density of the material, c is the heat capacity of the material, κ is the thermal diffusivity of the material, t is the time elapsed since the pulse hit, and w_0 is the beam radius of the incoming laser pulse.

3 Experiments and discussion

The aim of the study is the systematic investigation of the influence of the introduced energy on the resulting changes in the surface layer region. In the first step, investigations are carried out on a bulk system, using a hydrogen-enriched titanium sample as an example. The findings are then applied to a layer sample made of hydrogen-enriched yttrium oxide. In the third step, additional possibilities of the ablation and preparation process are demonstrated by creating a 3D-ablation and demonstrating inline LIBS analysis (Laser-Induced Breakdown Spectroscopy).

3.1 Hydrogen-enriched titanium sample

To analyze heat-induced changes in hydrogen concentration, two test fields were ablated on a hydrogen-enriched titanium sample using the laser. By selectively choosing the process parameters, the heat input was kept low in one of the test fields. The second test field was deliberately processed with parameters that result in a high heat-affected zone (both parameter sets are shown in Table 1). To improve comparability, the ablation depth for both test fields was adjusted to approximately 2.5 μm by modifying the number of passes.

Table 1: Laser process parameters for ablation with high and low heat input on titanium sample

	Heat input high	Heat input low
Focal length	100 mm	
Mark speed	1000 mm/s	
Line distance	5 μm	
Repetition rate (burst)	500 kHz	200 kHz
Pulses per burst	10	1
Average laser power	2,38 W	0,558 W
Pulse energy	0,47 μJ	2,79 μJ
Ablated layers	3	12

For the two cases considered, the temperature profile was simulated using the given laser and process parameters (see table 1). The simulation approach presented in section 2 was used to determine the maximum temperature at various depths during the process. Since the portion of energy used for ablation is no longer available as residual heat, the pulse energy in the simulation was adjusted so that 90 % of the boiling temperature of titanium is reached at the surface (the topmost remaining layer is just below the evaporation point). In 2010, C. Schäfer [5] demonstrated that the permeability of hydrogen in titanium changes dramatically with temperature fluctuations already below 300 °C. Based on this, a critical temperature of 250 °C was set for evaluating the results. Under these assumptions, the simulation (see Fig. 2) shows that for the parameter set with high heat input, an effect to a depth of about one micrometer is expected. For the parameter set with low heat input, however, only about one-tenth of that depth ($\approx 100 \text{ nm}$) is anticipated.

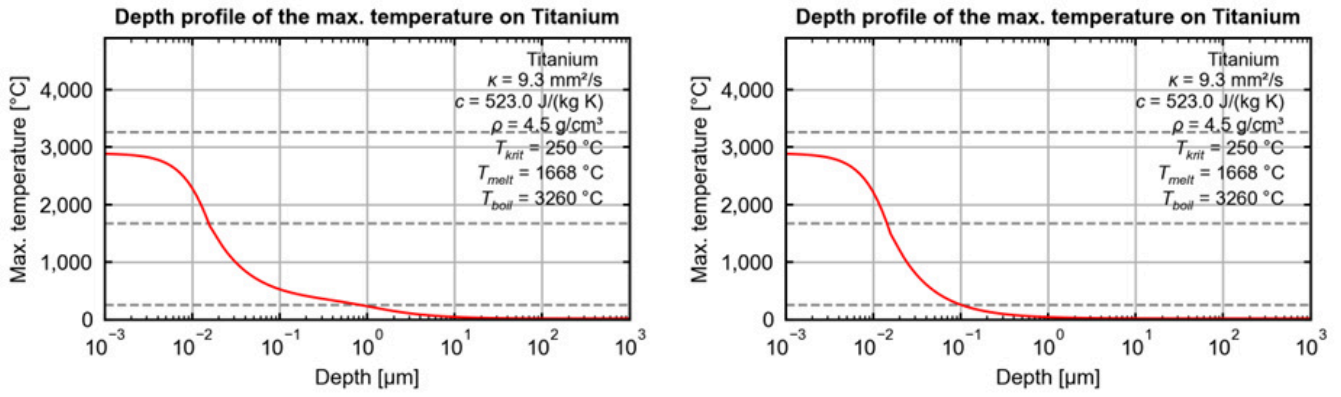


Figure 2: Simulated depth profile of the maximum temperature reached in titanium with the process strategies used. Left: Process strategy with high heat input. Right: Process strategy with low heat input. To reach 90 % of the melting point of titanium, the average laser power was adjusted to 0.169 W for high heat intake parameter set and 0.008 W for the low heat intake parameter set.

After laser processing, the sample was analyzed using ToF-SIMS measurements. A reference measurement was taken at an unprocessed location, along with one measurement on each of the two test fields. Fig. 3 shows the TiH/Ti ratio for the individual measurements. To rule out fluctuations in the detection efficiency of the instrument, this ratio was used to analyze the hydrogen concentration. After 200 s, there is hardly any significant difference between the unprocessed reference and the test field with low heat input. However, the measurement of the test field with increased heat input shows a clear deviation from the untreated reference for almost an hour (approx. 3000 s of measurement time).

Both the experiment and simulation show a penetration depth ratio of about 10:1 between high and low heat input. Assuming a typical sputter rate of just under 1 nm/s, the detected depth by the ToF-SIMS measurement matches the heat-affected depth of the simulation as well. This confirms the simulation as a practical tool for developing gentle ablation parameters, which can significantly accelerate the development and adjustment process for application to other materials, while also reducing potential material waste.

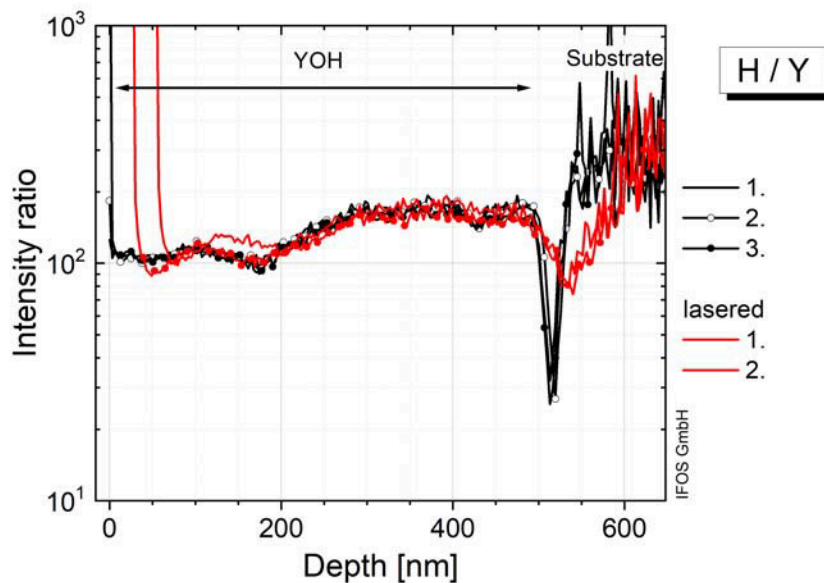


Figure 3: ToF-SIMS measurements of unprocessed surface (green), surface processed with high heat input (red) and surface processed with low heat input (blue).

3.2 Hydrogen-enriched Yttrium-oxide sample

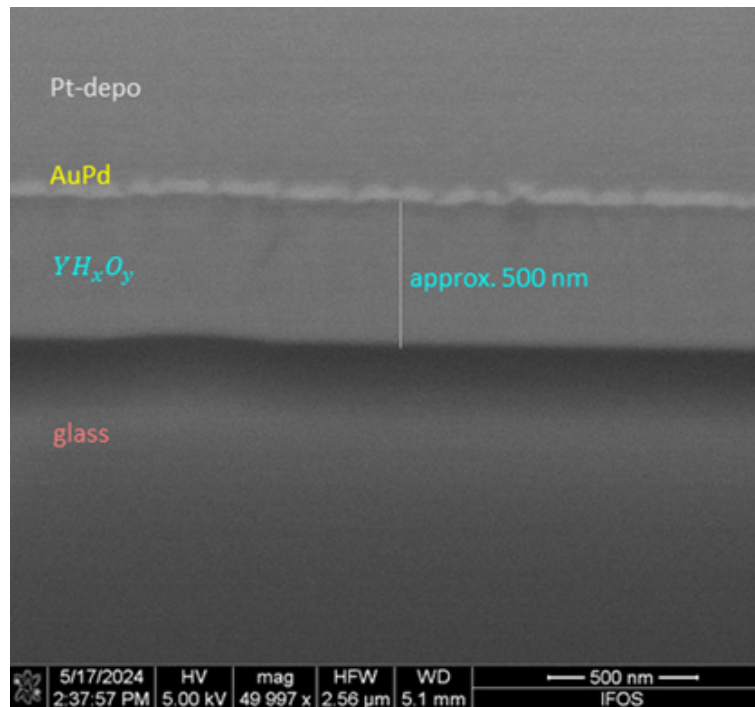


Figure 4: Structure of the YH_xO_y (hydrogen-enriched yttrium oxide) sample in cross-section, here as an SEM image of a FIB section. The AuPd-layer and the Pt-depo were only applied for analysis purposes

The precision and gentleness of the ablation process using the USP laser were examined on a 500 nm thick, hydrogen-enriched yttrium oxide layer applied to glass. A cross-section of the sample, prepared using a Focused Ion Beam (FIB) cut, is shown in Fig. 4. The gold-palladium layer and the platinum deposit visible in the image were applied solely for analysis using a Scanning Electron Microscope (SEM) and FIB and were not present in the subsequent steps presented here. The cross-section also reveals small irregularities in the glass substrate, which can lead to local variations in the thickness of the yttrium oxide layer of several tens of nanometers.

Due to the high temperature sensitivity of hydrogen and the thin layer thickness, this sample is particularly suitable for verifying the gentle ablation using the USP laser. A single pass was used to ablate as thin of a layer of the YH_xO_y coating as possible. To keep the heat intake as low as possible, the laser was used in single pulse mode (pulse energy of 2.68 μ J) with a low repetition rate of 50 kHz. The marking speed was set to 250 mm/s and a line distance of 10 μ m was used to create a rectangular ablation area of 2x2 mm². To determine the ablation depth, a height profile of the sample was subsequently created using white light interferometry (see Fig. 5). The irregularity caused by the glass substrate used as the base material and the ablation depth of 64 ± 3 nm are clearly visible. The regular shading observed in the optical image is caused by vignetting from the stitched individual images and does not affect the height data.

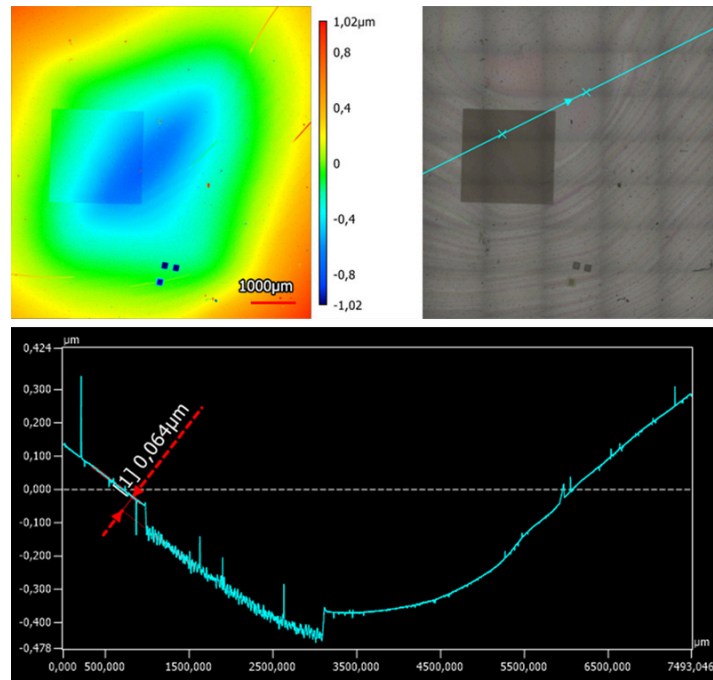


Figure 5: White light interferometry measurement of the YH_xO_y -surface with ablated test field. Top left: Height image of the sample, the surface form is clearly recognizable. Top right: optical image with the measurement position of the profile line marked. Both images show the same image section. Below: Profile line for measuring the removal depth, determined along the line marked in the optical image.

To analyze the temperature effects on the hydrogen concentration in the YH_xO_y -layer, the sample was examined at three reference points and two processed locations using ToF-SIMS analysis. The measured H/Y ratio is shown in Fig. 6. The measurements of the laser-processed areas were shifted along the x-axis so that the transition from YH_xO_y to glass aligns for all measurements. This alignment is clearly visible in the shifted onset of the graphs. The variation in the thickness of the YH_xO_y -layer between the two measurements of the laser-processed area can be explained by the previously mentioned thickness variation of the unprocessed YH_xO_y -layer.

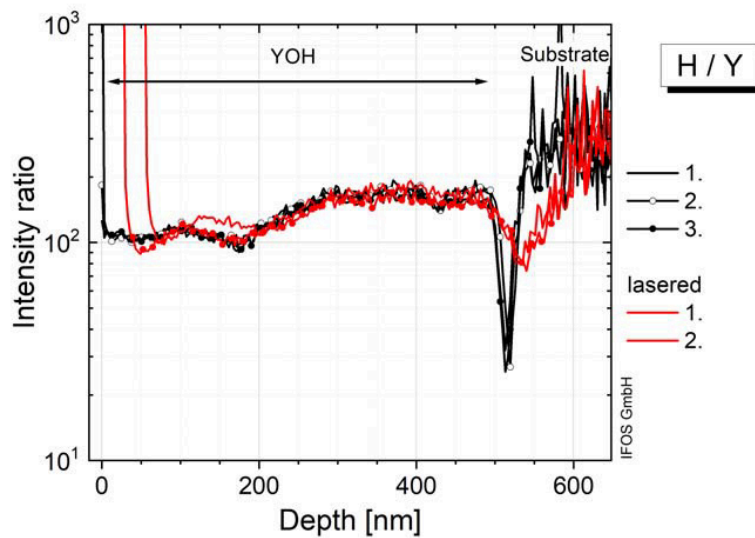


Figure 6: ToF-SIMS depth profile through the YH_xO_y -layer into the glass substrate, the ratio of H/Y is shown. Reference measurements of non-laser-processed areas are shown in black. The measurements of laser-processed areas are shown in red; these have been shifted along the x-axis so that the transition to the glass substrate is superimposed on all measurements.

Similar to the white light interferometry measurements, the ToF-SIMS measurements show a thickness difference of approx. 60 nm between the laser-processed and unprocessed areas. At the start of the ToF-SIMS measurement, there is a rapid decline in the H/Y concentrations across all measurements. Subsequently, the H/Y concentrations follow a very similar trend until the transition of the YH_xO_y -layer into the glass substrate. However, due to the roughness induced by the laser process, this transition in the depth profiles of the H/Y concentrations of the laser-prepared areas is not as sharp as for the reference areas. Overall, even with this very sensitive material combination, no residual heat influence of the laser process on the H/Y concentration of the remaining material could be observed.

3.3 Further options for sample preparation

After demonstrating that the USP laser can be used as a material-friendly ablation tool even for sensitive hydrogen-containing materials with the selection of appropriate process parameters, this section explores additional capabilities of USP laser ablation. As examples, we demonstrate the possibilities of continuous depth profiling on a piston of a combustion engine and inline LIBS analysis (Laser-Induced Breakdown Spectroscopy), shown on a NiP-Al-layer sample, during the laser process.

3.3.1 Continuous depth profile / 3D ablation

In addition to creating plateaus at defined depths, nearly any three-dimensional ablation geometry can also be prepared. The example of a continuous "ramp" is demonstrated below. Using laterally resolving measurement methods, continuous depth profiles can be created in just one measurement. In Fig. 7, this capability was realized and illustrated using the material of a piston from a combustion engine. The processed area measures 5x2 mm², with the "ramp" covering an area of 3x2 mm². This is seamlessly followed by a planar ablation of 2x2 mm² at an ablation depth of 53 μm. This ablation was created using the laser in burst mode with 3 pulses (approx. 2 μJ per pulse) and a repetition rate of 50 kHz. In combination with a mark speed of 250 mm/s and a line distance of 5 μm this created a smooth, low-roughness surface, while keeping the heat intake to the material very low. The ablation caused increase of the surface roughness S_a was determined to be approx. 130 nm. Significantly undercutting the roughness increase typically seen with sputtering (typically ≥ 10 nm per 1 μm of ablation).

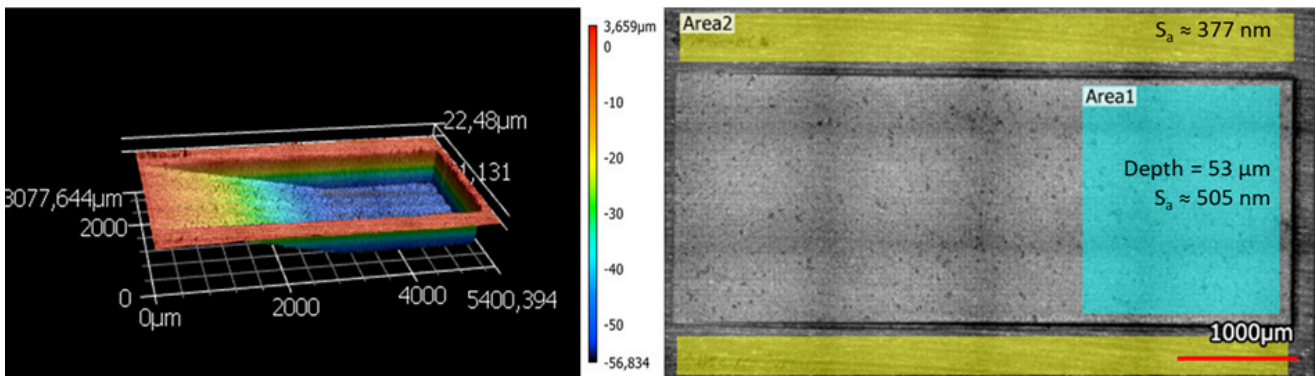


Figure 7: 'Ramp-shaped' removal, here realized on piston material. Left: 3D view of the measured height profile. Right: Depth profile and roughness measurement at the point of deepest removal and on an unmachined reference surface.

3.3.2 NiP-layer system on Al

For the tests conducted so far, the ablation per pass was determined, and the desired depth was then adjusted by modifying the number of passes. However, in layer systems, it can occur that the thickness of one or more of these layers varies, and yet the ablation needs to be stopped relative to a layer transition. Particularly in such cases, the plasma generated during the ablation process can be used for analysis through LIBS. Based on the detected spectra, stop criteria can be introduced or process parameters can be adjusted.

The carried-out investigations demonstrate this on an aluminum sample with an approx. 10 μm thick nickel-phosphorus layer on top. The laser was set to single pulse mode (pulse energy 2.68 μJ) and a pulse repetition rate of 50 kHz. With a marking speed of 250 mm/s and a line distance of 5 μm almost homogeneous layers were ablated. For each ablated layer, a LIBS spectrum ranging from 349.7 nm to 608.4 nm was measured using a spectrometer produced by Avantes. The spectrum was then transformed to its prin-

principal components (the basis was previously defined using PCA of a complete set of spectra, see Abdi et al. [6]). Fig. 8 shows the first 5 principal components of the resulting spectra layer by layer. To verify and validate the results, a second laser-processed test field was also analyzed using SNMS to quantify the elements and molecules present. Both measurements show a good agreement in the transition region of element concentrations from the NiP-layer to the aluminum. Since the surface roughness at this depth with $S_a \approx 90$ nm is significantly below the ablation per layer, it cannot explain the measured, gradual transition. This must be an effect of the material itself.

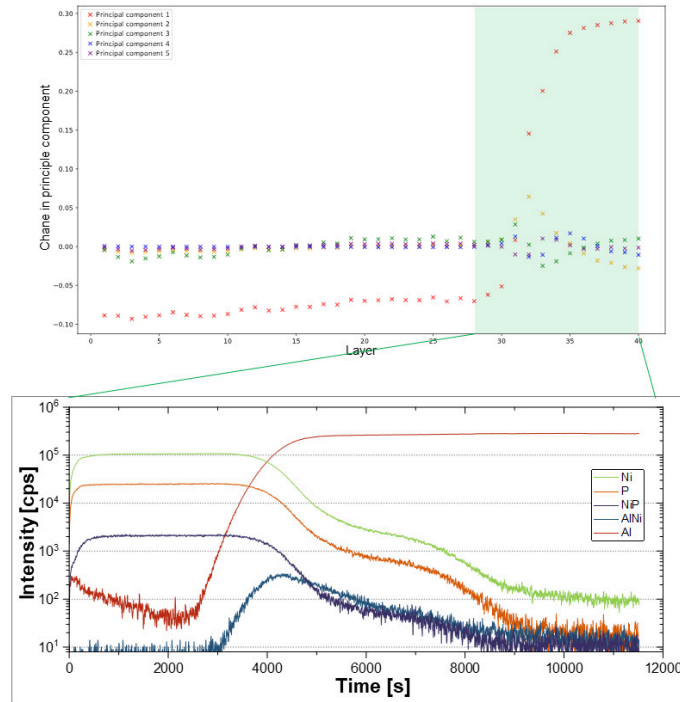


Figure 8: Top: Layer-by-layer principal component analysis of the ablation through the NiP-layer into the Al base material. Bottom: SNMS measurement carried out through the transition region on a laser-prepared test field.

4 Summary

This work presented the LAADP approach for precise material preparation and analysis, particularly hydrogen detection, in deep material layers. This approach is characterized by the combination of ultrashort pulse (USP) laser ablation and high-precision analytical methods, such as mass spectrometry. The use of the USP laser successfully overcomes the limitation of ablation depth in sputtering-associated methods like mass spectrometric measurements without significantly affecting the remaining material composition, such as the hydrogen concentration in the material. This was demonstrated through experiments with various materials, including hydrogen-loaded titanium and yttrium oxide, where the laser's influence on residual heat and, consequently, on hydrogen concentration was kept minimal. The approach also demonstrated potential extensions of USP laser-based ablation techniques, such as the creation of continuous depth profiles and inline LIBS analysis. Overall, the LAADP method can contribute to making bulk materials, previously inaccessible for analysis, available to precise analytical methods and thereby enhance scientific knowledge.

Acknowledgements

The work was conducted as part of the WaVe project, which was funded by the Bundesministerium für Wirtschaft und Klimaschutz under grant numbers “19I21028N” and “19I21028H”. Additionally, the authors would like to thank Prof. Dr. Primetzhofer's research group at Uppsala University (Sweden) for providing the hydrogen-loaded yttrium oxide sample used in this work.

References

- [1] Evans, M. H.; Richardson, A. D.; Wang, L.; Wood, R. J. K.: "Effect of hydrogen on butterfly and white etching crack (WEC) formation under rolling contact fatigue (RCF)", *Wear*, 306(1-2), 226-241 (2013)
- [2] Herrmann, T.; Harth, F.; Henrich, B.; L'huillier, J.; Hajri, M.: "How to improve efficiency in USP laser micromachining: a new generation of resonant scanners and innovative ultrashort pulse lasers allow for efficient and fast processing", *Laser Technik Journal*, 13(1), 16-19 (2016)
- [3] Villerius, V.; Kooiker, H.; Post, J.; Pei, Y. T.: "Ultrashort pulsed laser ablation of stainless steels", *International Journal of Machine Tools and Manufacture*, 138, 27-35 (2019)
- [4] Bauer, F.; Michalowski, A.; Kiedrowski, T.; Nolte, S.: "Heat accumulation in ultra-short pulsed scanning laser ablation of metals", *Optics express*, 23(2), 1035-1043 (2015)
- [5] Schäfer, C.: „*Diffusionseigenschaften bestimmter Metalle bei der Hochtemperatur-Wasserstoffabtrennung*“, Doctoral dissertation, Technische Universität München (2010)
- [6] Abdi, H.; Williams, L. J.: "Principal component analysis", *Wiley interdisciplinary reviews: computational statistics*, 2(4), 433-459 (2010)

Classification of surface structures in ultrashort pulse laser processing using machine learning based on light microscopic images

Thomas, R.¹; Westphal, E.¹; Schnell, G.¹; Seitz, H.^{1,2}

¹ University of Rostock, Chair of Microfluidics, Faculty of Mechanical Engineering and Marine Technology, Rostock, Germany

² University of Rostock, Department Life, Light & Matter, Rostock, Germany

A popular method to create micro- and nanoscale surface structures on various materials is to process them with ultrashort pulsed lasers. With ultrashort laser pulses, self-organized structures can be generated in the laser spot during the machining process. By employing appropriate scanning strategies, these intricate patterns can be scaled up to cover larger areas effectively. The formation of the surface structures depends on the laser parameters (such as laser fluence, polarization, scanning strategy and number of pulses), the material properties (such as chemical composition and physical properties) and the environmental conditions.

However, since the underlying formation mechanisms of the structures are very complex and depend on several non-linear relationships, it is a challenge to choose the right process parameters and scanning strategies for a desired surface modification. This poses problems in the production of surface structures with ultrashort laser pulses and represents an obstacle to the use of laser systems.

To solve this problem, we introduce a machine learning (ML) approach. In a first step, we present a successful AI-based image recognition of direct light microscopy images of different structure classes. The usage of light microscopy images enables inline process control and autonomous structure classification.

For image recognition, we generated three different structure classes (LIPSS, crater structure, microstructure) in comparison to the reference on two steel substrates (X37CrMoV5-1 and X5CrNi18-10). To train a pre-trained model, 250 different images of X37CrMoV5-1 steel from each structural class (4x) were used. The classification test of the trained models was performed with 30 additional images of each structural class of both steel substrates.

The results of the ML-based classification show that the generated direct light microscope images could be effectively used to train an ML algorithm, which was subsequently able to automatically classify new, unknown images with respect to the existing surface structure. A web application was developed to interact with the trained ML algorithm to analyse new microscopic images of different surface structures without specialized knowledge. Therefore, the machine learning-based classification of laser-induced surface structures holds significant promise for a wide range of in-line applications.

Multi-sensor conception for process monitoring in laser welding with beam oscillation

Ullmann, L.; Dittrich, D.; Boerner, S.; Jahn, A.; Wetzig, A.
Fraunhofer Institute for Material and Beam Technology IWS, Dresden, Germany

New multi-core fiber concepts, diffractive optical elements and beam shaping optics lead to unique process solutions in laser beam welding. Therefore, development of scientific process monitoring in laser beam welding represents a key for objective optimization of process parameters and enabling reliable process-control in serial application. The presented work concentrates on the conception of an optical setup for 3D beam shaping and multi-sensor systems. The developed architecture to collect synchronized process data of the multisensor system will be explained including accumulated process emissions generated with a unique processing head. Emissions of an acoustic sensor and a thermal camera signal in combination with process parameter were used to evaluate process behavior. The identified weld seam inhomogeneities of copper welding are explained through engineered data annotation, which teaches a cyber-physical model. Therefore, it is mandatory to collect sufficient amount of data on process stability and generate reliable information on the processing quality in order to establish a reliable inline process control. An automated approach to handle numerous influencing factors in the parameter space is emphasized. Furthermore, perspectives for process control loops of technical welding solutions will be presented.

Predictable laser material processing by combining ultrafast metrologies with modeling

Horn, A.; Pflug, T.; Engel, A.; Olbrich, M.
 Laserinstitut Hochschule Mittweida, Mittweida, Germany

Laser material processing is often implemented in product chains when high accuracy and high reproducibility are essential. In general, to improve laser material processing quantitative modeling is necessary to predict the right process parameters. In this paper, we demonstrate at three examples the entangled combination of multiple ultrafast metrologies with our selfdeveloped models describing laser radiation propagation, optical properties of the irradiated area during irradiation, and the dynamics of the irradiated matter at different phase states determining their thermophysical parameters.

We start firstly by laser processing below the ablation threshold. Thereby, we investigate the change in the magnetic properties of FeAl and FeV alloys ($\text{Fe}_{60}\text{Al}_{40}$ and $\text{Fe}_{60}\text{V}_{40}$) by determining the relative change of reflectance $\Delta R/R$ during and after laser excitation [1]. We observe a remarkable change of $\Delta R/R$ up to 200 ps after irradiation, see Fig. 1, resembling an ultrafast melting and reordering of the atoms. These rearrangements were accompanied by the emergence of ferromagnetism and were achieved without damaging the sample surfaces. Secondly, we elucidate the dynamics of a thin chromium layer irradiated by single-pulsed ultrafast laser radiation. Metrology as well as modeling reveal a complex formation of two ablation layers (Fig. 2). Using space- and time-resolved reflectometry [2], as well interferometry, we retrace the geometrical changes in the surface topography by implementing a smart model using the transfer matrix formalism for a multi-layer system. Lastly, we implement additional pulses in our investigations to describe multi-pulse ablation. Now, the laser radiation of subsequent pulses interacts not only with a modified surface, but also with an expanding ablation plume. The dynamics of the surface, as well as of the ablation plume are presented.

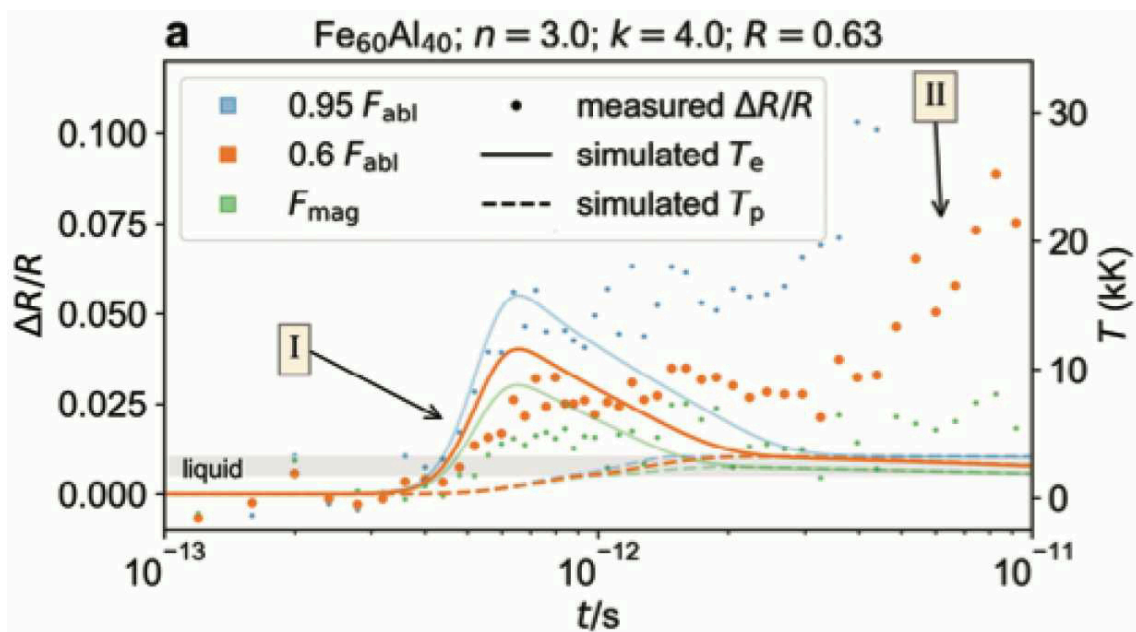


Figure 1: $\Delta R/R$ of the irradiated $\text{Fe}_{60}\text{Al}_{40}$ with the simulated T_e and T_p for different fluences of the pump radiation relative to the measured damage threshold fluence F_{abl} . [1]

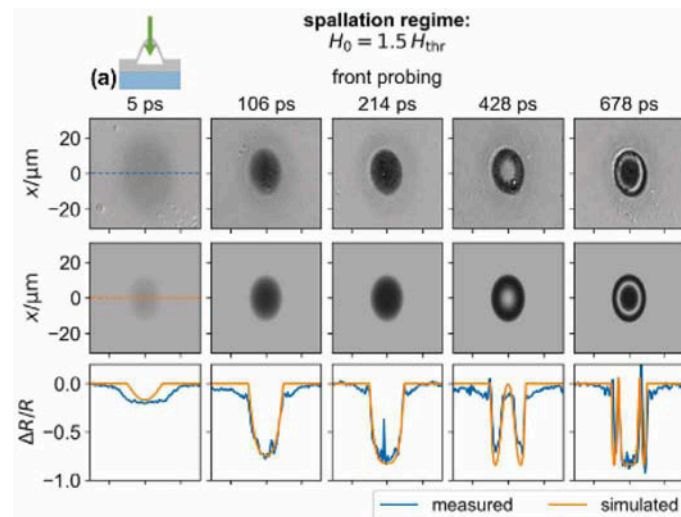


Fig. 2: Measured (top) and simulated (middle) $\Delta R/R$ as function of time in the spallation regime. [2]

References

- [1] T. Pflug, J. Pablo-Navarro, M. S. Anwar, M. Olbrich, C. Magén, M. R. Ibarra, K. Potzger, J. Faßbender, J. Lindner, A. Horn, R. Bali, *Adv. Funct. Mater.* 2023, 2311951
- [2] T. Pflug, P. Cejpek, M. Olbrich, C. Wüstefeld, M. Ernstberger, M. Motylenko, D. Rafaja, A. Horn, *Optics & Laser Technology*, Volume 172, 2024, 110540



Laser-Based Powder Deposition to generate Electrical Conductivity on PES Fabric

Meda Sarath Chandra¹, Michael Seiler¹, Andrea Barz¹, Annika Gambke², Yashas Shivakumar², Julia Ullrich², Jens Bliedtner¹

¹Ernst-Abbe-Hochschule Jena, Carl-Zeiss-Promenade 2, 07745 Jena

²Textilforschungsinstitut Thüringen-Vogtland e. V., Zeulenrodaer Str. 42, 07973 Greiz

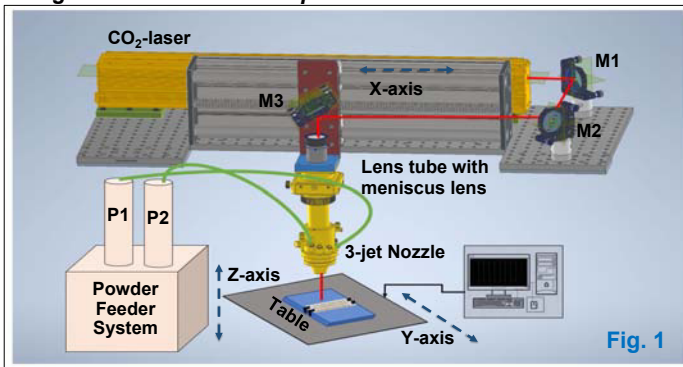
Fachbereich SciTec

Abstract

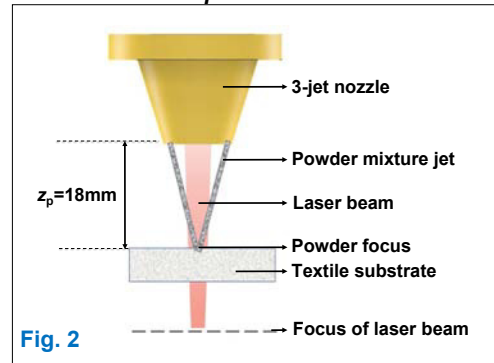
The research project with the Textile Research Institute Thuringia-Vogtland e.V. (TITV Greiz) developed a laser-based powder deposition process for achieving electrical conductive tracks on Polyethersulfone (PESU) fabrics. The one-step deposition of the process was developed at the University of Applied Sciences Jena (EAH Jena). With the help of a CO₂-laser, a mixture of TPU and metal powder is deposited onto the substrate surface. The machine setup has been designed, developed, and optimized for the new process. During the experiments, the feeding process of powder mixture, the programming of the applied structures, and the influence of laser parameters on the resulting tracks were investigated. To show the potential applications the formation of different geometries was confirmed. This technology is expected to add value to the production of electrically conductive textiles, offering fast production times, geometrical freedom and expanding the potential for smart textile applications.

Experimental and Measurement Setup

Design of the machine setup



Scheme of the Deposition Process

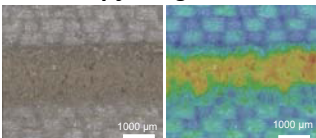


The process utilizes a custom-designed machine setup featuring a 30W Synrad CO₂-laser source. The laser beam is directed through a series of mirrors (M1-M3) and focused using a ZnSe meniscus lens with a focal length of 300 mm as shown in Fig. 1. The GTV powder feeder system delivers a mixture of TPU powder (P1) and Silver-coated Aluminum powder (P2) through a 3-jet nozzle onto the textile substrate. The laser radiation is defocused when it interacts with the surface. The powder jet is focused on the substrate which is positioned $z_p=18\text{mm}$ from the nozzle's bottom as shown in Fig. 2. The entire system is computer-controlled, while the axis movements are programmed and managed by Phylogic software. To investigate the key parameters optical microscopy (Keyence VHX 7000), electrical resistance measurements (Keithley multimeter 2001), and a digital dial indicator (Mahr METAV) were applied.

Results and Conclusion

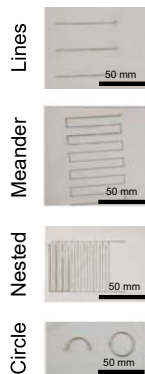
Process Test Parameters	
Power	2-20 W
Velocity	10-50 mm/sec
Defocus laser	47-87 mm
TPU	2.0 RPM
Metal Powder	1.3 RPM

Microscopy images

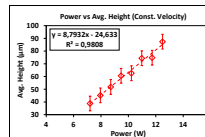
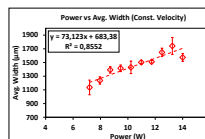


Left: normal light image and Right: color mapping of height of the same parameter combination

Geometries

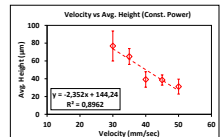
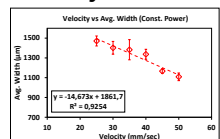


Power Variations



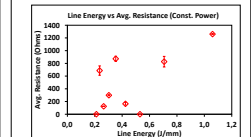
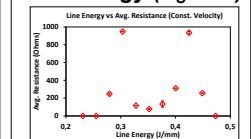
Strong correlation for power to Avg. width and Avg. height.

Velocity Variations



Strong correlation for velocity to Avg. width and Avg. height.

Line Energy ($E_s=P/V$)



Line Energy Bounds:
Const. Velocity:
 $0.26 < E_s < 0.47$
Const. Power:
 $0.21 < E_s < 1.06$

The laser-based powder deposition process has successfully created conductive tracks on PES fabric, demonstrating the ability to form geometries such as lines, meander structures, nested structures, and circles. With parameters set at 10.6 W power and 31.0 mm/sec velocity, the tracks were evenly deposited and exhibited proper conductivity without cuts.

Funding number IGF Nr. 22557 BR



Acknowledgements

We thank the Federal Ministry for Economic Affairs and Climate Action for funding the research project and all our industrial partners for the profound discussions during the meetings.



Layer-by-layer solidification of sodium silicate solutions using CO₂ laser radiation

Robin Hassel¹, Andrea Barz¹, Jens Bliedtner¹, Edda Rädlein²

¹University of Applied Sciences Jena, Carl-Zeiss-Promenade 2, 07745 Jena
²Ilmenau University of Technology, Ehrenbergstraße 29, 98693 Ilmenau

Objectives

Additive manufacturing processes enable the highly flexible and resource-efficient production of individual components from various materials. Alongside the growing demands for the accuracy and durability of 3D-printed parts, research is increasingly focusing on sustainable, reusable, and cost-effective material systems. For this reason, liquid alkali silicate glasses (water glasses) are being evaluated in the presented studies for their suitability as base materials for 3D printing. The approach is based on the layer-by-layer solidification of the liquid material through polycondensation reactions, induced by dehydration via CO₂ laser radiation ($\lambda = 10.6 \mu\text{m}$) [1].

Experimental setup

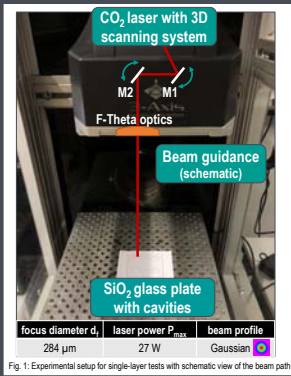


Fig. 1: Experimental setup for single-layer tests with schematic view of the beam path

Results of the single-layer-tests

Investigations of the interaction between laser radiation and material (sodium silicate 40/42)

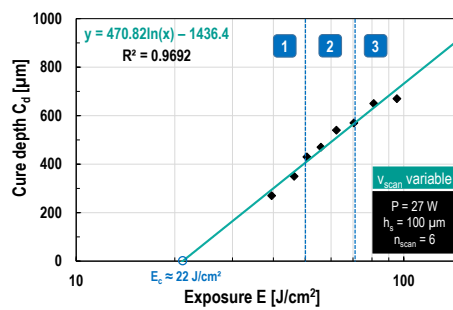
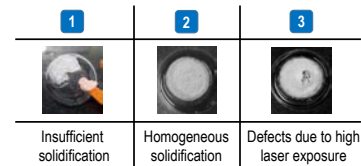


Fig. 2: Cure depth as a function of the logarithm of laser exposure for sodium silicate solution 40/42 [2]



$$(1) E_{max} = \frac{P}{v_{scan} \cdot h_s}$$

$$(2) C_d = D_p \ln \left[\frac{E_{max}}{E_c} \right]$$

Formulas for calculating maximum exposure (1) and cure depth (2) according to [3]

Additional results

Laser scanning strategy

- xy-hatch scanning (cross pattern) with constant hatch spacing is preferred
- Better crosslinking and contour fidelity compared to pure x-line scan

X-ray diffraction analyses (XRD)

- Clear evidence of X-ray amorphous samples

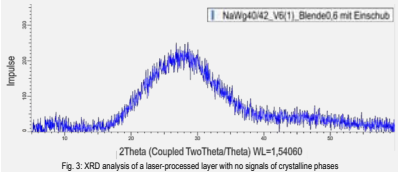


Fig. 3: XRD analysis of a laser-processed layer with no signals of crystalline phases

Chemical element analysis (SEM-EDX)

- Unwanted sodium accumulations (possibly Na₂CO₃) on the surface, likely formed by reaction with CO₂ from ambient air



Fig. 4: SEM image (1959x magnification) with EDX point analyses

- Not detectable within the layers
→ primarily silicate compounds there

Digital microscopy

- Hatch spacing (h_s) determines the degree of crosslinking within a layer

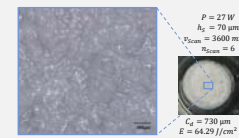


Fig. 5a: Digital microscope image of a single layer with h_s = 70 μm (100x magnification)

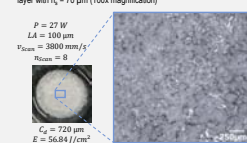


Fig. 5b: Digital microscope image of a single layer with h_s = 100 μm (100x magnification)

Outlook

Studies on process temperatures and laser-induced thermal stresses

Adjusted experimental setup (reproducibility, automation, resolution)

Adaptation of the process to 3D components and other water glass types

Research and testing of suitable additives for material modification

Conclusion: As part of our research, sodium silicate solutions are being examined for their suitability for additive manufacturing. The current experiments focus on investigating the fundamental interaction mechanisms between laser radiation and the material. To adapt the process for three-dimensional components and other types of alkali silicate solutions, adjustments to the experimental setup are essential.

[1] Bliedtner, J., et al. (2021). Verfahren zum dreidimensionalen additiven Aufbau eines Formkörpers aus Wasserglas (EP 3 566 868 B1). Europäisches Patentamt. <https://patents.google.com/patent/EP3566868B1/>
[2] Hassel, R., et al. (2023). Investigations on the layer-by-layer solidification of liquid alkali silicates using CO₂ laser radiation. Ilmenau, 06.09.2023. "Living Glass Surfaces XII", 60th Ilmenau Scientific Colloquium
[3] Jacobs, P.F. (1992). Rapid prototyping & manufacturing: fundamentals of stereolithography. Society of Manufacturing Engineers (SME). ISBN 978-0-872-634251

Contact:
Prof. Dr. Jens Bliedtner
phone: +49 3641 205 444
mail: jens.bliedtner@eah-jena.de

Acknowledgments: The research work presented here was primarily made possible by doctoral funding from the Ernst Abbe University of Applied Sciences Jena. We sincerely thank EAH Jena for its support of young academics, excellent infrastructure, and extensive professional development opportunities.

AG Bliedtner
www.ag-bliedtner.de

AI-based Part Recognition Based On Pointnet++

Sebastian Matthes, Patrick Ongom-Along, Sven Padutsch, Markus May



Motivation

In additive manufacturing, managing multiple repeat prints of identical or similar parts efficiently is a significant challenge due to the high demand for specific components and the variations among them. Quickly identifying and classifying these parts can greatly enhance time and resource efficiency, thus boosting overall productivity. This study aims to identify the most effective classification algorithms or AI techniques to address these challenges. Specifically, we explore advanced methods, including deep learning models like PointNet++ and Fourier transformations, to provide viable solutions.

Approach

Two methods for detecting similarities between 3D objects were compared: Fourier Fingerprint Search (FFS) and PointNet++. The FFS converts 3D objects into a frequency-based representation using Fourier transformations, extracting features that serve as an object's "fingerprint" for similarity comparison. PointNet++, a deep learning model, is designed specifically for point clouds, extracting global and local features of 3D objects. The methods' performance in recognizing 3D objects and their robustness to rotations and other transformations were evaluated, as well as their computational efficiency in terms of processing speed and scalability for real-time use.

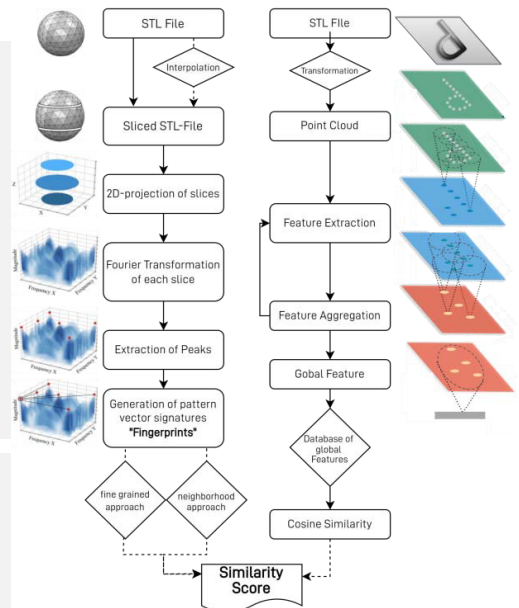


Figure: Schematic approach to similarity analysis of 3D components; left: Fourier fingerprint search; right: PointNet++

Results

Fourier Fingerprint Search (FFS)

- Rotational Robustness:
 - High consistency in similarity scores across various rotations.
 - Effective due to Fourier transformations applied to 2D projections of 3D objects.



Figure: Illustration of the Fourier Fingerprint Search (FFS) framework's handling of rotations

- Performance Metrics:
 - High precision in detecting exact and partial matches of 3D CAD models, effectively distinguishing between similar and dissimilar objects



Figure: Input of hex screw STL model from the FabWave dataset and similarity scores of best matches

- Limitations:
 - Reduced accuracy with highly deformed or incomplete objects
 - Decreased accuracy with significant topological changes



Figure: Test on database comprising 3000 randomly selected models from Thingiverse.com

PointNet++

- Generalization Ability:
 - Accurately identifies similarities in unseen classes, demonstrating strong adaptability



Figure: Input of hex screw and brackets STL model from FabWave dataset

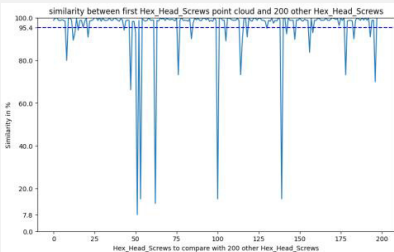


Figure: similarity score between a hex head screw and 200 other hex head screws from the FabWave dataset

- Computational Efficiency:
 - Overall faster processing and better scalability with large datasets due to direct feature extraction from point clouds, making it suitable for real-time use, especially with complex or diverse data.
- Quantitative Results:
 - Strong performance with non-rotated objects; less effective with rotations compared to FFS but generally more adaptable across different types of objects

Table: Comparison of similarity scores between hex head screws and brackets after rotation

Comparison	Screws		Brackets	
	- Screws	- Brackets	- Screws	- Brackets
Rotation	no	no	yes	yes
Average Similarity	95.4%	42.0%	88.3%	56.4%
Standard deviation	14.2	3.9	28.7	16.0

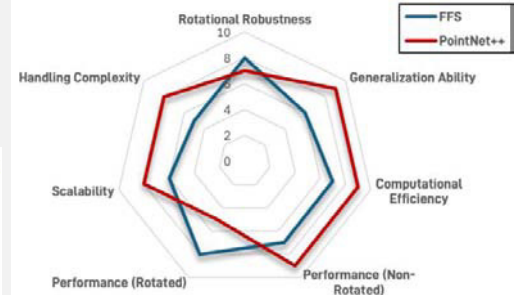


Figure: Comparison of FFS and PointNet++ Method

Conclusion

The results showed that PointNet++ achieved more accurate and consistent classification outcomes for 3D printed parts than Fourier Fingerprint Search (FFS), especially when dealing with complex geometries or diverse datasets. Leveraging its deep learning architecture, PointNet++ could distinguish finer differences between similar parts, resulting in higher classification accuracy. FFS, while faster in processing simpler objects, was less reliable with subtly varied or structurally complex objects. Therefore, our findings suggest that PointNet++ is more suitable for applications requiring adaptability and detailed feature extraction, whereas FFS may be preferred for simpler, less complex tasks.

Acknowledgement

The obtained results were achieved within the 3DOP project which has received co-funding from the EISMEA I3 program under grant agreement No. 101083997. Funded by the European Union. Views and opinions expressed are however those of the author(s) only and do not necessarily reflect those of the European Union or EISMEA. Neither the European Union nor the granting authority can be held responsible for them.



3Faktor GmbH Göschwitzstr. 22 07745 Jena
 Telefon: +49 (0) 3641 225 910 00 E-Mail: sebastian_matthes@3faktor.com
 Web: www.3faktor.com



Optical Characterization of Micro Spiral Phase Plates

S. Büttner, E. Thieme and S. Weissmantel

Laserinstitut Hochschule Mittweida, University of Applied Sciences Mittweida

Abstract: In 1992, Less Allen and colleagues could prove that Laguerre-gaussian laser modes carry orbital angular momentum (OAM) [1]. Subsequently, Allen and Padgett show that the OAM results form a helical-shaped wavefront and the helical trajectory of the Poynting vector [2]. That light can carry OAM led to a new understanding of photons and consequently to many new applications using this property, like the rotation of microparticles on a circular path in optical tweezers [3]. Moreover, it can be shown that single photons can carry OAM, and these quantum states can be entangled [4,5]. This enables the development of new quantum technologies with enormous potential [6-8]. However, the OAM can also be used to encode classical information for optical data transfer [9,10] and could increase the capacity of optical data communication channels. In our investigations, we focused on the generation of micro spiral phase plates (SPPs) in fused silica. Therefore, we developed a laser-based generation process and optical characterization method. These optical components can influence the OAM of transmitting electromagnetic fields and can be useful for future datacom and quantum optics applications.

Micro Spiral Phase Plates

The generation of micro spiral phase plates was done using the F_2 laser micro-structuring technique. This enables the generation of SPPs with different topological charges l , handedness, modulation depths m and level numbers N . Due to the high photon energy of the used laser of 7.9 eV, processing synthetic fused silica is possible. Moreover, the use of two semi circular masks enables the generation of a variety of different configured SPPs (Fig. 3). Therefore, the OAM can be influenced in a defined way.

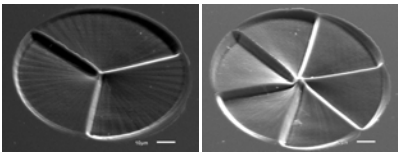


Fig. 1 and Fig. 2: SEM images of a 16-level SPP with a modulation depth of two and three phase jumps (l) and a 32-level SPP with a modulation depth of four and six phase jumps (r)

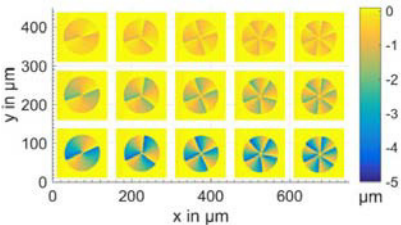


Fig. 3: Confocal microscope images of the generated SPPs with different numbers of phase jumps, modulation depth ($m = 1,2,4$ top to bottom row) and topological charges ($l = 2,3,4,5,6$ left to right).

Measurement Setup

The optical characterization was done using a frequency doubled Nd:YAG laser ($\lambda = 532 \text{ nm}$) as a back illumination source and a microscope, which can be moved along the optical axis of the SPPs. This allows to capture the optical response at defined distances to the SPPs. From the captured diffraction images, the rms and maximum radius of the ring-shaped distributions can be determined, as well as the divergence angle. For this we used a measurement beam with a beam waist of $37 \mu\text{m}$. Alternatively, we use a $90 \mu\text{m}$ beam waist for the generation of interferograms. Due to the beam waist being in the range of the SPP diameter ($100 \mu\text{m}$), interference between the modulated and unmodulated proportion of the transmitting field occurs, and the diffraction images show characteristic spiral intensity maxima. The number of maxima represents the number of intertwined phase fronts, which is directly related to the topological charge.

Calculations

Comparing the interferograms with the appropriate SPPs, it can be shown that the modulation depth and the number of phase jumps act on the transmitting field in the same way (compare Fig. 3 and Fig. 4). Therefore, we assume for our calculations that the topological charge follows eq. 1.

$$l = m \cdot j \quad (1) \quad E(x, y, z) = \frac{1}{r} \int \int E(x_0, y_0) e^{-ikr} dx_0 dy_0 \quad (2)$$

To verify the measurement results, the optical response was calculated using the diffraction formula (eq. 2). Moreover, we assume a gaussian distributed field in the form of eq. 3, which is in good agreement with the intensity distribution of the measurement laser. The sign of l represents the sense of rotation of the phase, which is also called handedness.

$$E(x, y, z_0) = E_0 \cdot e^{-\frac{x^2}{w_0^2}} \cdot e^{i2\pi l \phi} \quad (3)$$

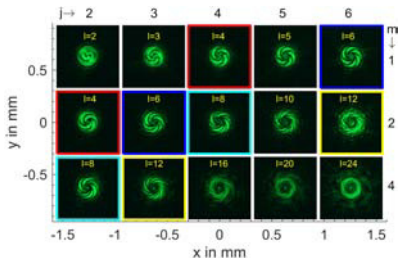


Fig. 4: Interferograms of the SPPs with different numbers of phase jumps, modulation depth and topological charges.

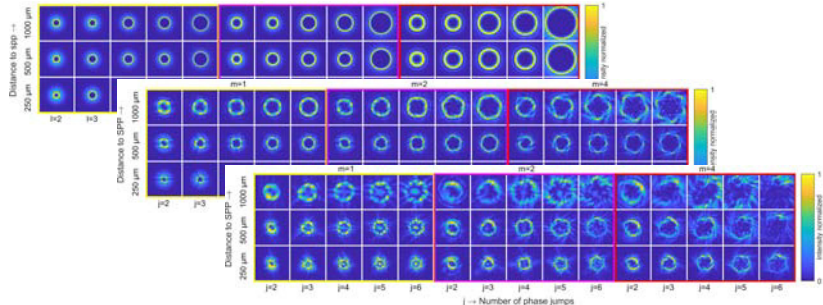


Fig. 5: Calculated ideal intensity distributions (top), calculated intensity distributions in consideration of the phase deviations (center) and measured intensity distributions for different topological charges, modulation depths and distances (bottom).

Results and Discussion

The comparison of the interferograms of SPPs with the same topological charge shows the same number of curved intensity maxima, since the modulation depth and the number of phase jumps have the same effect. Some of the interferograms also show asymmetries in the intensity distribution resulting from geometrical asymmetries and irregularities of the SPPs. In addition, the interferograms of SPPs with a topological charge >12 show strong scattering and distortion (Fig. 4). As the modulation depth increases with the number of steps N , the sloped region increases because the edges of the ablation regions are sloped. The slanted areas contain different phase information and do not contribute to the ideal helical phase. Therefore, the slope edges had a negative effect on the resulting wave front and increased the losses and distortion within the diffraction image. However, the results of the calculations are in good agreement with the measured radii of the intensity distributions (Fig. 6). As can be seen in Fig. 5, the measured intensity distributions (bottom) differ from the ideal ones (top). The deviation of the structure depth led to an inaccuracy of the phase modulation. Due to this, the diffraction images show several intensity maxima within the general ring-shaped intensity distributions. This is typically for fields with fractional topological charge. In consideration of the phase deviations, the calculated distributions also show these maxima (center). Moreover, the calculated radii are closer to the measured ones when the phase deviations are considered (Fig. 6). Nevertheless, the calculated radii are smaller than the measured ones, as is the divergence angle of the propagating fields. The reason for this could be a curved wavefront of the measurement laser. For future investigations, the setup will be improved by a wavefront sensor. As our calculations show, the rms and maximum radii depend linearly on the topological charge in the far field (Fig. 8) and the distance to the SPP (Fig. 9). This fulfills the expectations from a theoretical approach, which was given by Padgett [11]. Currently we are not able to capture diffraction images in the far field due to the scattering and distortion (Fig. 7).

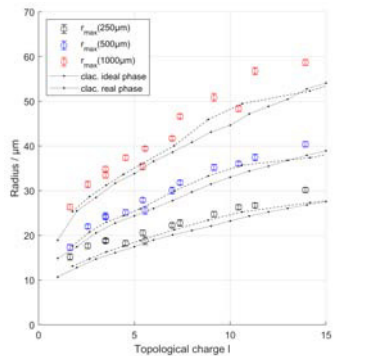


Fig. 6: Measured and calculated radii of the maximum ring-shaped intensity distributions depending on the topological charge.

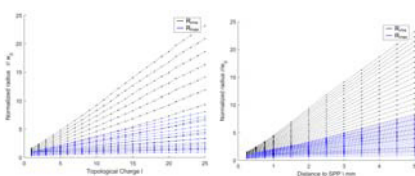


Fig. 8 and Fig. 9: Maximum and rms radius of the ring-shaped intensity distributions depending on the topological charge (up to 25) and for a distance from $250 \mu\text{m}$ to 5 mm .

Conclusion

We show the results of our investigations on the optical characterization of laser-fabricated micro SPPs. Therefore, we used two measurement configurations. The interferograms show the number of intertwined phase fronts and the equality of the modulation depth and number of phase jumps. Both act on the topological charge in the same way, and the resulting topological charge is the product of both parameters. Moreover, we captured the diffraction images with a reduced beam radius to suppress the interference between the modulated and unmodulated proportions of the propagating field. It could be shown that the calculated maximum radii of the ring-shaped intensity distributions are in good agreement with the measured. In consideration of the measured phase deviations, the values are getting even closer to the measured ones. The reason for the remaining deviations could be an uneven wave front in the modulation plane. Future, the measurement setup will be improved by adding a wavefront sensor. We also will improve the quality of the SPPs using a new micro-structuring method, which allows us to generate a variety of different SPPs with a continuous surface profile. This can reduce scattering and phase distortion and improve the conditions for the measurement. Finally, we will extend the range of our investigations regarding the topological charge and propagation behavior to the far field. This may connect our experimental data to the far field approximation of Padgett and colleagues [11].

References

- [1] Allen, L. et al. (1992). Physical Review A, 45(11), pp. 8185-8189.
- [2] Allen, L., Padgett, M. (2011). WILEY-VCH Verlag GmbH, pp. 1-12.
- [3] Grier, D. A. (2003). Nature 424, pp. 810-816.
- [4] Mair, A. et al. (2001). Nature, 412, pp. 313-316.
- [5] Fickler, R. et al. (2012). Science, 338(6107), pp. 640-643.
- [6] Fickler, R., et al. (2014). Nature Communications, 5:4502, pp. 1-6.
- [7] Cardano, F., et al. (2015). Science Advances, 1(2), p. e1500087.
- [8] Krenn, M., et al. (2017). Philosophical Transactions of the Royal Society A: Mathematical, Physical and Engineering Sciences, 375(2087).
- [9] Zhu, L., et al. (2018). Opt. Lett. 43, p. 1894-1897.
- [10] Xie, Z., et al. (2018). Photonics Research, 6(7), pp. 743-749.
- [11] Padgett, M., et al. (2015). New Journal of Physics, 17(2), p. 023011-.

Laserinstitut Hochschule Mittweida
 Technikumplatz 17, 09648 Mittweida
 Sebastian Büttner M. Sc.
 buettner@hs-mittweida.de | 03727/581373
 www.laser.hs-mittweida.de



Long-term stable 120W fiber CPA with 1.3GW peak power at 2 μ m central wavelength

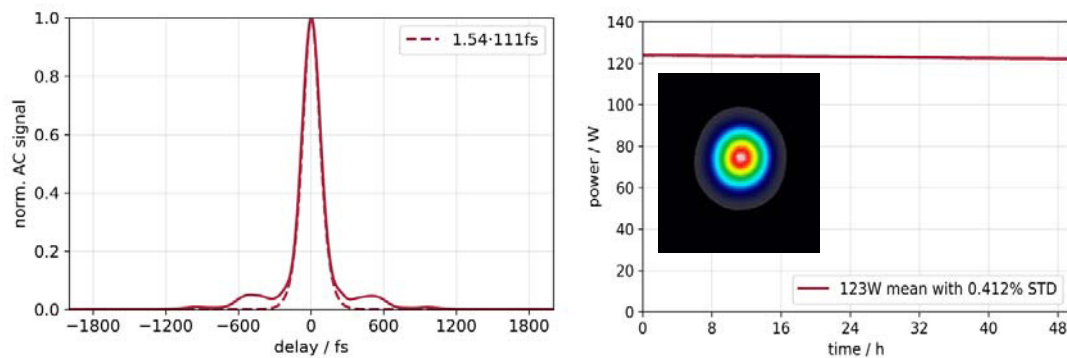
Christian Gaida, Tobias Heuermann, Oliver Herrfurth, Sven Breitkopf,
Tino Eidam*, Jens Limpert

Active Fiber Systems GmbH, Ernst-Ruska-Ring 17, 07745 Jena, Deutschland

*Corresponding author: publications@afs-jena.de

We present a high-power coherently combined thulium-doped fiber CPA system delivering over 228 μ J of pulse energy with a pulse duration of less than 120 fs at a repetition rate of 500 kHz. It demonstrates excellent long-term stability, with average power fluctuations of less than 0.5% RMS over more than 48 hours of operation, even at average power levels exceeding 120 W.

Thulium-doped fiber lasers have emerged as promising and straightforward candidates for creating efficient, high average- and peak-power ultrafast lasers in the 2 μ m wavelength range [1,2]. In this work, we demonstrate the coherent combination of four thulium-doped fiber amplifiers within a chirped-pulse amplification (CPA) scheme. Operating at a pulse repetition rate of 500 kHz, each channel produces a pulse energy of 67 μ J, resulting in an average power output of 33.5 W at a pump power of approximately 110 W and a center wavelength of 1940 nm. With a total combining efficiency of 95% and a compression efficiency of 90%, the laser system achieves a pulse energy of 228 μ J and a compressed pulse duration of less than 120 fs. Assuming conservatively that more than 70% of the pulse energy is contained in the main feature, the system delivers a peak power exceeding 1.3 GW. The laser system has been continuously operated and characterized over several days, maintaining an average output power of 123 W with excellent long-term stability, showing power fluctuations of less than 0.5% RMS over 48 hours. The Thulium-doped fiber provides a near diffraction-limited output beam ($M^2 < 1.2$), as confirmed by previous studies. Thanks to operating the high-power sections in a vacuum and using high-power optics, the excellent beam quality is preserved throughout the laser system and is available at the output. These output characteristics make this laser system uniquely suited for demanding scientific and industrial applications.



Left: Second-harmonic autocorrelation function of the output pulse corresponding to a pulse duration of <120fs (111fs, assuming sech²-shape) at 228 μ J pulse energy. Right: Average-power measurement over >48h operation time. The inset shows the output beam at the highest power level.

References

- [1] C. Gaida et al., "Thulium-doped fiber chirped-pulse amplification system with 2 GW of peak power", Opt. Lett. 41, 4130-4133 (2016).
- [2] C. Gaida et al., "Ultrafast thulium fiber laser system emitting more than 1 kW of average power", Opt. Lett. 43, 5853-5856 (2018).
- [3] M. Chambonneau, L. Lavoute, D. Gaponov, V.Y. Fedorov, A. Hideur, S. Février, S. Tzortzakis, O. Utéza, and D. Grojo, "Competing Nonlinear Delocalization of Light for Laser Inscription Inside Silicon with a 2- μ m Picosecond Laser", Phys. Rev. Appl. 12, 1 (2019).

Acktar coatings for stray light suppression in FSO

Alexander Telle^{1(*)}, Chen Orenshtein²



www.acktar.com

¹ACM Coatings GmbH (subsidiary of Acktar Ltd.), Jakobsring 3, 06618 Naumburg (Saale), Germany

²Acktar Ltd., 19 Topaz St., 8213513 Kiryat-Gat (Israel)

(*) alexander.telle@acktar.de

INTRODUCTION

Free Space Optical (FSO) communication systems use laser technology to transmit high-bandwidth data through space, offering secure, high-speed connections. Ensuring optimal signal integrity in these systems requires precise control of optical phenomena, especially stray light. With over 30 years of expertise, Acktar Ltd. provides advanced solutions to enhance FSO system performance by effectively managing stray light.

ACKTAR'S ROLE IN ENHANCING FSO SYSTEMS

- **Signal Isolation:**
Acktar coatings are employed on the internal surfaces of FSO terminal to reduce stray light reflections, thus ensuring the division between the uplink and downlink signals.
- **Beam Dumping:**
Acktar coated beam dumps also allow for a safe disposal of unwanted laser beams and reflections, improving signal quality and preventing damage to components. The coating's high emissivity also contributes to heat dissipation.
- **Sensor Protection:**
In cases of optical misalignment, the laser transmission might hit and damage components around the detector. This can be prevented by applying Acktar's high LIDT coatings on and around the sensor.

STRAYLIGHT IN FSO SYSTEMS

- **Straylight** refers to unintended light that enters an optical system and scatters or reflects within it, potentially interfering with the intended signal or image.
- **Signal Isolation:**
In FSO systems, signal isolation is critical to prevent the transmitted and received signals from interfering with each other. Stray light, caused by internal reflections, can lead to overlap between these signals, degrading communication quality.
- **Localized heating and material damage:**
Unwanted laser beams focusing on surfaces can lead to localized heating and damage to surfaces and optical components.



Acktar's advanced black coatings are strategically applied to absorb excess laser light, minimizing unwanted reflections and enhancing signal integrity.



VACUUM BLACK and MAGIC BLACK

Acktar's Vacuum Black and Magic Black coatings are the coatings of choice when it comes to suppressing straylight in FSO. Except their exceptional optical performance, the coatings deliver many other properties, such as:

- Essentially zero outgassing
- Vacuum and thermal-vacuum for cycling qualified
- Operating temperatures from (-)269°C to (+)350°C
- No participation
- Only a few microns thick (5 - 14 micron)
- Compatible with virtually all substrate materials

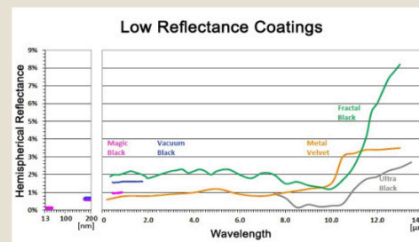


Credit: NASA/Dave Ryan

Both coatings are space qualified, and have been tested and qualified for thermal cycling, thermal vacuum cycling, cryogenic temperatures performance, outgassing, atox, reflectance after environmental exposure, adherence.

CONCLUSION

Acktar Ltd.'s high-performance black coatings are critical to the optimization of space-based FSO communication systems. By managing stray light and mitigating internal reflections, these coatings enhance signal fidelity, reduce optical noise, and safeguard sensitive components.



Acktar coatings' hemispherical reflectance as a function of wavelength

Headquarters:

Acktar Ltd.
Kiryat Gat, Israel
customer-support@acktar.com
+972-6-6814213

European subsidiary:

ACM coatings GmbH
Naumburg (Jena area)
info@acktar.de
+49-16097232200



Laser micro welding of thin multi-layered connections

Frank Rempt¹, Michael Güpner¹, Andreas Hopf¹, Jens Bliedtner¹

¹Ernst-Abbe-Hochschule Jena, Carl-Zeiss-Promenade 2, 07745 Jena

Approach & state of the art

Pouch cell for battery electric vehicles

[1] <https://ionknowledge.com/5-bauformen/5-3-pouch-zellen/ngallery/image/anode-kathode-in-grafik/>

Welding Situation:
Connection of thin multi-layered electrode foils to tab.

Conventional solution: Ultrasonic welding

Process causes high plastic deformations and defects in the upper thin foils due to the high mechanical forces

Alternative solution: laser welding with adapted clamping system

Experimental setup & patented clamping device

high-speed camera
3D scanning unit
pyrometer

feeding fibre
collimation
f-theta-lens
illumination LED
scanning field
x-y stage

3D scanning system coupled with a single-mode fibre laser from the company Coherent Inc. (focal diameter 20 – 85 μm, maximum output power 1.5 kW)

Step 1: Clamping upper foil

Step 2: Elastic deformation of the foil into a U-shape

Step 3: Transfer of deformation force to lower foil

Comparison between conventional fixture with clamping jaws (a) and the patented clamping system (b) (DE 102017128398 B3) with less distortion at the same welding parameters

First Results

Process window pure aluminium:
Thickness of a single foil: 20 μm
Thickness of the stack: 200 μm

Feeding rate in m/s vs Laser power in W

Conduction welding limits the process windows at power values smaller than 200 W. Higher power levels above 350 W are causing high process speeds of approximately 1.5 m/s. Melt pool instabilities, such as pre-humping and humping occur, reducing the quality of the weld seam.

Cross-sectional area of the aluminium foil stack (a) and the stack-to-tab weld (b). Welding parameters used: 250 W, 0.4 m/s. Due to the higher material thickness of the stack-to-tab connect, a higher power amount of 400 W is required to achieve full penetration welding.

First trails with pure copper: The small material thickness of the foils is an advantage in the processing of copper. As described in [2], the resulting high feeding rates lead to a stable melt pool. The laser micro welding process produces, homogeneous, defect-free weld seams (a), that are comparable in shape to (b) laser macro welding [2] of copper.

Comparison of cross-sections between a single foil with a material thickness of 100 μm and multi-layer system with 10 x 10 μm. The process parameters are directly transferable. A zero-gap condition is shown.

Conclusion and Outlook The initial version of the patented clamping system is a suitable solution for laser micro welding of thin multi-layered joints. Stacks of pure aluminium or copper with 10 layers can be welded with zero-gap between the joining partners. The next steps in the research project are the adaption and redesign of the clamping system to create stacks consisting of 20 to 50 layers. The target material thickness of a single foil is 5 μm. Electrical resistance and the tensile strength will be tested.



Laser material processing of ceramic foam materials

Andreas Hopf, Kerstin Götze, Jens Bliedtner
Ernst-Abbe-University of Applied Sciences, Carl-Zeiss-Promenade 2, 07745 Jena

Objectives

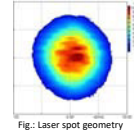
Technical ceramics are high-performance materials and their unique properties enable them to be used in highly stressed assemblies, at extreme temperatures or in aggressive environments. The const-intensive production is a disadvantage for widespread use, which often makes potential applications unusable. The research project intends to produce foam ceramics. Various components, such as ceramic particles, polymers and foaming agents are combined to form a compound for the production of green parts by material extrusion. The green parts are intended for a subsequent sintering process. After the extrusion process, a shaping process takes place in the green state. Laser material processing is used to segment the extruded sheet material economically and process it close to the near net shape. Appropriate process windows for high-quality laser material processing are to be determined experimentally for various compounds. One aim is to be able to provide flexible and customizable green processing for the entire process chain.

Materials and Methods

The investigations are carried out using a Slablaser „DC 020“ by Coherent Corp. (*Rofin-Sinar Laser GmbH*). For the development of the process models, injection molded samples from PE-LD / Al₂O₃ compounds are used. The ceramic powder content is 30, 35, 40, 45 and 50 vol%. Furthermore, various foaming agent concentrations are added to the compounds. The dimensions of the samples are 60 x 60 x 3 mm³.

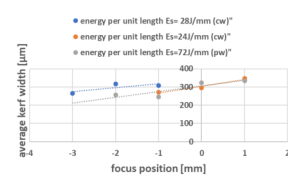
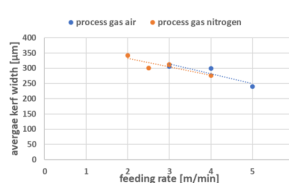
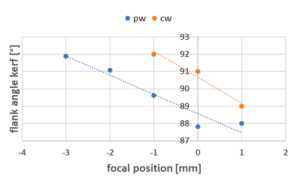
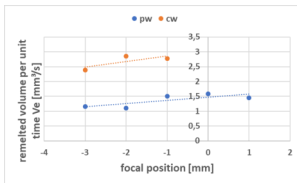
Experimental setup

- V_{Max} = 20 m/min
- λ = 10,6 μm
- P_{Max} = 2000 W
- puls length: 200 μs – continuous wave (cw)
- focus diameter: 180 μm



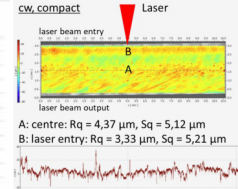
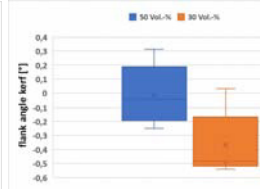
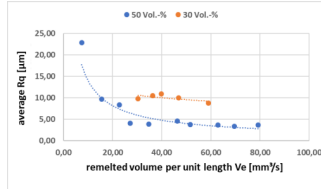
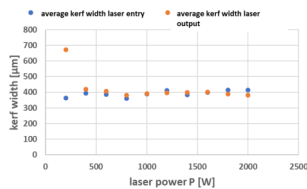
Preliminary investigations

The preliminary tests on the composite materials are intended to characterize the influence of the cutting gas, focus position, gas pressure and operating mode in relation to the kerf and its quality. The test showed, that the cutting gases used had no significant influence on the cutting quality. The flank angle, the kerf width and the melted volume per time unit depend on the selected focus position. For cw operating mode, the optimum focus position is 1 mm above the component surface, whereas for pw (pulsed operating mode), the focus should be placed below the components surface. Furthermore, it was found that cw operating mode had a better thermal efficiency than pw operating mode. The parameters from the preliminary tests on the dense samples were transferred to the samples supplemented with foaming agents. This revealed, that the foaming agent content has no significant influence on the flank angle and the kerf.



Further investigations

Based on the preliminary investigations, process parameters such as cutting gas type, gas pressure, focus position and operating mode could be determined. Further investigations will examine the process with regard to increasing efficiency. Various tests were carried out with different laser powers and feed rates. The results were evaluated on the basis of the flank angle, square roughness Rq and root mean square height Sq. The tests were carried out at constant energy per unit length. A larger kerf width can be seen at low laser power. Above a certain laser power value, a constant kerf can be measured. The similar effect can be seen in the surface qualities at the cutting edge. At low remelted volume per unit time, poorer surfaces can be detected. From a certain speed and melt volume, a constant surface quality is achieved. The achievable flank angle is 90° ± 0,5°.



Results

It was proven, that by optimizing the process parameters, a stable and efficient post-processing method for green composite materials using laser material processing is possible. Currently, investigations are in progress to transfer the generated process windows to complex contours. In addition, further experiments will be conducted to further increase process efficiency without reducing the required cutting quality. The knowledge acquired will later be transferred to extruded continuous strands in the project.

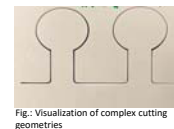


Fig.: Visualization of complex cutting geometries

The article presents results from the research and development project „KeraSchaum“ (reference number 03LB2044D), which is funded by the Federal Ministry for Economic Affairs and Climate Action of Germany (BMWK). The authors are responsible for the content of the publication.

Ernst-Abbe-University of Applied Sciences Jena
Prof. Dr. Jens Bliedtner
Carl Zeiss Promenade 2 | D-07745 Jena
Tel. +49 3641 205 444
E-Mail: Jens.Bliedtner@eah-jena.de
www.ag-bliedtner.de





Development of a laser-based dosing unit for the process of material extrusion

Denis Just, Andreas Hopf, Jens Bliedtner
Ernst-Abbe-University of Applied Sciences, Carl-Zeiss-Promenade 2, 07745 Jena

Objectives

The aim of the research project is to develop a dynamic laser-based switch to allow extrusion processes to be designed more flexibly and precisely. To achieve this, a temperature-controlled material flow is to be investigated. The objective is to develop and implement the dynamic laser-based switch as an example for an extrusion-based 3D printing process. If the project is successful, both the component quality can be significantly improved and the currently required extruder heating and changing times can be minimized. The principle is to heat the granulate slightly below the softening temperature. Laser irradiation is intended to bridge the temperature difference to the melting temperature, enabling the material to flow. If the material flow is to be stopped, the laser is switched off and the nozzle cools down with the aid of a cooling medium. The process is described in the patent specification EP 3558634 B1.

Extruder set-up

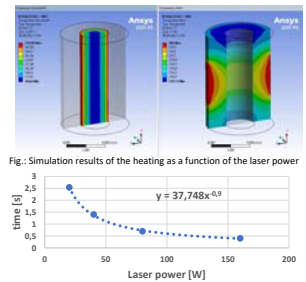
- single-screw extruder „ExOn8“ (Dohle Extrusionstechnik GmbH)
- 180 mm heating zone
- option for different nozzles
- extension of the set-up with temperature sensor and thermographic camera
- cooling by compressed air



Fig.: Extrusion System

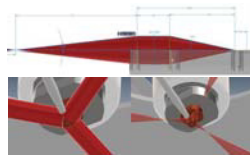
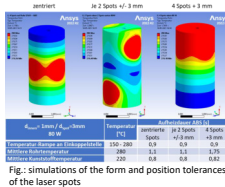
Simulation

- simulation of the heating of the nozzle as a function of the exposure and the heating rate of the respective thermoplastics (ABS, SAN, PP) → target temperature of 220 °C at the strand core
- simulation of various nozzle concepts → derivation of the optimal design
- development of a formal correlation between material heating time and required heating power



Design of the optical path

- design of the optical path for exposure of the extruder nozzle → focused or defocused
- fiber-coupled diode lasers (laser power 30 W) → characterization of the diode lasers (focus diameter, divergence, Rayleigh length) → design for optical beam focusing system
- flexible design of the optical system → variation of the raw beam diameter
- definition of the tolerances of form and position for the laser spots on the nozzle verified by simulation



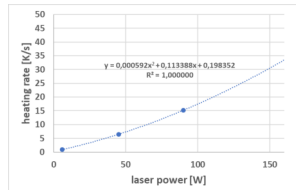
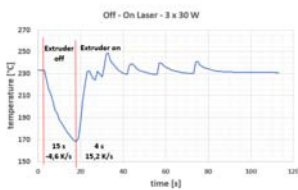
Experimental set-up

- constructive design and realization of the experimental set-up
- investigation of various nozzle materials, brass and copper with and without coating → coating reduced the degree of reflection to 3 %
- alignment of the diode lasers to the extrusion nozzle
- implementation of the temperature sensors and thermographic camera
- development and implementation of the temperature control system (laser diodes, cooling system) and integration of the metering technology into the user interface for the closed-loop control
- commissioning of all components



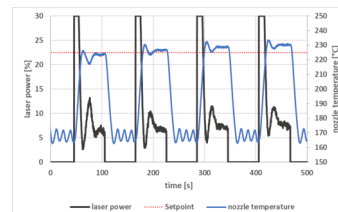
Preliminary investigations

- the nozzle was exposed with all three laser diodes at different power levels
- the heating zones of the extruder were set to 170 °C → measurement of the heating rate until the target temperature of 230 °C has been reached on the nozzle surface
- when heated with a laser power of 90 W, the system achieves a heating rate of 15.2 K/s
 - formal derivation from the test results to determine the heating rate in relation to the laser power
 - integration of the results into a higher-level control system to regulate the temperature input in order to avoid overshooting



Results and prospects

- development of a laser system with beam path, cooling system and extruder unit, as well as its transfer to an experimental set-up
- proof of concept of the start-stop function for material extrusion using laser heating
- development of a control system to regulate the nozzle temperature → reduction of nozzle temperature overshooting
- heating rates of up to 15.2 K/s, depending on the configuration
- in the next steps, the developed material dosing system is to be used and tested in the real additive manufacturing process of material extrusion (MEX)



The article presents results from the research and development project „Laser-FLM“ (reference number KK5091609CM1), which is funded by the Federal Ministry for Economic Affairs and Climate Action of Germany (BMWK). The authors are responsible for the content of the publication.

Ernst-Abbe-University of Applied Sciences Jena
Prof. Dr. Jens Bliedtner
Carl Zeiss Promenade 2 | D-07745 Jena
Tel. +49 3641 205 444
E-Mail: Jens.Bliedtner@eah-jena.de
www.ag-bliedtner.de





Funded by the European Union



Ernst-Abbe-Hochschule Jena University of Applied Sciences

Multi-sensors in the field of DED-LB/M

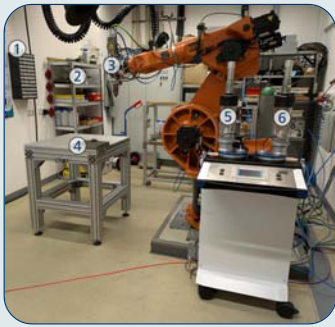
Michael Güpner¹, Frank Rempt¹, Jens Bliedtner¹, André Bötticher², Mathias Möser², Jörg Weber²

¹Ernst-Abbe-Hochschule Jena, Carl-Zeiss-Promenade 2, 07745 Jena

²orbit Sensorfusion GmbH, Engelplatz 11, 07743 Jena

The EMuPro research project is focused on the monitoring of powder based manufacturing processes using multi-sensing systems. Orbit Sensorfusion GmbH, a project partner is developing a system in cooperation with the EAH Jena for direct energy deposition. This additive manufacturing process is connected to a lot of influencing factors and process parameters. In addition to the selected process parameters, the quality of the welding result is dependent on the properties of the metal powder. Welding defects can be caused by critical ambient conditions such as high humidity. Using a multi-sensing system, the ambient conditions and the process can be monitored to avoid defects.

Approach & experimental setup



Measuring positions in robot cell for direct energy deposition with laser beam and metal powder:

- 1) lab climate
- 2) powder containers
- 3) welding head
- 4) near DED process
- 5) powder storage 1
- 6) powder storage 2

Multi-sensing approach:



Collecting data with gateway



Visualisation & analysis in dashboard



Different sensing units at relevant measuring positions



Upload & storage in data base

Detectable parameter per sensing unit:

humidity

light intensity

air pressure

temperature

solid angle

magnetic field change

CO₂-content

acceleration

pollutants

air quality index

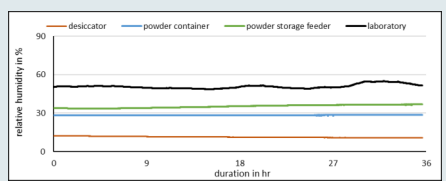
Results

Humidity in different powder storing situations:





Measuring the air humidity in a desiccator, a conventional powder container and in the powder storage of the feeder.

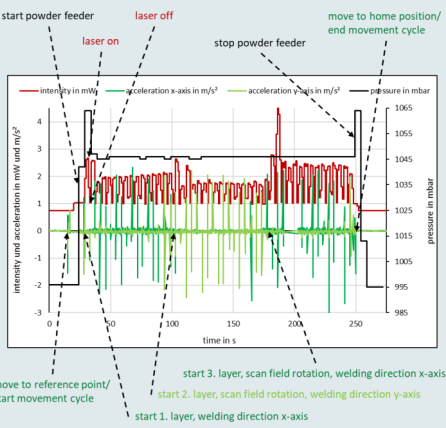


Nearly constant air humidities were detected at the tested powder storages over a 36hr period, in comparison to the ambient condition in the lab. The conventional powder container showed nearly the same values like the powder storage of the feeder.

Testing the multi-sensing approach at the DED-LB/M process:



The multi-layer metal deposition process of a cuboid with an edge length of 30 mm was monitored. 14 infill tracks are combined with 2 border tracks. A uni-directional scanning strategy was used. The entire welding path was rotated 90° layer by layer.



By utilising data from the sensors 3, 4 and 5/6, it is possible to detect the powder feeding, the process light emission and direction of robot movement simultaneously. By analysing the acceleration and light emission together, it is possible to distinguish between position and welding movement. This allows for the identification of single tracks, single layers and the scanning strategy.

Conclusion

The multi-sensing approach enables continuous monitoring of the powder storage conditions. It is possible to detect ambient conditions in various situations simultaneously. This enables the early recognition of the need for powder drying processes. Deviations in the powder feed rate, which are caused by high values of humidity levels, can be avoided. At the DED-LB/M process, the process light, the change in pressure at powder storage of the feeder and the acceleration values of the robot can be detected. This could be an approach for an efficient and cost-effective solution for controlling the interaction of laser system, robot and powder feeder.

Kontakt
 Prof. Dr.-Ing. Jens Bliedtner
 jens.bliedtner@eah-jena.de
 Ernst-Abbe-Hochschule Jena
 Carl-Zeiss-Promenade 2
 07745 Jena

Dr.-Ing. Jörg Weber
 joerg.weber@orbit-sensorfusion.de
 orbit Sensorfusion GmbH
 Engelplatz 11
 07743 Jena

The results were part of a research project funded by the German state of Thuringia and co-funded by the European Union (European Regional Development Fund). (project-no.: 2023 VDY 0016)



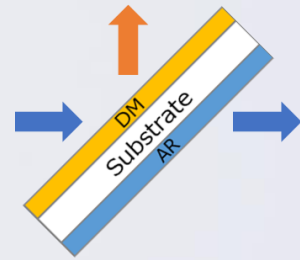
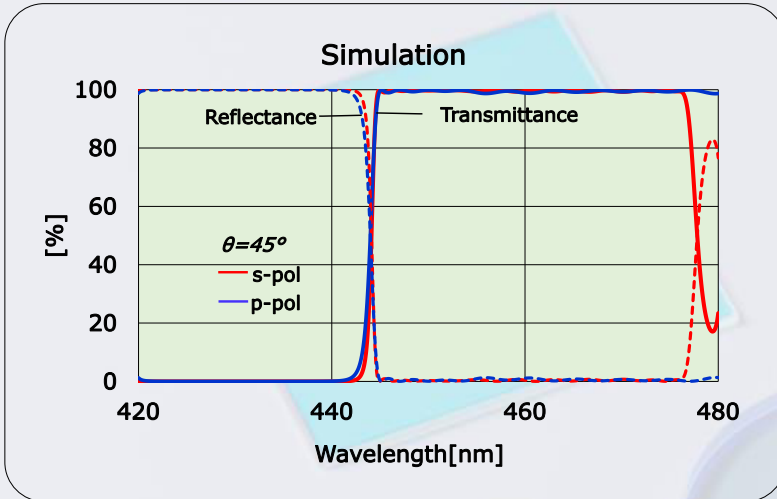


Optical products for blue lasers

Dichroic mirror

Advantage

Optical property with little polarization difference



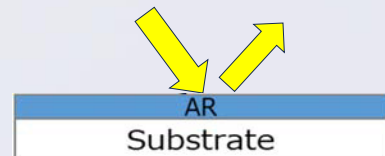
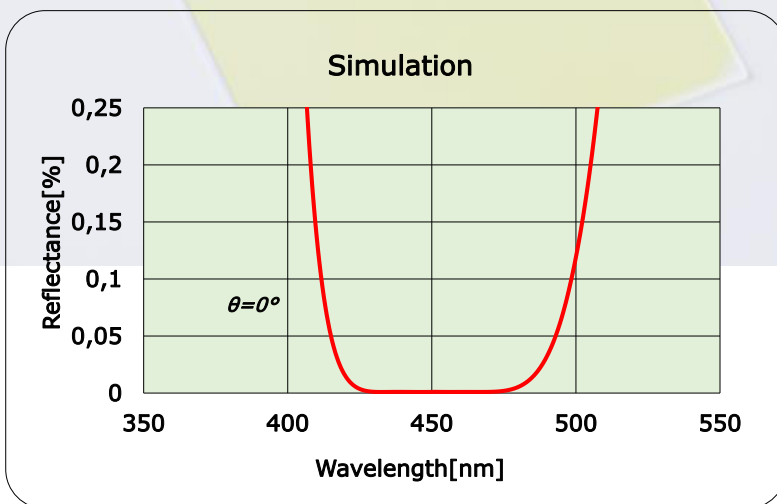
High reflectance:
 $R > 99\%$ at 440nm
High transmittance:
 $T > 97\%$ at 450nm

Steep spectral curve

Anti Reflection

Advantage

Super low anti-reflection



Anti-reflection:
 $R < 0.05\%$ at 440-460nm

Application

Laser processing · Fluorescence analysis

chance4change GmbH & Co. KG
 info@chance4change.de



www.ocj.co.jp

Shinmarunouchi Bldg.
 1-5-1 Marunouchi, Chiyoda-ku
 Tokyo 100-6530 Japan

Autor	Anschrift
Adomaitis, Martynas Msc.	OPTOMAN Ukmergės g. 427 LT-14185, Vilnius, Lithuania martynas.adomaitis@optoman.com
Aleshire, Christopher	Institute of Applied Physics, Abbe Center of Photonics Friedrich-Schiller-Universität Jena Albert-Einstein-Str. 15 07745 Jena, Germany
Andriukaitis, Deividas	EKSPLA UAB 237 Savanorių Av. 2300 Vilnius, Lithuania d.andriukaitis@ekspla.com
Banse, Henrik Dr.-Ing.	JENOPTIK Automatisierungstechnik GmbH Konrad-Zuse-Straße 6 07745 Jena, Germany henrik.banse@jenoptik.com
Barz, Andrea Dr.	Ernst-Abbe-Hochschule Jena Carl-Zeiss-Promenade 2 07745 Jena, Germany Andrea.Barz@eah-jena.de
Bäumel, Marcel	Thorey Gera Textilveredelung GmbH Lange Straße 71 07551 Gera, Germany m.baeuml@thotex.de
Berger, Niklas Dipl.-Phys.	Institut für Oberflächen- und Schichttechnik GmbH Trippstadter Straße 120 67663 Kaiserslautern, Germany and Landesforschungszentrum OPTIMAS RPTU Kaiserslautern-Landau 67655 Kaiserslautern, Germany berger@ifos.uni-kl.de
Bessler, Katharina M.Eng.	Capgemini Engineering Frankfurter Ring 81 80807 München, Germany katharina.bessler@capgemini.com
Bischoff, Christian	TOPAG Lasertechnik GmbH Nieder-Ramstädter Str. 247 64285 Darmstadt, Germany
Bliedtner, Jens Prof. Dr.-Ing.	Ernst-Abbe-Hochschule Jena Carl-Zeiss-Promenade 2 07745 Jena, Germany Jens.Bliedtner@eah-jena.de

Autor	Anschrift
Blothe, Markus M.Sc.	Friedrich Schiller University Jena, Institute of Applied Physics Abbe Center of Photonics, Albert-Einstein-Straße 15 07745 Jena, Germany markus.blothe@uni-jena.de
Bock, Wolfgang Dr. rer. nat. (Dipl.-Phys.)	Institut für Oberflächen- und Schichttechnik GmbH Trippstadter Straße 120 67663 Kaiserslautern, Germany and Landesforschungszentrum OPTIMAS RPTU Kaiserslautern-Landau 67655 Kaiserslautern, Germany bock@ifos.uni-kl.de
Boerner, Stephan	Fraunhofer Institute for Material and Beam Technology IWS Winterbergstraße 28 01277 Dresden, Germany
Breitkopf, Sven	Active Fiber Systems GmbH Ernst-Ruska-Ring 17 07745 Jena, Germany
Burkhardt, Immanuel	ROBUST AO GmbH Hans-Knöll-Straße 6 07743 Jena
Burkhardt, Thomas	Layertec GmbH Ernst-Abbe-Weg 1 99441 Mellingen thomas.burkhardt@layertec.de
Chambonneau, Maxime Dr.	Friedrich Schiller University Jena Institute of Applied Physics Abbe Center of Photonics Albert-Einstein-Straße 15 07745 Jena, Germany maxime.chambonneau@uni-jena.de
Christine Storch	Schott Technical Glass Solutions GmbH Otto-Schott-Str. 13 07745 Jena, Germany
Conrad, Daniel Dipl.-Ing. (FH)	ifw Jena - Günter-Köhler-Institut für Fügetechnik und Werkstoffprüfung GmbH Ernst-Ruska-Ring 3 07745 Jena, Germany dconrad@ifw-jena.de
Deparnay, Arnaud	Carl Zeiss Jena GmbH Carl-Zeiss-Promenade 10 07745 Jena
Dittrich, Dirk	Fraunhofer Institute for Material and Beam Technology IWS Winterbergstraße 28 01277 Dresden, Germany

Autor	Anschrift
Drechsler, Max	Layertec GmbH Ernst-Abbe-Weg 1 99441 Mellingen max.drechsler@layertec.de
Dreisow, Felix Dr.	Schott Technical Glass Solutions GmbH Otto-Schott-Str. 13 07745 Jena, Germany felix.dreisow@schott.com
Ehnert, Swen Dr. rer. nat. (Dipl.-Chem.)	Institut für Oberflächen- und Schichttechnik GmbH Trippstadter Straße 120 67663 Kaiserslautern, Germany and Landesforschungszentrum OPTIMAS RPTU Kaiserslautern-Landau 67655 Kaiserslautern, Germany ehnert@ifos.uni-kl.de
Eichler, Robert	Schott Technical Glass Solutions GmbH Otto-Schott-Str. 13 07745 Jena, Germany
Eidam, Tino	Active Fiber Systems GmbH Ernst-Ruska-Ring 17 07745 Jena, Germany
Eifel, Stephan Dr.	Pulsar Photonics GmbH Alte Würselener Straße 13 52080 Aachen, Germany info@pulsar-photonics.de
Engel, A.	Laserinstitut Hochschule Mittweida Technikumplatz 17 09648 Mittweida, Germany
Erler, Martin M.Sc.	Laserinstitut Hochschule Mittweida Technikumplatz 17 09648 Mittweida erler2@hsmittweida.de
Fischer, Matthias	ROBUST AO GmbH Hans-Knöll-Straße 6 07743 Jena
Fuchs, Ulrike Dr.	asphericon GmbH Stockholmer Str. 9 07747 Jena Germany u.fuchs@asphericon.com
Gaida, Christian	Active Fiber Systems GmbH Ernst-Ruska Ring 17 07745 Jena, Germany

Autor	Anschrift
Gečys, Paulius	Center for Physical Sciences and Technology Savanoriu Ave. 231 LT-02300 Vilnius, Lithuania
Gierschke, Philipp	Institute of Applied Physics, Abbe Center of Photonics Friedrich-Schiller-Universität Jena Albert-Einstein-Str. 15 07745 Jena, Germany and Fraunhofer Institute for Applied Optics and Precision Engineering Albert-Einstein-Str. 7 07745 Jena, Germany
Hanke, Philipp	Layertec GmbH Ernst-Abbe-Weg 1 99441 Mellingen philipp.hanke@layertec.de
Hashemzadeh, Mehri Dr.	INNOVENT e. V. Ilmstraße 18 07743 Jena, Germany M.Hashemzadeh@innovent-jena.de
Heinrich, Florian M.Sc.	Laserinstitut Hochschule Mittweida Technikumplatz 17 09648 Mittweida heinric1@hs-mittweida.de
Herrfurth, Oliver	Active Fiber Systems GmbH Ernst-Ruska-Ring 17 07745 Jena, Germany
Herrmann, J.	SCHOTT AG Hattenbergstraße 10 55122 Mainz, Germany
Heuermann, Tobias	Institute of Applied Physics, Abbe Center of Photonics Friedrich-Schiller-Universität Jena Albert-Einstein-Str. 15 07745 Jena, Germany and Active Fiber Systems GmbH Ernst-Ruska Ring 17 07745 Jena, Germany
Höche, T.	Fraunhofer Institute for Microstructures of Materials and Systems IMWS Walter-Hülse-Straße 1 06120 Halle (Saale), Germany
Horn, A.	Laserinstitut Hochschule Mittweida Technikumplatz 17 09648 Mittweida, Germany horn4@hs-mittweida.de

Autor	Anschrift
Jahn, Axel	Fraunhofer Institute for Material and Beam Technology IWS Winterbergstraße 28 01277 Dresden, Germany
Jahn, Simon Dr.	ifw Jena - Günter-Köhler-Institut für Fügetechnik und Werkstoffprüfung GmbH Ernst Ruska Ring 3 07745 Jena, Germany sjahn@ifw-jena.de
Jašinskas, Mantvydas	EKSPLA UAB 237 Savanori° Av. 2300 Vilnius, Lithuania
Jauregui, César	Institute of Applied Physics, Abbe Center of Photonics Friedrich-Schiller-Universität Jena Albert-Einstein-Str. 15 07745 Jena, Germany and Fraunhofer Institute for Applied Optics and Precision Engineering Albert-Einstein-Str. 7 07745 Jena, Germany
Jose, Anju	Schott Technical Glass Solutions GmbH Otto-Schott-Str. 13 07745 Jena, Germany
Katzer, Simeon	Carl Zeiss Jena GmbH Carl-Zeiss-Promenade 10 07745 Jena
Keça, Amorela B.Sc.	Friedrich Schiller University Jena Institute of Applied Physics Abbe Center of Photonics Albert-Einstein-Straße 15 07745 Jena, Germany amorela.keca@uni-jena.de
Knauff, Andreas B.Eng.	Ernst-Abbe-Hochschule Jena Carl-Zeiss-Promenade 2 07745 Jena, Germany Andreas.Knauff@eah-jena.de
Kohl, Hagen P.	Institute of Applied Physics, Abbe Center of Photonics Friedrich-Schiller-Universität Jena Albert-Einstein-Str. 15 07745 Jena, Germany hagen.kohl@uni-jena.de
König, Manfred	ifw Jena - Günter-Köhler-Institut für Fügetechnik und Werkstoffprüfung GmbH Ernst Ruska Ring 3 07745 Jena, Germany mkoenig@ifw-jena.de

Autor	Anschrift
Kraus, Mathias	Carl Zeiss Jena GmbH Carl-Zeiss-Promenade 10 07745 Jena Mathias.Kraus@zeiss.com
Kroll, Lothar Prof. Dr.-Ing. habil.	Technische Universität Chemnitz Professur Strukturleichtbau und Kunststoffverarbeitung Reichenhainer Straße 31/33 09126 Chemnitz, Germany slk@mb.tu-chemnitz.de
Kuckelkorn, Thomas	Schott Technical Glass Solutions GmbH Otto-Schott-Str. 13 07745 Jena, Germany
L'huillier, Johannes PD Dr. rer. nat. habil. (Dipl.-Phys.)	Institut für Oberflächen- und Schichttechnik GmbH Trippstadter Straße 120 67663 Kaiserslautern, Germany and Landesforschungszentrum OPTIMAS RPTU Kaiserslautern-Landau 67655 Kaiserslautern, Germany lhuillier@ifos.uni-kl.de
Lange, Johannes M.A.	ifw Jena - Günter-Köhler-Institut für Fügetechnik und Werkstoffprüfung GmbH Ernst Ruska Ring 3 07745 Jena, Germany jlange@ifw-jena.de
Langebach, Jan Dr.-Ing.	JENOPTIK Automatisierungstechnik GmbH Konrad-Zuse-Straße 6 07745 Jena, Germany jan.langebach@jenoptik.com
Lenski, Mathias	Institute of Applied Physics, Abbe Center of Photonics Friedrich-Schiller-Universität Jena Albert-Einstein-Str. 15 07745 Jena, Germany mathias.lenski@uni-jena.de
Limpert, Jens	Institute of Applied Physics, Abbe Center of Photonics Friedrich-Schiller-Universität Jena Albert-Einstein-Str. 15 07745 Jena, Germany and Fraunhofer Institute for Applied Optics and Precision Engineering Albert-Einstein-Str. 7 07745 Jena, Germany and GSI Helmholtzzentrum für Schwerionenforschung Planckstraße 1 64291 Darmstadt, Germany and ... <i>continued on next page</i>

Autor	Anschrift
Limpert, Jens	<i>continued from previous page</i> Helmholtz-Institute Jena Fröbelstieg 3 07743 Jena, Germany and Active Fiber Systems GmbH Ernst-Ruska-Ring 17 07745 Jena, Germany
Ludwig, Andreas	Thorey Gera Textilveredelung GmbH Lange Straße 71 07551 Gera, Germany a.ludwig@thotex.de
Lundén, H.	SCHOTT Primoceler Oy Vesiroineenkatu 3 33720 Tampere, Finland
Määttänen, A.	SCHOTT Primoceler Oy Vesiroineenkatu 3 33720 Tampere, Finland
Mäder-Heinrich, Marisa	Fraunhofer Institute for Microstructures of Materials and Systems IMWS Walter-Hülse-Straße 1 06120 Halle (Saale), Germany
Markogiannaki, Styliani M.Sc.	Friedrich Schiller University Jena Institute of Applied Physics Abbe Center of Photonics Albert-Einstein-Straße 15 07745 Jena, Germany s.markogia@gmail.com
Matthäus, Lisa	Institute of Applied Physics, Abbe Center of Photonics Friedrich-Schiller-Universität Jena Albert-Einstein-Str. 15 07745 Jena, Germany
Meudtner, Andreas Dipl.-Ing.	LCP Laser-Cut-Processing GmbH Heinrich-Hertz-Str. 16 07629 Hermsdorf, Germany andreas.meudtner@lcp GmbH.de
Münch, Marcella B. Sc.	Friedrich-Schiller-Universität Jena Fürstengraben 1 07743 Jena, Germany marcella.muench@gmail.com
Myslivets, Aliaksandr	I-Photonics UAB Parko st. 3 Avizieniu, 14180 Lithuania, a.myslivets@i-photonics.lt

Autor	Anschrift
Nolte, Stefan Prof. Dr.	Friedrich Schiller University Jena Institute of Applied Physics, Abbe Center of Photonics Albert-Einstein-Straße 15 07745 Jena, Germany and Fraunhofer Institute for Applied Optics and Precision Engineering IOF Albert-Einstein-Straße 7 07745 Jena, Germany stefan.nolte@uni-jena.de
Ohlinger, A.	SCHOTT AG Hattenbergstraße 10 55122 Mainz, Germany
Olbrich, M.	Laserinstitut Hochschule Mittweida Technikumplatz 17 09648 Mittweida, Germany
Passlack, Sven Dipl.-Phys.	Institut für Oberflächen- und Schichttechnik GmbH Trippstadter Straße 120 67663 Kaiserslautern, Germany and Landesforschungszentrum OPTIMAS RPTU Kaiserslautern-Landau 67655 Kaiserslautern, Germany passlack@ifos.uni-kl.de
Pflug, T.	Laserinstitut Hochschule Mittweida Technikumplatz 17 09648 Mittweida, Germany
Pfuch, Andreas Dr.	INNOVENT e. V. Prüssingstraße 27 B 07745 Jena, Germany ap@innovent-jena.de
Polojärvi, V.	SCHOTT Primoceler Oy Vesiroineenkatu 3 33720 Tampere, Finland
Prowaznik, Robert	ifw Jena - Günter-Köhler-Institut für Fügetechnik und Werkstoffprüfung GmbH Ernst Ruska Ring 3 07745 Jena, Germany rprowarznik@ifw-jena.de
Reichenbächer, Maria M. Eng.	ifw Jena - Günter-Köhler-Institut für Fügetechnik und Werkstoffprüfung GmbH Ernst-Ruska-Ring 3 07745 Jena, Germany mreichenbaecher@ifw-jena.de
Reinlein, Claudia Dr.	ROBUST AO GmbH Hans-Knöll-Straße 6 07743 Jena

Autor	Anschrift
Reuter, Justus B.Sc.	Laserinstitut Hochschule Mittweida Technikumplatz 17 09648 Mittweida jreuter1@hs-mittweida.de
Rochholz, Christian M.Eng.	LCP Laser-Cut-Processing GmbH, Heinrich-Hertz-Str. 16 07629 Hermsdorf, Germany christian.rochholz@lcp GmbH.de
Schäfer, Mareike Dr. rer. nat. (Dipl.-Ing.)	Institut für Oberflächen- und Schichttechnik GmbH Trippstadter Straße 120 67663 Kaiserslautern, Germany and Landesforschungszentrum OPTIMAS RPTU Kaiserslautern-Landau 67655 Kaiserslautern, Germany schaefer@ifos.uni-kl.de
Schippel, Stefan Dr. rer. nat.	Layertec GmbH Ernst-Abbe-Weg 1 99441 Mellingen stefan.schippel@layertec.de
Schlutow, Henrike	asphericon GmbH Stockholmer Str. 9 07747 Jena, Germany
Schmidt, Jürgen Dipl.- Ing.	INNOVENT e. V. Ilmstraße 18 07743 Jena, Germany js@innovent-jena.de
Schmitz, Martin Dipl.-Ing., Dipl.-Wirtsch.-Ing.	ifw Jena - Günter-Köhler-Institut für Fügetechnik und Werkstoffprüfung GmbH Ernst Ruska Ring 3 07745 Jena, Germany mschitz@ifw-jena.de
Schnell, G.	University of Rostock Chair of Microfluidics Faculty of Mechanical Engineering and Marine Technology Justus-von-Liebig Weg 6 18059 Rostock, Germany
Schob, Bernd Dipl.-Ing.	Technische Universität Chemnitz Professur Strukturleichtbau und Kunststoffverarbeitung Reichenhainer Straße 31/33 09126 Chemnitz, Germany bernd.schob@mb.tu-chemnitz.de
Schönherr, Andy M.Sc.	Technische Universität Chemnitz Professur Strukturleichtbau und Kunststoffverarbeitung Reichenhainer Straße 31/33 09126 Chemnitz, Germany andy.schoenherr@mb.tu-chemnitz.de

Autor	Anschrift
Schusser, G.	Fraunhofer Institute for Microstructures of Materials and Systems IMWS Walter-Hülse-Straße 1 06120 Halle (Saale), Germany
Seiler, Michael M.Eng.	Schott Technical Glass Solutions GmbH Otto-Schott-Str. 13 07745 Jena, Germany michael.seiler@schott.com and Ernst-Abbe-Hochschule Jena Carl-Zeiss-Promenade 2 07745 Jena, Germany
Seitz, H.	University of Rostock Chair of Microfluidics Faculty of Mechanical Engineering and Marine Technology Justus-von-Liebig Weg 6 18059 Rostock, Germany and University of Rostock Department Life, Light & Matter Albert-Einstein-Str. 25 18059 Rostock, Germany
Seyfarth, Brian	Institute of Applied Physics, Abbe Center of Photonics Friedrich-Schiller-Universität Jena Albert-Einstein-Str. 15 07745 Jena, Germany
Steckermeier, A.	SCHOTT AG Hattenbergstraße 10 55122 Mainz, Germany
Streek, André Prof. Dr.-Ing.	Laserinstitut Hochschule Mittweida Technikumplatz 17 09648 Mittweida streek@hs-mittweida.de
Thomas, Jens Ulrich Dr.	SCHOTT AG Hattenbergstraße 10 55122 Mainz, Germany jensulrich.thomas@schott.com
Thomas, Robert Dipl.-Ing.	Universität Rostock, Lehrstuhl für Mikrofluidik Justus-von-Liebig Weg 6 18059 Rostock robert.thomas@uni-rostock.de
Ullmann, Linda	Fraunhofer Institute for Material and Beam Technology IWS Winterbergstraße 28 01277 Dresden, Germany linda.ullmann@iws.fraunhofer.de

Autor	Anschrift
Ulrich, Stefan	ROBUST AO GmbH Hans-Knöll-Straße 6 07743 Jena stefan.ulrich@robustao.de
Voigt, Sven Dipl.-Ing.	Fraunhofer-Institut für Elektronische Nanosysteme (ENAS) Technologie-Campus 3 09126 Chemnitz, Germany sven.voigt@enas.fraunhofer.de
Wang, Ziyao	Institute of Applied Physics, Abbe Center of Photonics Friedrich-Schiller-Universität Jena Albert-Einstein-Str. 15 07745 Jena, Germany
Westphal, E.	University of Rostock Chair of Microfluidics Faculty of Mechanical Engineering and Marine Technology Justus-von-Liebig Weg 6 18059 Rostock, Germany
Wetzig, Andreas	Fraunhofer Institute for Material and Beam Technology IWS Winterbergstraße 28 01277 Dresden, Germany
Xu, Qian	Institute of Applied Physics, Abbe Center of Photonics Friedrich-Schiller-Universität Jena Albert-Einstein-Str. 15 07745 Jena, Germany